

Photophysical and Electronic Properties of Heterogeneous, Coupled Systems Containing Organic Semiconductors

Dissertation

der Mathematisch-Naturwissenschaftlichen Fakultät
der Eberhard Karls Universität Tübingen
zur Erlangung des Grades eines
Doktors der Naturwissenschaften
(Dr. rer. nat.)

vorgelegt von
Christoph Pirmin Theurer
aus Friedrichshafen

Tübingen
2023

Gedruckt mit Genehmigung der Mathematisch-Naturwissenschaftlichen Fakultät der Eberhard Karls Universität Tübingen.

| | |
|-----------------------------------|------------------------------------|
| Tag der mündlichen Qualifikation: | 09.02.2024 |
| Dekan: | Prof. Dr. Thilo Stehle |
| 1. Berichterstatter: | Prof. Dr. Dr. h.c. Frank Schreiber |
| 2. Berichterstatterin: | JProf. Dr. Jannika Lauth |

Deutsche Zusammenfassung

In dieser Dissertation werden die optischen, elektronischen, strukturellen und photophysikalischen Eigenschaften gekoppelter Systeme analysiert. Speziell werden heterogene Systeme untersucht, die als einen Hauptbestandteil organische Halbleiter enthalten. Organische Halbleiter sind konjugierte Verbindungen, die hauptsächlich aus Kohlenstoff bestehen und die im Festkörper charakteristische Eigenschaften von Halbleitern aufweisen, wozu eine signifikante Leitfähigkeit bei Raumtemperatur und die Fähigkeit zur Absorption und Emission von Licht gehören. Durch diese Eigenschaften stellen organische Halbleiter vielversprechende Materialien für den Einsatz in (opto-) elektronischen Bauelementen wie z.B. Solarzellen und Leuchtdioden dar. Für viele Anwendungen sind jedoch reine organische Halbleiter nicht besonders gut geeignet, unter anderem da sie im Allgemeinen eine relativ geringe Leitfähigkeit aufweisen. Deshalb sind in den letzten Jahren zunehmend gemischte, gekoppelte Materialien in den Fokus der Forschung gerückt, da diese vielversprechendere Eigenschaften als reine organische Halbleiter besitzen können. Um Eigenschaften zu erzielen, die über die Eigenschaften der reinen Komponenten hinaus gehen, sind Kopplungen in diesen gemischten Systemen von entscheidender Bedeutung. Diese Kopplungen und die daraus resultierenden Eigenschaften sind jedoch nicht vollständig verstanden und bilden daher den Forschungsgegenstand dieser Dissertation.

In dieser Arbeit werden drei verschiedene Kategorien heterogener, gekoppelter Systeme betrachtet, in denen verschiedene Arten von Kopplungen von besonderer Bedeutung sind. Die Systeme der ersten Kategorie bestehen aus Donator-Akzeptor Mischungen organischer Halbleiter, die in dünnen Filmen analysiert werden. Donator-Moleküle zeichnen sich durch ein geringes Ionisationspotential (IP) und Akzeptor-Moleküle durch eine hohe Elektronenaffinität (EA) aus, wodurch bei gegebener elektronischer Kopplung ein Ladungstransfer zwischen diesen Molekülen stattfinden kann. Die Stärke der elektronischen Kopplung ist hierbei für die Art des Ladungstransfers bedeutsam. Verschiedene Ladungstransferarten sind z.B. für die Erhöhung der Leitfähigkeit organischer Halbleiter mittels Dotierung und für die Ladungstrennung in organischen Solarzellen von entscheidender Bedeutung. In dieser Dissertation werden die vier verschiedenen Kombinationsmöglichkeiten zweier Donator Materialien und zweier Akzeptor Materialien in gemischten dünnen Filmen systematisch untersucht. Mithilfe experimenteller und theoretischer Methoden wird gezeigt, dass verschiedene Ladungstransferarten in diesen Filmen auftreten. Des Weiteren wird der Einfluss des IP und der EA, des

Mischungsverhältnisses sowie der elektronischen Kopplung auf die Art des Ladungstransfers aufgezeigt. Außerdem wird die Photophysik dieser Filme untersucht, wobei ein besonderes Augenmerk auf die Singulett-Spaltung (SF, von engl. singlet fission) gelegt wird, die in den reinen Donator Materialien nachgewiesen wurde. Dieser Prozess beschreibt die spontane Umwandlung eines fotogenerierten Singulett Exzitons in zwei Triplett Exzitonen, der über einen gekoppelten Triplet Paar Zustand verläuft. Mithilfe der SF könnte der Wirkungsgrad organischer Solarzellen gesteigert werden. Zudem ist der Triplet Paar Zustand aufgrund seiner Kopplung und seines Multi-Exzitonen Charakters von grundlegendem Interesse. Es wird gezeigt, dass SF auch in Mischungen mit geringem Akzeptor Anteil auftritt, was die Robustheit des SF-Prozesses verdeutlicht. Diese Robustheit ist für die tatsächliche Nutzung der SF in organischen Solarzellen entscheidend. Zusätzlich wird bei tiefen Temperaturen eine starke Emission aus dem Triplet Paar Zustand des einen Donator Materials festgestellt, was aufgrund des Multi-Exzitonen Charakters dieses Zustandes ein interessantes Ergebnis ist, welches als Ausgangspunkt für moderne quantenchemische Rechnungen dienen kann.

Die zweite Kategorie gekoppelter Systeme, die in dieser Arbeit diskutiert wird, umfasst organische dünne Filme auf Gittern aus plasmonischen Nanostrukturen. Diese Systeme eignen sich hervorragend, um starke Licht-Materie Kopplung zu erforschen. Bei dieser Kopplungsart hybridisieren die elektronischen Anregungen im organischen Halbleiter mit den kollektiven Gitterresonanzen des plasmonischen Gitters, wodurch sich die Energieniveaus im organischen Halbleiter verschieben, was wiederum dessen photophysikalische und chemische Eigenschaften beeinflussen kann. In dieser Dissertation wird starke Licht-Materie Kopplung in polykristallinen Filmen auf plasmonischen Gittern, welche scharfe, kollektive Gitterresonanzen aufweisen, belegt. Die offene Struktur der plasmonischen Kavität sowie die gute Herstellbarkeit polykristalliner Filme sorgen für eine technologische Relevanz dieser Beobachtung. Zudem wurde ein System geschaffen, mit dessen Hilfe der theoretisch vorhergesagte Einfluss der starken Licht-Materie Kopplung auf die SF untersucht werden kann.

Als dritte Kategorie werden gekoppelte organisch-anorganische Halbleitersysteme in dieser Dissertation erforscht. In diesen Materialien ist es möglich, die vorteilhaften Eigenschaften beider Komponenten zu kombinieren und neue Eigenschaften zu kreieren. Hierfür ist ein elektronisches Koppeln der verschiedenen Materialien sowie die Beschaffenheit der Grenzfläche von entscheidender Bedeutung. Besonders vielversprechend sind hybride Materialien aus organischen Halbleitern und anorganischen Halbleiternanopartikeln, da sich die optischen und elektronischen Eigenschaften beider Komponenten gezielt modifizieren lassen. Zudem können die organischen Halbleiter chemisch an die Nanopartikel gebunden werden, wodurch ein chemisch gekoppeltes Netzwerk realisierbar ist. Die exakte Art der Bindung und die Anordnung der organischen und anorganischen Komponenten ist jedoch, trotz ihrer großen Bedeutung, noch weitgehend unerforscht. Daher werden diese beiden Aspekte in dieser Dissertation an zwei Modellsystemen detailliert untersucht, wodurch die Bindungsart sowie die Anordnung entschlüsselt wird. Zudem wird ein Einfluss dieser chemischen Bindung auf die optischen und photophysikalischen Eigenschaften der Systeme beobachtet, jedoch werden keine klaren

Hinweise auf eine elektronische Kopplung gefunden, was die Komplexität dieser hybriden Systeme verdeutlicht. Prinzipiell könnten in solche organisch-anorganischen Hybridsysteme zum Beispiel auch SF-Materialien integriert werden, wodurch eine effektive Extraktion der Triplett Exzitonen vorstellbar ist.

Zusammengefasst wird in dieser Arbeit der Zusammenhang zwischen verschiedenen Kopplungsarten und den strukturellen, elektronischen, optischen und photophysikalischen Eigenschaften heterogener Systeme hergestellt. Die erlangten grundlegenden Erkenntnisse tragen zu einem besseren Verständnis dieser vielversprechenden Materialien bei, was einen wichtigen Schritt in Richtung ihrer technologischen Anwendung darstellt.

Contents

| | | |
|----------|--|-----------|
| I | Introduction and Fundamentals | 1 |
| 1 | Introduction | 3 |
| 2 | Fundamentals | 7 |
| 2.1 | Coupling | 7 |
| 2.2 | Organic semiconductors | 10 |
| 2.2.1 | Single molecules | 10 |
| 2.2.2 | Thin films | 11 |
| 2.2.3 | Excited states and transitions of single molecules | 12 |
| 2.2.4 | Excitons in molecular solids | 18 |
| 2.2.5 | Singlet fission | 20 |
| 2.2.6 | Blends of organic semiconductors | 22 |
| 2.3 | Inorganic semiconductor nanoparticles | 27 |
| 2.3.1 | Electronic structure of quantum dots | 28 |
| 2.3.2 | Optical properties of quantum dots | 30 |
| 2.3.3 | Quantum dots coupled with organic semiconductors | 31 |
| 2.4 | Plasmonics and light-matter coupling | 32 |
| 2.4.1 | Localized surface plasmons | 32 |
| 2.4.2 | Surface lattice resonances | 35 |
| 2.4.3 | Strong light-matter coupling | 38 |
| 3 | Materials and sample preparation | 41 |
| 3.1 | Substrates | 41 |
| 3.2 | Organic semiconductor samples | 42 |
| 3.2.1 | Acenes | 42 |
| 3.2.2 | Acceptors | 44 |
| 3.2.3 | Organic molecular beam deposition | 45 |
| 3.3 | Organic-inorganic semiconductor samples | 46 |
| 3.3.1 | Aryleneethynylene derivatives | 46 |
| 3.3.2 | CdSe quantum dots | 47 |

| | | |
|-----------|---|-----------|
| 3.3.3 | Sample preparation from solution | 49 |
| 3.4 | Plasmonic silver nanoparticle arrays | 50 |
| 3.4.1 | Electron-beam lithography | 51 |
| 3.4.2 | Metal deposition | 51 |
| 3.4.3 | Atomic layer deposition | 52 |
| 4 | Characterization techniques | 55 |
| 4.1 | X-ray diffraction | 55 |
| 4.1.1 | X-ray reflectivity | 56 |
| 4.1.2 | Grazing-incidence X-ray diffraction | 57 |
| 4.2 | Infrared spectroscopy | 58 |
| 4.2.1 | Fourier-transform infrared spectroscopy | 58 |
| 4.2.2 | Polarization-modulation infrared reflection-absorption spectroscopy | 59 |
| 4.3 | UV-vis-NIR spectroscopy | 60 |
| 4.4 | Photoluminescence spectroscopy | 62 |
| 4.5 | Transient absorption spectroscopy | 62 |
| 4.5.1 | Setup and technique | 63 |
| 4.5.2 | Signals in transient absorption spectra | 64 |
| 4.5.3 | Transient absorption data analysis | 66 |
| 4.5.4 | Experimental setup used in this work | 67 |
| II | Results and Discussion | 69 |
| 5 | Charge transfer complexes of tetracene with strong acceptors | 71 |
| 5.1 | Introduction | 71 |
| 5.2 | X-ray diffraction | 72 |
| 5.3 | Optical spectroscopy | 73 |
| 5.4 | Vibrational spectroscopy | 75 |
| 5.5 | Ab initio calculations | 76 |
| 5.6 | Transient absorption spectroscopy | 80 |
| 5.7 | Conclusion | 88 |
| 6 | Ion pairs and charge transfer complexes of pentacene with strong acceptors | 89 |
| 6.1 | Introduction | 90 |
| 6.2 | X-ray diffraction | 90 |
| 6.3 | Optical spectroscopy | 92 |
| 6.4 | Vibrational spectroscopy | 93 |
| 6.5 | Transient absorption spectroscopy | 94 |
| 6.6 | Discussion | 101 |
| 6.7 | Conclusion | 105 |

| | | |
|------------|--|------------|
| 7 | Pentacene triplet pair state emission | 107 |
| 7.1 | Introduction | 107 |
| 7.2 | Sample description | 108 |
| 7.3 | Temperature dependent photoluminescence spectroscopy | 109 |
| 7.4 | Discussion | 111 |
| 7.5 | Conclusion | 114 |
| 8 | Strong light-matter coupling in pentacene on plasmonic arrays | 117 |
| 8.1 | Introduction | 117 |
| 8.2 | Sample description | 118 |
| 8.3 | Extinction measurements of the uncoupled systems | 120 |
| 8.4 | Extinction measurements of the coupled systems | 124 |
| 8.5 | Discussion | 126 |
| 8.6 | Conclusion | 128 |
| 9 | CdSe quantum dots coupled with aryeneethylenes | 129 |
| 9.1 | Introduction | 129 |
| 9.2 | Vibrational spectroscopy | 130 |
| 9.3 | X-ray diffraction | 134 |
| 9.4 | Optical spectroscopy | 136 |
| 9.5 | Transient absorption spectroscopy | 138 |
| 9.6 | Discussion | 143 |
| 9.7 | Conclusion | 147 |
| 10 | Conclusion and Outlook | 149 |
| 10.1 | Conclusion | 149 |
| 10.2 | Outlook | 152 |
| III | Appendix | 155 |
| A | Tetracene:acceptor blends | 157 |
| A.1 | Reciprocal space maps | 157 |
| A.2 | Details to the TA data of neat TET | 159 |
| A.3 | Details to the TA data of the neat acceptors | 160 |
| A.4 | Details to the TA data of the blends | 161 |
| B | Pentacene:acceptor blends | 163 |
| C | Pentacene triplet pair state emission | 169 |
| D | Pentacene on plasmonic arrays | 171 |

| | |
|--|------------|
| E Organic-inorganic thin films | 175 |
| E.1 Thickness and morphology | 175 |
| E.2 TA excitation density | 177 |
| E.3 Further TA data | 178 |
| F Contributions | 179 |
| G List of abbreviations | 181 |
| Bibliography | 185 |

Part I

Introduction and Fundamentals

1. Introduction

Our modern society relies heavily on the use of semiconductors in various applications. Integrated circuits, used in computers, mobile phones, and almost all types of controllers, as well as optoelectronic devices, including solar cells and light-emitting diodes, to name only a few, depend on semiconductors [1]. Nowadays, most of these devices are based on inorganic semiconductors, especially silicon, due to its abundance and favorable properties like the ease to produce insulating silicon oxide layers during the manufacturing process [2]. However, for specific applications, organic semiconductors (OSCs) that mainly consist of carbon can offer several advantages, as detailed below [3]. Therefore, they are predicted to play an important role in the 21st century and can partially replace inorganic semiconductors [4].

A key advantage of OSCs is the possibility to tune their (opto)-electronic properties, such as the absorption and emission spectra, by chemical modification [5]. Moreover, OSCs can exhibit large absorption cross sections and a high quantum yield of luminescence [6]. These beneficial properties facilitated their successful implementation in organic light-emitting diodes (OLEDs) [7]. Displays based on OLEDs are commercially available and offer excellent brightness, contrast, and energy efficiency [8]. The availability of cost- and energy-efficient production procedures combined with the sufficiency of ultra-thin films for many applications are further advantages of OSCs [5]. The use of ultra-thin films opens the possibility to manufacture lightweight, transparent devices on flexible substrates, which is especially important for large-area applications [3]. Due to the mentioned properties, there is also great hope for the widespread use of OSCs in organic photovoltaic cells [9, 10]. Power conversion efficiencies exceeding 16 % have been achieved in single-junction cells [11]. To further increase the power conversion efficiency, so-called third generation solar cells are being developed that go beyond standard single-junction solar cells [12].

One process that has been intensively studied in this context in the last decade is singlet fission (SF) [13–15]. In this spin-allowed process, one photoexcited singlet exciton spontaneously splits into two triplet excitons via an intermediate, electronically coupled triplet pair state with overall singlet character [16, 17]. Consequently, the absorption of one high-energy photon results in the formation of two lower-energy excitons. This down-conversion process might be utilized by applying a sensitizing SF layer on top of a solar cell [18, 19]. The active material of the underlying solar cell should have a bandgap that is similar in energy to the triplet exciton energy in the SF material. Then, high-energy photons can be absorbed in the

sensitizing SF layer and two low-energy triplet excitons can be transferred to the solar cell, which promises to increase the power conversion efficiency and to overcome the Shockley-Queisser limit for single-junction solar cells [14, 20, 21]. The complex SF process is also of fundamental interest, especially due to the involved coupled triplet pair state as an important intermediate [16, 22]. This rich photophysics makes SF materials interesting research objects for this thesis and they serve as examples of the importance of electronic coupling in neat OSC materials [23].

Yet, for many applications, neat OSCs are not ideally suited, *inter alia* due to their generally low conductivity [3]. As a result, various heterogeneous systems that capitalize on coupling effects between the different components have attracted considerable research efforts in recent years [24–26]. Such coupled systems that can exhibit improved properties compared to neat OSC materials are the main focus of this thesis.

The first category of heterogeneous coupled systems that are investigated in this work are mixed OSC materials. In these systems, electronic coupling between different kinds of molecules is fundamentally important as it provides the basis for charge transfer (CT) between electron-donating and electron-accepting molecules [27–31]. Two different kinds of CT can be discerned, namely excited state CT and ground state CT. While excited state CT is of critical importance for charge separation in organic solar cells [27, 32, 33], ground state CT is exploited in molecular doping to increase the generally small conductivity of OSCs [26, 34]. There exist two different ground state CT mechanisms, namely partial and integer CT [35]. For molecular doping purposes, integer CT, thus ion pair formation, is favorable due to the larger amount of free charge carriers at room temperature [36]. Partial CT results instead in the formation of charge transfer complexes (CTCs), which are fundamentally interesting due to the hybridization of the frontier orbitals of the constituent molecules [35]. Such CTCs can have very small band gaps, rendering them promising candidates for near-infrared (NIR) photodetectors [37]. Which CT mechanism is realized for a certain material combination is difficult to predict and depends on the properties of the neat materials as well as the electronic coupling between them, which in turn depends on the molecular arrangement [38, 39]. The occurrence of different CT mechanisms is investigated in this thesis in the model systems of tetracene (TET) and pentacene (PEN) as two SF materials in blends with two prototypical strong electron acceptors [35, 40–42]. Additionally, the photophysical properties of these blends are studied with a special focus on the SF process and its robustness to the presence of electron-accepting molecules.

Mixing different OSC materials into blends is not the only alternative to chemical modification in order to tune the properties of OSC materials. Another promising approach that received increasing interest in recent years capitalizes on the possibility of strongly coupling light and matter [25, 43, 44]. In the strong coupling regime, it is not possible anymore to consider excitons and photons independently, but instead, new quasi-particles, which are called exciton-polaritons, are formed [45, 46]. Such strong light-matter coupling can, for instance, be realized in OSCs inside a microcavity composed of two mirrors that confine the photons,

or in an OSC crystal or thin film on top of a plasmonic array [47–50]. As hybrid light-matter states, the formed exciton-polaritons exhibit mixed properties from both the photon and the exciton component [46, 51]. They feature fascinating effects like an enhancement of the exciton diffusion length or polariton lasing with promising application possibilities [51–54]. Furthermore, as a consequence of the polariton formation, the energy landscapes of the excited states of an OSC material can be modified, which can lead to an altered chemical reactivity and modified excited state dynamics [25, 55, 56]. Consequently, strong light-matter coupling might also be used to influence the SF process, which has recently been predicted in theoretical reports and investigated in first experiments [57–62]. To date, most studies of strong light-matter coupling have been conducted on single crystals of OSCs or on dye molecules dissolved in a host matrix [47, 63]. Additionally, mainly closed microcavities have been used so far, which complicates the in- and out-coupling of light and the contacting of the organic layer [48, 51, 61]. In this thesis, strong light-matter coupling in polycrystalline PEN thin films on open plasmonic arrays is demonstrated. This system can provide a valuable platform to study the influence of strong light-matter coupling on the SF process.

Finally, the combination of organic and inorganic semiconductors in one hybrid material provides the possibility to create new functional materials that capitalize on the electronic coupling between the two different material classes [64, 65]. Especially promising are hybrid materials composed of OSCs and inorganic semiconductor nanoparticles, called quantum dots (QDs), since the energy levels and optical properties of both components can be tuned [24, 65]. In hybrid materials, the advantages of organic and inorganic materials can be exploited and the emerging properties can be beyond the sum of the properties of the individual components [24, 66]. Optoelectronic devices like diodes, photodetectors, and solar cells have been realized based on such hybrid systems [67–70]. The organic and inorganic components in these hybrid systems can be either randomly mixed or arranged in an ordered, interconnected network as a result of direct chemical bonding [71, 72]. Since charge and energy transfer processes across the organic-inorganic interface are of fundamental importance to achieve new functionality, the latter approach is very promising as it allows to control this interface [24, 73]. Consequently, such coupled organic-inorganic nanostructures are promising candidates for, e.g., photon upconversion, optical communication, and solar cells [74–79]. However, the details of the organic-inorganic interface, like the structural arrangement and the chemical bonding, are less investigated for these coupled organic-inorganic nanostructures. This represents a major challenge for their further development and widespread application [24]. Therefore, two model systems are studied in this thesis with a focus on the details of the organic-inorganic interface and the electronic coupling between the different material classes.

Taken together, there is a wide variety of possible ways in which the properties of OSCs can be adapted and enhanced to suit specific applications. Most of these approaches have in common that they utilize coupling effects between different components to achieve new functionality [80]. Within this thesis, examples of different heterogeneous, coupled systems

that contain OSCs as a major part are investigated to broaden the fundamental understanding of their structural, electronic, optical, and photophysical properties.

This thesis is structured as follows. First, the fundamentals and physical concepts relevant for understanding the results of this work are introduced in Chapter 2. Specifically, the general concept of coupling as well as important properties of the different investigated material classes, namely OSCs, inorganic semiconductor nanoparticles and plasmonic metallic nanoparticles, are briefly described. In Chapter 3, the specific materials and the sample preparation methods for the purely organic semiconductor samples, the organic-inorganic semiconductor samples and the plasmonic nanoparticle arrays are presented. It follows a description of the employed experimental techniques in Chapter 4, which were used to characterize the structural, vibrational, optical, and photophysical properties of the samples and to obtain the results presented in Part II of this thesis.

This second part of the thesis starts with the discussion of the results of the purely organic donor:acceptor systems. In Chapter 5, the CT interactions between TET and two strong acceptors are investigated and the photophysics of these interesting samples are established. The study of blends of PEN with the same two acceptors, presented in Chapter 6, provides even deeper insights into the CT mechanisms in OSCs. Additionally, the impact of the intermixed acceptor molecules on the SF process in PEN is investigated in these blends. The SF process in PEN is also connected to the results presented in Chapter 7, in which the emission properties of neat PEN thin films are discussed with a focus on the emission from the electronically coupled triplet pair state at low temperatures. In Chapter 8, strong light-matter coupling in polycrystalline PEN thin films on plasmonic arrays is successfully demonstrated, and the possibility to influence the SF process via strong light-matter coupling is discussed. Last but not least, in Chapter 9, the chemical and electronic coupling as well as the short-range organization in the hybrid organic-inorganic semiconductor samples are analyzed, which contributes to a better understanding of the organic-inorganic interface. Finally, in Chapter 10, the results are summarized and an outlook on further possible research is given.

2. Fundamentals

This chapter provides a brief overview of the fundamentals relevant to this thesis. First, the general concept of coupling is introduced using the demonstrative example of coupled harmonic oscillators, as several kinds of coupling play a central role in this thesis. Subsequently, the different classes of materials studied, namely OSCs, inorganic semiconductor QDs, and metallic nanoparticles, are introduced. The electronic, optical, and photophysical properties of OSCs and QDs are explained, and the different coupling phenomena within and between these two material classes are illustrated. Finally, the plasmonic properties of arrays of metallic nanoparticles are discussed, and the fundamentals of strong light-matter coupling are presented.

2.1 Coupling

In this thesis, coupling phenomena in various forms play an important role. In the most general way, two objects are called coupled if they interact with each other. This is a very wide definition that spans any kind of interaction and thus applies to almost everything. Here, specifically the case of coupled harmonic oscillators will be discussed as a descriptive example, which provides the basis to understand also other coupling phenomena [44, 81]. In a classical picture, a harmonic oscillator can be imagined as a mass m , connected by a spring with spring constant k to a fixed point. If the masses of two such oscillators are connected by an additional spring, they interact with each other and exchange energy via this spring. Therefore, the two oscillators are coupled. Such a system is schematically depicted in Figure 2.1a. The coupling of the system is given by κ , which is in this model the spring constant of the connecting spring.

For the uncoupled, undamped oscillators the eigenfrequencies are given by $\omega_1 = \sqrt{k_1/m}$ and $\omega_2 = \sqrt{k_2/m}$, respectively. Here, the masses of both oscillators are chosen identical to simplify the expressions calculated below for the coupled model. If we now introduce the coupling by choosing $\kappa > 0$, the equations of motion of the system can be written as [81]

$$m\ddot{x}_1(t) + k_1x_1(t) + \kappa(x_1(t) - x_2(t)) = 0 \quad (2.1a)$$

$$m\ddot{x}_2(t) + k_2x_2(t) - \kappa(x_1(t) - x_2(t)) = 0. \quad (2.1b)$$

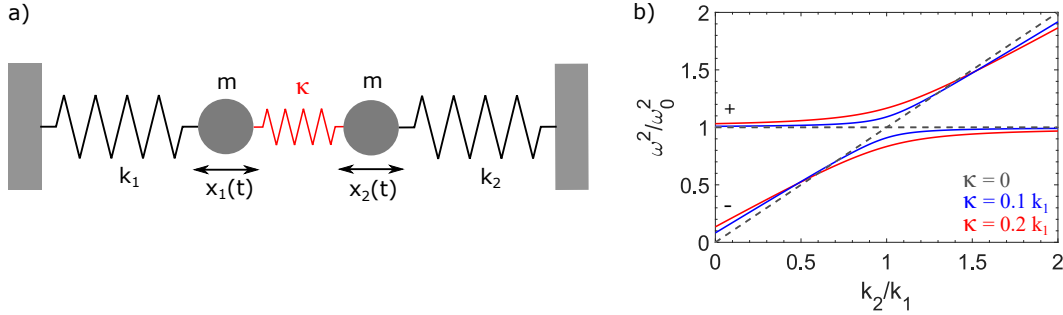


Figure 2.1: a) Schematic illustration of two coupled harmonic oscillators with identical mass m , spring constants k_1 and k_2 , positions $x_1(t)$ and $x_2(t)$, and a coupling spring with constant κ . b) Eigenfrequencies $\omega_{\pm}^2/\omega_0^2$ (from Equation 2.3 with $\omega_0^2 = (k_1 + \kappa)/m$) as a function of k_2 for three different κ . For $\kappa = 0$ (black dashed line), $\omega_+ = \omega_-$ at $k_2 = k_1$, while for $\kappa > 0$ an anticrossing at $k_2 = k_1$ is obtained, which is proportional to κ . Inspired by Ref. [81].

Similar to the uncoupled case, an ansatz in the form of $x_i(t) = x_i^0 \exp(-i\omega_{\pm}t)$ is used, now with the new eigenfrequencies ω_{\pm} as a consequence of the coupling. By inserting this ansatz into Equation 2.1, Equation 2.2, written in the matrix representation, is obtained:

$$\begin{bmatrix} m\omega_{\pm}^2 - k_1 - \kappa & \kappa \\ \kappa & m\omega_{\pm}^2 - k_2 - \kappa \end{bmatrix} \begin{bmatrix} x_1^0 \\ x_2^0 \end{bmatrix} = \mathbf{M} \begin{bmatrix} x_1^0 \\ x_2^0 \end{bmatrix} = 0. \quad (2.2)$$

The non-trivial solutions for the new eigenfrequencies are found by $\det \mathbf{M} = 0$. In the following, the square of the eigenfrequencies (ω_{\pm}^2) is considered, since it is proportional to the energy of the oscillations, which is the important property for the coupling phenomena discussed below. Consequently, ω_{\pm}^2 of the coupled system results as

$$\omega_{\pm}^2 = \frac{1}{2} \left[\frac{k_1 + \kappa}{m} + \frac{k_2 + \kappa}{m} \pm \sqrt{\left(\frac{k_1 - k_2}{m} \right)^2 + 4 \frac{\kappa^2}{m^2}} \right]. \quad (2.3)$$

The first two terms in Equation 2.3 can be understood as the eigenfrequencies of the two oscillators composed of a mass m and two springs with constants k_i and κ . The expression under the square root is the more interesting part concerning the coupling. While the first term under the square root is related to the difference between the eigenfrequencies of the two uncoupled oscillators, the second term is directly related to the coupling strength of the system. Therefore, the two oscillators cannot be described individually anymore but the entire coupled system with new, hybrid eigenfrequencies needs to be considered [44]. Only for weak coupling strengths, the properties of the coupled oscillator system can be approximated by the properties of the individual oscillators [81]. In Figure 2.1b, the eigenfrequencies of the coupled system are plotted in dependence of k_2 while keeping k_1 constant. For a non-vanishing κ , an anticrossing of the two frequencies is observed, which is characteristic for

strong coupling [81]. For $k_1 = k_2$, thus when the eigenfrequencies ω_1 and ω_2 of the uncoupled oscillators are equal, the splitting follows as

$$\omega_+^2 - \omega_-^2 = \frac{2\kappa}{m}. \quad (2.4)$$

Equation 2.4 demonstrates that the splitting between ω_+^2 and ω_-^2 is proportional to the coupling strength κ , resulting in a larger splitting for higher coupling strengths.

Note that in the example described so far, any damping of the coupled oscillator system was ignored, which could be added by $\gamma_i \dot{x}_i$ terms in Equation 2.1, describing a friction in dependence of the velocity [81]. This would result in complex frequency eigenvalues, with the imaginary part representing the linewidth related to the energy dissipation. A splitting of the frequencies is then only observable if the coupling strength is larger than the dissipation in each system, which can be considered as a criterion for strong coupling [81]. Instead, if the decay rate of one or both oscillators is larger than the energy transfer rate, weak coupling is realized [82].

This simple mechanical example can, of course, not quantitatively describe all different coupling possibilities, but often it can provide an intuitive picture, e.g. for strong light-matter coupling, which is detailed in Section 2.4.3. Similarly, the concept of Frenkel excitons in OSCs and the appearance of a Davydov splitting (cf. Section 2.2.4), due to rather long ranged Coulomb coupling [83], can be understood at the example of coupled harmonic oscillators. For neutral molecules or QDs, the dipole-dipole coupling is the most important part of the Coulomb interaction, and, e.g., the Förster resonance energy transfer (FRET) process (cf. Section 2.2.6) can be explained by weak dipole-dipole coupling [82]. Another important kind of coupling for this work results from orbital or wavefunction overlap between neighboring molecules or QD, which can give rise to electron exchange contributions and CT mediated coupling [83, 84]. This short-range coupling due to orbital overlap is, e.g., important for Dexter energy transfer and CT phenomena (cf. Section 2.2.6), the Davydov splitting (cf. Section 2.2.4), and coupled triplet pair states (cf. Section 2.2.5). Coulomb coupling and coupling due to orbital overlap are of major importance for many phenomena investigated in this work and can be summarized as electronic coupling [85]. Often, the mathematics of coupling problems can be expressed in a perturbative approach by a Hamiltonian that resembles Equation 2.2 [85]. Then, the energy of the uncoupled objects or states appears on the diagonal of \mathbf{M} and the coupling energy between them as the off-diagonal elements. Similarly to the mechanical analog, the new eigenstates (energies) of the coupled system can be determined by diagonalizing \mathbf{M} [25]. They are in general different from the energies of the uncoupled system and can show an energy splitting, depending on the coupling strength [82].

2.2 Organic semiconductors

In this section, OSCs are introduced as they are involved in all parts of this thesis. Further details can be found in textbooks [3, 4, 6, 86, 87], which were also used as basis for this chapter. OSCs consist mainly of carbon and hydrogen atoms, but may also contain a few other elements, like nitrogen, oxygen and fluorine for the molecules investigated in this work. In the solid state, e.g. in crystals, thin films or nanoparticles, they exhibit semiconducting properties like the absorption and emission of visible light and a non-negligible conductivity [6]. In general, two different classes of OSCs are distinguished, namely small-molecule OSCs with a relatively low molecular weight and polymers that can consist of thousands of covalently linked monomers [3]. In this thesis, only small-molecule OSCs were investigated and the term OSC is used for this material class in the following.

2.2.1 Single molecules

As the name suggests, these OSCs consist of small molecules containing generally 10-100 atoms [3]. The backbone of these molecules is built mainly from carbon atoms that are sp^2 -hybridized, implying that they can form three bonds in a plane to neighboring atoms, while the last atomic p_z -orbital is oriented perpendicular to this plane (Figure 2.2a) [4]. The three bonds in the plane are relatively strong, localized σ -bonds with an angle of $\sim 120^\circ$ in between them [89]. For this reason, many OSCs exhibit a planar structure and hexagonal rings. In contrast to the sp^2 -hybrid orbitals, the remaining p_z -orbitals of neighboring carbon atoms only weakly overlap above and below this plane, which leads to the formation of additional, weaker bonds called π -bonds [89]. If several sp^2 - (or sp -) hybridized carbon atoms are bound to each other, as shown in Figure 2.2b at the example of benzene, the electrons in the π -bonds can be delocalized over the entire conjugated system, resulting in a stabilization of the molecule [89]. This delocalization can be described by introducing molecular π -orbitals (Figure 2.2c), which can be approximately described as a superposition of the atomic p_z -orbitals [6]. The overall number of orbitals remains hereby constant, but the constructed molecular orbitals have different energies depending on the relative phase

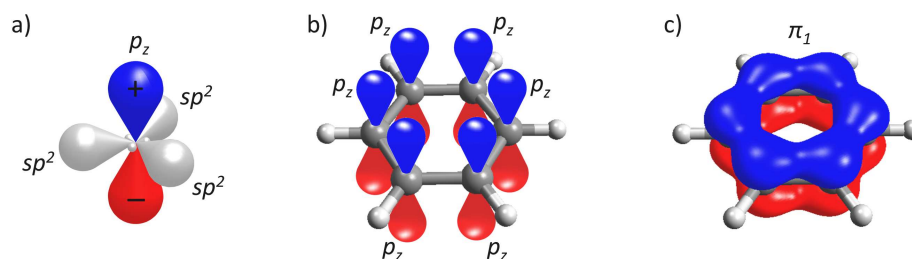


Figure 2.2: Atomic and molecular orbitals. a) sp^2 -hybridized carbon atom, with the three sp^2 -orbitals in one plane and the remaining p_z -orbital perpendicular to this plane. b) Atomic p_z -orbitals in benzene before hybridization. c) Energetically lowest, hybridized molecular π -orbital in benzene. The colors represent the relative phase of the orbitals. Adapted from Ref. [88].

of the atomic orbitals that are combined [89]. In the ground state, the energetically lower half of the molecular π -orbitals is filled with two electrons each and the other half is empty, resulting in an energetically highest occupied molecular orbital (HOMO) and an energetically lowest unoccupied molecular orbital (LUMO) [6]. The energy splitting between the different molecular π -orbitals is relatively small, which is a crucial characteristic for OSCs, as it implies that transitions of electrons between these orbitals can be excited by visible light (cf. Section 2.2.3) [4]. The energy of these transitions depends on the size of the conjugated system [6]. Another important fact is that the π -orbitals are localized above and below the plane of the molecule (Figure 2.2c). Therefore, they can overlap with π -orbitals of adjacent molecules which significantly influences the intermolecular interactions [4].

2.2.2 Thin films

The intermolecular interactions mentioned above are important for the formation of solid materials out of the semiconducting molecules. These molecular solids consist of the single molecules which are mainly bound to each other by relatively weak van-der-Waals interactions [4]. Depending on the intermolecular interactions, also the preferred orientation of the molecules to each other is defined and consequently the crystal structure [90]. One typical motive that is found for many OSCs is the so-called edge-to-face orientation, which leads to the formation of a herringbone structure, see Figure 2.3a [91]. This herringbone structure is found for some of the OSCs that are investigated in thin films in this work. Such OSC thin films can be either grown by organic molecular beam deposition (OMBD) (see Section 3.2.3) or by deposition from solution (Section 3.3.3). The thin films grown via OMBD generally exhibit a higher degree of structural order [6]. In the OMBD process, the molecules condense from the gas phase to the substrate, diffuse on the substrate and finally nucleate, which gives them time to arrange in a preferred orientation [92, 93]. Generally, the growth of OSC thin films is a complex, non-equilibrium process and several growth modes exist [92, 93], but this is not further investigated and discussed in this thesis. In the following, only the most commonly observed final structures of OSC thin films on weakly interacting substrates are briefly described.

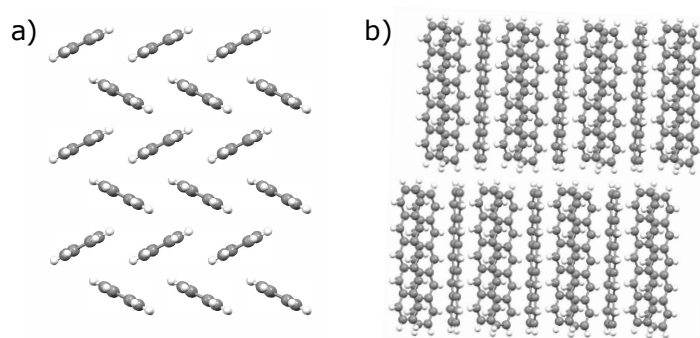


Figure 2.3: Herringbone structure depicted at the example of PEN [94]. a) Top view of a single layer. b) Side view on two stacked layers. Inspired by Ref. [88].

In general, OSC thin films can be categorized as either polycrystalline or amorphous, and the polycrystalline films can be further divided into uniaxially anisotropic and isotropic films, as well as further, special cases [95, 96]. The structural order obtained depends on the specific molecules, their interactions with each other and with the substrate, and the growth process, as mentioned above [92, 93]. Amorphous thin films exhibit no long-range order. Polycrystalline thin films, on the other hand, consist of many coalesced crystallites. In each crystallite, the molecules are located at specific positions with a specific orientation, as for macroscopic single crystals, thus a long-range order is given. The orientation of the different crystallites with respect to each other is, however, not defined. For isotropic polycrystalline films, the crystallites are completely randomly oriented with respect to each other and the substrate. In contrast, for uniaxially anisotropic films, the orientation of the crystallites with respect to the substrate normal is defined, and only the in-plane orientation of the crystallites is randomly distributed. Thus, one axis is preferred, giving rise to different in-plane and out-of-plane properties. The terms "in-plane" and "out-of-plane" are defined with respect to the substrate plane and are used accordingly throughout this thesis unless otherwise stated. Typical examples of uniaxially anisotropic polycrystalline films are neat films of TET and PEN on weakly interacting substrates [97, 98]. These films exhibit molecular planes parallel to the substrate in which the molecules are arranged in a herringbone structure. Along the surface normal, these molecular planes are stacked on top of each other (Figure 2.3b). This results in a dominant electronic coupling between the molecules in the plane and only weak out-of-plane interactions [4].

2.2.3 Excited states and transitions of single molecules

A large fraction of this thesis is devoted to the optical and photophysical properties of OSCs, including the absorption and emission of light as well as the excited state dynamics. These processes can be described by transitions between molecular states, which are introduced in this section. The optical properties of an OSC are mainly governed by transitions between the different electronic states of the molecules, which are related to the electronic wavefunction. An additional important characteristic of an electronic state is the overall spin of the electrons in the molecule, which can be described by the spin wavefunction. Finally, transitions between vibrational states of an OSC, related to the vibrational wavefunction, are important, too, e.g., for the characterization of the purely organic and organic-inorganic semiconductor samples in this work. Thus, these transitions and states are briefly introduced in this section. Only some areas of this large field can be outlined here, while more detailed overviews can be found in the literature, e.g. in Refs [6, 87, 99].

Excited states

The molecular orbitals described in Section 2.2.1, which are obtained by a superposition of atomic orbitals, are so-called one-electron orbitals. This implies that any electron-electron

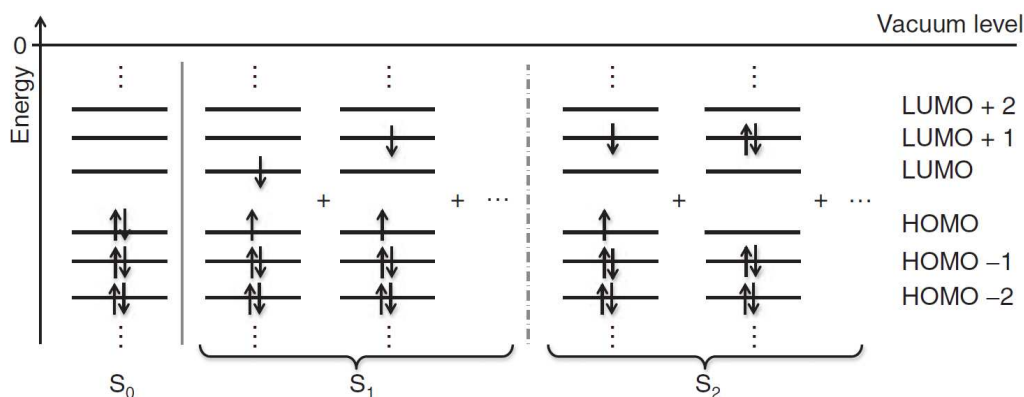


Figure 2.4: Configurations of electronic states. For the excited states S_1 and S_2 two possibly contributing configurations are depicted, which can contribute to different degrees to these states, while also further configurations could be included. Adapted from Ref. [6].

interactions in the molecule are ignored, which is a rough approximation [6]. In order to adequately describe optical processes like absorption and emission in OSCs, it is required to take the entire state of the molecule into account, instead of considering single transitions of electrons between one-electron orbitals. This is done by constructing electronically excited states of the molecule as a linear combination of different configurations, which is called configuration interaction, see Figure 2.4 [6]. Configuration denotes here the distribution of electrons in the molecular orbitals. These constructed states are adiabatic states, which implies that they are eigenstates of the total Hamiltonian of the system and are related to the experimental observables like absorption energies [16]. In contrast, the configurations can be considered as diabatic states, which have a clear and intuitive physical interpretation. Diabatic states are, however, in general no eigenstates of the total Hamiltonian of the system [100]. This discrimination between diabatic and adiabatic states is important for the description of the SF process in Section 2.2.5.

For most molecules, the state with the lowest energy is given by the configuration in which all electrons are paired and found in the lowest possible orbitals. This state has overall spin zero, which makes it a singlet (S) state (*vide infra*), and it is called the ground state S_0 of the molecule. The energy of this ground state is usually set to zero. To the first excited singlet state S_1 , several configurations with overall singlet character contribute. In the following, all orbitals energetically below (above) the mentioned ones are considered to be completely filled (empty). The dominant contribution to the S_1 state is generally from the configuration with one electron in the LUMO and one electron in the HOMO. But also other configurations, with, e.g., one electron in the HOMO-1, two in the HOMO and one in the LUMO, might contribute to a smaller degree (cf. Figure 2.4). It is also worth noting that the energy of the S_1 state is generally smaller than the HOMO-LUMO gap due to the Coulomb attraction between electron and hole [6]. For higher excited singlet states, like S_2 or S_3 , similarly several configurations contribute to different degrees (cf. Figure 2.4). Taken together, by including

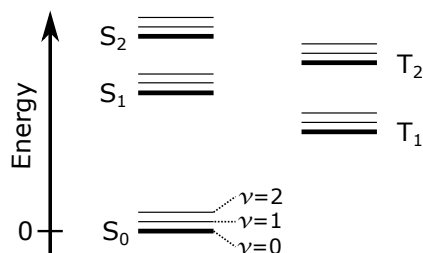


Figure 2.5: Energies of molecular states. The vibrational states are only explicitly labeled for the electronic ground state S_0 .

the configuration interaction, the electronic wavefunction of a state, depending on the electron and nuclei positions, can be constructed.

To fully describe the state of a molecule, also the spin wavefunction and the vibrational wavefunction need to be considered [6]. The spin wavefunction describes the overall spin of the electrons in the molecule. Since electrons in completely filled orbitals have anti-parallel spins, only the unpaired electrons need to be considered. In the configurations considered so far, the two unpaired electrons have anti-parallel spins, which results in overall spin zero and singlet states. If the two unpaired electrons have a parallel spin, the overall spin adds up to one and a triplet state is realized [6]. These triplet states are, similar to the singlet states, denoted as T_1 , T_2 , ... with increasing energy (Figure 2.5). The energy of T_1 is smaller than the energy of S_1 due to the exchange energy [6]. This lowered energy can be classically understood by a reduced Coulomb repulsion of the two unpaired electrons in the triplet state as they have a larger average distance from each other.

Finally, the vibrational wavefunction of the molecule should be considered, which is related to the oscillations of the nuclei. The covalently bound atoms of the molecule can vibrate against each other, which gives rise to vibrationally excited states, denoted by ν . A non-linear molecule has $3N - 6$ normal modes of vibration, with N being the number of atoms in the molecule [101]. Thus, for typical OSCs, a very large number of vibrational modes exist. Often, some of these normal modes can be assigned to functional groups, which are mainly vibrating at a given frequency [102]. Generally, the vibrational states have a smaller energy spacing than the electronic states. In Figure 2.5, the energies of the molecular states are schematically illustrated, with only one vibrational mode explicitly drawn for simplicity. Within the Born-Oppenheimer approximation, which was implicitly used so far, the overall wavefunction of the molecular state can be calculated as the product of the electronic, the vibrational, and the spin wavefunction [6]. This approximation uses the assumption that the different wavefunctions can be calculated independently from each other, which is often a good approximation, since the electrons are much lighter and faster than the nuclei. As a consequence, the electrons can quasi-instantaneously follow the movement of the nuclei and react much faster to any perturbations like electromagnetic radiation [87], which is the subject of the next section.

Radiative transitions between molecular states

As already mentioned above, many OSCs can be excited by the absorption of light in the visible range. This absorption of a photon leads to the formation of a bound electron-hole pair, which is called an exciton. During the excitation process, the electronic (and possibly the vibrational) state of the molecule is changed. Without external influences, the molecule is in the ground state S_0 before the absorption process. After the absorption, the molecule is in an excited singlet state S_n , thus at a higher energy state. Classically, the absorption process can be understood as an interaction of the bound electrons of the molecule with the incoming electromagnetic wave, which drives them to oscillate. Within the dipole approximation, this perturbation of the electron distribution of the molecule by the electromagnetic wave is proportional to $\vec{E}(t) \cdot e \cdot \vec{r}$, with the electric field $\vec{E}(t)$, the elementary charge e , and the position vector \vec{r} [87]. It is assumed that the electromagnetic wave interacts directly only with the electronic wavefunction, since it causes the electrons to oscillate, while the nuclei are too heavy to react to the fast oscillations. This is called the Franck-Condon principle [87]. In the quantum mechanical picture, by applying Fermi's golden rule, the transition rate between the initial and the final state can be calculated in dependence of this perturbation [6]. It is found that only transitions between states of equal spin are allowed in the absence of spin-orbit coupling. Thus, from the singlet ground state only singlet excited states can be reached by the absorption of a photon. Similarly, from an (excited) triplet state, only higher lying triplet states can be excited by a photon. Second, to be dipole allowed, the transition needs to have a non-vanishing transition dipole moment (TDM) $\vec{\mu}$, which is related to the electronic wavefunction overlap and parity of the initial and final state and the dipole operator. The transition rate is proportional to $\vec{\mu} \cdot \vec{E}(t)$ and the TDM is connected to the oscillator strength of a transition, which is a measure for the ability to absorb a photon [6].

Finally, the vibrational wavefunctions of the initial and final state also need to overlap to render a transition allowed. This is illustrated in Figure 2.6, in which the S_0 and S_1 state potentials with the first vibrational states and wavefunctions are sketched in dependence of the nuclear configuration coordinate Q . This nuclear configuration coordinate describes the positions of all nuclei of the molecule and its equilibrium value is generally different for the S_0 and the S_1 states due to the changed electron distribution [6]. Since the nuclei are, however, too slow to directly react to the electromagnetic wave, the electronic state of the molecule is changed without a change in Q , thus by a vertical transition in Figure 2.6. Generally, the molecule is in the vibrational ground state ($\nu = 0$) of S_0 before the excitation, illustrated by the blue wavefunction, and the overlap of this vibrational wavefunction with the (red) vibrational wavefunctions of the S_1 state (Franck-Condon factor) determines the strength of the transition [87]. The transitions into excited vibrational states ($\nu \neq 0$) of the electronic S_1 state are called vibronic transitions, since they involve a vibrational and an electronic transition. These transitions lead to the characteristic vibronic progression found in the absorption spectrum of many OSCs. For single molecules in the gas phase at low temperatures, different vibrational modes can be distinguished as sharp lines in the

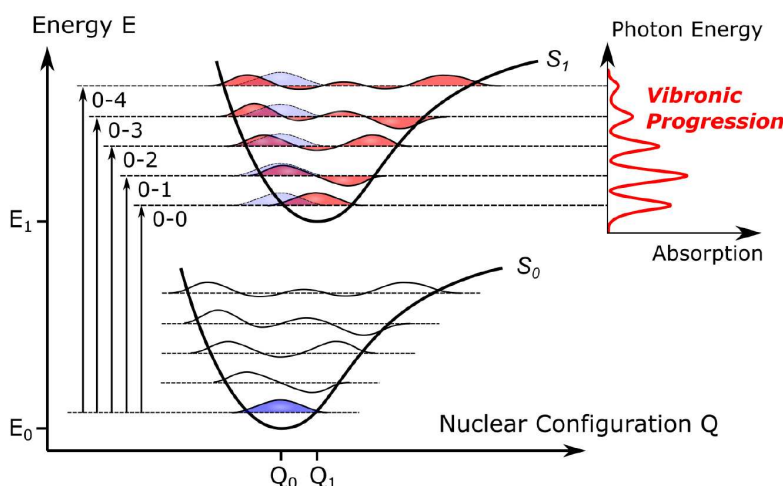


Figure 2.6: Illustration of the vibrational wavefunctions of the S_0 and S_1 state and their overlap. On the right side, the resulting vibronic progression in the absorption spectrum is shown. Adapted from Ref. [88].

absorption spectrum [6]. For thin films, these lines are inhomogeneously broadened and the different vibrational modes cannot be discerned anymore. Instead, the experimentally found vibronic progression can often be described by a single effective vibrational mode [6], that results from a superposition of the individual vibrational modes. The vibronic transitions are labeled by $\nu - \tilde{\nu}$, with ν being the (effective) vibrational state of S_0 (the initial electronic state) and $\tilde{\nu}$ the (effective) vibrational state of S_1 (the final electronic state) (see Figure 2.6).

The fluorescence from a molecule can be understood as the reverse of the absorption process and follows the same principles outlined above. According to Kasha's rule [103], the emission process starts from the vibrationally relaxed S_1 state, since the non-radiative relaxation from higher electronic and vibrational states to the vibrationally relaxed S_1 state have generally higher rates than the direct radiative decay [6]. The final state after the emission process can be a vibrationally excited S_0 state, which results in the occurrence of a vibronic progression in the fluorescence spectrum, too. Additionally, for some OSCs with sufficient spin orbit coupling, also phosphorescence can be observed, which is the radiative decay from the T_1 state to the ground state. Since this transition involves a spin flip, it has generally a very small rate [87]. The absorption and emission processes can be depicted in a Jablonski diagram (Figure 2.7), which shows molecular states and transitions between these states. Additionally to the absorption from the ground state, also absorption processes starting from an excited singlet or triplet state (excited state absorption (ESA)) are depicted in Figure 2.7, which are important for the transient absorption (TA) measurements (compare Section 4.5.2).

So far, electronic and vibronic transitions were described. There is, however, also the possibility of purely vibrational transitions within one electronic state, which can be excited by infrared light. Importantly, to be infrared active, the vibration of the molecule needs to lead to a net change of its dipole moment [101]. Then, the incoming electromagnetic wave

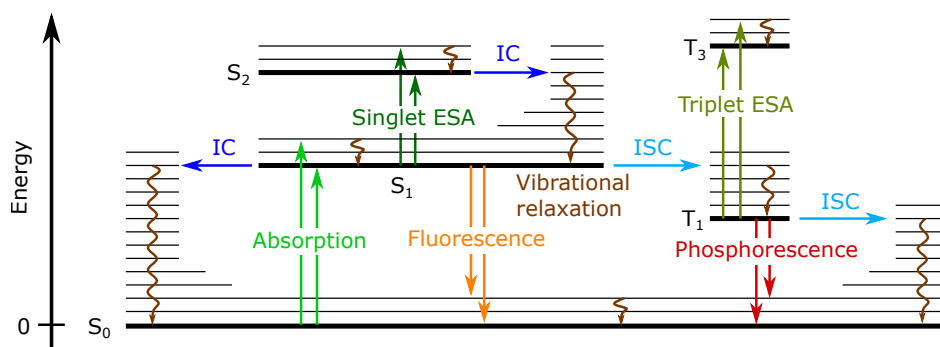


Figure 2.7: Jablonski diagram, illustrating transitions between molecular states. IC abbreviates internal conversion and ISC intersystem crossing. The singlet and triplet ESA is important for the TA measurements (see Section 4.5) and therefore included here. If the fluorescence is stimulated by an incident photon, it is called stimulated emission (in the TA signal). Inspired by Ref. [4].

can drive the oscillation of the nuclei and excite the molecule into a higher vibrational state. Importantly, the equilibrium position of the nuclei does not change during this transition, thus the Franck-Condon principle is not violated. As already mentioned above, a typical OSCs has a very large number of vibrational modes, with some of them being infrared active. Generally, vibrational transitions between neighboring vibrational states ($\Delta\nu = \pm 1$) have the highest transition probabilities [87].

Non-radiative transitions and photophysics

Additionally to the radiative transitions described in the last section, also non-radiative transitions between molecular states can occur. They are summarized, together with the radiative transitions, in the Jablonski diagram in Figure 2.7. First, as mentioned above, a molecule can thermally relax to the vibrational ground state of an electronic state by dissipating energy to its environment. This vibrational relaxation is generally very fast and can outcompete other transitions [104]. Second, there is the possibility of internal conversion, which describes an isoenergetic transition between electronic and vibronic states of the same spin manifold, e.g., from S₂ to the vibrationally excited S₁ state, or from T₂ to T₁. The rate of an internal conversion process depends approximately exponentially on the energy difference between the vibrationally relaxed initial and final electronic state, and becomes larger for smaller energy differences [6]. This is known as the energy gap law. The third possibility is a transition between electronic and vibronic states of different spin manifolds, e.g., from T₁ to S₀ or from S₁ to T₁. These transitions are called intersystem crossing and require a spin flip. Consequently, the rate of these transitions is generally small except for molecules with strong spin-orbit coupling [105]. The energy gap law applies for intersystem crossing, too [6]. All the radiative and non-radiative processes, which can occur after the initial electronic or vibronic excitation of the molecule, are summarized in the term photophysics.

2.2.4 Excitons in molecular solids

So far, the excited states and transitions of single OSC molecules were described. However, isolated molecules in the gas phase are mainly of fundamental and theoretical interest, whereas most investigations and applications are based on solid OSC thin films or crystals. Therefore, aggregation effects must be taken into account. Since in molecular solids the intermolecular binding forces are mostly given by rather weak van-der-Waals interactions (cf. Section 2.2.2), the electronic structure and properties of the constituent molecules are only moderately altered [4]. A few selected effects of aggregation are mentioned in the following, and further details can be found in the literature, e.g., Refs. [4, 6].

Unspecific interactions

The first alteration that shall be considered here is due to the fact that the polarizability α of the environment changes from the isolated molecule to the aggregate [6]. An isolated molecule (in vacuum) has no environment to interact with. As soon as there is any material in the environment, this material will react to an external electric field \vec{E} with an induced electric dipole via $\vec{p}_{\text{ind}} = \alpha\vec{E}$. Similarly, the electric field of an existing electric dipole will induce electric dipoles in the environment, which reduces the potential energy of the initial dipole. A nonpolar OSC molecule possesses only a small dipole moment in the ground state, which results from fluctuations of the electrons. Therefore, the ground state energy of the molecule will only be slightly lowered by embedding it in an environment [6]. On the other hand, the same molecule possesses a larger dipole moment in an excited state after an electronic transition, leading to a larger reduction of the excited state energy [6]. Taken together, this reduces the energy of a given transition of the molecule when the molecule is embedded in a polarizable environment (cf. Figure 2.8).

From these considerations, a second effect can be explained, too, namely the broadening of absorption and emission spectra in the condensed phase. Since the reduction of the transition energy depends on the exact configuration of the surrounding, a statistic, Gaussian distribution of transition energies of different molecules with different environments is seen in recorded spectra. This effect is enhanced with increasing temperature, since then additionally dynamic disorder contributes [106].

Electronic coupling to adjacent molecules

Additionally to the unspecific interactions of OSC molecules with any environment, there are more specific interactions of an OSC molecule with other OSC molecules in molecular solids like thin films or crystals. Here, first the example of two identical molecules with two states and one transition, each, is considered, following the description by Kasha [107]. They shall have a small intermolecular electron overlap so that the two molecules preserve their individuality. This case is called a physical dimer. If this dimer is excited by the absorption of one photon, it cannot be distinguished which molecule was excited, since the two molecules are identical. Thus, the excitation can also be transferred between the two molecules and

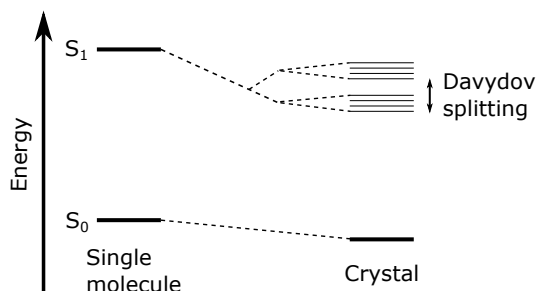


Figure 2.8: Illustration of the effects of aggregation on the energies of the ground and excited states in molecular systems. Inspired by Ref. [6].

the situation can be approximately described as a system of two coupled oscillators (compare Section 2.1). This leads to a splitting of the excitation energies in the dimer, with the magnitude depending on the coupling strength. This coupling is called Coulombic coupling [83]. In the quantum mechanical picture, the physical dimer can be described by the Hamiltonians of the single molecules, expanded by a perturbing term resulting from their interaction. The two new eigenstates of the excited system have then two different energies.

This concept can be generalized from the dimer to extended systems like molecular crystals, which allows to explain the formation of exciton bands [6]. Each molecule is coupled to the neighboring molecules, resulting in a set of new eigenstates with slightly different energies, forming a band. In these exciton bands, the single excitation is shared by many molecules, which is then called a Frenkel exciton [108]. In these Frenkel excitons, the electron and hole are always located on the same molecule but the electron-hole pair is delocalized over many molecules. Due to the relatively small dielectric constant of OSCs, the binding energy of these excitons is large, on the order of hundreds of electronvolts [6]. A more detailed description can be found in Ref. [83], where additionally the coupling to vibrations is considered, resulting in vibronic coupling. Also the appearance of a Davydov splitting [109] in the absorbance spectrum of OSCs is related to the Coulombic coupling between the molecules. A Davydov splitting is observable, if a molecular crystal has at least two molecules with non-parallel TDMs per unit cell, like in the herringbone arrangement described in Section 2.2.2. For the case of two molecules per unit cell, these two basis molecules can be considered as a dimer, which can be described by the dimer model outlined above [6]. For non-parallel TDMs of these basis molecules, the transitions from the ground state to the two new excited eigenstates have non-vanishing oscillator strengths, leading to the two Davydov components (DCs) in the absorption spectrum. In a simplified picture, the Davydov splitting can be described by the vector addition of the TDMs of the two molecules in the unit cell, yielding two new transitions with perpendicularly polarized TDMs. As a result of the Coulomb coupling between the unit cells in the crystal, each of the excited eigenstates of the dimer splits into a band of delocalized exciton states [6], which is depicted in Figure 2.8.

Especially for PEN and TET, however, it has been shown that the experimentally obtained Davydov splitting cannot be adequately described by the Kasha and Frenkel model [110, 111]. Instead, another type of excitons, namely charge transfer (CT) excitons, should be involved

in the description [110, 111]. Such excitons cannot occur in a single molecule. Yet, in a molecular solid, there is the possibility to have the electron on one molecule and the hole on a neighboring molecule, which is called a CT exciton. These excitons can be formally produced, in the simple molecular orbital picture, by transferring one electron from the HOMO of one molecule to the LUMO of the neighboring molecule, explaining the term CT exciton. A prerequisite for the formation of CT excitons is the presence of short-range coupling due to intermolecular orbital overlap in the OSC aggregate (cf. Section 2.1). As for the Frenkel states, different configurations of (diabatic) CT states can mix. Additionally, also CT and Frenkel states can be coupled, which lead to a significant mixing of these states if they are energetically not too far apart, resulting in new, mixed states [111, 112]. These new, adiabatic states (cf. Section 2.2.3) can be described by the weighted contributions from the diabatic states, like the Frenkel and CT excitons. CT exciton admixtures to the Frenkel states can have a significant impact on the Davydov splitting [111] and on the SF process described next [113].

2.2.5 Singlet fission

In this section, SF is introduced, which is an interesting photophysical process that occurs in some of the here investigated OSC materials. SF describes the spontaneous splitting of one singlet exciton into two triplet excitons in a spin-allowed process [13]. It can be written as a three step process [16],



where S_1 denotes the initial, (photoexcited) singlet exciton in the molecular solid, ${}^1(\text{TT})$ an electronically coupled triplet pair state with overall singlet character, ${}^1(\text{T}\dots\text{T})$ a triplet pair state that has lost electronic coupling but retains spin coherence, and T_1 a free triplet exciton. In the first step, the adiabatic S_1 state, which can have contributions from CT states, as indicated above, is converted to an electronically coupled triplet pair state. This ${}^1(\text{TT})$ state is a multiexciton state with overall singlet character, which makes this process spin-allowed. In the ${}^1(\text{TT})$ state, the two triplets are bound to each other and reside on neighboring molecules [17]. Due to the electronic coupling, the ${}^1(\text{TT})$ state is slightly lower in energy than two individual T_1 states [114]. It can be formally reached in the simplified molecular orbital picture by transferring two electrons between neighboring molecules without a spin flip (cf. Figure 2.9). There are several recent reviews which are concerned with this ${}^1(\text{TT})$ state in the SF process [16, 17, 115]. In the next step, the electronic coupling of the triplet pair state is lost, due to coupling to the phonon bath and spatial separation of the triplet excitons [16]. The obtained ${}^1(\text{T}\dots\text{T})$ state has only spin coherence, but behaves electronically as two individual T_1 excitons. Thus, the SF rate has been suggested to be defined as the rate of ${}^1(\text{T}\dots\text{T})$ formation [16]. In the last step, the spin coherence is lost. The entire process can also occur in the reverse direction, which is then called triplet-triplet

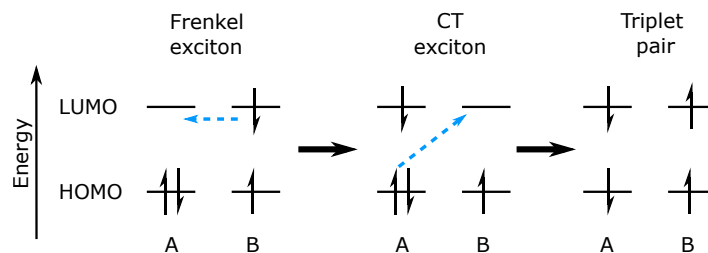


Figure 2.9: Simplified scheme of the SF process based on molecular orbitals and diabatic states in a dimer composed of two identical molecules A and B. The blue arrows indicate electron transfer processes. Inspired by Ref. [111].

fusion. This process can give rise to delayed fluorescence from the reproduced S_1 state and can reduce the effective triplet yield.

There are two important prerequisites for a molecular solid to be able to undergo SF. First, the energy of the initial S_1 state ($E(S_1)$) should be approximately twice the energy of the T_1 state ($E(T_1)$). The overall energy balance of the SF process can be defined as

$$\Delta E_{\text{SF}} = 2E(T_1) - E(S_1). \quad (2.6)$$

If ΔE_{SF} is negative, the entire process is exothermic and can be very fast. If ΔE_{SF} is slightly positive, the entire process is endothermic and generally slower than for the case of $\Delta E_{\text{SF}} < 0$. It is worth noting that the conversion from the $^1(\text{TT})$ state into free triplet excitons can require thermal activation for both considered cases [114]. Triplet-triplet fusion and thus delayed fluorescence is mainly observed for systems with $\Delta E_{\text{SF}} > 0$. The second prerequisite for SF is that the molecules in the solid are electronically coupled to each other via orbital overlap to allow a transfer of electrons between them [111].

Several mechanisms have been proposed for the SF process [113, 116–119], which are briefly described with the help of Figure 2.9. In a very simplified model, including only the frontier orbitals and diabatic states in a dimer of molecule A and B, the first step of the SF process in Equation 2.5 can be described by the transfer of two electrons between the two molecules as depicted in Figure 2.9 [111]. Only one configuration of each diabatic state is shown for simplicity, but, as detailed above, all similar configurations, like, e.g., molecule A being excited in the beginning, are mixed [16]. From Figure 2.9, it becomes clear that CT states can be intermediate states for the conversion from the Frenkel excitons to the triplet pair. If the process occurs as depicted in Figure 2.9, thus in two steps, it is called sequential CT-mediated SF, and if both electrons are transferred simultaneously, it is called direct SF [120]. Yet, as mentioned, this is a very simplified picture that considers only diabatic states of a dimer. In larger molecular aggregates, the excitons are delocalized, which can significantly influence the energy of the diabatic states and consequently their mixing into adiabatic states (cf. Section 2.2.3) [113], which was neglected in the description so far. Generally, for larger molecular aggregates, the coupling between the diabatic Frenkel, CT, and $^1(\text{TT})$ states becomes more pronounced [113]. If strong coupling between these

diabatic states is realized, they are significantly mixed into new adiabatic states. In this case, already the initially excited adiabatic S_1 state contains some diabatic CT and diabatic $^1(\text{TT})$ character [121]. Then, the character of this superposition state can evolve into the adiabatic $^1(\text{TT})$ state by dephasing due to the phonon bath [113]. Finally, the adiabatic $^1(\text{TT})$ can separate in two individual triplet excitons. This process is called coherent SF and can be very fast for materials with $\Delta E_{\text{SF}} < 0$ [16, 118]. If the coupling between the diabatic states is weaker than the coupling to the phonon bath, an incoherent SF mechanism can be realized [16]. In this case, the SF process can be captured by conventional rate equations that describe a vibrationally driven transition from S_1 to $^1(\text{TT})$ [16]. Finally, vibrations play a significant role in the SF process, namely by providing or accepting the energy difference ΔE_{SF} of the SF process. They can further promote vibronic coupling between the diabatic Frenkel, CT, and $^1(\text{TT})$ states [118, 119]. These models of the SF process are still under debate and their applicability to different SF materials are still investigated, too [16, 113].

2.2.6 Blends of organic semiconductors

In the previous sections, only neat OSC materials were considered and introduced. In this section, first binary blends of OSCs are introduced in general, before focusing on the special case of mixtures of electron-donating (donors) and electron-accepting molecules (acceptors) and their CT interactions. The classification of molecules into donors and acceptors can be based on their electron affinity (EA) and ionization potential (IP). The EA is defined as the energy that is gained by adding an electron to a neutral molecule in the ground state, while the IP is defined as the energy that is required to remove an electron from a neutral molecule in the ground state [6]. In the simplified picture of molecular orbitals, this can be described as adding an electron to the LUMO or removing an electron from the HOMO, respectively, which again neglects the electron-electron interactions (cf. Section 2.2.3). Thus, the energy of the LUMO (HOMO) is only a rough estimate for the EA (IP) of a molecule [6]. Instead, a cationic and an anionic state for the molecule can be defined, comparable to the excited states above. Generally, an acceptor can be defined as a molecule with a relatively large EA, while a donor can be defined as a molecule with a relatively small IP.

Molecular mixing scenarios

The mixing and ordering behavior of two compounds A and B in binary blends of OSCs is essential for their structural, electronic and optical properties. Depending on the desired application, intermixing, e.g., of dopants in a host material [26], or phase separation, e.g., in solar cells [122], might be favorable. Generally, three possible mixing scenarios are considered for molecular crystals, namely a solid solution with randomly distributed molecules A and B (Figure 2.10a), a phase separation of pure domains of A and B (Figure 2.10c), and ordered molecular complexes of A and B (Figure 2.10b) [123]. In addition, mixing scenarios in between the mentioned ones, e.g. limited intermixing, can be realized [124]. Which mixing behavior is found for a specific system composed of molecules A and B depends on their

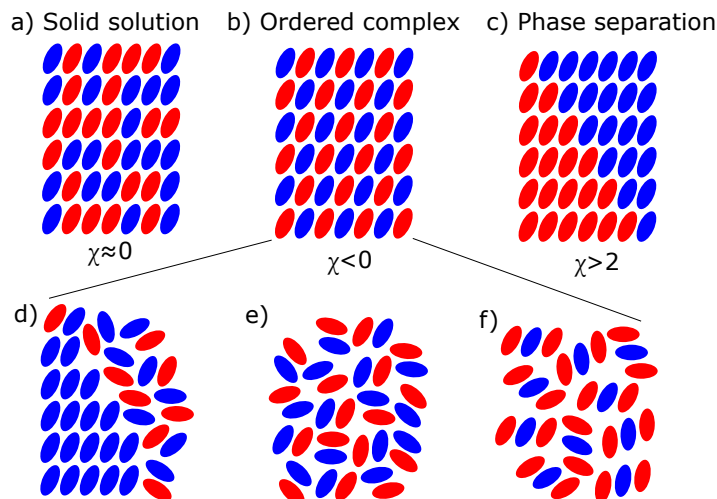


Figure 2.10: Schematic of possible mixing scenarios depending on the interaction parameter χ for molecular crystals (a-c) and for (partially) amorphous donor:acceptor blends with $\chi < 0$ (d-f), depending on the mixing ratio. Inspired by Ref. [125].

steric compatibility and their interactions. If steric compatibility is not given, as, e.g., for the case of planar OSCs with the spherical C_{60} molecule, generally a phase separation is observed [125]. For molecules that are sterically compatible, like the planar OSCs investigated in this work, the mixing behavior close to equilibrium is determined by the interactions between A and B [125]. The free energy of a mixture of molecules A and B can be written in a simplified model of spheres with only nearest neighbor interactions as [123]

$$F_{\text{mix}} = k_{\text{B}}T[x_A \ln(x_A) + x_B \ln(x_B) + \chi x_A x_B], \quad (2.7)$$

with x_A and x_B denoting the fraction of molecules A and B , respectively, T the temperature and k_{B} the Boltzmann constant. The first two terms of Equation 2.7 describe the entropy of the system, which dominates for high T , leading to the formation of a solid solution. However, at lower T , the third term of Equation 2.7 can dictate the ordering behavior. This term critically depends on the interaction parameter χ , which is defined as [123]

$$\chi = \frac{Z}{k_{\text{B}}T}[W_{AA} + W_{BB} - 2W_{AB}], \quad (2.8)$$

with the coordination number Z , the interaction energies W_{AA} and W_{BB} between identical molecules, and the interaction energy W_{AB} between molecules A and B .

If $\chi \approx 0$, thus if the interaction energy between similar and dissimilar molecules is roughly equal, a solid solution is preferred also for low temperatures (Figure 2.10a). For the case of $\chi > 2$, a phase separation between A and B is found for low temperatures, since the interactions between similar molecules are much stronger than between dissimilar molecules (Figure 2.10c). Finally, if $\chi < 0$, ordered $A : B$ complexes are formed, since the interactions between A and B are stronger than the interactions in the pure systems (Figure 2.10b) [125]. In this case it is favorable for molecule A to have neighboring molecules B and vice versa.

For mixtures of strong donors and acceptors, generally the last case with $\chi < 0$ is given, due to the electron-donating and -accepting behavior of the different molecules.

Thin films of donors and acceptors can also be amorphous due to kinetic effects during the growth (cf. Section 2.2.2), which is schematically depicted in the lower row of Figure 2.10. In equimolar donor:acceptor blends, there are often stoichiometric 1:1 complexes formed (Figure 2.10e). In non-equimolar mixtures, either complexes with another stoichiometry can be realized (e.g., 2:1, see Figure 2.10f), or a phase separation into a neat (crystalline) phase and a 1:1 mixed phase can be observed (Figure 2.10d) [125]. The exact mixing behavior is difficult to predict and also depends on the growth conditions, since the growth process is a dynamic, non-equilibrium process, as mentioned in Section 2.2.2 [125].

Charge transfer mechanisms

Next, specifically the case of donor:acceptor blends is considered and different possible CT mechanisms between a donor and an acceptor are introduced. These CT mechanisms are mainly determined by the IP of the donor and the EA of the acceptor as well as the strength of the electronic coupling between the donor and the acceptor [126]. In Figure 2.11, three possible CT scenarios are depicted in the simplified picture of molecular orbitals. Again, it is noted that electron-electron interactions are neglected in this descriptive picture. In Figure 2.11a, the HOMO of the donor is energetically well below the LUMO of the acceptor. In this case, an excited state CT is possible, resulting in a CT exciton as described above. However, in a donor:acceptor system, the CT has a favored direction and the CT exciton can have a small energy. Direct CT excitations, illustrated by the lower right orange arrow in Figure 2.11a, have generally a small oscillator strength due to a small orbital overlap. Alternatively, an excitation of the donor and a consecutive transfer of the excited electron to the acceptor is possible, which is indicated by the other two orange arrows in Figure 2.11a. This kind of excited state CT is crucial for the charge separation in organic solar cells [32, 127]. Furthermore, excited state CT can also occur between organic and inorganic semiconductors, depending on their energy levels, which is detailed in Section 2.3.3.

Besides this excited state CT, ground state CT can be realized in OSC blends, which is illustrated in Figure 2.11b,c. This type of CT can occur if the EA of the acceptor is close to, or larger, than the IP of the donor [28]. Two different ground state CT mechanisms are possible, which are discussed in the following based on the simplified molecular orbital picture. Ground state CT is especially important for doping of OSCs [26, 29].

First, if the HOMO of the donor and the LUMO of the acceptor are energetically and spatially close to each other (Figure 2.11b), allowing strong electronic coupling between the two molecules, a CTC can be formed [26, 35, 128]. A CTC is characterized by the hybridization of the frontier orbitals of the donor and the acceptor [29, 35]. This hybridization is facilitated by a face-to-face stacking in case of planar molecules, since the π -orbital overlap can be maximized in this geometry. In a simplified picture, in which only the HOMO of the donor and the LUMO of the acceptor are considered, the two orbitals mix with each other and split up into two new orbitals, one with a lower energy and one with a higher energy (cf.

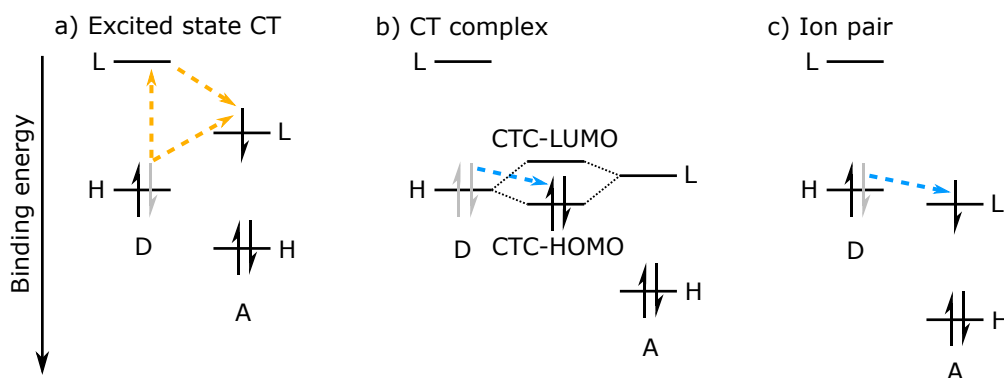


Figure 2.11: Possible CT mechanisms between a donor (D) and an acceptor (A) molecule, illustrated in the molecular orbital picture, only considering their HOMO (H) and LUMO (L) orbitals. Black arrows depict electrons and gray arrows depict transferred electrons/holes after the CT. The orange arrows in a) indicate two possible excitation pathways to result in an excited state CT, while the blue arrows in b) and c) illustrate spontaneous electron transfers, resulting in ground state CT. Inspired by Ref. [29].

Figure 2.11b) [29]. In the ground state, the lower energy orbital is occupied by two electrons from the HOMO of the donor, thus it can be denoted as the CTC-HOMO, and the higher energy orbital is empty, thus representing the CTC-LUMO. This also implies that there are only paired electrons, which can be detrimental for doping purposes [35]. The energy splitting between the CTC-HOMO and the CTC-LUMO depends on the energy of the donor HOMO ($E_{D,H}$) and the acceptor LUMO ($E_{A,L}$) and the intermolecular resonance integral β , which describes their electronic coupling and depends on the parental orbital shape and overlap [29]. In a Hückel-type model, the energy of the CTC-HOMO ($E_{CTC,H}$) and the CTC-LUMO ($E_{CTC,L}$) results as [26]

$$E_{CTC,H/L} = \frac{E_{D,H} + E_{A,L}}{2} \pm \sqrt{(E_{D,H} - E_{A,L})^2 + 4\beta^2}. \quad (2.9)$$

Equation 2.9 closely resembles Equation 2.3 for the frequency splitting of the coupled harmonic oscillators, demonstrating the universality of the coupled harmonic oscillator model.

The character and localization of the CTC orbitals is given by the fraction of acceptor-LUMO and donor-HOMO that they contain. The character of the CTC-HOMO determines the degree of charge transfer (δ_{CT}), since the electrons from the donor are partially delocalized onto the acceptor. This partial CT is another important characteristic of CTCs [28]. It can be determined using infrared spectroscopy (cf. Section 4.2), since the frequencies of the vibrational modes of the involved molecules are modified due to the changed electron density in the bonds (cf. Section 5.4) [28, 129, 130]. Finally, also transitions between the electronic states of the CTC can be detected, which are generally found at low energies, often in the NIR [28, 29]. In the simplified picture used above, the lowest energy transition can be imagined as the transition of one electron from the CTC-HOMO to the CTC-LUMO, but as detailed in Section 2.2.3, the configuration interaction and exciton binding energy should be considered, which further decrease the excitation energy.

The second ground state CT mechanism is depicted in Figure 2.11c and is known as integer ground state CT or ion pair formation [26]. This type of CT can occur if the EA of the acceptor is larger than the IP of the donor. Additionally, the electronic intermolecular coupling should be small to prevent the formation of CTCs, which is realized by a small parental orbital overlap [36]. Hence, ion pair formation is more likely in disordered regions without a face-to-face stacking [38]. In the simplified orbital picture, ion pair formation is realized by transferring one electron from the HOMO of the donor to the LUMO of the acceptor, see Figure 2.11c, resulting in a cationic donor and an anionic acceptor molecule. The second electron is generally not transferred, since the EA of the acceptor anion is smaller than the EA of the neutral acceptor, and the IP of the donor cation is larger than the IP of the neutral donor [26]. This demonstrates the limitations of the illustrative molecular orbital picture. For some strong acceptors, however, also the formation of dianions has been reported [131, 132]. Integer CT can be detected experimentally by UV-vis-NIR absorption spectroscopy as the formed ions exhibit characteristic absorption peaks [38]. Additionally, the integer degree of CT can be demonstrated by vibrational spectroscopy, as mentioned above [28]. Ion pair formation is considered to be the most effective doping mechanism in OSCs, but the electron and the hole are still bound by their Coulomb binding energy [26, 38].

Energy transfer

In this section, energy transfer between two molecules in neat OSC thin films or blends is introduced as a second possible transfer process besides CT. Generally, energy transfer can be written as



where the asterisk symbolizes the excitation and B and C denote the excitation energy donor and the excitation energy acceptor, respectively. They should not be confused with the electron donors and acceptors defined above and are thus abbreviated differently. During an energy transfer process, the energy from the excited donor B is transferred to the acceptor C , which was before in the ground state. After the process, the excitation energy acceptor C is in an excited state and the excitation energy donor B is in the ground state [84]. B and C can be identical or different molecules in this general scheme. If they are identical, Equation 2.10 can be understood as the (undirected) migration of an exciton through the material. If B and C are different molecules, the energy transfer has a favored direction from the higher band gap molecule B to the lower band gap molecule C . Thus, the band gap can be used to define the excitation energy acceptor and the excitation energy donor for an energy transfer process.

There are two different mechanisms for energy transfer, namely FRET and Dexter energy transfer [84]. The FRET process depends on the resonant coupling of molecular dipoles (Coulomb coupling) in the weak coupling regime [82] and can be imagined as energy transfer via the emission of a virtual photon by the excitation energy donor which is then absorbed

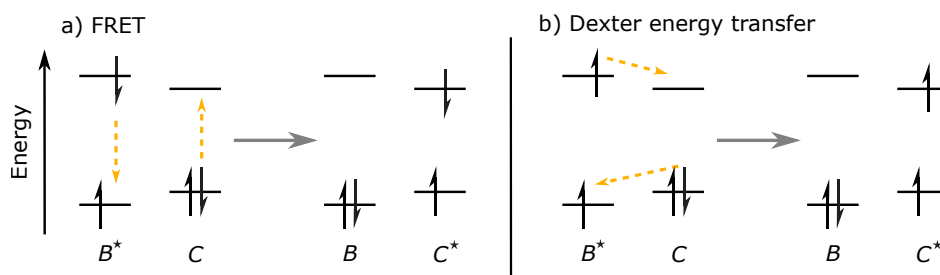


Figure 2.12: Simplified energy transfer scheme between the excitation energy donor B and the excitation energy acceptor C . They can be molecules, then the energy levels represent HOMO and LUMO orbitals, respectively, but also QDs, as discussed in Section 2.3.3. The orange arrows illustrate the electron movements. a) FRET, illustrated for a singlet exciton transfer and b) Dexter energy transfer, exemplary shown for a triplet exciton transfer. Inspired by Ref. [84].

by the excitation energy acceptor (Figure 2.12a). Consequently, the FRET rate depends on the overlap of the emission spectrum of B and the absorption spectrum of C . Additionally, the orientation of the involved TDMs enters the FRET rate as well as the emission rate of molecule B and the distance R between the two molecules as R^{-6} [133]. FRET is important for the migration of singlet excitons and can be efficient over relatively long distances of several nanometers, due to the underlying dipole-dipole interaction. For triplet excitons, the FRET mechanism is spin-forbidden.

Dexter energy transfer, on the other hand, is based on the exchange of two electrons between neighboring molecules. Specifically, in the simplified HOMO-LUMO scheme, an electron from the LUMO of B is transferred to the LUMO of C and an electron from the HOMO of C is transferred to the HOMO of B (Figure 2.12b). Thus, electronic coupling of the two molecules via orbital overlap is required to allow Dexter energy transfer. Consequently, this transfer is limited to short distances. However, electrons with different spins can be exchanged, which renders Dexter energy transfer the dominant transfer mechanism for triplet excitons [84].

2.3 Inorganic semiconductor nanoparticles

In this section, the properties of inorganic semiconductor nanoparticles, also called QDs, are briefly introduced. Such QDs are discussed in Chapter 9 in hybrid structures with OSCs. Generally, inorganic semiconductors are solid materials, consisting of covalently bound atoms, that have a relatively small band gap between the conduction and the valence band, often below 2 eV [134]. Consequently, at room temperature, some electrons can be thermally excited from the valence band to the conduction band, resulting in a non-vanishing conductivity. Since the dielectric constant of these atomic crystals ($\epsilon_r \approx 10$) is much higher than the one of OSCs ($\epsilon_r \approx 3.5$), the excited electron and the hole are screened more effectively, resulting in a smaller exciton binding energy [6]. For this reason, either directly free charge carriers or Wannier-Mott excitons [135] with a large average distance between the electron and the

hole are created by thermal or optical excitation [3]. This is in contrast to the Frenkel and CT excitons in OSCs. There are elemental semiconductors, like silicon and germanium, and compound semiconductors, like lead-sulfide, gallium arsenide, or cadmium selenide (CdSe). If the dimensions of these materials are reduced to the nanoscale, new properties arise and the obtained nanoparticles can be considered to reside somewhere between atoms and molecules on the one hand and bulk solid materials on the other hand [136]. In the following, only the electronic and optical properties of QDs and QDs coupled with OSCs are shortly introduced.

2.3.1 Electronic structure of quantum dots

As mentioned above, QDs can be considered to reside between bulk semiconductors, with an electronic structure that can be explained by a band theory [134], and molecules, which are described by their molecular orbitals [4], see Figure 2.13. If we start from the molecular orbitals derived by the linear combination of atomic orbitals, introduced above for OSCs (cf. Section 2.2.1), a QD can be described as a large molecule with a large number of molecular orbitals. In a qualitative picture, these molecular orbitals are split into two energy regions, a bonding and an antibonding one, with a large number of orbitals in the center of each region and fewer orbitals at their edges. Thus, there are still discrete energy levels available for the electrons in a QD, but the spacing between these levels in one energy region decreases as the size of the QD increases. Additionally, the band gap of the QD decreases with increasing size, compare Figure 2.13. Finally, in the bulk limit, a conduction and a valence band are formed, describable by the tight binding approximation, and the band gap of the bulk semiconductor is reached [137].

Coming from the bulk side, QDs can be described by the crystal structure of the semiconducting material, but with reduced dimensions in all three Cartesian directions, leading to the terminology of a zero-dimensional material. Consequently, the electronic structure of the QDs follows from the band structure of the semiconductor under consideration of the reduced dimensions. Generally, if electrons are excited in a semiconductor, they are found close to the bottom of the conduction band, and the holes are found close to the top of the valence

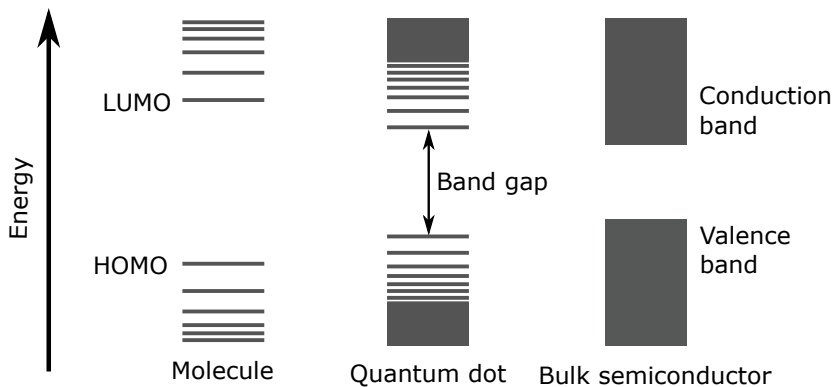


Figure 2.13: Schematic comparison of the energy levels in a molecule, a QD and a bulk semiconductor. Inspired by Ref. [137].

band [134]. In these regions, the band dispersion can often be approximated by a parabola, similar to the free electron dispersion, but with an effective mass for the electron and for the hole, which is known as the effective mass approximation [134]. The effective mass of the electrons and holes is therein determined by the potential of the atomic cores and depends on the specific material considered [138]. Generally, the effect of the reduced dimensions can now qualitatively be understood by the simple picture of a particle in a spherical confining potential of infinite depth, which has discrete quantum numbers k that are proportional to the inverse of the sphere size [138–140]. Thus, the density of states becomes a spectrum of discrete energies instead of a continuous band. The energy separation of the discrete states that stem from one band becomes larger for smaller particles, and the band gap of the QD also increases. The energy of the first excited electronic state of a QD is approximately given by [138]

$$E^* \approx E_g + \frac{\hbar^2 \pi^2}{2R^2} \left[\frac{1}{m_e^*} + \frac{1}{m_h^*} \right] - \frac{1.8e^2}{\epsilon R}, \quad (2.11)$$

with the bulk band gap E_g , the reduced Planck constant \hbar , the radius R of the QD, the effective masses m_e^* and m_h^* of the electron and the hole, respectively, the elementary charge e and the dielectric constant ϵ of the material. The second term in Equation 2.11, showing a $1/R^2$ dependence, is the confinement energy of the electron and the hole resulting from the reduced dimensions. The third term describes the Coulomb attraction between the electron and the hole, which scales with $1/R$ and which is relatively small due to the large dielectric constant of inorganic semiconductors [138]. For the case of strong confinement, when the size of the QD is smaller than the Bohr exciton radius (of the Wannier-Mott exciton) in the bulk solid, the confinement energies of the electron and the hole dominate over the Coulomb attraction due to their $1/R^2$ dependence, allowing to consider the electron and the hole as individual particles [141]. This strong confinement region is realized in the QDs used for this work [142]. The effective mass approximation for QDs has been later modified, by choosing a finite potential to account for the possibility that the electrons and holes are slightly delocalized into the surrounding medium, e.g. the ligands, yielding better results for small particles [143]. Further modifications of the model have been required to describe the optical spectra of QDs as the valence band can be degenerated, necessitating the introduction of several bands with different effective hole masses [144]. For CdSe, which is the material of the QDs investigated in this work, the valence band is formed from Se p-atomic orbitals and is inherently sixfold degenerated [142]. This degeneration is partially lifted by spin-orbit coupling, resulting in a fourfold degenerated band and a twofold degenerated "split-off" band at $k = 0$. In CdSe QDs, these bands mix again [140]. In contrast, the conduction band is not degenerated in CdSe [142]. The resulting nomenclature for the electron and hole states is described next.

The electron and hole states of a QD are labeled similarly to the atomic orbitals, in consistency with the description of QDs as "artificial atoms" [142]. Following from the "particle-in-

a-sphere" description, the electron (hole) states are described by an envelope function which is labeled by its angular momentum L_e (L_h), denoted as S for $L = 0$, P for $L = 1$, D for $L = 2$ and so on, and its radial quantum number n_e (n_h) (1, 2, 3 ...) [140]. The energetically lowest electron (e) states in CdSe QDs are the $1S(e)$, $1P(e)$, and $1D(e)$ states, with increasing energy in this order [145]. For the hole (h) states, an additional subscript, denoting the total hole angular momentum, is introduced due to the band mixing mentioned above. Thus, the energetically lowest hole states in CdSe QDs are labeled as $1S_{3/2}(h)$, $1P_{3/2}(h)$, and $2S_{3/2}(h)$ with increasing energy [145].

2.3.2 Optical properties of quantum dots

The optical properties of QDs result directly from their electronic structure described above. As seen from Equation 2.11, the band gap of QDs increases with decreasing size, leading to a blue shift of the absorption and emission spectra. Owing to the discrete nature of the hole and electron states, the absorption spectrum shows resolved transitions. These electronic transitions are generally labeled by the involved electron and hole states, since the electron and hole can be considered as individual particles as discussed above. For CdSe QDs, the energetically lowest transitions are the $1S(e) - 1S_{3/2}(h)$, $1S(e) - 2S_{3/2}(h)$, $1P(e) - 1P_{3/2}(h)$, and $1S(e) - 1S_{1/2}(h)$ transitions. Thus, in three of the four lowest transitions the $1S(e)$ state is involved, which follows from the closer energy spacing of the hole states due to the multiple involved bands. This degeneracy of the valence band and the larger effective mass of the holes compared to the electrons leads to a much higher occupation probability of the $1S(e)$ state than of the individual hole states after optical excitation, since the hole population is thermally spread over many adjacent states at room temperature [145]. This results in a dominant contribution of the electrons to the bleaches in the TA signal of QDs (cf. Section 4.5).

Similar to Kasha's rule for molecules (cf. Section 2.2.3), generally band gap emission can be detected from QDs. For QDs with well passivated surfaces, quantum yields of over 80 % can be observed [146]. However, due to the high surface-to-volume ratio for small particles, the surface of the QDs is critical for their fluorescence properties. For the bare QD core, the atoms at the surface have fewer binding partners than the ones in the bulk. Therefore, the surface atoms exhibit so-called dangling bonds [146]. This can lead to surface states with energies lying within the band gap of the QD, which can trap electrons and holes [146]. Additionally, also impurities or defects in the QDs or surface vacancies and surface reconstruction can lead to trap states [146]. In a trap state, the electron or hole is localized, which leads to a quenching of the band edge emission. Instead, sometimes emission from these trap states at lower energies can be observed. Otherwise, the electron and the hole can recombine non-radiatively [146].

The number of surface trap states can be reduced by saturating the dangling bonds at the surface of the QDs with organic ligands or an inorganic shell. As inorganic shell, ideally a larger band-gap material with a similar crystal structure is chosen, which results in a

confinement of the electron and/or hole in the QD core and can lead to very high quantum yields [147]. Alternatively, different types of organic ligands can be used to passivate the surface of the QDs. Depending on the material, the surface composition, and the synthesis method, different classes of ligands are applied to saturate the dangling bonds. There are L-type (Z-type) ligands that donate (accept) two electrons to (from) the surface atoms of the QDs or X-type ligands that form a covalent bond to a surface atom by providing one electron [148]. Also with this method, a high quantum yield can be reached [146].

2.3.3 Quantum dots coupled with organic semiconductors

The organic ligands used during the synthesis of QDs to control the shape and size of the QDs and to passivate the surface of the QDs generally exhibit long aliphatic tails. These molecules have a large band gap and are insulators [149]. They can passivate the surface states of the QDs but do not electronically couple to the QDs, which prohibits charge or energy transfer between the QD and the ligands. In addition, these insulating ligands impede the electronic coupling between neighboring QDs in solid thin films or crystals due to the large distance they introduce between adjacent QDs. This limits the applicability of the as-synthesized QDs in solid state devices.

To overcome these limitations and to introduce new functionality, the native, insulating organic ligands can be replaced by OSC ligands, yielding hybrid organic-inorganic semiconductor materials [24]. Owing to the smaller band gap of these OSCs, their HOMO and LUMO orbitals can be energetically close to the lowest electron and highest hole states of the QDs, which are for CdSe QDs the $1S(e)$ and the $1S_{3/2}(h)$ state, respectively. Depending on the exact energetic position of these states and orbitals, four types of energy level alignment can be discerned (Figure 2.14) [65]. In the type I alignment (Figure 2.14a), the $1S(e)$ and the $1S_{3/2}(h)$ states of the QD both lie energetically in between the HOMO and the LUMO of the OSC, which results in the confinement of a photo-generated exciton in the QD. If the OSC is excited, an energy transfer to the QD can be possible via FRET or Dexter energy transfer, compare Figure 2.12. Generally, a type I alignment is also found for the native ligands. For a type II alignment with staggered energy levels, two possibilities are shown in Figure 2.14b,c. Here, an excited state CT between the OSC and the QD could occur (compare Figure 2.11a).

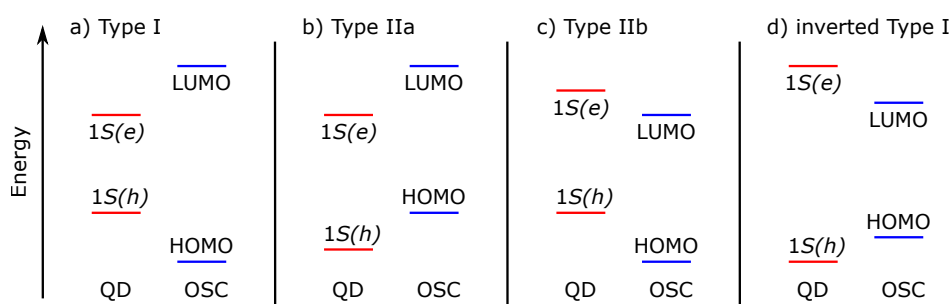


Figure 2.14: Simplified representation of the possible alignment of the frontier orbitals of an OSC molecule and the lowest electron and highest hole states of a QD. The subscript of the hole state was omitted for clarity. Inspired by Ref. [65].

In the type IIa alignment, after excited state CT, the hole would reside on the OSC and the electron on the QD and vice versa for a type IIb alignment, no matter if the QD or the OSC was initially excited. Additionally, also FRET could be possible if there is only dipole coupling between the two components but no orbital overlap. Finally, in the inverted type I alignment (Figure 2.14d) the HOMO and the LUMO of the OSC are found in between the $1S(e)$ and the $1S_{3/2}(h)$ states of the QD, which opens the possibility for an energy transfer from the QD to the OSC. Theoretically, also an alignment in which both the HOMO and the LUMO of the OSC are located above (below) the $1S(e)$ ($1S_{3/2}(h)$) state of the QD can be imagined. This could allow ground state CT between the organic and inorganic components.

As detailed in Section 2.2.6 for the organic blends, electronic coupling between the electron (excitation energy) donors and electron (excitation energy) acceptors is required to render a CT (energy transfer) possible. This is also true for the hybrid materials composed of OSCs and QDs and can be generalized from Section 2.2.6. In the type II configurations, an excited state CT between the OSC and the QD is possible if there is some orbital overlap between the OSC and the QD. Electronic coupling via orbital overlap is also required for Dexter energy transfer between the OSC and the QD, while FRET can also occur via dipole-dipole interactions without orbital overlap. If chemical coupling, hence a binding of the OSCs to the QDs, as well as electronic coupling is given in the hybrid material, it falls into the category of coupled organic-inorganic nanostructures [65]. These coupled organic-inorganic nanostructures can exhibit properties that exceed the sum of the properties of the individual compounds [24]. The organic-inorganic interface is of fundamental importance for these materials [24] and is, therefore, one focus of this thesis.

2.4 Plasmonics and light-matter coupling

In this section, the plasmonic properties of metallic nanoparticles, the optical properties of cavities formed by such particles, and the light-matter interaction in OSCs coupled to these cavities are discussed, which are relevant for the results presented in Chapter 8. Again, only a brief introduction into the large fields of plasmonics and light-matter coupling can be given, while details can be found in the literature [25, 82, 150].

2.4.1 Localized surface plasmons

In the previous sections, organic and inorganic semiconducting materials were discussed. In this section, metals are briefly introduced with a focus on their plasmonic properties. Metals are solids with a partially filled conduction band and, thus, a high conductivity. They can be described as solids that consist of a rigid ionic lattice of the atomic cores with bound core electrons and a gas of free conduction electrons. The interaction of these free conduction electrons with electromagnetic radiation forms the basis for the occurrence of plasmons. The oscillating electric field of the incoming electromagnetic wave drives the free conduction electrons to collectively oscillate against the background of the fixed, positive atomic cores.

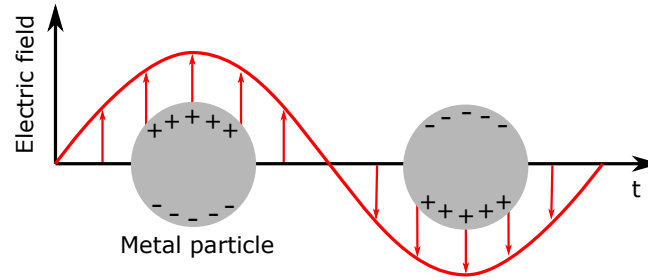


Figure 2.15: Simplified illustration of localized surface plasmons in metallic nanoparticles. Inspired by Ref. [153].

These charge-density oscillations are called plasmons [82]. There are bulk plasmons, surface plasmons, and localized surface plasmons. Only localized surface plasmons will be described in the following as they are important for this work.

Localized surface plasmons are non-propagating excitations of the conduction electrons in small metallic particles with dimensions on the order or below the wavelength of the incident light [150]. Due to the small size of the particles, the oscillations of the electrons are geometrically confined and localized on the particle as illustrated in Figure 2.15. The shift of the electron cloud, induced by the electric field of the incident light, leads to an excess of electrons on one side of the particle, resulting in a negative net charge, and a lack of electrons on the other side of the particle, resulting in a positive net charge due to the ionic cores. Thus, a dipole-like charge distribution is realized. The curved surface of the particles and the built-up electric field lead to an effective restoring force on the displaced electrons [150]. The electron oscillations are damped by electron-lattice collisions (intraband damping), formation of electron-hole pairs (interband damping), and emission of photons (radiation damping) [151]. Consequently, the system can be described as a damped, driven oscillator [150]. The resonance of this oscillator is called the localized surface plasmon resonance (LSPR), which is typically found in the visible to NIR spectral region for nanoparticles of noble metals [152]. When the resonance is met by the incident light, a large near-field intensity enhancement at the surface of the nanoparticles can be observed. Since the damping of the oscillations of the conduction electrons is relatively high, the LSPR has a broad appearance [152].

For spherical metal particles that are much smaller than the wavelength λ of the excitation light, the LSPR can be analytically calculated in the quasi-static approximation, which is, e.g., detailed in Refs. [82, 150]. In this approximation, a sphere with radius r and a complex dielectric function $\epsilon(\omega)$ is assumed in a static electric field. The surrounding medium is taken as non-absorbing and isotropic and is characterized by a dielectric constant ϵ_m . Under these assumptions, the electric field outside the sphere can be described as a superposition of the applied field and the field of a dipole located at the center of the particle. The dipole inside the sphere is induced by the applied field as depicted in Figure 2.15. The magnitude of the

dipole moment is proportional to the applied field amplitude and the polarizability α of the particle, which is found in this approximation as [82]

$$\alpha(\omega) = 4\pi\epsilon_0 r^3 \frac{\epsilon(\omega) - \epsilon_m}{\epsilon(\omega) + 2\epsilon_m}, \quad (2.12)$$

with ϵ_0 denoting the vacuum permittivity. Thus, a maximal polarizability and consequently a maximal dipole moment is achieved if $\epsilon(\omega) + 2\epsilon_m$ is minimized, which is given at a certain frequency ω , namely the LSPR. The importance of the dielectric constant of the surrounding medium on the LSPR follows directly from Equation 2.12 and an increase in ϵ_m generally red-shifts the LSPR [154]. The scattering cross section, thus the total radiated power by the sphere divided by the intensity of the exciting wave, can be calculated as [82]

$$\sigma_{\text{sca}} = \frac{k^4}{6\pi\epsilon_0^2} |\alpha(\omega)|^2 = \frac{8\pi}{3} k^4 r^6 \left| \frac{\epsilon(\omega) - \epsilon_m}{\epsilon(\omega) + 2\epsilon_m} \right|^2, \quad (2.13)$$

with k denoting the wave vector of the incoming light in the surrounding medium. The absorption cross section, thus the fraction of the power of the exciting wave that is dissipated inside the sphere, is given by [82]

$$\sigma_{\text{abs}} = \frac{k}{\epsilon_0} \text{Im}(\alpha(\omega)) = 4\pi k r^3 \text{Im} \left(\frac{\epsilon(\omega) - \epsilon_m}{\epsilon(\omega) + 2\epsilon_m} \right). \quad (2.14)$$

Finally, the extinction cross section follows as $\sigma_{\text{ext}} = \sigma_{\text{abs}} + \sigma_{\text{sca}}$. Thus, the extinction is the total intensity lost from the incident light. It is experimentally accessible via transmission measurements (cf. Section 4.3). From Equation 2.13 and Equation 2.14 follows that the scattering of the sphere scales with r^6 , while the absorption scales with r^3 . This implies that scattering is the dominant contribution to the extinction for larger particles, whereas absorption is the dominant contribution to the extinction for small particles with $r \ll \lambda$ [150]. The dominant scattering for larger particles is important for the occurrence of surface lattice resonances (SLRs), vide infra.

For more complex geometries and inhomogeneous environments, generally simulations or experiments are used to determine the plasmonic properties of metallic nanostructures. In doing so, it is found that the resonance frequency depends on the particle material, size and shape, as well as the refractive index of the surrounding dielectric medium as discussed above. The influence of the particle size on the resonance frequency is not captured by the quasi-static approach described above, which breaks down for larger particles. Instead, additional retardation effects and an increased radiative damping need to be considered for larger particles [150]. For noble metals a red-shift of the LSPR is observed for increasing particle sizes. Thus, by modifying one or several of the mentioned particle parameters, the LSPR frequency/energy can be shifted and, e.g., adjusted to the transition energy of a molecule. For elongated, rod-shaped particles, two LSPRs are obtained, which can be selectively excited by light polarized along the respective axis [150].

2.4.2 Surface lattice resonances

Single metal nanoparticles exhibit a relatively broad LSPR, which is related to the short lifetime of the localized surface plasmons resulting from the damping of the electron oscillations. These properties are linked to the ratio of the energy stored to the energy lost by an oscillator, which is reflected by the quality factor Q of the resonance that can be estimated as $Q = \lambda_m / \Delta\lambda$ [152]. Here, λ_m denotes the resonance wavelength and $\Delta\lambda$ the full width at half maximum of the resonance. To observe strong light-matter coupling, a small damping and thus a high quality factor is required, which is not achievable with single plasmonic particles. One possibility to achieve a high quality factor is to arrange many plasmonic particles in a periodic array, which can effectively decrease the damping from radiation losses [152].

In such a lattice or array, the scattered field from one particle influences the response of the neighboring particles. If the distance between neighboring particles in the periodic array is on the order of the wavelength of the excitation light, the particles can be electromagnetically coupled via their far-fields. This scenario can be described by the coupled dipole approximation, which is detailed in Refs. [152, 154–156], while here only the main ideas are summarized. In this approximation, each particle in the array is considered as an electric point dipole. These dipoles all have the same polarizability and a defined position on the lattice. The induced dipole in each particle is given by the product of the polarizability of the particle and the local electric field, as already introduced above for a single nanoparticle. Yet, the local electric field is now given by the sum of the incident field and the retarded fields from all other dipoles in the array. Under the right conditions, the scattered fields from the other dipoles arrive in phase with the illumination field, which leads to a large polarization of the particle and the excitation of a SLR. In this case, the scattered fields from the neighboring particles can act against the damping of a single particle and reinforce its resonance, which leads to a significantly increased quality factor. Due to the radiation pattern of a dipole, the coupling in an array of dipoles occurs mainly in the direction perpendicular to the direction of the dipoles, which is defined by the polarization of the excitation light (Figure 2.16) [157]. The electric field of the resulting SLR is oriented parallel to the polarization of the incident light [158]. Furthermore, SLRs are delocalized and provide a large field intensity in between the particles [159].

The conditions for the appearance of a SLR are met close to diffraction edges, also called Rayleigh anomalies, where the incoming light is diffracted into the plane of the array and can be rescattered by the particles [152, 156, 160, 161]. These diffraction edges follow from the grating equation and are found for wavelengths at which a diffraction order changes from a radiative to an evanescent behavior. For a one-dimensional grating with a lattice constant a_x , at the interface between two media with refractive indices n_1 and n_2 (front view in Figure 2.16), the grating equation is given by [162]

$$n_{\text{diff}} \sin(\theta_{\text{diff}}) \pm n_1 \sin(\theta_{\text{in}}) = |m_x| \frac{\lambda}{a_x}, \quad (2.15)$$

with the refractive index n_{diff} of the medium in which the diffraction is considered (n_1 for reflection and n_2 for transmission), the angle of diffraction θ_{diff} in the respective medium, the angle of incidence θ_{in} in medium 1, the vacuum wavelength λ and the diffraction order m_x , which is an integer number. For $m_x < 0$ the + sign holds in Equation 2.15 and for $m \geq 0$ the - sign. To find the diffraction edges, one applies the condition for the diffraction in the plane of the array, $\theta_{\text{diff}} = 90^\circ$, to Equation 2.15. Further, Snell's Law is used to connect θ_{in} to the (measured) incidence angle θ in vacuum, $\sin(\theta) = n_1 \sin(\theta_{\text{in}})$, resulting in

$$\lambda_{m_x} = \frac{a_x}{|m_x|} (n_{\text{diff}} \pm \sin(\theta)) \quad (2.16)$$

for the wavelengths in vacuum λ_{m_x} , under which the diffraction edges occur. The first diffraction edges ($m_x = \pm 1$) are the most important for the SLRs investigated in this work, which follow from Equation 2.16 as

$$\lambda_{\mp 1} = a_x (n_{\text{diff}} \pm \sin(\theta)). \quad (2.17)$$

From Equation 2.17, several conclusions can be drawn. First, for normal incident light ($\theta = 0$), the $\lambda_{\mp 1}$ diffraction edge appears when the wavelength of the light in the medium equals the lattice constant. If the refractive indices n_1 and n_2 of the media above and below the lattice are different, diffraction edges in the two media occur at different wavelengths. This is detrimental to sharp SLRs, which are, for normal incidence, only observable if the contrast between n_1 and n_2 is small [152]. In this case, n_{diff} in Equation 2.17 can be replaced by an experimentally determined effective refractive index n_{eff} between n_1 and n_2 [159]. Furthermore, for oblique incidence ($\theta \neq 0$), the $m_x = \pm 1$ diffraction edges appear at different wavelengths, one with a spectral blue shift and one with a red shift, which is approximately linear for small θ . This indicates that the wavelengths of the diffraction edges can be tuned by changing the incidence angle, which becomes important later on.

So far, a one-dimensional grating was considered as the simplest case, but the results obtained above are similarly valid for a two-dimensional, rectangular lattice under the illumination conditions chosen in this work, compare Figure 2.16. The incident light is polarized along the y -direction and has only a k_z and a k_x component ($k_y = 0$) of the wave vector \vec{k} . Thus, the angle θ is defined in the x - z -plane with respect to the z -axis, which is the surface normal. Under these conditions (transverse electric (TE), with respect to the plane of incidence [63]), the diffraction edges corresponding to the diffraction of the light along the x -axis are given by Equation 2.17. They appear when the diffraction orders m_x become evanescent and the $m_x = \pm 1$ diffraction edges are the ones related to the SLRs investigated in this thesis. They are denoted as $(\pm 1, 0)$ diffraction edges in the following, since in general, in a rectangular, two dimensional lattice in the x - y -plane, (m_x, m_y) diffraction orders are found [159].

With these diffraction edges in mind, an alternative view on the appearance of SLRs is possible, which allows to intuitively understand their energy position in dependence of the

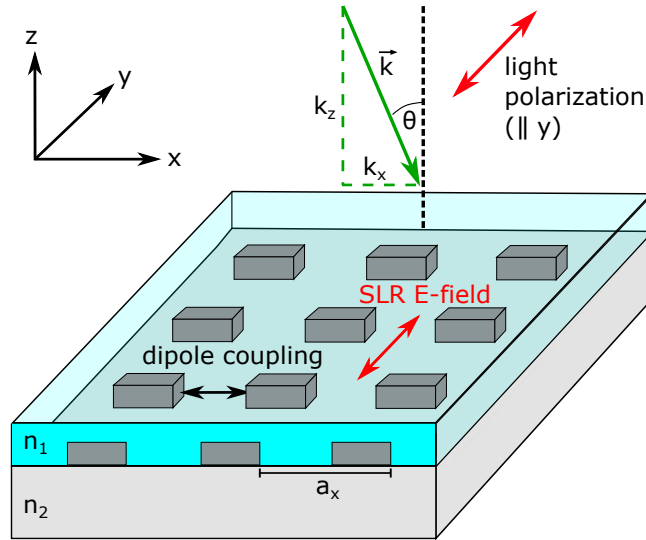


Figure 2.16: Schematic illustration of a SLR-supporting lattice, demonstrating the lattice geometry and the illumination conditions. The resulting dipole coupling and the direction of the electric field of the SLR are also indicated.

illumination angle θ . Namely, a SLR can be considered to result from the coupling of the LSPR of the single plasmonic particles with a diffraction edge of the array. In this picture, the occurrence of a SLR can be described in the frame of coupled oscillators (cf. Section 2.1). The plasmons in the particles, connected to the oscillations of the conduction electrons, can be considered as one oscillator and the diffraction edge, connected to the photons scattered in the plane of the array, as the other oscillator. They exchange energy at a rate q which couples them. Then, as introduced in Section 2.1, the system can be described by a Hamiltonian with the energies (and the losses) of the LSPR and the diffraction edge on the diagonal and the energy exchange rate q as the off-diagonal coupling elements. The wavelength and consequently the energy position of the diffraction edge depends on the incidence angle θ of the light (Equation 2.17). By diagonalizing this Hamiltonian, the eigenenergies of the hybrid plasmonic-photonic modes of the coupled system are extracted (cf. Equation 2.3 and Figure 2.1b) [49, 163]. For a large energy detuning between the diffraction edge and the LSPR, the coupling only slightly modifies the energy and character of the original oscillators, resulting in a SLR that appears close to the diffraction edge. In this case, the SLR mode has mainly photonic character, which leads to a small linewidth, a high quality factor, and an approximately linear angle dispersion for small θ . The other mode has in this case mainly plasmonic character from the LSPR and does not show an angle dependence of its energy. Consequently, in the literature [58, 159] and in Chapter 8, this mode is referred to as LSPR, according to its main character. If the energy detuning between the LSPR and the diffraction edge becomes smaller, the coupling significantly alters the character, energy, and dispersion of the two modes. For zero energy detuning, an avoided crossing between the LSPR and the diffraction edge can be found and the new modes have strongly mixed character, see, e.g., Refs. [49, 159, 164]. Therefore, the energy and the quality factor of a SLR can be manipulated

by the illumination angle as well as the lattice and particle parameters, which determine the energies of the diffraction edges and the LSPR, respectively. With high quality SLRs, strong light-matter coupling in OSCs can be realized, which is described in the next section.

2.4.3 Strong light-matter coupling

Finally, the coupling between light and matter is briefly introduced in this section at the example of a system consisting of a plasmonic array and an OSC material. In general, strong light-matter coupling can also be observed for organic or inorganic semiconductors in microcavities consisting of two opposed mirrors, in which the light is reflected multiple times, which results in the formation of cavity modes with certain resonance frequencies. Further details about strong light-matter coupling can be found in the literature [25, 43, 44].

In the exemplary system considered here, the plasmonic array is assumed to support one SLR with energy $E_{\text{SLR}}(\theta)$. For the OSC material, only one optical transition that leads to the formation of an exciton with energy E_{X} is considered. The SLR of the array can be considered as a cavity mode with photonic and plasmonic character and a certain resonance frequency [163]. If there would be no coupling in this system, the energy introduced by an incident photon could be either contained in the cavity mode or in an exciton in the OSC, until it is dissipated. Instead, if the energy can be transferred between the two mentioned subsystems, they interact with each other and are consequently coupled. Strong coupling is achieved, if the energy transfer rate between the cavity mode and the exciton is higher than their averaged energy dissipation rate [25]. In this case, the two subsystems cannot be treated independently anymore, but the entire system needs to be considered, in close analogy to the coupled harmonic oscillators discussed in Section 2.1 [82]. Here, the SLR as the cavity mode can be treated as one oscillator and the optical transition related to the exciton as the other oscillator. Consequently, a Hamiltonian \mathbf{H} , analogues to \mathbf{M} in Equation 2.2 and to the Hamiltonian for the coupling between the LSPR and the diffraction edge described above, can be constructed as [25]

$$\mathbf{H} = \begin{pmatrix} E_{\text{SLR}}(\theta) & \hbar g \\ \hbar g & E_{\text{X}} \end{pmatrix}, \quad (2.18)$$

with $\hbar g$ describing the collective coupling strength of N molecules that can couple to the SLR field. By diagonalizing \mathbf{H} in Equation 2.18, the eigenvalues are obtained as

$$E_{\pm}(\theta) = \frac{1}{2} \left[E_{\text{SLR}}(\theta) + E_{\text{X}} \pm \sqrt{(E_{\text{SLR}}(\theta) - E_{\text{X}})^2 + (2\hbar g)^2} \right], \quad (2.19)$$

analogues to Equation 2.3. These eigenvalues represent the energies of the new, hybridized modes which are called plasmon-exciton polaritons [163]. These quasi-particles have mixed plasmonic, photonic and excitonic character and are referred to as polaritons in the following. For zero detuning between the energy of the SLR and the energy of the exciton ($E_{\text{SLR}}(\theta)=E_{\text{X}}$), an avoided crossing of the upper and lower polariton is obtained (cf. Figure 2.1b), which is

characteristic for strong coupling. With this condition ($E_{\text{SLR}}(\theta)=E_X$) inserted in Equation 2.19, the Rabi splitting $\hbar\Omega$ [43] of the avoided crossing is obtained as

$$\hbar\Omega = E_+ - E_- = 2\hbar g. \quad (2.20)$$

The Rabi splitting can be experimentally determined, e.g., from transmission measurements, allowing to examine the coupling strength of the system. The Rabi splitting is visible, if it is larger than the mean linewidth of the two oscillators, γ_{SLR} of the SLR and γ_X of the exciton transition, thus if the condition $\hbar\Omega > (\gamma_{\text{SLR}} + \gamma_X)/2$ is fulfilled [63, 165]. This condition is also chosen to define strong coupling [25, 63]. These linewidths are connected to the damping of the oscillators and consequently to their energy dissipation rate, which was already introduced above as critical quantity for strong coupling.

The collective coupling strength of N molecules to the electric field component \vec{E}_0 of the SLR can also be calculated within the dipole approximation as [25]

$$\hbar g = \sqrt{N} \vec{\mu} \cdot \vec{E}_0 = \vec{\mu} \cdot \hat{e}_{\text{cav}} \sqrt{\frac{N E_{\text{SLR}}}{2\epsilon_0 V}} = \frac{\hbar\Omega}{2}, \quad (2.21)$$

where $\vec{\mu}$ denotes the TDM of the molecular transition, V the cavity mode volume, ϵ_0 the vacuum permittivity, and \hat{e}_{cav} an unitary vector in the direction of the cavity electric field. From Equation 2.21, the importance of the relative orientation and magnitude of $\vec{\mu}$ and \vec{E}_0 becomes apparent. Additionally, a scaling with \sqrt{N} , thus the number of coupled molecules, appears [43]. If the entire mode volume is assumed to be filled with molecules, the factor N/V in Equation 2.21 corresponds to the molecule density in the OSC material [44]. By strong coupling, the energy landscape of the excited states of the OSC can be modified, which allows to influence the chemical and photophysical properties of the OSC, e.g., the SF and triplet-triplet fusion process [57, 58].

3. Materials and sample preparation

Within this work, three different sample categories were prepared and investigated. Their differing composition, namely purely organic thin films, mixed organic-inorganic semiconductor thin films and OSC thin films on metal plasmonic structures, necessitated different preparation methods for all three sample categories. Additionally, due to the demands of the applied characterization methods, different substrates were used which are described first in this chapter, since they were the basis for all samples. Then, the used materials and preparation methods for the three sample categories are presented, beginning with the purely organic samples that consist of small molecule OSCs. These were prepared via OMBD. It follows the description of the aryleneethynylene (AE) derivatives and the cadmium selenide (CdSe) QDs, which were investigated in hybrid organic-inorganic thin films prepared from solution. Finally, the plasmonic samples are described, which consist of silver nanoparticle arrays and were produced by electron beam lithography.

3.1 Substrates

The various employed characterization methods, which are detailed in Chapter 4, require specific, adapted substrates which are presented in this section. For the optical measurements in transmission mode, different glass substrates, namely JGS1 and Menzel coverslips, were used. Furthermore, 0.5 mm thick single-side polished, and 1.5 mm thick double-side polished silicon wafers, both covered by a native oxide layer, were chosen for X-ray diffraction and photoluminescence (PL) measurements and, the latter, for Fourier-transform infrared (FTIR) measurements in transmission mode. Additionally, for the polarization-modulation infrared reflection-absorption spectroscopy (PMIRRAS) measurements, silicon wafers with a thin gold film (~ 200 nm) on one side were used.

All substrates were ultrasonically cleaned consecutively for ten minutes in acetone and isopropanol each and dried in a nitrogen flow. The substrates for the organic-inorganic thin films were additionally treated by ultraviolet (UV) irradiation for ten minutes to further clean and activate the surface for the sample preparation from the liquid phase.

3.2 Organic semiconductor samples

One part of this thesis is dedicated to purely organic semiconductor systems with ground state CT between donor and acceptor molecules. As donors, the acene molecules TET and PEN were used in these CT blends, since they have been thoroughly investigated and are known to exhibit SF [13]. This is also the reason for the choice of PEN for the light-matter coupling samples described below. The two strong acceptors 2,3,5,6-tetrafluoro-7,7,8,8,-tetracyanoquinodimethane (F4-TCNQ) and 2,2'-(perfluoronaphthalene-2,6-diylidene)dimalononitrile (F6-TCNNQ) were chosen due to their high EA. Besides, for blends of PEN and F4-TCNQ, different doping scenarios have been reported which were further investigated in this work. In this section, the used acenes and acceptors, and the preparation of the mixed organic films via OMBD are presented.

3.2.1 Acenes

Acenes are an important and intensely studied class of OSCs due to their outstanding electronic and optical properties [166, 167]. They consist of linearly fused six-membered rings of carbon atoms, are fully conjugated, and form planar molecules. Especially TET and PEN (Figure 3.1) have received a lot of attention due to their high charge carrier mobilities and usability in organic transistors and solar cells [168, 169]. With the renewed interest in SF due to a possible improvement of the efficiency of solar cells [21], the number of studies on TET and PEN as prototypical SF materials has further increased [114, 121, 170, 171]. Their SF capability and the lack of a detailed understanding of their interactions with strong electron acceptors made them interesting materials for the investigation within this work. Since TET and PEN are neighboring members of the acene class (namely containing four and five rings, respectively), they behave similar in many regards while differences in their state and transition energies occur due to the changed length (of the conjugated system). This allows to systematically compare these two materials and their interactions with acceptors with respect to the changed state energies. Particularly important for the CT behavior as donors are their IPs. Literature values (from Refs. [172–174] and references therein) for the IPs of TET and PEN in thin films and crystals are in the range of 5.10-5.43 eV and 4.85-5.04 eV, respectively, indicating the slightly better donor behavior of PEN.

As neat materials, TET and PEN crystallize in a herringbone arrangement with two molecules per primitive unit cell [175]. Different polymorphs have been reported for both materials, one thin film phase and several bulk phases each [94, 175–177]. The thin film phase is induced by weakly interacting substrates and, hence, as the name suggests, is mainly important for thin films [178]. It is characterized by nearly upright-standing molecules on the substrate, resulting in a large out-of-plane lattice spacing [94]. With increasing film thickness, bulk phases become more important, which have a larger inclination angle of the molecules with respect to the surface normal, resulting in a smaller out-of-plane lattice spacing [179].

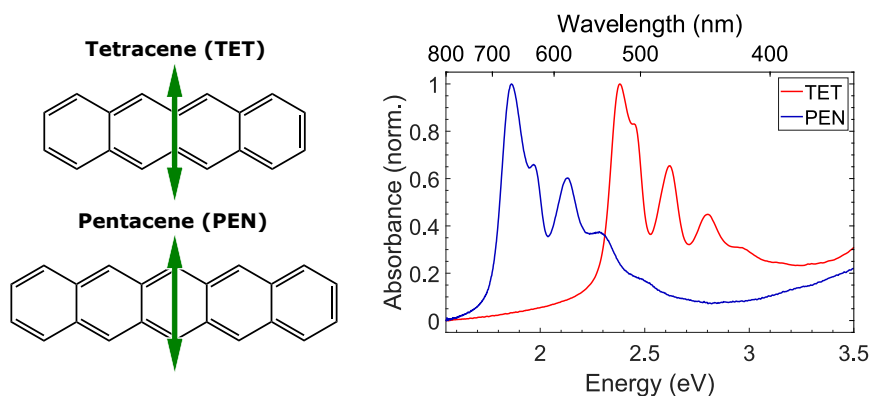


Figure 3.1: Chemical structure and normalized absorbance spectra of thin films of TET and PEN in the energy region of the $S_0 \rightarrow S_1$ transition. The green arrows in the chemical structures illustrate the orientation of the TDM of the $S_0 \rightarrow S_1$ transition.

This makes the thin film phase distinguishable from bulk phases by X-ray reflectivity (XRR) measurements (see Section 4.1).

Owing to the herringbone arrangement of the molecules in all these crystal structures, thin films and crystals of TET and PEN exhibit a Davydov splitting of the lowest-energy transition (Figure 3.1). The magnitude of the Davydov splitting is different for the two materials and also slightly dependent on the polymorph [180]. It is larger in PEN (~ 120 meV) than in TET (~ 80 meV) [83] due to the larger CT admixture to the energetically lower DC in PEN [83, 111]. The overall shape of the absorbance spectra of thin films of the two materials around the lowest-energy optical transition is, however, similar and both materials show a clear vibronic progression (Figure 3.1). As a consequence of the larger conjugated system of PEN compared to TET, the spectrum of the PEN thin film is red-shifted by ~ 0.5 eV relative to the spectrum of the TET thin film. The energy of the $S_0 \rightarrow S_1$ transition ($E(S_1)$) of PEN and TET in thin films was determined from the intersection of the absorbance and emission spectrum and found to be 1.84 eV and 2.35 eV, respectively, and the TDM is oriented along the short molecular axis (see Figure 3.1) [181]. PEN and TET exhibit only weak fluorescence due to the SF process which provides a rapid, non-radiative relaxation path for the photoexcited singlet excitons.

One important prerequisite for a material to be able to undergo SF is a favorable energy balance between the photoexcited initial S_1 state and the final triplet (T_1) states (cf. Section 2.2.5). This renders the energy of T_1 ($E(T_1)$) highly important, which is taken from the literature as $E(T_1) = 1.25$ eV and $E(T_1) = 0.86$ eV for TET and PEN, respectively [182, 183]. Thus, the energy balance of the SF process (Equation 2.6) is $\Delta E_{\text{SF}} = 150$ meV and $\Delta E_{\text{SF}} = -120$ meV for TET and PEN, respectively. Consequently, the entire SF process is endothermic in TET while it is exothermic in PEN, resulting in different SF mechanisms for the two materials [13]. This classification remains still valid after considering that the intermediate $^1(TT)$ state is bound by approximately 30 meV with respect to the free triplets for both materials [114]. For TET an incoherent SF mechanism is found while for PEN coherent SF is most likely [113, 184–186]. These different mechanisms and energetics are also

3. Materials and sample preparation

reflected in the triplet pair formation time constants of ~ 100 ps and ~ 100 fs for TET and PEN, respectively, which have been reported in the literature [116, 118, 170, 187, 188].

Both TET and PEN were purchased as crystalline powders from Sigma-Aldrich (now Merck) with 99 % and 99.995 % purity, respectively, and used as received.

3.2.2 Acceptors

As acceptors for the investigation of the different CT mechanisms with the SF materials, F4-TCNQ and F6-TCNNQ were used, as they are among the strongest organic acceptors known [189]. Furthermore, they both contain cyano groups, which is beneficial for determining the degree of CT in blends with donors [190]. The chemical structures of both acceptors are shown in Figure 3.2. The high EA of both molecules is achieved by the fluorine and cyano substituents which withdraw electrons from the aromatic core. The EA, which is a measure for the acceptor strength, has been determined to be 5.08-5.33 eV and 5.37-5.60 eV for F4-TCNQ and F6-TCNNQ, respectively, implying that F6-TCNNQ is the slightly stronger acceptor [191–195]. Owing to the high EA of these acceptors, also doubly negatively charged ions, denoted dianions, have been reported for both materials [132, 196].

Thin film absorbance spectra of both compounds are also included in Figure 3.2, which are both relatively unstructured, in consistency with the literature [29, 132, 197]. The F6-TCNNQ thin film spectrum exhibits a first absorption maximum at ~ 2.4 eV while the F4-TCNQ thin film spectrum exhibits a first absorption maximum at ~ 2.8 eV, and both show a pronounced tail toward lower energies. The smaller optical band gap of F6-TCNNQ can be related to the slightly larger conjugated system compared to F4-TCNQ and the absorbance tail is most likely due to significant light scattering by these samples due to the high roughness of the films.

Both acceptors crystallize in at least two different polymorphs with differing number of molecules per unit cell and different space groups [198–200]. In thin films, amorphous phases and a lack of preferred orientation of the formed crystallites with respect to the substrates have been found [35, 130].

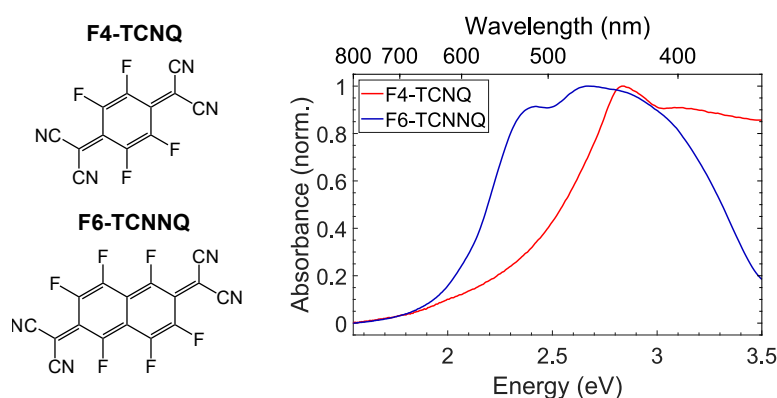


Figure 3.2: Chemical structures and normalized thin film absorbance spectra of F4-TCNQ and F6-TCNNQ.

F4-TCNQ was purchased from Sigma-Aldrich (now Merck) with 99% purity and F6-TCNNQ from Novaled GmbH with 99.9% purity and both were used as received.

3.2.3 Organic molecular beam deposition

To prepare thin films of the donors and acceptors presented above, OMBD was used in this work [93, 201]. In this method, small organic molecules are thermally evaporated in a high or ultrahigh vacuum chamber and are deposited onto the desired substrates. A scheme of the used setup is shown in Figure 3.3. For the OMBD process, the molecular, crystalline powder is placed in a crucible which is placed inside a Knudsen cell. The temperature of the crucible can be controlled by applying a current to the heating coil around the crucible. Consequently, also the evaporation rate of the contained molecules can be controlled. Owing to the high vacuum, the molecules travel as a molecular beam toward the sample holder with the mounted substrates and condense on them. Two different compounds can be evaporated simultaneously from two cells, enabling to grow thin film blends of molecules. The deposition rates are monitored by two independent quartz crystal microbalances (QCMs), see Figure 3.3. The QCMs measure the deposited mass during the evaporation and convert it with an arbitrary density into a thickness. By relating the post-growth measured thickness of a neat film to the measured thickness by the QCM (d_{QCM}), a scale factor (s.f.) can be calculated, which depends on the position of the QCM and the sample with respect to the cell and the density of the evaporated material. With this scale factor, the growth rate of each compound, given by $r = (d_{\text{QCM}} \cdot \text{s.f.})/t$, with t denoting the time, can be monitored during the growth.

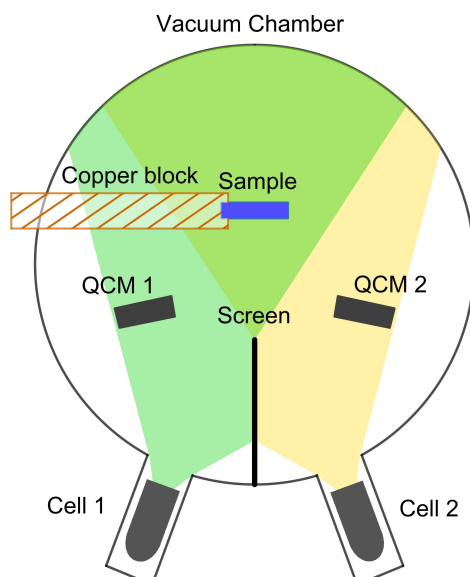


Figure 3.3: Schematic presentation of the OMBD setup with two independent cells and QCMs. Lengths are not to scale. The colored areas depict the molecular beams and the copper block can be externally cooled.

From the volume occupied by one molecule, determined by the size of the unit cell of a reported crystal structure and the number of molecules therein, the stoichiometric mixing ratio of the molecules in blended films is obtained. This molecular mixing ratio is the important parameter for the blends and is used to define the samples in this thesis. The errors of the QCMs are estimated to be $\pm 10\%$, which affects the overall thickness and the mixing ratio of the films. For better readability, only the nominal mixing ratio of the blends is given in the results chapters.

The base pressure of the vacuum chamber used for this thesis was $\leq 2 \times 10^{-8}$ mbar. The samples were glued with a silver paste to the sample holder to ensure good thermal contact. Before the film deposition, the cleaned substrates were heated in vacuum to ~ 570 K overnight to remove any residual adsorbed molecules, including water. During the deposition process, the sample holder was cooled through a copper block with liquid nitrogen to achieve a sample temperature of ~ 250 K. This ensures a small desorption rate of the molecules from the samples which is especially crucial for the samples containing the volatile molecules TET and F4-TCNQ. The overall growth rate was adjusted to ~ 6 Å/min and the nominal thickness of the films was 80 nm if not otherwise stated.

3.3 Organic-inorganic semiconductor samples

This section describes the materials used to prepare the organic-inorganic semiconductor samples, namely the AE derivatives and the CdSe QDs. First, the AEs are presented, chosen for their ability to bind to the CdSe QDs and for their structural similarity but differing chemical substitutions, which allowed systematic investigations. Next, the CdSe QDs are presented, which were chosen because they have already been extensively studied and exhibit absorption and emission in the visible range. This section concludes with the preparation method of the hybrid samples from solution.

3.3.1 Aryleneethynylene derivatives

AE derivatives, also known as cruciforms due to the shape of their molecular backbone (Figure 3.4), consist of two linear, conjugated segments that are connected through a central benzene core [202]. One of these segments is an AE branch composed of three phenylene groups that are connected by two ethynylene groups. The other segment is either a second AE branch, resulting in a highly symmetric molecule, or a distyrylbenzene branch which renders the two segments distinguishable. On the peripheral aromatic rings, different substituents can be placed, which can be used to induce a spatial separation of the frontier orbitals, resulting in interesting optical properties and the possibility to use AEs as sensors [203]. These different substitutions also lead to differing electrical and emission properties while keeping the overall structure and size of the molecules similar [204]. Finally, there is also the possibility to introduce binding groups as substituents. Taken together, the mentioned points render AE

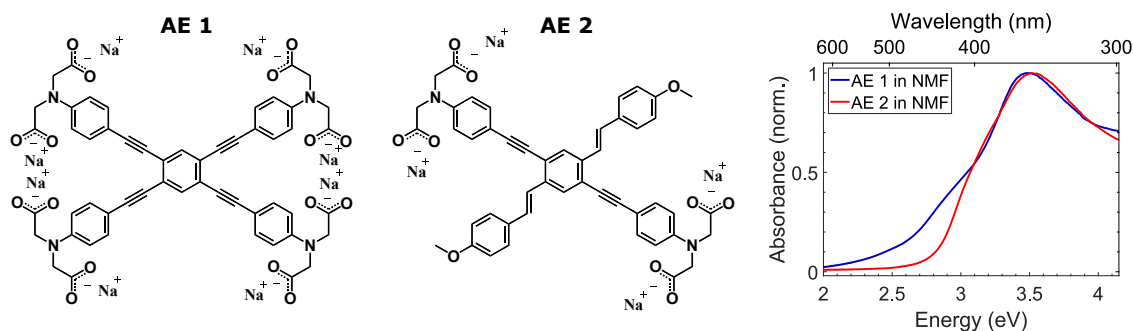


Figure 3.4: Chemical structure of the two AE derivatives and their absorbance spectra in NMF.

derivatives promising candidates for systematic investigations in coupled organic-inorganic structures.

In this work, two different AE derivatives were investigated, namely sodium 2, 2', 2'', 2''', 2''''', 2''''''', 2''''''''-(((benzene-1,2,4,5-tetrayltetrakis(ethyne-2,1-diyl)) tetrakis(benzene-4,1-diyl)tetrakis(azanetriyl))octaacetate (AE 1) and sodium 2, 2', 2'', 2'''-(((2,5-bis((E)-4-methoxystyryl)-1,4-phenylene)bis(ethyne-2,1-diyl))-bis(4,1-phenylene))bis(azanetriyl))tetraacetate (AE 2). The molecules were provided by Dr. Markus Bender from the group of Prof. Dr. Uwe H. F. Bunz in Heidelberg, as part of a collaboration, and their chemical structures are shown in Figure 3.4. AE 1 contains two AE segments and symmetric substituents while AE 2 contains one AE and one distyrylbenzene segment and differing substituents, yielding a molecule with reduced symmetry and the possibility of frontier orbital separation. Both molecules exhibit several carboxylate groups which are possible binding sites for CdSe QDs [205]. The absorbance spectra of both molecules in N-methylformamide (NMF) are also included in Figure 3.4. They both show an absorption maximum around 3.5 eV and a shoulder at smaller energies, which is at ~ 3.0 eV and ~ 3.2 eV for AE 1 and AE 2, respectively. The solutions of the AEs in NMF were used for the preparation of the neat and mixed organic-inorganic films. The preparation method is described in Section 3.3.3.

3.3.2 CdSe quantum dots

CdSe QDs were chosen as the inorganic semiconducting part of the hybrid films. Reasons for this choice were the facts that CdSe QDs have been long and extensively studied and that their absorption and emission spectra can be tuned to make energy transfer processes with the AEs likely [144–146, 206]. Well-established synthesis protocols for nearly monodisperse CdSe QDs exist and many structural and optical properties have been already characterized due to the profound research effort during the last decades, which also resulted in commercial applications [207–209]. CdSe QDs can be synthesized in a wurtzite (hexagonal) or zincblende (cubic) structure and exhibit clearly quantized, size dependent absorption spectra [144, 210]. The fluorescence properties of CdSe QDs strongly depend on their surface chemistry. To achieve a high fluorescence quantum yield, a good passivation of surface (quenching)

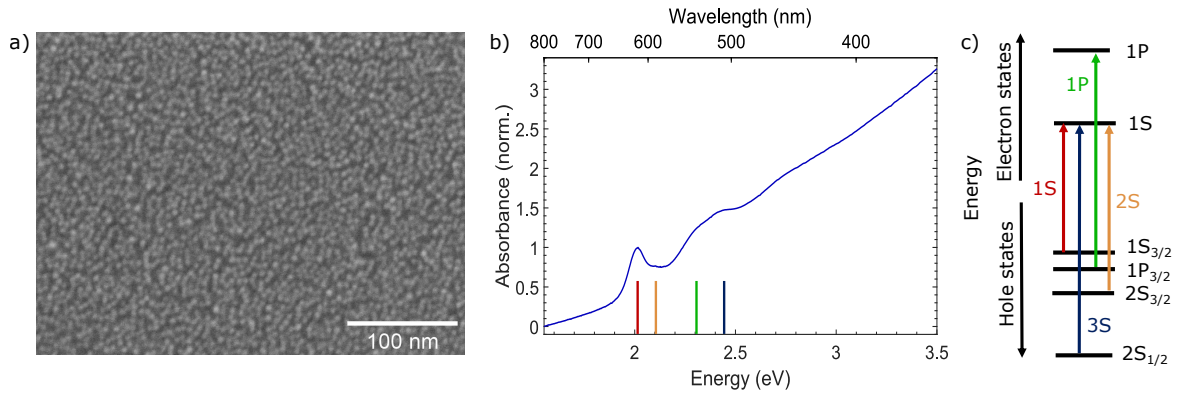


Figure 3.5: a) SEM image of the as-synthesized CdSe QDs with the native ligands dried on a substrate. The SEM image was taken and provided by Andre Maier. b) Absorbance spectrum (normalized to the first absorption peak) of the same particles dissolved in hexane. The vertical bars indicate the energy positions of the transitions between the hole and electron states shown in c) as a scheme. c) Inspired by Ref. [216].

states is required [146]. This surface passivation can be achieved either by organic ligands or an inorganic shell (e.g. of ZnS) and is additionally influenced by the relative precursor concentrations [211]. With different approaches quantum yields over 80% have been achieved [146]. With small size distributions and a good passivation, suppressing deep trap emission, very sharp emission lines have been obtained [212].

The CdSe QDs used for this thesis were synthesized and provided by Patrick Michel, Dr. Krishan Kumar and Dr. Björn Märker from the group of Prof. Dr. Marcus Scheele. The synthesis protocol is described in Ref. [213] and follows the one reported in Ref. [207]. The as-synthesized wurtzite CdSe QDs stabilized by the native ligands hexadecylamine, trioctylphosphineoxide, trioctylphosphine, and oleate (cadmium selenide quantum dots with the native ligands (CdSe/nat)) were dispersed in hexane. A scanning electron microscope (SEM) image of these nanoparticles dried on a substrate is shown in Figure 3.5, from which a relatively small size distribution can be inferred. Since the size of the QDs is close to the resolution limit of the SEM, the average particle size was determined from the absorption spectrum, which is a common procedure [136]. The absorption spectrum is also shown in Figure 3.5. From the position of the first absorption maximum at ~ 2 eV ($\lambda = 616$ nm), corresponding to the $1S(e) - 1S_{3/2}(h)$ (1S) transition, a diameter D of approximately 5.4 nm can be calculated, based on the following, empirical calibration equation [214]:

$$D = (1.6122 \times 10^{-9})\lambda^4 - (2.6575 \times 10^{-6})\lambda^3 + (1.6242 \times 10^{-3})\lambda^2 - (0.4277)\lambda + (41.57).$$

The sharpness of the lowest-energy transition additionally indicates a small size distribution in the sample [215]. At higher energies, further transitions are visible, namely the $1S(e) - 2S_{3/2}(h)$ (2S) transition at ~ 2.1 eV, the $1P(e) - 1P_{3/2}(h)$ (1P) transition at ~ 2.3 eV, and the $1S(e) - 2S_{1/2}(h)$ (3S) transition at ~ 2.45 eV (cf. Figure 3.5c) [142, 216], where the abbreviations for the transitions in brackets follow the ones introduced in Ref [145].

Since a direct exchange of the native ligands by the AE derivatives turned out to be not successful, an intermediate step was included. In this step, the native ligands were removed by adding ammonium iodide, precipitation of the QDs and redispersion of the iodide stabilized cadmium selenide quantum dots (CdSe/I^-) in NMF, following the procedure described in Ref. [207]. This ligand exchange was also done by Patrick Michel from the group of Prof. Dr. Marcus Scheele. The resulting dispersion of the CdSe/I^- was then used for the preparation of the organic-inorganic nanostructures described below.

3.3.3 Sample preparation from solution

The organic-inorganic thin films investigated in this work, consisting of AE derivatives and CdSe QDs, were prepared from the liquid phase with a drop casting method. Drop casting is a very simple and widely-used method to deposit nanoparticles onto a surface [217] and is also used for OSCs [218]. For thin film preparation by this method, a droplet of the desired material in a suitable solvent is dropped on the substrate to cover it completely. While the solvent evaporates, either at ambient conditions or at raised temperature, depending on the solvent, a film of the material is formed. The resulting films are often non-uniform in thickness due to the evaporation process [217] which is, however, not critical for the properties investigated in this work. Drop-casting is also suitable to prepare mixed organic-inorganic thin films if the compounds can be dissolved in the same solvent. Then, two droplets containing the organic and inorganic compound, respectively, can be dropped simultaneously onto the substrate, leading to an intermixing directly on the substrate.

The exact preparation procedure differed slightly for the different samples. For the neat reference films of the organic compounds, namely AE 1 and AE 2, around 50 μL of the respective AE, dissolved in NMF ($\sim 2 \times 10^{-4}$ mol/L) were dropped onto the desired substrate, left undisturbed for 1 h and annealed afterward at 383 K for 1 h. The samples only slowly dried at 383 K owing to the high boiling point of NMF [219], which was found to yield the best films in terms of material distribution. The thickness of these films was determined by profilometer measurements on several scratches through the thin films, see Appendix E.1 for details. The average thickness of the neat AE films was 20 nm to 60 nm. The thickness variations resulted from the drop casting method. The films of the CdSe/nat , also used as a reference, were prepared similarly. Yet, they were dispersed in hexane ($\sim 7 \times 10^{-6}$ mol/L) which evaporates at room temperature, leading to dry films already before the annealing step with average thicknesses between 180 nm and 270 nm.

Further reference films of the CdSe/I^- were prepared slightly differently, since the simple drop casting method led to either too thick, intransparent or too thin, incompletely covered films. Therefore, single droplets of a concentrated dispersion ($\sim 1.4 \times 10^{-4}$ mol/L) in NMF were dropped on a tilted substrate. In consequence of the slight tilt, the droplet slowly glided down the substrate, leaving behind a thin CdSe/I^- film, comparable to a dip coating technique [220]. Again, the sample was left undisturbed for 1 h before it was annealed for

another hour at 383 K. With this technique, films with an average thickness of 220 nm to 330 nm were obtained, similar to the CdSe/nat films.

For the preparation of the mixed films of iodide stabilized cadmium selenide quantum dots and aryeneethynylene derivatives (CdSe/I⁻/AE) a drop casting method with direct intermixing on the substrate was chosen. Approximately 50 μL of the respective AE solution and $\sim 35 \mu\text{L}$ of a diluted CdSe/I⁻ dispersion ($\sim 1.4 \times 10^{-5} \text{ mol/L}$), both in NMF, were dropped onto the substrate and left undisturbed for at least 1 h to allow an intermixing and binding of the AEs to the QDs. Afterward, the sample was quickly dried at 383 K and washed three times to remove unbound AEs. In these washing steps, the sample was covered with NMF for ~ 1 min, followed by spinning it off. The remaining mixed thin film was finally annealed at 383 K for 1 h. The average thicknesses of these CdSe/I⁻/AE films ranged from 130 nm to 290 nm.

The entire preparation of the samples was done in a nitrogen filled glovebox, in which also the compounds were stored, to prevent oxidation of the CdSe QDs [221]. The exposure of the prepared samples to air was also minimized during the handling and the measurements, which were conducted either in vacuum or in a nitrogen atmosphere. The samples were stored in vacuum.

3.4 Plasmonic silver nanoparticle arrays

The third category of samples prepared for this thesis consists of PEN thin films on plasmonic silver nanoparticle arrays to investigate light-matter coupling effects. Since PEN and its thin film preparation method, OMBD, were already described above, this section focuses on the material properties and preparation of the silver nanoparticle arrays.

To achieve strong light-matter coupling, cavities with high quality resonances are required (cf. Section 2.4). Such cavities were realized in this work in the form of ordered arrays of silver nanoparticles that can support high quality SLRs (cf. Section 2.4.2). As substrates, Menzel coverslips with an refractive index of $n = 1.51$ were used. Silver was chosen because it is a noble metal and its threshold for interband transitions lies above 3 eV [222]. This implies that plasmon resonances below this energy, which are the ones investigated in this work, do not suffer from increased interband damping (cf. Section 2.4) [223]. Different samples with varying particle dimensions and arrangements were prepared for this thesis in order to optimize the strength, sharpness and position of the SLR. Furthermore, reference samples were fabricated for comparison reasons.

The fabrication of the plasmonic samples was done in several steps. The size and shape of the nanostructures was defined using electron-beam lithography, followed by the development of the sample and metal deposition. After the lift of step, a protective Al₂O₃ layer was deposited and finally a polymeric reference layer or the target molecular PEN layer was deposited. The single steps are shown in Figure 3.6 and detailed in the following.

3.4.1 Electron-beam lithography

Electron-beam lithography was chosen to prepare the arrays of nanostructures for the plasmonic samples. As a first step, the cleaned substrates were spin-coated with a poly(methyl methacrylate) (PMMA) layer (from DuPont with an average chain length of 4041 monomers) as positive electron-beam resist in which the structures can be written (Figure 3.6a). For the spin coating process, the substrate was covered with a solution of 2.5% PMMA in methyl isobutyl ketone and spun in two steps. First, the substrate was spun for 6 s at 2600 rpm with a ramp up time of 6 s and then further accelerated within 6 s to 5000 rpm, where it was spun for another 60 s. Afterward, the layer was annealed at 423 K for 5 min. Since a conducting layer was required for the lithography step, a second layer, consisting of a conducting polymer (AR-PC 5090.02 (Electra 92) from Allresist), was spun directly onto the still warm PMMA layer at 4000 rpm for 40 s with a ramp time of 6 s. Finally, it was annealed for another 2 min at 423 K.

The electron-beam lithography process was performed on one of the two available SEMs, either a FEI XL30 SEM or a JOEL JSM-6500F SEM (Figure 3.6b). Both were equipped with a Xenos XPA 2 pattern generator. The pattern generator was controlled by the ECP software. In this software, the desired pattern was programmed which was then exposed by the electron-beam under the control of the pattern generator. The impinging electrons caused an increase in solubility of the exposed PMMA parts. Thus, these parts could be removed in the following development step (Figure 3.6c). As acceleration voltage 30 keV were used. The used field size was $25 \times 25 \mu\text{m}^2$, on which the nanostructures were written by deflection and blanking of the beam of the SEM, yielding arrays consisting of approximately 60×60 nanostructures. The same SEMs were also used to take images of the final samples, after the atomic layer deposition step. These images were taken with an acceleration voltage of 5 keV.

Before the development of the sample, the Electra 92 was removed by placing the sample for 30 s in deionized water. For the following development, a mixture of isopropanol and methyl isobutyl ketone was prepared in a 3:1 ratio. The sample was gently moved in this solution for 70 s, washed with pure isopropanol immediately after and dried in a nitrogen flow. After this step, the sample exhibited holes with the desired pattern in the resist (3.6c).

3.4.2 Metal deposition

The silver deposition (Figure 3.6d) on the developed samples was done via thermal evaporation of silver, similar to the OMBD process described in Section 3.2.3, with the difference that prior to evaporation the silver melts. The process was carried out in a Pfeiffer Vacuum PLS 570 setup. Silver pellets were placed in a resistive heated boat in the vacuum chamber and the samples were mounted above. Since small silver structures do not stick well to the glass substrates, a thin (~ 2 nm) titanium layer was first evaporated to increase the adhesiveness. This was performed by electron-beam physical vapor deposition in the same setup directly before the silver deposition. Both deposition processes were monitored by a thickness-calibrated QCM and the final silver thickness was 35 nm, again with an uncertainty

3. Materials and sample preparation

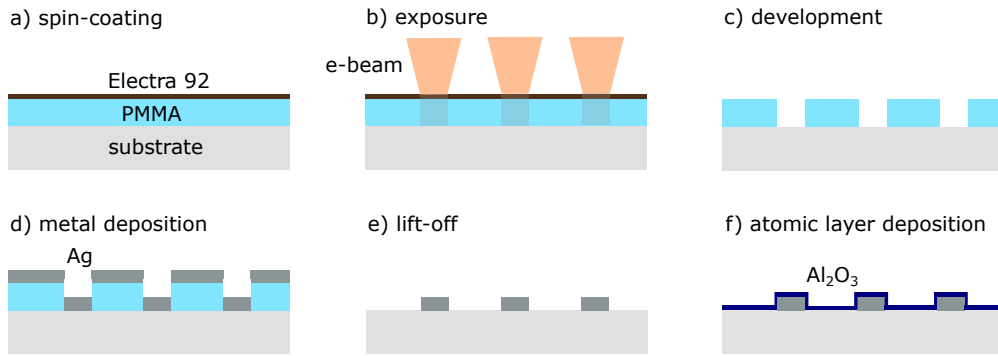


Figure 3.6: Scheme of the steps during the preparation of the plasmonic structures. Details are given in the text.

of $\pm 10\%$ for the film thickness as verified by profilometer measurements on reference samples. The deposition rates were ~ 1.5 nm/min and ~ 1 nm/min for Ti and Ag, respectively.

After the metal deposition the samples were placed in acetone for several hours to remove the remaining resist with the metal on top (Figure 3.6e). This process is called lift-off and was assisted by a stream of acetone in the end. The samples with the silver structures were then rinsed with isopropanol and dried with nitrogen.

3.4.3 Atomic layer deposition

Since silver reacts with atmospheric hydrogen sulfide, carbonyl sulfide and particulate chloride in humid environments [224], a protective Al₂O₃ layer, with a thickness of either ~ 5 nm or ~ 10 nm, was added in the final step via atomic layer deposition (Figure 3.6f) [225]. This layer also inhibited a direct electron transfer between the organic layer and the silver structures. The atomic layer deposition was carried out in a Picosun R-200 Advanced setup. First, the chamber was evacuated to ~ 4 mbar and the samples were heated to 523 K. During the deposition, the chamber was flushed by H₂O and trimethyl aluminum by turns with pulse times of 0.1 s each. Nitrogen was used as carrier gas with a flow of 150 sccm and 200 sccm for trimethyl aluminum and H₂O, respectively. The respective precursor covered the surface of the sample and the unbound molecules were flushed away by pure nitrogen. The purging times were 5 s and 6 s for trimethyl aluminum and H₂O, respectively. Then the other precursor was let into the chamber and reacted with the bound precursor in a self-limiting surface reaction [225]. Afterward, the chamber was flushed by nitrogen again and the next cycle was started. By this, the thickness of the deposited film could be precisely controlled by the number of cycles. Either 50 or 100 cycles were performed for the different samples. Since the precursors bind to all surfaces, also the sides of the nanostructures were covered and a very uniform film was obtained that protects the underlying silver. After this step, the quality and the exact particle dimensions of the prepared samples were characterized via SEM imaging.

These final plasmonic samples were then either covered by PEN via OMBD (Section 3.2.3) or by polystyrene (PS) in a spin coating process for reference measurements. PS was chosen as reference material due to its refractive index of $n = 1.59$, which is similar to the one of

PEN ($n \approx 1.6$ for frequencies other than the exciton transition frequencies [226]). For the PS layer, a ~ 2.5 wt% PS solution in toluene was prepared. 50 μL of this solution were dropped onto the rotating sample (2500 rpm) and spun for 60 s, yielding 125 nm to 140 nm thick films.

4. Characterization techniques

This chapter describes the main experimental methods used to characterize the samples and to obtain the results presented in Chapters 5-9. Only a brief overview of the used techniques and setups is given while more details can be found in the cited literature. First, the X-ray diffraction techniques are introduced, namely XRR and grazing-incidence X-ray diffraction (GIXD). They were applied to obtain information on the structure of the sample, which can be crucial to interpret the electronic, optical and photophysical properties of the prepared system. It follows a description of the two infrared spectroscopy techniques FTIR and PMIRRAS, which were employed to get insights into vibrational properties. They are important for the investigation of CT and binding events. The steady-state optical properties were measured by UV-vis-NIR and PL spectroscopy. These methods are introduced before the TA spectroscopy, which was the technique chosen to characterize the dynamics of the investigated systems and concludes this section.

4.1 X-ray diffraction

X-ray diffraction techniques were used during this work to characterize the structure of the prepared samples, allowing conclusions to be drawn about the organization and mixing behavior of the compounds in the thin films. This is very important information for systems composed of several compounds and can give first insights into the interactions between the compounds. The spatial information is also used for the interpretation of the optical and vibrational data. Only a brief description of the methods used can be given here, for further details the reader is referred to textbooks [227, 228].

In X-ray diffraction techniques, a beam of X-rays is directed toward the sample. The X-rays are scattered by the electrons of the atoms in the sample and the intensity of the scattered X-rays in certain directions is detected. The technique capitalizes on the fact that the wavelength of X-rays is on a similar length scale as the size of the molecules, giving the possibility for interference phenomena that can be detected and related to the structure of the sample. Constructive interference is expected under angles θ where the path difference between scattered X-rays is a multiple of the wavelength, known as Bragg's law

$$2d \sin(\theta) = n\lambda, \tag{4.1}$$

with the distance d between the scattering objects, often crystal planes, an integer number n and the wavelength λ of the X-rays. The techniques used for this thesis and described in the following rely on elastic scattering of the X-rays, implying that the energy and hence the wavelength and the magnitude of the wave vector, given by $k = 2\pi/\lambda$, is not modified by the scattering event. Depending on the used scattering geometry, the structural properties in different directions and on different length scales can be analyzed.

4.1.1 X-ray reflectivity

The out-of-plane structure of thin films, especially of the purely organic small molecule semiconductor samples, was characterized by XRR measurements. The general measurement geometry is shown in Figure 4.1a. A monochromatic X-ray beam is directed under a certain incidence angle θ to the sample and the scattered intensity is measured under specular conditions, meaning that the exit angle (θ) is kept equal to the incidence angle. By scanning θ , an XRR intensity curve is generated. It is generally displayed as a function of the scattering vector \vec{q} , which is defined as

$$\vec{q} = \vec{k}_{\text{out}} - \vec{k}_{\text{in}}, \quad (4.2)$$

with the wave vector \vec{k}_{in} (\vec{k}_{out}) of the incoming (outgoing) X-rays. Considering the geometry in Figure 4.1a, \vec{q} has only a z -component which is given by

$$q_z = 2k \sin(\theta). \quad (4.3)$$

Combining Equations 4.1 and 4.3, one receives

$$q_z = \frac{2\pi n}{d} \quad (4.4)$$

as condition for constructive interference, independent of the chosen wavelength. With equation 4.4, two important features of XRR curves can be directly related to real space distances. First, Bragg peaks appear at certain values of q_z , which can be converted to the out-of-plane lattice spacing of the crystal planes of the sample. This lattice spacing can give information about the molecular orientation on the substrate and insights into the mixing behavior of blends [229]. The second feature are Kiessig fringes which appear at small q_z as a result of the interference of X-rays scattered at the air-film interface with X-rays scattered at the film-substrate interface. Their period is linked to the overall film thickness, another important parameter for thin films, which can also be used to obtain the scaling factors for the thin film growth. The damping of the Kiessig fringes depends on the film roughness and they are only visible for relatively smooth films. During this work, all XRR curves were taken on a General Electric XRD 3003TT instrument with Cu-K $_{\alpha 1}$ -radiation ($\lambda = 1.541 \text{ \AA}$).

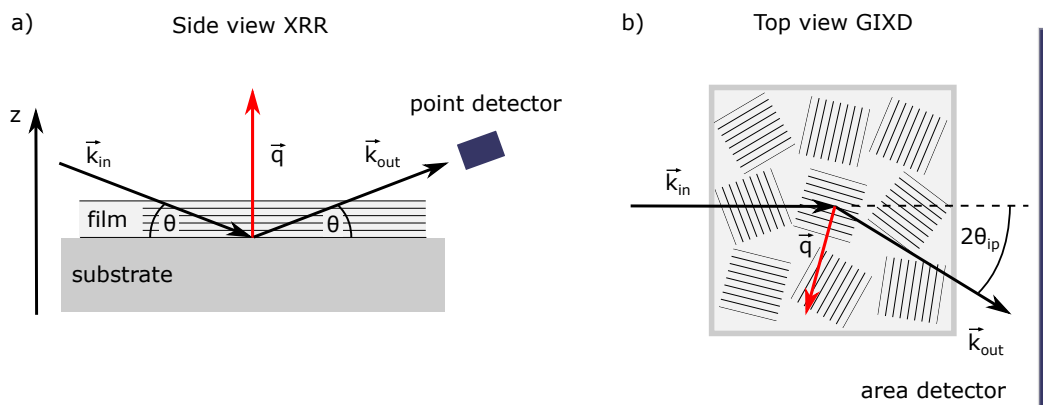


Figure 4.1: X-ray scattering geometries. a) Side view of the XRR geometry with \vec{q} pointing in z -direction and b) top view on the grazing-incidence wide-angle X-ray scattering (GIWAXS) geometry with the in-plane scattering angle $2\theta_{ip}$ and \vec{q} having an in-plane and a z -component. For small-angle scattering, the area detector is placed far from the sample. Inspired by Ref. [93].

4.1.2 Grazing-incidence X-ray diffraction

With GIXD, the in-plane structure of a sample can be resolved. GIXD was used in two different geometries for this thesis. First, by placing the detector close to the sample, wide angle detection was realized to characterize the crystallites and their orientation with respect to the substrate in the purely organic thin films (see Figure 4.1b). Second, by inserting a flight tube, the detector can be placed further away from the sample, allowing to measure the scattering under small angles, which correspond to larger distances in real space. This was used to investigate the organization and average distances of the QDs in the mixed organic-inorganic thin films. Both techniques have in common that an X-ray beam is directed with a fixed grazing angle of incidence toward the sample and the scattered intensity behind the sample is measured by an area detector. In general, the angle of incidence is chosen close to the critical angle of the substrate, resulting in a high sensitivity to scattering by the thin film. With the known detector and sample positions with respect to the incoming beam, the scattering pattern on the detector can be converted to a reciprocal space map, spanned by q_{xy} and q_z . The two in-plane scattering vector components q_x and q_y are herein combined to one in-plane scattering vector component $q_{xy} = \sqrt{q_x^2 + q_y^2}$ because the investigated samples are (at most) uniaxially anisotropic, with the preferred axis being normal to the surface. If distinct peaks appear in the reciprocal space map, the crystallites have a preferred orientation on the substrate and the peak positions can be compared to peak positions from known crystal structures. From the appearance of rings at constant absolute q values in the reciprocal space maps, one can conclude on a random orientation of the crystallites in the sample. Using Equation 4.4 and replacing q_z with q , these q values can be correlated to real-space distances d . Most of the data shown in this thesis were taken at an angle of incidence of 0.2° on a Xeuss 2.0 (Xenocs) laboratory instrument equipped with a microfocus X-ray source ($\lambda = 1.542 \text{ \AA}$) and a Dectris Pilatus 3 R 300K detector. These measurements were done in

vacuum. Only the measurements on the samples containing TET were done in nitrogen at beamline I07 at the Diamond Light Source Ltd., Oxfordshire, U.K. with a Dectris Pilatus 3 R 100K detector, a wavelength of $\lambda = 0.954 \text{ \AA}$ and an angle of incidence of 0.11° .

4.2 Infrared spectroscopy

Infrared absorption spectroscopy is a method used to characterize the vibrational (and rotational) properties of molecules. Within this work, changes in the vibrational spectra were analyzed to draw conclusions on CT in the purely organic thin films [190]. Additionally, infrared spectra of the mixed organic-inorganic thin films were acquired to verify the incorporation of the organic molecules into the samples and further, high quality spectra were taken to detect the binding of the AEs to the QDs. Generally, infrared spectroscopy relies on the excitation of molecular vibrations (and rotations) through the absorption of low-energy, infrared photons. Only vibrations that change the dipole moment of the molecule can be excited and details can be found in Refs. [230, 231]. Two different measurement geometries were used for this thesis which are described in the following.

4.2.1 Fourier-transform infrared spectroscopy

The most commonly used infrared spectroscopy method is FTIR spectroscopy due to its high throughput, sample flexibility, and ease of handling [230]. Here, FTIR spectra were taken from thin films deposited on double-side polished silicon substrates in transmission mode using the transparency of silicon for the wavelength region of interest. The general setup of a FTIR spectrometer is shown in Figure 4.2. Its central part is the Michelson interferometer. An infrared beam, generated by a suitable source, is collimated by a mirror and directed onto a beam splitter, where it is divided into two beams of equal intensity. These beams enter the two arms of the interferometer. Both beams are reflected by mirrors back to the beam splitter, where they are recombined. Though, the mirror at the end of one arm is movable to modulate the distance traveled by the light in this arm, leading to changing interference in the recombined beam. Then, this beam is directed toward the sample and the transmitted light is detected, yielding an interferogram given by the measured intensity as function of the mirror displacement. The mirror displacement is hereby itself tracked by the interference pattern of an incorporated laser (cf. Figure 4.2). By applying a fast Fourier transform, the Fourier components of the frequencies contained in the interferogram are extracted and a spectrum with intensity as function of wavenumber is obtained. As reference to calculate the transmittance or absorbance (see Section 4.3), the spectrum of a blank substrate was used. All measurements were performed with a Vertex 70 spectrometer from Bruker. The beam size was set to 2 mm by an aperture after the source and 1000 scans were averaged per measurement. The entire instrument, including the sample chamber, was purged with nitrogen for at least 15 min before the start of and during each measurement to reduce artifacts from water vapor and carbon dioxide.

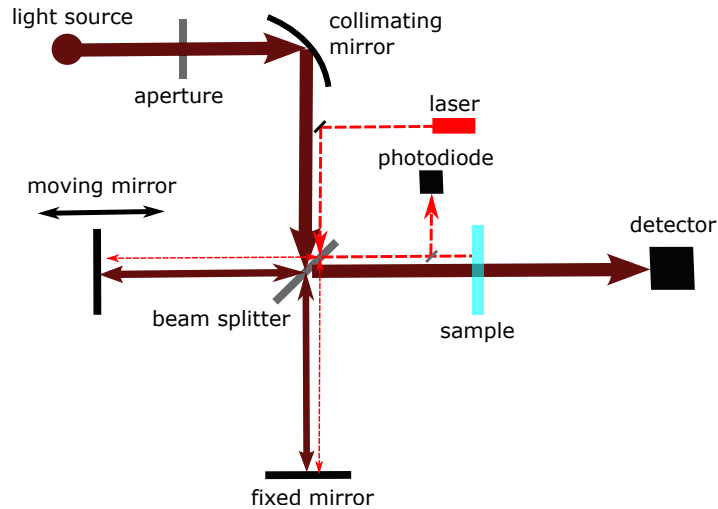


Figure 4.2: Schematic setup of a FTIR spectrometer, inspired by Ref. [231].

4.2.2 Polarization-modulation infrared reflection-absorption spectroscopy

Since for a more detailed analysis of the binding of the AEs to the QDs in the hybrid samples a high signal to noise ratio was required, PMIRRAS was performed as an additional infrared spectroscopy technique. This technique exploits the fact that the electric field components of an incident electromagnetic wave that are parallel and perpendicular to a metal surface behave differently. While the parallel component vanishes close to the metal surface, the perpendicular field component is enhanced [232]. By correlating the reflected intensity for s- and p-polarized incident light (with respect to the optical plane, the plane of the paper in Figure 4.3), the signal arising from the thin film on the metal substrate can be distinguished from the signal arising from absorption of gases, especially H_2O , in the optical path. By that, the background signal can be efficiently reduced and the signal to noise ratio increased. Here, only a short description of the working principle of PMIRRAS is given, more details can be found in Refs. [232–234].

Figure 4.3 schematically shows the setup for PMIRRAS. The unpolarized infrared light beam from the FTIR spectrometer described above is redirected after the interferometer into the compartment for the PMIRRAS measurements. There, it is first linearly polarized by a fixed polarizer and hereafter directed through a photoelastic modulator (PEM), whose optical axis is oriented at an angle of 45° with respect to the polarization. The PEM is used to periodically change the polarization of the infrared light between s- and p-polarization (with respect to the optical plane, in Figure 4.3 the plane of the paper) [232]. The beam is then directed to the sample and reflected to the detector. The intensity reaching the detector is time modulated owing to the periodic modulation of the polarization of the infrared light, additionally to the slower modulation introduced by the moving mirror. With a lock-in amplifier set to the modulation frequency of the PEM, it is possible to extract the difference and the sum signals of the reflected intensities from p- and s-polarized light. These signals are Fourier-transformed and ratioed to yield a differential reflectance spectrum. The resulting

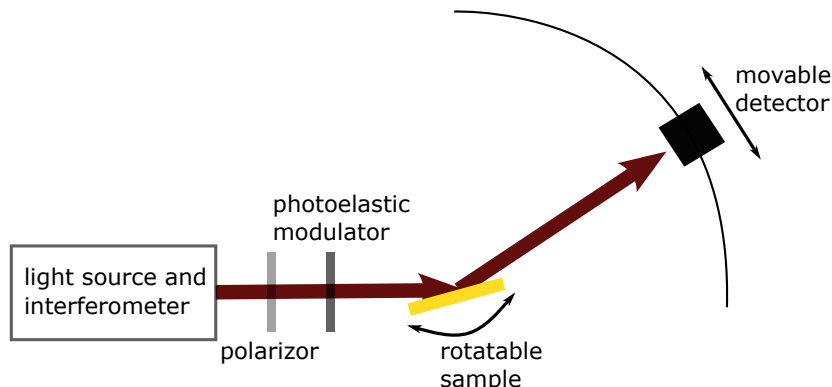


Figure 4.3: Schematic PMIRRAS setup. The infrared light from the FTIR spectrometer shown in Figure 4.2 is polarized and modulated, reflected by the gold substrate and detected. The sample is mounted on a rotatable sample holder and the detector can also be moved on a circular track to allow measurements under different angles. Focusing optics are omitted for clarity. Inspired by Ref. [233].

spectrum is, due to the modulation by the PEM, superimposed with a second order Bessel function as background [235]. Finally, the absorption spectrum is obtained by dividing by the fitted Bessel function baseline and normalizing to its maximum. Since the PEM driving amplitude is optimized for one wavelength λ_0 of the incident light, for which exactly a half-wave retardation is introduced, the received spectrum should only be used in a range of a few hundred wavenumbers around λ_0 . It should also be noted that the vanishing of the electric field component parallel to the metal surface leads to the surface selection rule [232], meaning that only vibrations with a TDM component perpendicular to the metal can be excited. This can be used to analyze the orientation of molecules with respect to the surface but is of minor interest for the here investigated, drop-casted and probably randomly oriented samples.

During this work, PMIRRAS measurements were performed on a PMA 50 unit by Bruker as extension to the Vertex 70 FTIR spectrometer. It contains a ZnSe PEM 90 from Hinds Instruments which is driven at 50 Hz and coupled to a SR830 DSP lock-in amplifier from Stanford Instruments. The signal is detected by a liquid nitrogen cooled MCT detector. Gold-coated silicon wafers were used as substrates. The half-wave retardation of the PEM was set at a wavenumber of 1500 cm^{-1} to examine the fingerprint region of the used AEs. The angle of incidence was set to 80° to get an optimal signal. For each spectrum 1000 scans with a resolution of 4 cm^{-1} were averaged. The background correction was carried out with the OPUS software from Bruker.

4.3 UV-vis-NIR spectroscopy

The absorption of light in the UV, visible (vis) and NIR spectral region by the prepared samples is a very important piece of information, since allowed electronic transitions, their oscillator strength, and their energies are directly detected [236]. The absorption is an important optical property of the used materials and changes in the absorption spectrum upon

mixing different compounds can give insights into possible interactions like for example CT [29]. For this thesis, UV-vis-NIR absorption spectra of the thin films were taken on glass substrates in transmission mode. In such transmission measurements, a small part of the spectrum of a lamp, chosen by slits, is directed onto the sample and the intensity of the transmitted light I_t is detected. By correlating I_t to the incident intensity I_0 , measured in a reference beam, the transmittance

$$T = \frac{I_t}{I_0} \quad (4.5)$$

is calculated for each chosen wavelength. Hence, the transmittance is a measure for the number of photons that still reach the detector after passing through the sample. The other part of the incident light is either absorbed, scattered or reflected by the sample. Absorption (a), scattering (s) and reflection (r) reduce the light intensity by the fraction T_a , T_s and T_r , respectively, hence the total transmittance can be split into three different contributions

$$T = T_a \cdot T_s \cdot T_r. \quad (4.6)$$

Based on the transmittance, two new quantities can be defined, namely the extinction as $Ex = 1 - T$ and, with Equation 4.6, the absorbance as

$$A = -\log_{10}(T) = -\log_{10}(T_a \cdot T_s \cdot T_r) = A_a + A_s + A_r, \quad (4.7)$$

with $A_j = -\log_{10}(T_j)$. As mentioned above, the absorption by the thin film, A_a in Equation 4.7, is the interesting quantity. Fortunately, A_a is the dominant contribution to the absorbance in the here investigated organic and organic-inorganic semiconductor samples and the only source of sharp peaks, while the scattering and the reflection from the sample can be seen as broader background.

Since plasmonic nanostructures additionally exhibit significant scattering and reflection of light, for these samples extinction or transmission spectra are commonly shown in the literature [164, 237]. In this thesis, extinction spectra are shown, but it should be mentioned that a fraction of the scattered light is collected due to the objective used. This slightly enhances the apparent transmission and hence reduces the extinction, but does not significantly influence the shape of the spectra.

The absorbance spectra shown in this thesis were taken on a Perkin Elmer Lambda 950 UV-vis-NIR spectrometer with a measuring range from 200 nm to 3000 nm. Spectra were acquired with a resolution of 0.5 nm.

The extinction spectra of the plasmonic samples were measured on an inverse Nikon (Eclipse 80i) microscope coupled to a grating spectrometer (LOT SR-303i-B). A 20x objective with a numerical aperture of 0.45 was used to collect the transmitted light. Together with the 100 μm entrance slit of the spectrometer, this results in a $5 \times 5 \mu\text{m}^2$ area that was measured. Illumination was realized by a halogen lamp with two pinholes in the illumina-

tion path to yield collimated light. A polarizer was introduced in the illumination path to excite specific directions in the samples. To calculate the background corrected extinction spectrum, not only the transmitted intensity I_{raw} at the area of interest (e.g. the array) was measured, but also the transmitted intensity I_{BG} beside the area of interest (e.g. beside the array) was measured under the same illumination condition as background. Additionally, the detector signal without illumination I_{dark} was recorded. With these three intensities, the final, background corrected extinction Ex was calculated as

$$Ex = \frac{I_{\text{BG}} - I_{\text{raw}}}{I_{\text{BG}} - I_{\text{dark}}}. \quad (4.8)$$

All extinction spectra shown in this work are background corrected spectra, calculated by Equation 4.8.

4.4 Photoluminescence spectroscopy

PL spectroscopy was used during this work to investigate the emission properties of the prepared samples [236]. Especially for the organic-inorganic thin films the PL spectra of the mixed films compared to the reference neat films can give insights into potential charge or energy transfer processes. During a PL measurement, the sample is illuminated with (generally) monochromatic light to excite a fraction of the molecules or quantum dots to a higher electronic state. The light emitted during the relaxation to the ground state is then collected and measured with a spectrometer. During this work, a Horiba Jobin Yvon LabRAM HR spectrometer was used. Two different excitation lasers with 532 nm and 633 nm wavelength, respectively, could be focused by a 50x objective on the sample and the emitted light was collected through the same objective. After a long-pass filter to suppress scattered laser light, the collected light was directed through a diffraction grating onto a CCD-1024×256-OPEN-3S9 detector to receive a wavelength resolved PL spectrum. The samples were either kept in nitrogen or vacuum during the measurement and liquid nitrogen or helium were used to cool the samples down in a cryostat.

4.5 Transient absorption spectroscopy

The dynamics of electronic processes in OSCs after photoexcitation are of crucial importance for their potential application in optoelectronic devices. One possibility to access the photophysics on ultrafast timescales is using TA spectroscopy [238]. TA spectroscopy as a pump-probe technique relies on two short consecutive laser pulses with a known and adjustable time difference. By measuring the absorption of the sample at different times after the excitation, the dynamics of the evolution of the excited states can be followed. An introduction to the technique, setup, and data analysis is given in the following, and more details can be found in Refs. [238, 239] and references therein.

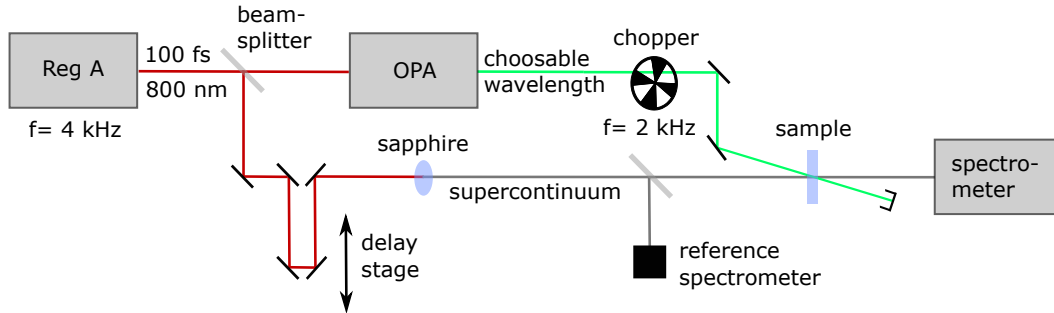


Figure 4.4: Schematic TA spectrometer setup. Reg A denotes the regenerative amplifier which provides the fundamental, short laser pulses. OPA abbreviates optical parametric amplifier, which is used to receive pump pulses at the desired wavelengths. Further details are given in the main text. Inspired by Ref. [239].

4.5.1 Setup and technique

A schematic of a TA setup, including the most important parts, is shown in Figure 4.4. As starting point for a TA measurement, short and intense laser pulses are required. They are produced in a regenerative amplifier by pumping a Ti:sapphire with a strong continuous-wave laser and extracting the stored energy with a pulsed seed laser [240]. In the setup used for this thesis, the regenerative amplifier outputs ~ 100 fs long pulses with 800 nm wavelength at a frequency of 4 kHz. This output is directed through a beamsplitter that reflects a small fraction of the light to give the probe pulse while the larger fraction is used as pump pulse. The pump pulses are directed to an optical parametric amplifier in which nonlinear optical processes are used to generate pulses with a specific, choosable wavelength λ_{exc} for excitation [241]. Every second pump pulse is hereafter blocked by a chopper, and the remaining pulses are directed to the sample for excitation. The probe pulses, on the other hand, are directed through a delay stage, allowing to change the traveled path length and hence the relative time delay Δt between the pump and the probe pulse. Since the probe pulses need to be spectrally broad to give a transient absorption spectrum, they are directed through a (sapphire) crystal which generates a white light supercontinuum. Depending on the used crystal, a supercontinuum in different wavelength regions can be generated, spanning from the UV to the NIR region. A fraction of each probe pulse is afterward directed via a second beamsplitter toward a reference spectrometer, which is used to monitor the intensity of each pump pulse, while the remaining part is focused on the sample. The transmitted light of the probe pulses is then collected by the spectrometer. Before the start of a measurement, the spatial overlap of the two pulses on the sample is maximized by adjusting the pump path at the last mirror and the temporal overlap is adjusted with the position of the delay stage. During the measurement, the time delay between the pump and the probe pulse is then scanned by moving the delay stage.

From the measured transmitted intensities of the probe pulses at Δt after excitation of the sample, $I_{\text{on}}(\lambda, \Delta t)$, and without excitation of the sample $I_{\text{off}}(\lambda, \Delta t)$ (because the pump pulse was chopped), a TA signal is calculated by

$$\Delta A(\lambda, \Delta t) = A_{\text{on}}(\lambda, \Delta t) - A_{\text{off}}(\lambda, \Delta t) \quad (4.9)$$

$$= -\log_{10} \left(\frac{I_{\text{on}}(\lambda, \Delta t)}{I_{0,\text{on}}(\lambda, \Delta t)} \right) + \log_{10} \left(\frac{I_{\text{off}}(\lambda, \Delta t)}{I_{0,\text{off}}(\lambda, \Delta t)} \right) \quad (4.10)$$

$$\approx \log_{10} \left(\frac{I_{\text{off}}(\lambda, \Delta t)}{I_{\text{on}}(\lambda, \Delta t)} \right). \quad (4.11)$$

The incoming probe pulse intensities $I_{0,\text{on}}(\lambda, \Delta t)$ and $I_{0,\text{off}}(\lambda, \Delta t)$ are hereby expected to be very similar because $I_{\text{on}}(\lambda, \Delta t)$ and $I_{\text{off}}(\lambda, \Delta t)$ are measured from consecutive pulses due to the chopper. If, due to laser power fluctuations, the intensities of the probe pulses measured at the reference spectrometer still vary too much, the signal is automatically discarded and remeasured. For each delay time, thousands of spectra are acquired and averaged. Spectra from a few negative delay times, implying that the pump pulse arrives after the probe pulse at the sample, are taken as reference. Since the TA signal at these negative delay times should vanish, these spectra can be subtracted as background from the entire data set, which allows to remove baseline offsets and (some) artifacts from scattered laser light.

4.5.2 Signals in transient absorption spectra

The TA spectrum is defined as the difference in absorbance between the excited and unexcited sample (Equation 4.9). Several processes can give rise to changes in the absorbance after photoexcitation, which are briefly discussed in the following. From a macroscopic viewpoint, it is expected that neither the scattering nor the reflection from the sample is significantly changed after excitation, so no ΔA signal is expected from them. This is different for the absorption, which leads to a direct dependence of the TA signal from the changes in the absorption coefficient α . If one expresses α as $\alpha(\lambda, \Delta t) = n(\Delta t)\sigma(\lambda, \Delta t)$, with the density n of absorbers and the absorption cross section σ of a single absorber [236], two different contributions to the changes in the absorption coefficient can be distinguished:

$$\Delta\alpha(\lambda, \Delta t) = \Delta n(\Delta t)\sigma(\lambda, \Delta t) + n(\Delta t)\Delta\sigma(\lambda, \Delta t). \quad (4.12)$$

The first term on the right hand side of Equation 4.12 is related to a change in the density of absorbers. Here, an absorber is defined as, e.g., a molecule in a specific electronic state, so changes in the electronic states will change the densities of absorbers while the total density of molecules remains the same. The second term takes changes in the absorption cross section of the absorbers into account. For organic molecules, the first term often dominates, allowing to directly follow the state population distribution with time. There are several processes that contribute to the TA signal originating from this term [239], compare Figure 2.7:

- Ground state bleach (GSB): The pump pulse excites a small fraction of the molecules to a higher, excited state. Therefore, the number of absorbers in the ground state is

reduced, which leads to a reduced absorption at the wavelengths at which the sample absorbs in the ground state. Consequently, a negative ΔA signal appears, which resembles the absorption spectrum. This GSB is present as long as the absorbers are not relaxed back to the ground state. In QDs, the corresponding effect is known as change in state filling, describing the case that if an electron is already excited to a certain state, the transition probability for a second one is decreased, giving rise to a similar signal [242].

- Stimulated emission (SE): Molecules that are excited by the pump pulse and reside in a bright state can be stimulated by the probe pulse to emit a photon in the same direction as the stimulating photon. By this process, the number of photons reaching the detector is increased, leading to a negative ΔA signal. In this work, SE is most prominently found for molecules in the S_1 state, resulting in a signal that resembles the emission spectrum of the thin film. This signal disappears when the S_1 state is depopulated, e.g. by relaxation to the ground state or triplet states, or by CT.
- Photoinduced absorption (PIA) and ESA: These terms are often used interchangeably in the literature and refer to positive ΔA signals that result from transitions from excited states, populated by pumping, to higher excited states. The term ESA is used within this thesis to describe signals arising from transitions from S_1 to S_n and T_1 to T_n states, while PIA is used for signals arising from transitions in charged species and for the positive signals in the QD-containing samples. These signals disappear as soon as the species from which the transition starts is depopulated.

The second term on the right hand side of Equation 4.12 is mainly important for the QD containing samples. It describes the changed absorption cross section of the single absorber after photoexcitation of the sample. In QDs, electrons and holes can be treated more independently from each other and several excitations can reside on a single QD [141, 243]. This leads to the possibility that on an already excited QD (by the pump pulse) a second electron-hole pair can be excited by the probe pulse. The already excited QD has, however, a different electronic configuration and consequently transitions at slightly different energies than in the ground state. Therefore $A_{\text{on}}(\lambda, \Delta t)$ is spectrally slightly shifted with respect to $A_{\text{off}}(\lambda, \Delta t)$, leading to a first derivative-like feature (of the absorption spectrum) in the TA signal. This is called biexciton effect and is mainly observed for short wavelength pump pulses [243].

The second effect that will be discussed briefly in the context of a changed absorption cross section is the trapped-carrier induced Stark effect [142]. This effect describes that due to the trapping of the electron and/or hole after the pump pulse, an electric field is generated, which induces a shift of the transition energies and a redistribution of oscillator strength. In the limit of small fields and broad absorption linewidths, this effect can give rise to a signal that resembles the second derivative of the absorption spectrum [142]. It is worth noting that

a Stark effect is also seen in the TA data of the organic CT blends, where ion pair formation is induced by photoexcitation, which similarly leads to electric fields in the sample [244].

Additionally, a measurement artifact called heating effect or thermal effect is mentioned at this point, since it is also caused by a change in the absorption cross section of the molecules [188, 245]. Owing to the relatively high pulse energies applied during a TA measurement, the sample can be locally heated by the laser pulse. This temperature change, induced by the pump pulse, can lead to a changed absorption cross section of the molecules in the ground state and, hence, a first derivative-like feature in the TA spectrum, similar to the one induced by the biexciton effect described above. Such thermally-induced effects have been observed in TA measurements of TET and PEN thin film samples [188, 245, 246].

4.5.3 Transient absorption data analysis

From a TA measurement, a TA signal $\Delta A(\lambda, \Delta t)$ as function of the wavelength and the time difference between the pump and probe pulse is obtained. It can be presented as a two-dimensional TA map with the wavelength on the horizontal axis, the time delay on the vertical axis, and the signal represented by a color code. A horizontal cut through such a TA map yields a TA spectrum at a certain delay time, while a vertical cut yields a timetrace at a certain wavelength. In the TA spectra at certain times, signals from the effects described in the previous section can be found and, consequently, conclusions on the present species in the sample can be drawn. Species denote in this case molecules or QDs in a certain electronic state. From the timetraces, ideas about the dynamics of the involved processes can be gained.

Since, however, all the signals from the effects described in the previous section might be superimposed in a TA spectrum, single TA spectra and timetraces are often not sufficient to unravel the processes in the sample and their dynamics. Therefore, additionally to fits to single timetraces, a global analysis (GA) of the TA data is performed. In a GA, a model consisting of a defined number N of different species, which are either assumed to evolve into each other (sequential) or to decay in parallel, is fitted to the experimental data. In a least-squares fitting process, transient spectra $\epsilon(\lambda)$ of the different species with their concentrations $c(\Delta t)$ are determined to yield the modeled two-dimensional TA data set [247]

$$\Delta A_{\text{model}} = \sum_{i=1}^N c_i(\Delta t) \epsilon_i(\lambda),$$

that best describes the experimental data. For the parallel model, it is assumed that all species are directly excited by the pump pulse and the concentrations decay exponentially, namely

$$c_i(\Delta t) = a_i \exp\left(-\frac{\Delta t}{\tau_i}\right),$$

with the decay time constants τ_i and the normalization parameters a_i that are chosen such that the sum of the concentrations is normalized to 1.

For the sequential model, the assumption is that only species 1 is excited by the pump pulse and then decays to species 2 with a time constant τ_1 . The concentration of species 2 hence rises with the time constant τ_1 and, consequently, decays with τ_2 to the next species and so on, until the last species decays to the ground state. By GA, time constants associated with specific TA spectra are obtained, which can be assigned to transient species, giving more robust information about the dynamics than single timetraces. The transient spectra of a sequential model are called evolution associated spectra (EAS) [248]. The choice of the model is, however, very important and relies on a priori knowledge about possible involved processes. The number of involved species is also of crucial importance. Here, several GAs with different numbers of involved species were performed on each data set and the one with the lowest number of species that still resulted in a fit without systematic residuals was chosen as the appropriate one.

Since the TA setup has a finite time resolution due to the duration of the pulses and the read-out speed, the TA signal does not rise instantaneously, and an infinitely fast decay would be seen with a certain temporal width. This temporal width is given by the instrument response function, which can be approximated by a Gaussian and is taken into account in the GA by convolution with each timetrace.

GA of the TA data acquired during this work was done with the open source software Glotaran [248]. This software also allows to do some pre-processing of the data such as a background correction by subtracting the spectra at negative delay times and a correction for the group velocity dispersion. This effect describes that photons with different wavelengths in the probe pulse arrive at different times at the sample, giving a curved trace of time zero points in the two-dimensional TA map. This trace is fitted by a third order polynomial, which is then used to shift the timetraces to a common time zero.

4.5.4 Experimental setup used in this work

The TA measurements were conducted in Heidelberg on a commercial HELIOS TA spectrometer from Ultrafast Systems. The fundamental, ~ 100 fs short pulses with a central wavelength of 800 nm were provided from a Ti:sapphire amplified laser system (Astrella, Coherent) with a repetition rate of 4 kHz. The optical parametric amplifier TOPAS Prime from Light Conversion was used to generate the pump pulses at wavelengths of 350 nm, 400 nm, 495 nm, 520 nm, and 620 nm for the different experiments, respectively. Three different white light supercontinuum spectral ranges from 330 – 675 nm, 450 – 770 nm, and 830 – 1400 nm, generated by focusing the 800 nm pulses on different sapphire crystals, were used as probe pulses. The pump-probe delay was scanned by a motorized delay stage, allowing to investigate the dynamics up to 8 ns after the excitation. The pump beam pulses are focused on the sample to a diameter of ~ 300 μm and the excitation density was controlled by gray filters in the pump path. The probe beam was focused to a smaller area to probe only on the excited area. Magic angle polarization between the two beams was used for all measurements.

4. Characterization techniques

To avoid photo-degradation during the measurements, the samples were encapsulated by a second glass in nitrogen atmosphere.

Part II

Results and Discussion

5. Charge transfer complexes of tetracene with strong acceptors

In this chapter, the ground state CT interactions of the SF material TET with the two strong acceptors F4-TCNQ and F6-TCNNQ are described. The formation of CTCs is found for both material combinations as a result of the strong electronic coupling between the different OSC molecules. Particular focus is put on the photophysics of the CTC containing blends in comparison to the photophysics of the neat compound films. The results presented in this chapter have been published in Ref. [129] and were obtained in collaboration with the research groups of Prof. Dr. Petra Tegeder and Prof. Dr. Caterina Cocchi. For details about the contributions see Appendix F.

5.1 Introduction

The separation of electrons and holes in organic solar cells or the doping of organic materials is realized by CT between organic donor and acceptor molecules, as detailed in Chapter 1. As a result, considerable research effort has been devoted to the study of different CT mechanisms and donor:acceptor systems (cf. Section 2.2.6) [36, 128, 249]. Yet, still open questions concerning the preferred CT mechanism for specific donor:acceptor combinations remain. In this chapter, the CT interactions in blends of the SF material TET with the two prototypical, strong acceptors F4-TCNQ and F6-TCNNQ are discussed. The molecular structures and the EAs and IPs of the three molecules are shown in Figure 5.1. The close energetic proximity of the IP of TET to the EAs of F6-TCNNQ and F4-TCNQ renders ground state CT likely. Though, the IPs and EAs of the components determined in neat films might be significantly altered in blends [39] and, thus, only serve as a starting point for the experimental investigation. In the blends, the formation of different CTCs, depending on the acceptor molecule and the mixing ratio, was found by UV-vis-NIR and FTIR spectroscopy and further confirmed by theoretical calculations. Especially the photophysics of CTCs with NIR absorption has been barely investigated so far. Here, the photophysics of the neat compounds and of the blends containing the CTCs was investigated by performing TA spectroscopy.

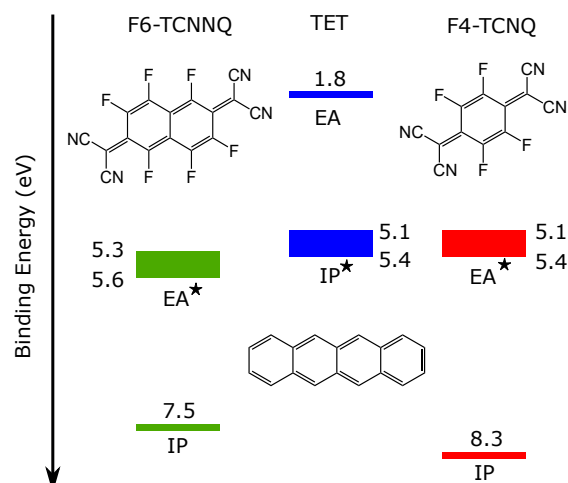


Figure 5.1: Molecular structures, EAs, and IPs of TET and the two acceptors F6-TCNNQ and F4-TCNNQ. All values are given in eV. The IPs of F6-TCNNQ and F4-TCNNQ were taken from Refs. [192, 194] and the EA of TET from Ref. [250]. For the EAs of the acceptors and the IP of TET, marked by an asterisk, an energy range is given, since these are the decisive values for CT. The IP values for TET, measured by UV photoelectron spectroscopy, were taken from Refs. [172, 174] and the EA values for F6-TCNNQ and F4-TCNNQ, measured by cyclic voltammetry and inverse photoemission spectroscopy, were taken from Refs. [191–194, 197]. Modified from Ref. [129].

5.2 X-ray diffraction

To investigate the structure of the neat and mixed thin films, XRR and GIWAXS measurements were carried out. XRR scans of the TET:F6-TCNNQ and TET:F4-TCNNQ blends and of the neat films are shown in Figure 5.2. For the neat TET films, the Bragg peaks of the thin film phase at $q_z = 0.48 \text{ \AA}^{-1}$ and $q_z = 0.97 \text{ \AA}^{-1}$, corresponding to a lattice spacing of $d_z = 12.95 \pm 0.07 \text{ \AA}$, are strongly pronounced [178, 251]. The Bragg peaks of the bulk phase, at slightly higher q_z , are only weakly expressed, but, at least in the 80 nm thick film, clearly resolved [178, 251].

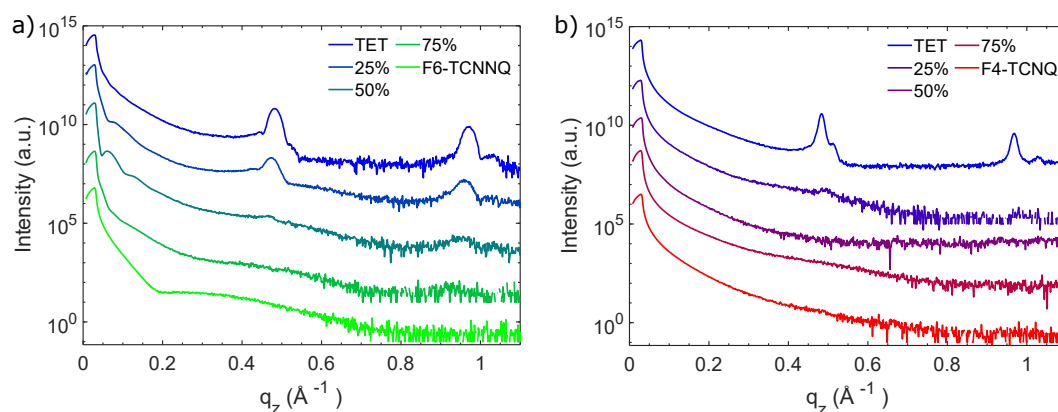


Figure 5.2: XRR data of a) 20 nm thick TET:F6-TCNNQ blends and b) 80 nm thick TET:F4-TCNNQ blends. In the legend, the molar acceptor fraction is given. The curves are vertically offset for clarity.

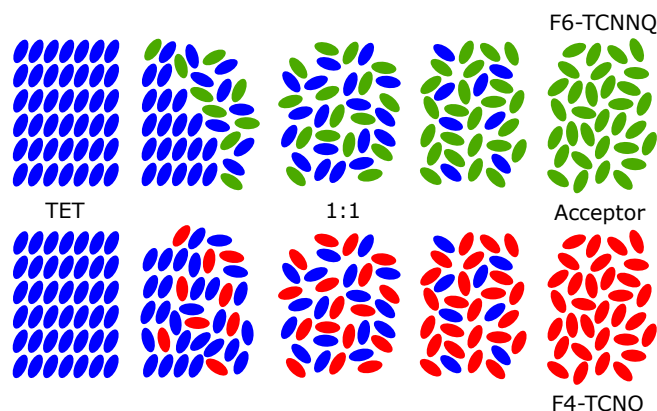


Figure 5.3: Schematic mixing scenario for the two TET:acceptor systems. Modified from Ref. [129].

For the neat F6-TCNNQ and F4-TCNQ films and the blends with an excess of acceptor molecules, no Bragg peaks are visible, indicating a lack of long-range out-of-plane order, consistent with earlier reports [35, 130]. The XRR scans of the blends with an excess of TET exhibit Bragg peaks assignable to the TET thin film polymorph, indicating some TET crystallites in these films. These peaks are much more pronounced in the XRR data of the blends with F6-TCNNQ than in the XRR data of the blends with F4-TCNQ, and are also weakly observable for the equimolar blend with F6-TCNNQ. A similar trend of stronger Bragg peaks assignable to the TET thin film polymorph for the blends with F6-TCNNQ than for the blends with F4-TCNQ is found by the GIWAXS data presented in Appendix A.1. Taken together, the X-ray diffraction data suggest an amorphous mixed phase of TET and the respective acceptor, and, for blends with an excess of TET, a phase separation of neat TET crystallites from this mixed phase. This phase separation is more strongly pronounced for TET:F6-TCNNQ blends than for TET:F4-TCNQ blends and leads to the mixing scenario presented in Figure 5.3.

5.3 Optical spectroscopy

Having established the structure and mixing behavior of the blends, the resulting optical properties are analyzed next. UV-vis-NIR absorbance spectra of both systems are presented in Figure 5.4. The spectrum of the neat TET film exhibits the characteristic Davydov splitting (see Section 3.2.1) around 2.4 eV and a clear vibronic progression. In contrast, the spectra of the two neat acceptor films show only very broad peaks and no resolved vibronic progression in accordance with the literature [29, 197]. The energetically lowest optical transitions of the F6-TCNNQ and F4-TCNQ films are around 2.35 eV and 2.67 eV, respectively.

The absorbance spectra of the blends show distinctly different features than the spectra of the neat compound films, which is a sign for electronic coupling between the donor and acceptor molecules. Most prominently, the spectra of all blends of both series exhibit absorption features at low energies, below 1 eV, while the neat films only absorb at higher energies.

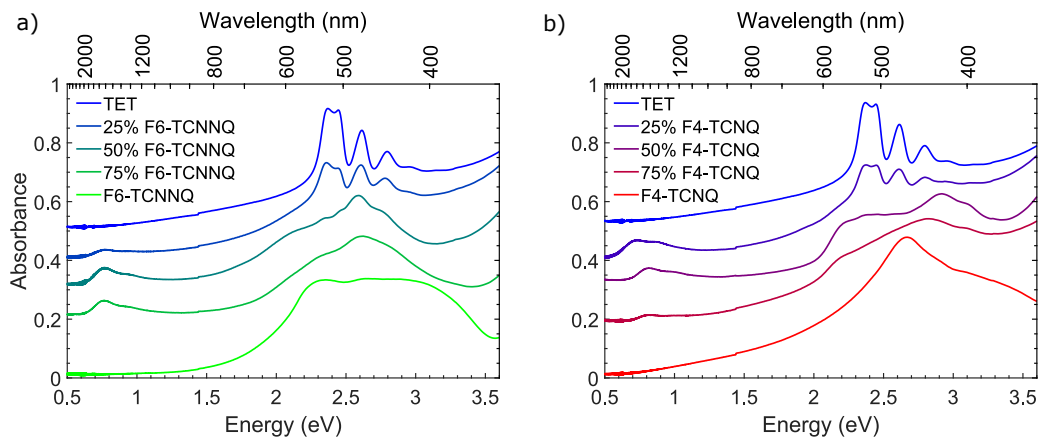


Figure 5.4: UV-vis-NIR absorbance spectra of a) TET:F6-TCNNQ and b) TET:F4-TCNQ blends, vertically offset for clarity. Modified from Ref. [129].

The absence of sharp ion peaks in the spectra of the blends, which would be expected at 1.4 eV and 1.6 eV for F4-TCNQ⁻ anions [28], at 1.1 eV and 1.3 eV for F6-TCNNQ⁻ anions [191], and at 1.4 eV and 1.7 eV for TET⁺ cations [252], indicates the absence of integer CT with ion pair formation. Instead, the relatively broad appearance of the low-energy features suggest the formation of CTCs [28]. This indicates a relatively strong electronic coupling between the donor and acceptor molecules in the blends [36]. For all blends of TET with F6-TCNNQ, these peaks are found at an energy of 0.77 eV, with a weaker vibronic replica at 0.92 eV. They are most pronounced in the equimolar blend. These features most likely correspond to transitions between the ground state of a CTC and its first excited state, as verified by the theoretical calculations presented below. Furthermore, the shoulder in the spectra of the blends around 2.1 eV, thus below the band gap of both neat materials, is assigned to transitions in the CTCs, too. It is also worth noting that the spectrum of the blend with 25% F6-TCNNQ can be described as a superposition of the spectra of the equimolar blend and the neat TET film (see Figure A.2 in the Appendix), underpinning the proposed mixing scenario in Figure 5.3.

The absorbance spectra of the TET:F4-TCNQ blends (Figure 5.4b) also exhibit absorption peaks below 1 eV and an absorption shoulder below the band gap of the neat materials, namely around 2.2 eV. Thus, a similar conclusion of CTC formation as for the TET:F6-TCNNQ blends can be drawn, which is again substantiated by the *ab initio* calculations presented below. However, the low-energy absorption features show a distinctly different behavior in the blends with F4-TCNQ compared to the blends with F6-TCNNQ. For the equimolar blend and the blend with an excess of F4-TCNQ, the lowest absorption peak is found at 0.81 eV, with a vibronic replica at 0.96 eV [253]. Thus, they are found at slightly higher energies than the peaks in the TET:F6-TCNNQ blends. In contrast, in the spectrum of the blend with 25% F4-TCNQ, the energetically lowest transition is observed at 0.70 eV and its vibronic replica at 0.86 eV, thus clearly shifted toward smaller energies. Additionally, the intensity of these peaks is increased compared to the equimolar blend. Taken together, this demonstrates

a sensitivity of the CTC formation on the mixing ratio for the blends with F4-TCNQ but not for the blends with F6-TCNNQ. This peculiarity will be further analyzed below by involving *ab initio* calculations.

5.4 Vibrational spectroscopy

If electrons are added to or withdrawn from a molecule, the stiffness of the bonds between its atoms is altered, resulting in changes in the vibrational spectrum. Therefore, FTIR spectroscopy is often used to examine the degree of charge transfer (δ_{CT}) in mixed films and CTCs [28, 42, 130, 190, 197]. Generally, the changes in the $C\equiv N$ stretching mode energies between uncharged molecules and the corresponding anions are significant, since the excess charge is preferentially localized on the cyano groups [197]. Additionally, the peak shift of this mode is assumed to be linear with δ_{CT} , which allows a straight-forward determination of δ_{CT} [28, 190]. In Figure 5.5, FTIR spectra of the neat acceptor films, the equimolar blends, and the blends with an excess of TET are presented. Neat TET does not show any peaks in this wavenumber region [253]. Thus, the visible peaks of the stretching mode of the cyano groups of the acceptors are well suited for the determination of δ_{CT} in the blends. For the neat F4-TCNQ film, one sharp peak is observed at 2228 cm^{-1} and a weak one at 2216 cm^{-1} , consistent with the literature [28]. The main peak shifts by 4 cm^{-1} toward lower wavenumber in the equimolar blend, see Figure 5.5a. In the F4-TCNQ⁻ anion spectrum, the peak of the $C\equiv N$ stretching mode has been reported to be located at 2194 cm^{-1} [28, 254], resulting in $\delta_{CT} = (0.12 \pm 0.05) e$ for the equimolar blend with the assumed linear dependence. The error estimation is based on the measurement resolution and the fitting accuracy. This result is in good agreement with the value of $\delta_{CT} \sim 0.15 e$ that has been reported for TET:F4-TCNQ 1:1 single crystals [42, 253].

Notably, for the blend with an excess of TET, which showed the red-shifted NIR absorption peaks, a much stronger peak shift of the $C\equiv N$ stretching mode is observed. The higher-energy peak is shifted to 2215 cm^{-1} and the lower, now dominant peak, to 2206 cm^{-1} . From the shift of the higher-energy peak, $\delta_{CT} = (0.38 \pm 0.05) e$ is obtained, hence a significantly larger value than for the equimolar blend.

The interpretation of the FTIR spectra of the F6-TCNNQ containing blends (Figure 5.5b) is more intricate and a more complex connection between the vibrational spectra and δ_{CT} than for F4-TCNQ has been reported before [197]. Already the neat F6-TCNNQ film exhibits several strong peaks assigned to $C\equiv N$ stretching modes in accordance with the literature [130, 197]. For the two blends, the main peak shifts only by $\sim 1\text{ cm}^{-1}$ toward smaller wavenumbers. Additionally, the spectral shape and relative intensities of the peaks are slightly altered, consistent with the observations in Ref. [130] for blends of another donor with F6-TCNNQ. Therein, also only a slight shift of the main peaks has been observed in PMIRRAS spectra, but a significant degree of charge transfer has been concluded from the appearance of a weaker peak at smaller wavenumbers [130]. Such a peak might not be visible in the FTIR

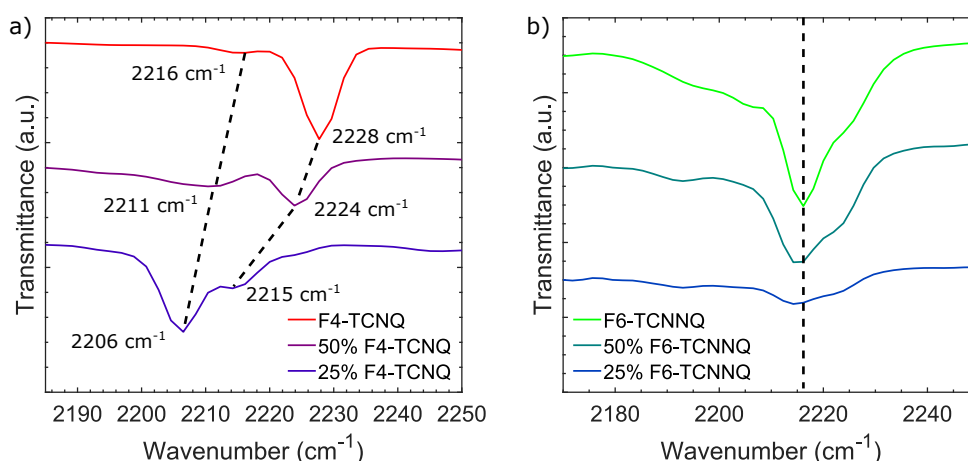


Figure 5.5: FTIR spectra of the TET blends with a) F4-TCNQ and b) F6-TCNNQ in the energy region of the cyano group stretching mode. The spectra are vertically offset for clarity and the dashed black lines are guides to the eye. In b) only a vertical line is drawn to illustrate the small peak shift. Modified from Ref. [129].

spectra presented in Figure 5.5b. Additionally, it has been concluded in Ref. [130] that a combined analysis of the modifications of the C=C and C≡N stretching modes is required to conclusively determine δ_{CT} for CTCs with F6-TCNNQ. Since the wavenumber region of the C=C stretching mode is obscured by artifacts from water vapor in the measurement atmosphere (see, e.g., Figure 9.1), this is not possible with FTIR measurements. Thus, δ_{CT} for the TET:F6-TCNNQ blends was addressed by the theoretical calculations presented next.

5.5 Ab initio calculations

Ab initio density-functional theory and many-body perturbation theory calculations were performed by Dr. Ana M. Valencia from the group of Prof. Dr. Caterina Cocchi to verify the CTC formation, to determine δ_{CT} , and to analyze the differences between the blends of TET with F6-TCNNQ and with F4-TCNQ. Details about the calculations can be found in Ref. [129]. The calculations were carried out on isolated clusters in vacuum, consisting of one acceptor molecule and either one TET molecule (dimer, simulating the equimolar blends) or three TET molecules (tetramolecular cluster, simulating the blends with excess of TET). As a first step, the geometry of the clusters was obtained by structural optimization, starting from the molecular positions extracted from the TET:F4-TCNQ cocrystal [42]. Due to the lack of a corresponding reference for the molecular positions in TET:F6-TCNNQ cocrystals, the same starting positions were used for both systems. The resulting geometries are shown in Figure 5.6. For the dimers, a cofacial arrangement was obtained, which is in line with reported calculations on similar materials [35]. For the tetramolecular clusters, two different geometries were considered, namely a stacked and a lateral one (Figure 5.6), to simulate different orientations and interactions.

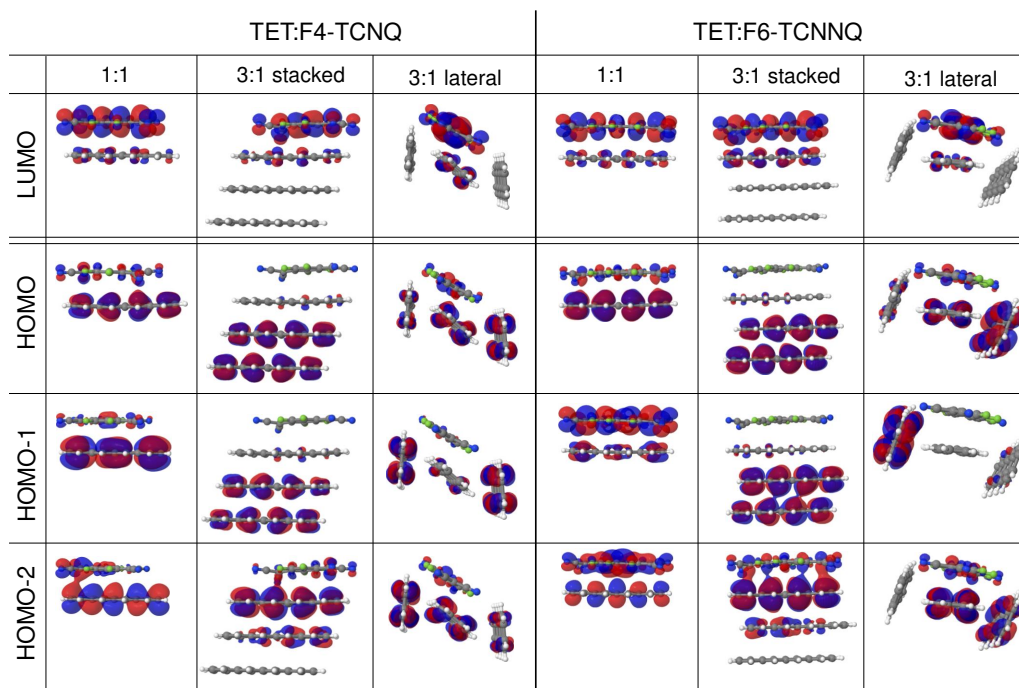


Figure 5.6: Optimized molecular geometries and corresponding molecular orbitals of the investigated TET:F4-TCNQ and TET:F6-TCNNQ clusters, obtained from density-functional theory calculations (CAM-B3LYP functional). The uppermost molecule in each cluster is the acceptor. Modified from Ref. [129].

Figure 5.6 additionally contains some calculated molecular orbitals, namely the LUMO, the HOMO, the HOMO-1, and the HOMO-2, since they are the most relevant ones for the low-energy optical transitions, *vide infra*. It is apparent that the mentioned orbitals are delocalized on both molecules in the TET:F4-TCNQ as well as the TET:F6-TCNNQ dimer, which is indicative for CTC formation [26, 28, 38, 126]. The hybridization is, however, less pronounced than for other CTCs that have been reported [28, 255], which indicates a lower δ_{CT} .

In the tetramolecular clusters, the LUMO is, as for the dimers, mostly localized on the acceptor and only slightly delocalized to the facing donor. The occupied molecular orbitals shown in Figure 5.6 for the tetramolecular clusters are more strongly delocalized over the cluster. In the stacked geometry, the HOMO and HOMO-1 are nearly exclusively localized on the two TET molecules that are the furthest away from the acceptor, while the HOMO-2 is delocalized mostly over the acceptor and the facing TET molecule. In the lateral clusters, the HOMO and HOMO-2 are distributed over all four molecules.

Based on the density-functional theory calculations, also δ_{CT} , as an important quantity of the CTCs, was evaluated by a Hirshfeld charge analysis [256]. For the TET:F4-TCNQ and the TET:F6-TCNNQ dimers, $\delta_{CT} = 0.24 e$ and $\delta_{CT} = 0.25 e$, respectively, were obtained. This value for the TET:F4-TCNQ dimer is larger than the experimentally found value of $\delta_{CT} = 0.12 e$ for the equimolar blend with F4-TCNQ, but still on the same order. The similar δ_{CT} found for the two different dimers indicates similar CT interactions in the equimolar blends

of TET with F4-TCNQ and with F6-TCNNQ. For the tetramolecular cluster, larger δ_{CT} values were obtained. In the lateral clusters $\delta_{CT} = 0.25 e$ and $\delta_{CT} = 0.30 e$ was calculated for F4-TCNQ and F6-TCNNQ as acceptor, respectively, and in the stacked clusters $\delta_{CT} = 0.33 e$ was found, independent of the acceptor. Especially the latter value is in good agreement to the experimentally determined value of $\delta_{CT} = 0.38 e$ for the blend with 25 % F4-TCNQ. However, the calculated values for the tetramolecular clusters with both acceptors are similar. Thus, the experimentally found differences between the two blends with 25 % acceptor molecules cannot be directly explained from these calculations. Instead, the differences in the structure of the two blends need to be taken into consideration, too, as detailed below.

Finally, absorption spectra of the described dimers and tetramolecular clusters were calculated (Figure 5.7) for comparison with the experimental spectra (Figure 5.4) and to assign the features in the ultrafast spectroscopy data shown below. Figure 5.7a shows the calculated spectra of the two dimers. They are, especially in the low-energy region, in good agreement to the experimental spectra of the equimolar blends and exhibit the same trends. In the calculated TET:F6-TCNNQ and TET:F4-TCNQ dimer spectra, the lowest-energy absorption peak, whose dominant contribution is the HOMO-LUMO transition of the CTCs, is found at 0.84 eV and 0.91 eV, respectively. This is nicely consistent with the trend found in the experimental spectra (0.77 eV and 0.81 eV), with only minor absolute energy shifts.

The absorption shoulder below the band gap of the neat compound films, which was experimentally discovered for both equimolar blends (at 2.1 eV and 2.2 eV, respectively), was also reproduced in the calculated spectra of the TET:F6-TCNNQ and TET:F4-TCNQ dimers at 2.0 eV and 2.4 eV, respectively. Again, the absolute energy positions are slightly shifted, but the trend is reproduced. For higher energies, the differences between the experimental and calculated spectra become larger, most likely due to the increasing amount of configurations that need to be considered in the configuration interaction.

The calculated absorption spectra of the tetramolecular TET:F4-TCNQ clusters, displayed in Figure 5.7b, are clearly different from the dimer spectrum. The lowest absorption peak is red-shifted for both tetramolecular clusters, to an energy of 0.82 eV and 0.73 eV for the stacked and the lateral cluster, respectively, resulting in a shift of 0.09 eV and 0.18 eV with respect to the corresponding dimer absorption peak. Thus, the experimentally determined shift of 0.11 eV between the lowest absorption peak in the equimolar blend and the blend with an excess of TET can be rationalized by the formation of such tetramolecular clusters. Interestingly, a stacked cluster of two TET molecules and one F4-TCNQ molecule does not produce a shifted spectrum, see Ref. [129] for details.

For the tetramolecular TET:F6-TCNNQ clusters, similar trends as for the tetramolecular TET:F4-TCNQ clusters are observed (Figure 5.7). The calculated absorption spectra of the TET:F6-TCNNQ clusters (Figure 5.7c) exhibit a red-shift of the lowest absorption peak compared to the dimer, too, namely by 0.09 eV and 0.11 eV for the lateral and the stacked cluster, respectively. This is in contrast to the experimental spectrum of the TET:F6-TCNNQ blend with an excess of TET, which is not shifted relative to the spectrum of the equimolar blend.

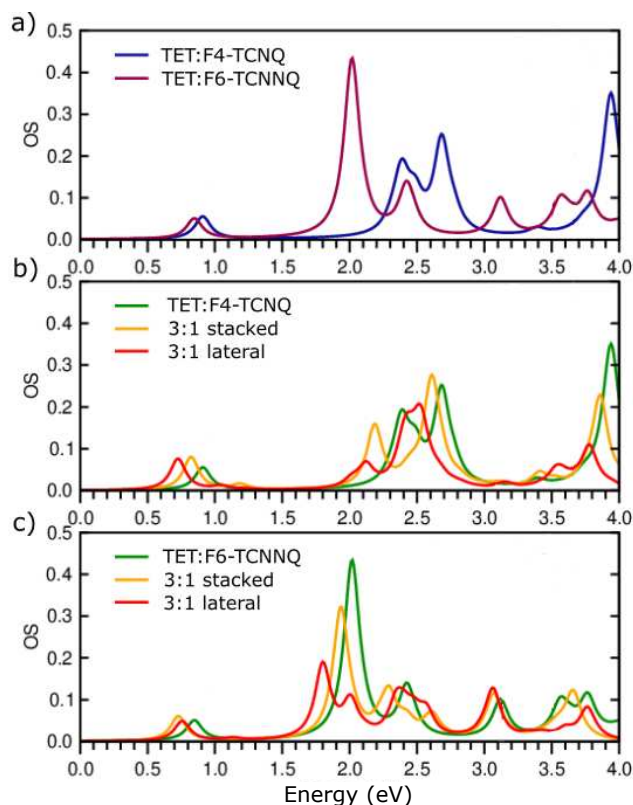


Figure 5.7: Calculated absorption spectra of a) the two dimers, b) the TET:F4-TCNQ dimer and clusters, and c) the TET:F6-TCNNQ dimer and clusters. OS abbreviates oscillator strength. Modified from Ref. [129].

A likely explanation for the discrepancy between the calculated spectrum of the tetramolecular clusters and the experimental spectrum of the 25 % F6-TCNNQ blend, in contrast to the similarity between these spectra found for the F4-TCNQ containing system, is extracted from the structural results presented in Section 5.2. There, a clear long-range order of phase separated TET domains was found in the 25 % F6-TCNNQ blend, while for the 25 % F4-TCNQ blend only weak indications for TET domains were observed. Together with the insights gained from the calculations, this can be interpreted in the way that F4-TCNQ molecules are incorporated in the TET domains, forming CTCs consisting of one F4-TCNQ molecule and several TET molecules, while such clusters are not formed in blends with F6-TCNNQ. This is possibly a result of the smaller size of F4-TCNQ compared to F6-TCNNQ, which might result in less steric hindrance for the incorporation of F4-TCNQ molecules into TET domains. The scenario of multi-donor CTCs in TET:F4-TCNQ blends with an excess of TET is further supported by the FTIR measurements which demonstrated a stronger shift of the $C\equiv N$ stretching mode and, thus, a higher δ_{CT} in the blend with an excess of TET compared to the equimolar blend. In contrast, the non-appearance of a shift of the low-energy absorption peaks for TET:F6-TCNNQ blends with an excess of TET and the high structural order in the phase separated TET domains indicate the formation of neat TET crystallites and the absence of multi-donor CTCs with F6-TCNNQ.

5.6 Transient absorption spectroscopy

In this section, the results of the TA measurements of the neat films and the blends are presented, which were performed to investigate the photophysics of the formed CTCs. The TA data of the neat TET and the two acceptor films are discussed before the focus is placed on the blends. As excitation wavelengths $\lambda_{\text{exc}} = 520 \text{ nm}$ (2.38 eV) and $\lambda_{\text{exc}} = 400 \text{ nm}$ (3.10 eV) were chosen because by the former, TET, F6-TCNNQ, and the CTCs can be efficiently excited (compare Figure 5.4), while the latter is used for the excitation of the F4-TCNQ film and the F4-TCNQ containing blends.

The photophysics of neat TET thin films has been extensively studied due to the SF capability of TET [187, 188]. In Figure 5.8, the TA data of a neat TET film with $\lambda_{\text{exc}} = 520 \text{ nm}$ is shown. The TA features and their evolution can be seen in the TA map in Figure 5.8a and they are assigned in the following based on their wavelength position and the literature [187, 188]. The negative feature around 480 nm is assigned to the first vibronic replica of the GSB, whose main feature at 520 nm is obscured by scattered laser light of the pump laser. Thus, this wavelength region is left blank in the shown TA map. The strong negative feature around 535 nm, together with the vibronic replica around 570 nm, can be assigned to SE. The positive features around 660 nm and above 700 nm are assigned to singlet ESA and triplet ESA, respectively. Finally, the positive features below 520 nm can be explained by a heating effect [245, 246].

The differences between the TA spectra after 1 ps and 200 ps (Figure 5.8b), namely the disappearance of the SE and appearance of the triplet ESA, demonstrate the occurrence of SF in this time range. The small oscillations above 550 nm in these and the following spectra are measurement artifacts, resulting from interference effects between the two glass slides that sealed the films. From the timetraces of the before assigned features, shown in Figure 5.8c, an impression of the time constants can be obtained. The singlet ESA and SE decay relatively fast while the GSB and the triplet ESA are still visible after 8 ns, the maximal delay time, due to the long lifetimes of the triplets. The fast rise of the timetrace at 750 nm results

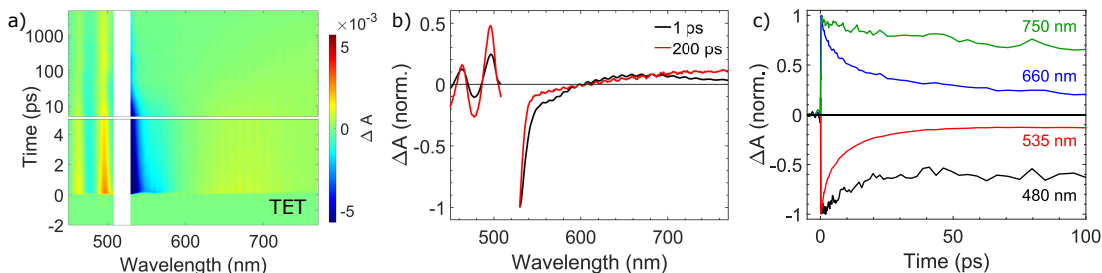


Figure 5.8: TA data of the neat TET film with $\lambda_{\text{exc}} = 520 \text{ nm}$ and an excitation density of $1.2 \times 10^{19} \text{ cm}^{-3}$. a) TA map in which the wavelength region of scattered pump laser light is left blank. b) TA spectra, averaged between 0.5 ps and 1.5 ps (black), and between 180 ps and 220 ps (red). c) Timetraces for selected wavelengths, representing characteristic features. They are all averaged over 10 nm around the wavelength position given in the legend (e.g. from 745 nm to 755 nm). Modified from Ref. [129].

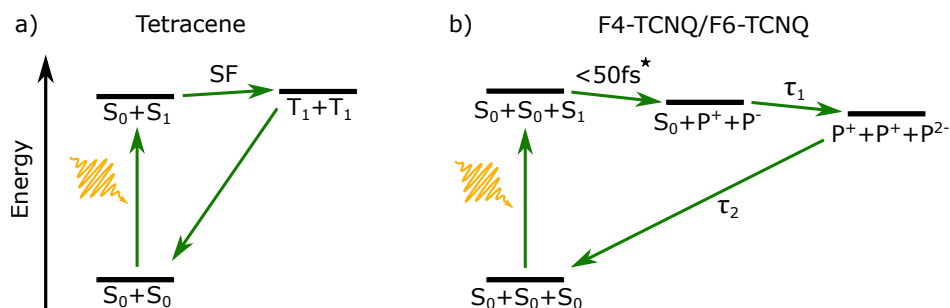


Figure 5.9: Kinetic model for a) TET and b) the acceptors F4-TCNQ and F6-TCNNQ. P^+ , P^- and P^{2-} denote cation, anion and dianion states, respectively. Time constants are given in the main text. *This upper bound for the time constant was taken from Ref. [196]. Modified from Ref. [129].

from the overlapping singlet ESA signal, which could be deconvoluted by a GA. However, a strong dependence of the extracted lifetime of the S_1 state on the excitation density has been reported, mainly due to singlet-singlet annihilation [184, 187]. In this process, two singlet excitons (S_1) can annihilate to form one higher-energy singlet exciton (S_n), which generally rapidly relaxes back to S_1 via internal conversion and vibrational relaxation. As a result, the number of singlet excitons is reduced. Consequently, the singlet exciton lifetime is determined by both, the SF rate and the singlet-singlet annihilation rate. A fluence dependence of the determined lifetimes by GA was also found in this work, indicating that the smallest excitation densities are still too large to prevent singlet-singlet annihilation, see Appendix A.2 for details about the excitation densities and the GA. Without singlet-singlet annihilation, SF time constants between 75 ps and 110 ps have been reported [116, 187, 188]. A scheme of the SF process in TET is shown in Figure 5.9a.

In contrast, the photophysics of F4-TCNQ and F6-TCNNQ has been barely investigated, since these acceptors are mainly used as dopants in host films [131]. There is, however, one report of the formation of F4-TCNQ $^-$ anions and, consecutively, F4-TCNQ $^{2-}$ dianions in F4-TCNQ single crystals after photoexcitation [196], which provides the basis for the interpretation of the here presented thin film data. A scheme of the proposed decay mechanism is given in Figure 5.9b. The data obtained from a TA measurement with $\lambda_{\text{exc}} = 400$ nm of the F4-TCNQ thin film is shown in Figure 5.10. Similar pump fluences as for the measurement of the TET film were used for the neat acceptor films (see Appendix A.2), but no fluence dependence was observed. Therefore, the pump fluence is not explicitly given in each figure but the used range is given in Appendix A.2. The TA map (Figure 5.10a) is dominated by a long-lived, strong bleach below 500 nm and a weaker negative signal that extends over the entire measured wavelength range. Only within the first 10 ps, a significant spectral evolution is observable, see Figure 5.10b. Based on the steady-state absorbance and on Ref. [196], the strong bleach just below 500 nm is assigned to the GSB. The negative signal at longer wavelengths might be the result of SE, bleached trap states or reduced scattering and is superimposed to the reported PIA of the F4-TCNQ $^{2-}$ dianions [196] appearing on longer time scales, see Appendix A.3 for details. Interestingly, the GSB becomes stronger within the first

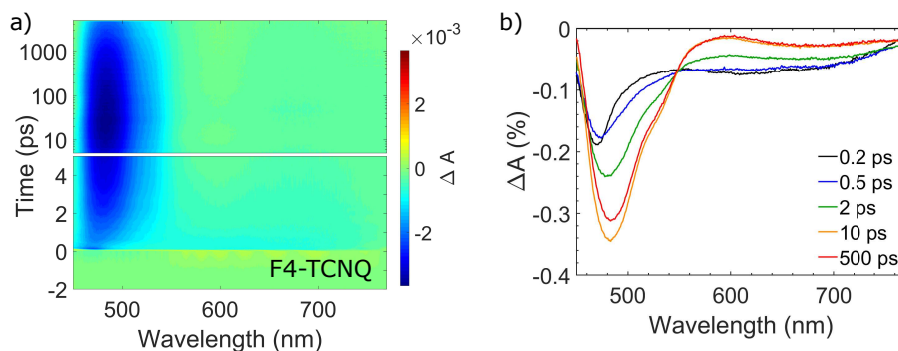


Figure 5.10: TA data of an F4-TCNQ thin film with $\lambda_{\text{exc}} = 400$ nm. a) TA map, b) selected TA spectra, averaged around the delay times given in the legend. The time ranges were chosen from 0.1 ps to 0.3 ps, 0.4 ps to 0.6 ps, 1.6 ps to 2.4 ps, 8 ps to 12 ps and 400 ps to 600 ps. For the TA spectra in the following figures, similar time ranges ($\sim \pm 20\%$, except for very short delay times) were chosen. Since the exact time ranges over which the spectra are averaged are not crucial for the obtained TA spectra, the time ranges are omitted in the following figure captions for better readability. Modified from Ref. [129].

10 ps, indicating that further molecules are no longer in the ground state. This is consistent with the model shown in Figure 5.9b, which was proposed in Ref. [196]. Therein, the time constant for the anion formation could not be determined because it was below the temporal resolution of 50 fs. The temporal resolution of the TA setup used for this thesis was ~ 100 fs, so this step cannot be resolved here either. This explains why a sequential model with two species was sufficient to fit the obtained data by a GA. As time constants, $\tau_1 = (3.0 \pm 0.2)$ ps and $\tau_2 > 7$ ns were obtained, independent of the excitation fluence. The uncertainty of τ_1 was extracted from several measurements with different pump fluences. The corresponding EAS are shown in Figure A.5a in the Appendix. Based on the scheme in Figure 5.9b, τ_1 is the time constant corresponding to the formation of the F4-TCNQ²⁻ dianions from F4-TCNQ⁻ anions, which is in good agreement to the 4 ps time constant reported for this process in single crystalline F4-TCNQ [196]. The weak PIA of F4-TCNQ⁻ anions above 650 nm that has been reported in Ref. [196] is too weak to be resolved here, due to the superimposed negative signal (cf. Appendix A.3). The second time constant, τ_2 , is related to the decay of these dianions, which are rather long lived. Since the longest possible delay time was 8 ns, only a lower bound for τ_2 can be given.

The TA data of a neat F6-TCNNQ thin film, measured with $\lambda_{\text{exc}} = 520$ nm, is shown in Figure 5.11. The TA signal looks different from that obtained from the F4-TCNQ thin film, especially due to the positive feature around 720 nm. However, overall similar trends are observable, namely a pronounced bleach that becomes stronger at intermediate delay times, a very broad negative feature, a significant spectral evolution during the first 10 ps, and only a slow decay of the signal thereafter. Owing to these similarities, also for F6-TCNNQ a photoinduced dianion formation is proposed (Figure 5.9b). The negative feature below 600 nm is assigned to the GSB, based on the steady-state absorbance spectrum. The positive feature around 720 nm, at short delay times, might be identified as a PIA of F6-TCNNQ⁻ anions, which have been reported to absorb in the NIR [132, 191]. The TA data of the

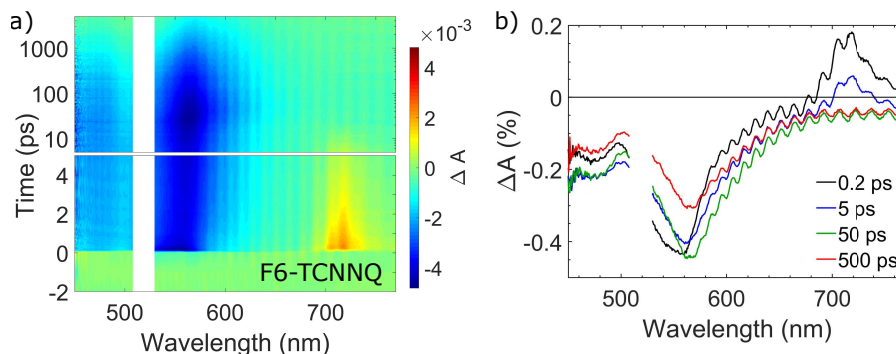


Figure 5.11: TA data of an F6-TCNNQ thin film with $\lambda_{\text{exc}} = 520$ nm. a) TA map, b) selected TA spectra, averaged around the delay times given in the legend (cf. Figure 5.10). Modified from Ref. [129].

F6-TCNNQ thin film was also fitted globally. However, a sequential model with two species, as for F4-TCNNQ, was not sufficient to describe the TA data of the F6-TCNNQ thin film. Instead, since only two clearly distinct spectra are found in the data set, a target analysis with two species but three decay times was performed. The underlying model assumed a species 1 that evolves exponentially into a species 2, which then decays with two different time constants to the ground state. A possible explanation for the necessity to involve two time constants for the decay of species 2 might be that this species actually decays non-exponentially, due to molecules in different environments. This scenario could be described by a Gaussian distribution of exponential decays with different time constants [257]. For the exponential evolution of species 1 to species 2, the time constant $\tau_1 = (6.3 \pm 0.6)$ ps was found. The assignment of the species was chosen in analogy to F4-TCNNQ, as discussed above, hence τ_1 describes the time constant for the formation of F6-TCNNQ²⁻ dianions from F6-TCNNQ⁻ anions (Figure 5.9b). The uncertainty in τ_1 was extracted from measurements with different excitation fluences. The species associated spectra are shown in Figure A.5b in the Appendix.

After having established the photophysics of the neat films, the TA data of the blends will be discussed in the following. The focus is placed on the photophysics of the CTCs. Here, the absorption of the CTCs in the visible spectral region, which was found in the steady-state absorbance measurements and verified by the theoretical calculations, was utilized to follow the dynamics. First, the TA measurements on the equimolar blends are analyzed. The TA maps, spectra, and timetraces of both, the TET:F4-TCNNQ and the TET:F6-TCNNQ equimolar blends, are presented in Figure 5.12. The two TA maps reveal a strong similarity between these systems. Indeed, they both exhibit negative features at short wavelengths and positive ones at long wavelengths, which rapidly decay simultaneously. In both cases, the negative features can be assigned to the GSB of the CTCs, as they appear at the wavelength positions of the absorption shoulders in the steady-state absorbance spectra (at 590 nm (2.1 eV) and 480 nm (2.6 eV) for F6-TCNNQ and at 560 nm (2.2 eV) for F4-TCNNQ). Based on the simultaneous decay of the positive features and the GSBs in both blends, apparent from the

5. Charge transfer complexes of tetracene with strong acceptors

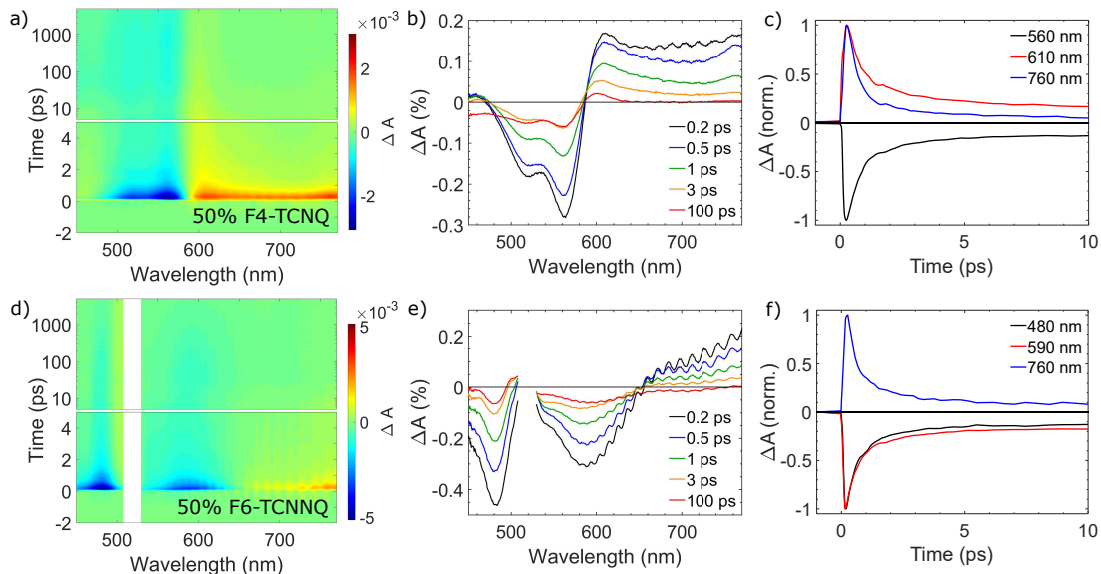


Figure 5.12: TA data of the equimolar TET:F4-TCNQ (a-c) and TET:F6-TCNNQ (d-f) blends with $\lambda_{\text{exc}} = 400$ nm and $\lambda_{\text{exc}} = 520$ nm, respectively. The spectra in b) and e) are averaged around the delay times given in the legend (cf. Figure 5.10). The timetraces (c and f) are averaged over 20 nm around the wavelength position given in the legend. Modified from Ref. [129].

spectra and timetraces in Figure 5.12, the positive features are assigned to an ESA of the CTCs. Furthermore, the timetraces reveal a dominant decay already during the first few picoseconds, which is analyzed in detail by GA.

A sequential model with three species was used to fit the data. As for the neat acceptor films, neither a fluence dependence nor a dependence on λ_{exc} was observed (for the TET:F4-TCNQ blend, $\lambda_{\text{exc}} = 400$ nm or $\lambda_{\text{exc}} = 520$ nm, see Figure A.6 in the Appendix). The extracted time constants for both equimolar blends are summarized in the table in Figure 5.13. For both equimolar blends, a dominant, sub-picosecond decay is obtained, which is assigned to the relaxation of excited CTCs to the ground state. This relaxation is faster for the TET:F6-TCNNQ blend which showed the lower-energy absorbance peaks in the steady-state spectra (Figure 5.4). This is consistent with the energy gap law [258] and a report of fast geminate recombination in CTCs of a polymer and small acceptors [259].

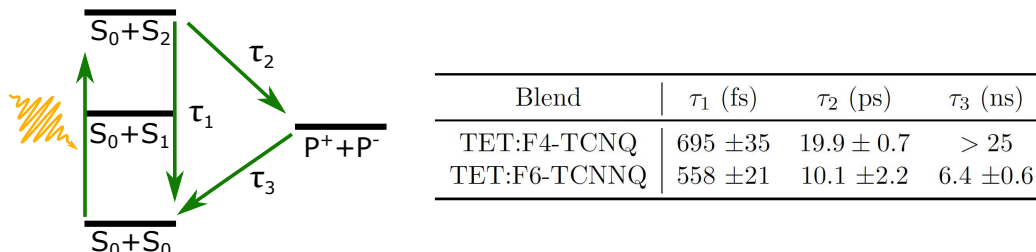


Figure 5.13: Kinetic model for the equimolar CTCs. S_n denote singlet states of the entire CTC and P^+ and P^- charged CTCs. The corresponding time constants are summarized in the table. Modified from Ref. [129].

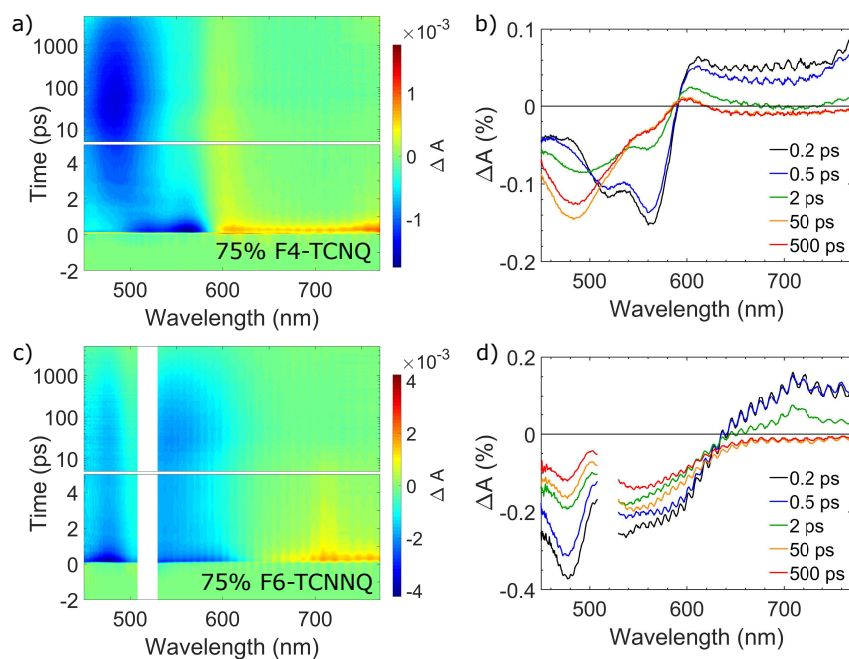


Figure 5.14: TA data of a,b) the TET:F4-TCNQ blend with 75 % F4-TCNQ ($\lambda_{\text{exc}} = 400$ nm) and c,d) the TET:F6-TCNNQ blend with 75 % F6-TCNNQ ($\lambda_{\text{exc}} = 520$ nm). The spectra in b) and d) are averaged around the delay times given in the legend (cf. Figure 5.10). Modified from Ref. [129].

The longer time constants τ_2 and τ_3 , in the ps and ns range, respectively, are also smaller for the F6-TCNNQ containing equimolar blend. They are assigned to the formation and decay of a small fraction of charged CTCs in accordance with Ref. [259]. These can be formed by the transfer of an electron from an excited CTC to a neighboring CTC or molecule and exhibit a long lifetime due to the charge separation. A scheme of the relevant energy levels and processes with their time constants is shown in Figure 5.13. The EAS from the GA are shown in Figure A.7 in the Appendix.

Finally, the discussion of the dynamics of the non-equimolar blends concludes this section. The TA data of the TET:F4-TCNQ and TET:F6-TCNNQ blends with 75 % of the acceptor are shown in Figure 5.14. The TA signal of these blends can be described as a superposition of the TA signal of the equimolar blends and the respective neat acceptor film. This is demonstrated in Figure A.8 in the Appendix, where the scaled TA signal of the equimolar blends is subtracted from the signal of the 75 % acceptor blend. In both cases, the resulting calculated TA maps look nearly identical to the signal of the neat acceptor films and the time constants are almost perfectly reproduced. This is a strong indication for the absence of charge or energy transfer processes between the CTCs and the surrounding acceptor molecules and, instead, indicates independent decays. For the TET:F4-TCNQ blend with 75 % F4-TCNQ this conclusion is additionally supported by the TA measurement of this film with $\lambda_{\text{exc}} = 520$ nm (Figure A.9 in the Appendix). This measurement yields a similar TA signal as obtained for the equimolar blend, thus confirming the expectation, since neat F4-TCNQ cannot be excited at this wavelength.

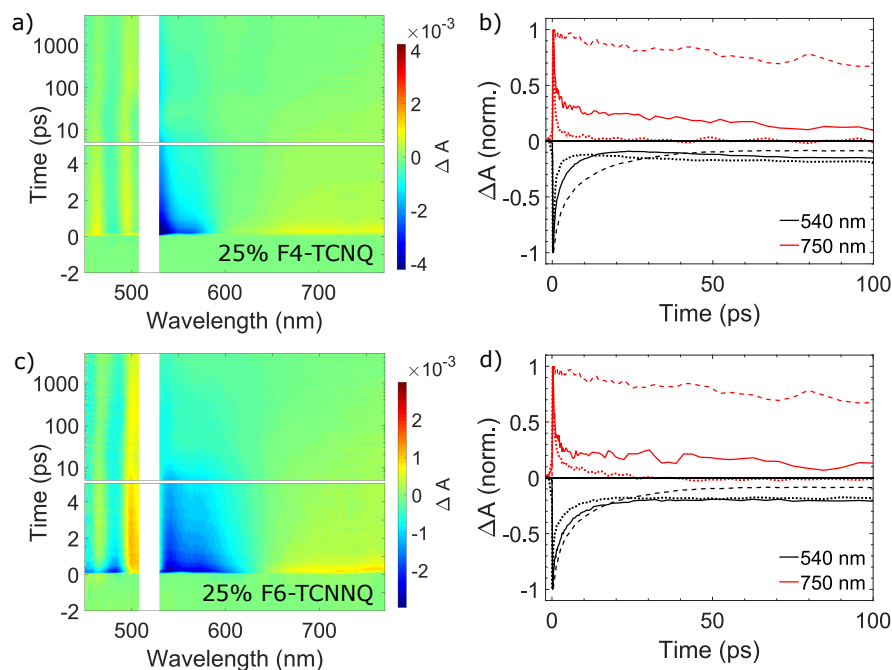


Figure 5.15: TA data of a,b) the TET:F4-TCNQ blend with 25 % F4-TCNQ and c,d) the TET:F6-TCNNQ blend with 25 % F6-TCNNQ, both excited with $\lambda_{\text{exc}} = 520$ nm. The time-traces in b) and d) are averaged over 10 nm and 40 nm around 540 nm and 750 nm, respectively. The solid line corresponds to the blend with 25 % of the acceptor, the dashed line to the neat TET film and the dotted line to the equimolar blend for comparison. Modified from Ref. [129].

As expected from the structural, steady-state optical, and theoretical investigations, the blends with an excess of TET exhibit the most complex photophysics. The obtained TA data are shown in Figure 5.15. In the TA maps, signatures from both, the CTCs and neat TET, are observable. The CTCs reveal themselves by the broad positive and negative features at very short delay times. The TET contributions are found especially at wavelengths below 500 nm. A complete description of the TA signal by a superposition of the TA signal of the neat TET film and the equimolar blends is, however, not possible. For the F4-TCNQ containing blend, this was expectable due to the presence of the multi-donor CTCs in this blend, which are absent in the equimolar blend. For the blend with F6-TCNNQ, it suggests that there is some kind of interference between the decay paths of the CTCs and the neat TET molecules.

The structural analysis revealed that in the 25 % F6-TCNNQ blend neat TET domains exist and, to a smaller degree, also in the 25 % F4-TCNQ blend. Thus, different species in different environments are photoexcited in the TA measurements, namely CTCs and TET molecules. Consequently, an unambiguous GA of the TA data of these films is not possible due to the wealth of involved states and decay processes. Nevertheless, from timetraces at selected wavelength positions, namely at 540 nm and 750 nm, some viable information can be extracted. These timetraces are plotted in Figure 5.15b,d together with the timetraces extracted from the neat TET film and the equimolar blends. The timetrace at 750 nm was

chosen because in this wavelength region the ESA of TET triplets is located (cf. Figure 5.8). For both equimolar blends, a rapidly decaying ESA of the CTCs is detected at this wavelength, which is also reflected in the blends with an excess of TET. This signal, however, vanishes after 20 ps in the equimolar blends, allowing to assign the remaining signal in the blends with an excess of TET to TET triplet ESA. Thus, indications for SF are found in these blends, most likely occurring in the phase-separated TET domains discovered by the structural investigations. The faster decay of the TET triplet ESA in the 25% acceptor blends (completely disappeared after ~ 0.5 ns and ~ 1.5 ns for the blend with F6-TCNNQ and F4-TCNQ, respectively) compared to the neat TET film (remaining over the entire measurement range of 7.8 ns) indicates that the TET triplets decay faster in these blends, probably due to charge or energy transfer from TET molecules in the T_1 state to the CTCs. This scenario seems likely because the S_1 state of the CTCs is even lower in energy than the T_1 state of TET.

The timetraces at 540 nm were chosen because they mainly reflect the SE from TET, which is directly linked to the TET S_1 population. To estimate the singlet lifetime, these timetraces of the measurements with the lowest excitation densities were fitted. It is noted, as already mentioned above, that even at these low fluences of $\sim 25 \mu\text{J}/\text{cm}^2$ the signal is influenced by singlet-singlet annihilation. Nevertheless, for the neat TET film and the 25% F6-TCNNQ containing blend the decay between 0.26 ps and 200 ps could be approximated by a single exponential fit with a time constant of 22 ps and 10 ps, respectively. For the 25% F4-TCNQ containing blend, a single exponential fit was not sufficient to adequately describe the timetrace at 540 nm due to the overlapping signals from the CTCs and TET. Hence, first the time constant of 0.7 ps for the GSB decay of the CTCs was extracted by a single exponential fit of the timetrace of the equimolar TET:F4-TCNQ blend, in perfect agreement to τ_1 obtained by GA (table in Figure 5.13). Then, the timetrace of the 25% F4-TCNQ containing blend was fitted by a double-exponential decay with the first time constant set to 0.7 ps. By this, a second time constant of 7 ps was obtained (related to the SE decay of TET), which is similar to that obtained for the blend with F6-TCNNQ but significantly shorter than that obtained for neat TET. This reduction in TET singlet lifetime is, again, most likely related to charge or energy transfer to the CTCs, now directly from TET molecules in the S_1 state, as demonstrated in Ref. [260].

The insights into the photophysics of the neat films and especially the blends, gained by the TA measurements, are schematically summarized in Figure 5.16. The photophysics of neat TET is well known [187, 188] and was confirmed by the above presented data. The processes in the neat acceptor films, namely the formation of dianions after photoexcitation, were established by the investigations presented in this work [129] and are based on the report of the photophysics in an F4-TCNQ crystal [196]. Finally, the photophysics of the small band gap CTCs was revealed by the investigation of their higher-energy transitions and their interaction with additional TET or acceptor molecules by the analysis of the TA signal of the non-equimolar blends.

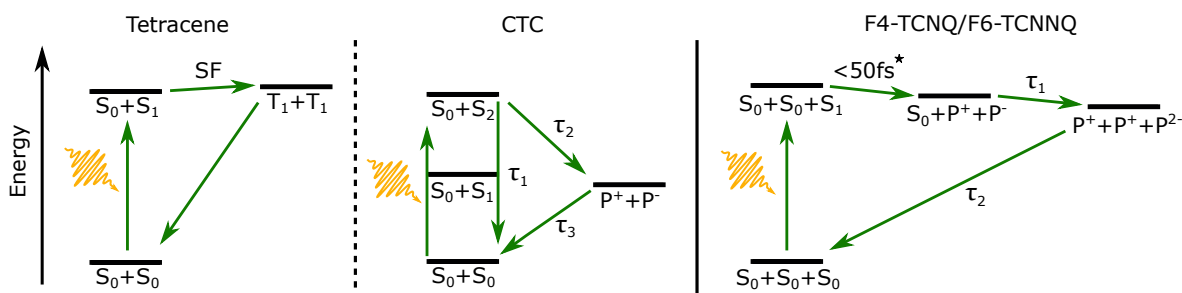


Figure 5.16: Kinetic model for the neat films and the blends. The dashed line between TET and the CTCs symbolizes the charge or energy transfer processes from TET to the CTCs, while the solid line between the CTCs and the acceptors illustrates the absence of such processes between them. *This upper bound for the time constant was taken from Ref. [196]. Modified from Ref. [129].

5.7 Conclusion

In this chapter, the structural, electronic, optical, and photophysical properties of CTCs formed by TET and the two prototypical acceptors F4-TCNQ and F6-TCNNQ were characterized by experimental and theoretical studies. The formation of CTCs indicates a relatively strong electronic coupling between the donor and acceptor molecules in all blends. A small band gap well below 1 eV was found for CTCs formed by both molecular combinations. For blends of TET with F4-TCNQ, a mixing ratio dependence of the band gap and δ_{CT} was detected, which was explained by the formation of multi-donor CTCs based on the theoretical calculations. The absence of indications for multi-donor CTCs in the blends with F6-TCNNQ could be explained by a more pronounced phase separation of neat TET domains found in the structural analysis. With the optical transitions of the CTCs in the visible range, identified by the theoretical calculations, the photophysics of the CTCs was investigated by TA measurements probing the visible spectral region. An ultrafast, sub-picosecond exciton decay was discovered, which is faster for the CTCs containing F6-TCNNQ. In the equimolar blends and the blends with an excess of acceptor molecules, no SF was found, as the TET molecules are incorporated into the CTCs. However, for the blends with an excess of TET, indications for SF were detected, most likely occurring in the TET domains. Finally, the SF process seems to compete with charge or energy transfer from TET molecules in the S_1 state to CTCs. The reduced lifetime of the TET triplets indicates a charge or energy transfer from TET molecules in the T_1 state to CTCs, too, permitted by the small band gap of the CTCs.

6. Ion pairs and charge transfer complexes of pentacene with strong acceptors

In order to get an even deeper insight into the different ground state CT mechanisms and to examine the influence of the donor material, blends of PEN with the same two acceptors as in the TET blends, namely F4-TCNQ and F6-TCNNQ, are analyzed in this chapter. For these PEN blends, the coexistence of ion pairs and CTCs, thus of integer and partial CT, is found, illustrating the effect of the slightly different IP of PEN. The impact of the ground state CT on the SF process in PEN is further analyzed in this chapter. The results presented in this chapter have been published in Ref. [261] and the study was conducted in collaboration with the group of Prof. Dr. Petra Tegeder, see Appendix F for details about the contributions.

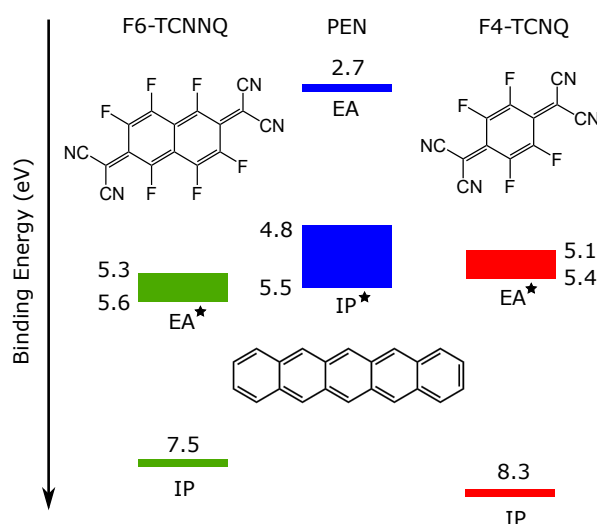


Figure 6.1: Molecular structures, EAs, and IPs, all in eV, of PEN, F4-TCNQ and F6-TCNNQ, taken from Refs. [173, 191–194, 197]. * For the EAs of the acceptors and the IP of PEN, hence the decisive values for the CT, an energy range is given based on different reported values. The EA values for F4-TCNQ and F6-TCNNQ were measured by cyclic voltammetry and inverse photoemission spectroscopy [191–194, 197]. The IP values of PEN are summarized in Ref. [173], measured by ultraviolet photoelectron spectroscopy for different molecular orientations. For upright-standing molecules on weakly interacting substrates as the ones chosen here, $IP_{PEN} \sim 4.9$ eV is given therein. Modified from Ref. [261].

6.1 Introduction

The formation of CTCs and thus partial CT, which was discussed in the last chapter for blends of TET with F4-TCNQ and F6-TCNNQ, is only one possibility of ground state CT. As introduced in Section 2.2.6, CTCs can be formed if the IP of the donor and the EA of the acceptor are energetically close to each other and if an orbital overlap between the donor and the acceptor can be realized [36]. The second possibility of ground state CT is integer CT (cf. Section 2.2.6), resulting in the formation of an ion pair, which can occur if the EA of the acceptor is larger than the IP of the donor [26]. To study these different CT mechanisms, PEN was investigated in this chapter as donor in blends with F4-TCNQ and F6-TCNNQ, since PEN has a slightly smaller IP than TET (cf. Figures 6.1 and 5.1). Additionally, PEN features a different SF mechanism than TET (cf. Section 3.2.1), which might also influence the photophysics of the blends. Furthermore, for blends of PEN with F4-TCNQ, different experimental reports of either ion pair or CTC formation have been published [35, 41]. Recently, this model system has also been revisited from the theoretical perspective, leading to the conclusion that it is located at the boundary between CTC and ion pair formation [40]. The UV-vis-NIR and FTIR spectra presented in this thesis bring these results together and demonstrate the possibility of ion pair *and* CTC formation within a single blend. In contrast, for blends of PEN with F6-TCNNQ, only ion pair formation was found. Consecutively, the photophysics of the different blends with a focus on the PEN SF was investigated using TA spectroscopy.

6.2 X-ray diffraction

First, the structure of the prepared samples was investigated using XRR and GIWAXS. The XRR scans of the PEN:F4-TCNQ and PEN:F6-TCNNQ blends are shown in Figure 6.2. The PEN thin film shows a pronounced Bragg peak of the thin film phase at $q_z = 0.407 \text{ \AA}^{-1}$

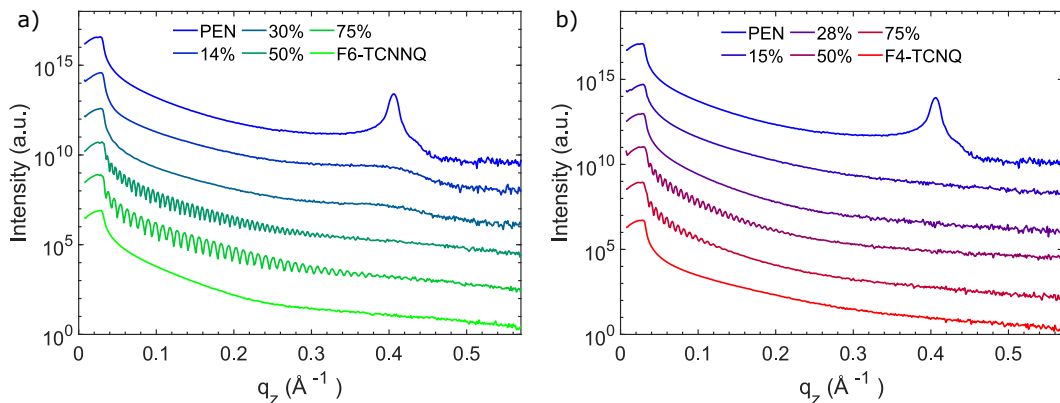


Figure 6.2: XRR data of the a) PEN:F6-TCNNQ blends and b) PEN:F4-TCNQ blends. In the legend, the molar acceptor fraction is given and the curves are vertically offset for clarity. Modified from Ref. [261].

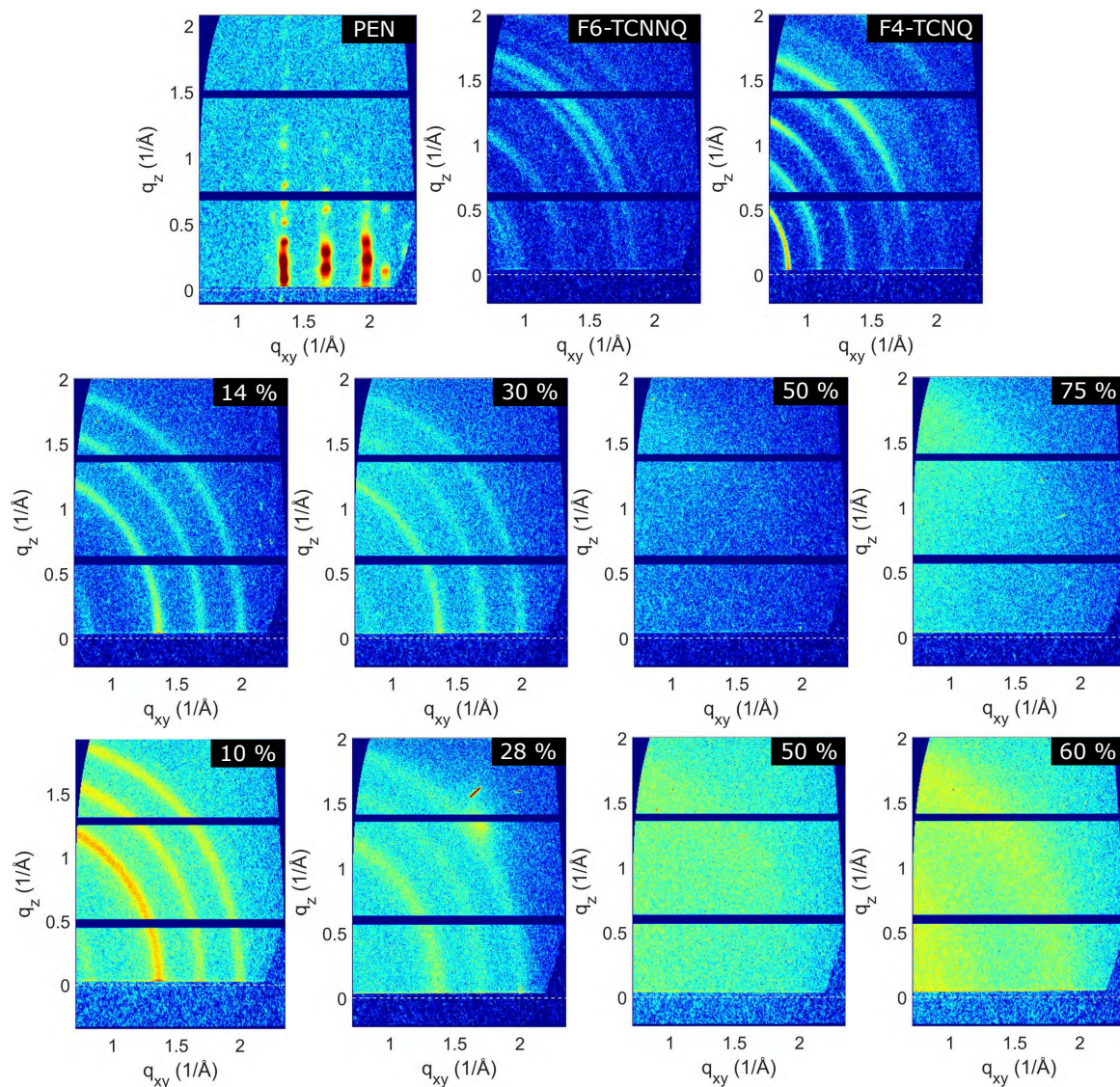


Figure 6.3: Reciprocal space maps of the neat films (upper row), the PEN:F6-TCNNQ blends (middle row) and the PEN:F4-TCNNQ blends (lower row). The molar acceptor fraction is given in the upper right corner of the reciprocal space maps of the blends. The intensity is displayed on a logarithmic scale. Modified from Ref. [261].

[94] and a weakly expressed Bragg peak of a bulk phase at slightly higher q_z [175]. The neat acceptor films exhibit no Bragg peaks and hence no long-range out-of-plane order, as already discussed in Chapter 5. Similarly, none of the XRR scans of the blends show a clear Bragg peak, indicating the absence of a long-range out-of-plane order also in these films, consistent with reports of doped PEN films in the literature [35, 262]. Only for the F6-TCNNQ containing blends with an excess of PEN, a weak signal in the region of the PEN Bragg peaks is observed, which could indicate some PEN domains with differing tilt angles with respect to the substrate. It is also worth noting that for the equimolar blends and the blends with an excess of acceptor nicely resolved Kiessig fringes appear, revealing the evenness of these films, consistent with reports of other mixed small molecule systems [263].

The reciprocal space maps shown in Figure 6.3 give further insights into the structure of the samples. The one obtained from the PEN thin film shows the expected Bragg peaks of the thin film structure of PEN [94], confirming the dominance of this phase. The two reciprocal space maps of the acceptors show partial diffraction rings, indicating the existence of long-range order but with various orientations of the crystallites with respect to the substrate. The partial rings appear at absolute q values that are assignable to the F6-TCNNQ crystal structure reported in Ref. [200] as form II and to the F4-TCNQ crystal structure reported in Ref. [198], respectively. For the equimolar blends and the blends with an excess of acceptor, only a broad scattering background is obtained, indicating amorphous blends. For all blends with an excess of PEN, however, the existence of PEN domains is demonstrated by the reciprocal space maps. They all exhibit diffraction rings from powder-like PEN, indicating that the PEN domains lack a preferred orientation with respect to the substrate. This explains the absence of clear Bragg peaks in the XRR scans. Overall, a similar mixing behavior as for the TET:acceptor blends is obtained (compare Chapter 5). The equimolar blends and blends with an excess of acceptor consist of an amorphous mixed phase, while for the blends with an excess of PEN randomly oriented, phase-separated, crystalline PEN domains exist.

6.3 Optical spectroscopy

As a next step, the UV-vis-NIR spectroscopy data is analyzed to find indications of ground state CT. Thus, the focus is placed on the NIR spectral region. For the blends with F6-TCNNQ, the spectra presented in Figure 6.4a exhibit narrow peaks below the band gap of the neat compounds. By a comparison to reported ion spectra of the two compounds [191, 264, 265] (see vertical lines in Figure 6.4a), these peaks at 1.06 eV, 1.26 eV, and 1.45 eV can be assigned to F6-TCNNQ⁻ anions and PEN⁺ cations in the blends. Hence, integer

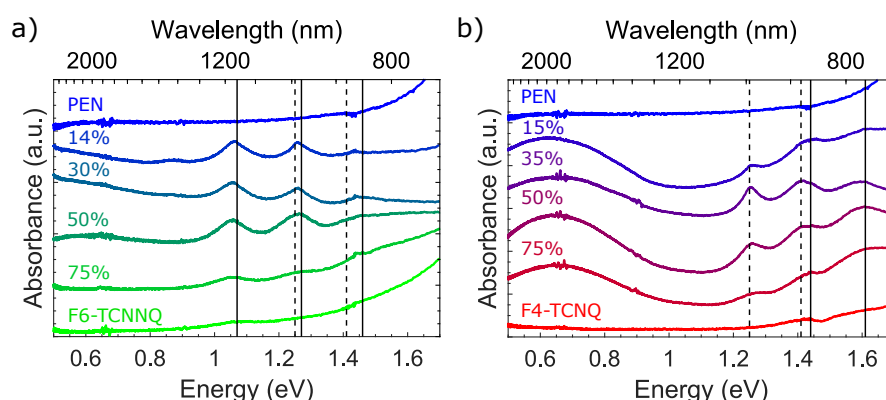


Figure 6.4: NIR spectra of the a) PEN:F6-TCNNQ and b) PEN:F4-TCNQ blends on sapphire substrates. In the legend, the acceptor fraction is given. The spectra are vertically offset for clarity. The dashed lines in a) and b) indicate the PEN⁺ cation peak positions reported in Ref. [264], the solid lines in a) the F6-TCNNQ⁻ anion peak positions reported in Ref. [191], and the solid lines in b) the F4-TCNQ⁻ anion peak positions reported in Ref. [28]. Modified from Ref. [261].

CT and the formation of ion pairs can be concluded for the PEN:F6-TCNNQ blends. For the blends with an excess of PEN, additionally a weak, broad peak below 0.7 eV could be presumed which could indicate a small fraction of CTCs.

In contrast, the spectra of the PEN:F4-TCNQ blends in Figure 6.4b show a dominant, broad peak around 0.65 eV, which is indicative for a pronounced CTC formation in these blends [28], as discussed for the TET blends in Section 5.3. However, also narrow peaks at 1.26 eV, 1.42 eV, 1.44 eV, and 1.60 eV are displayed. The former two match the energy positions of the PEN^+ cation peaks [264], while the latter two match the energy positions of the F4-TCNQ^- anion peaks [28, 131]. Hence, a coexistence of CTCs and ion pairs is revealed in the blends of PEN with F4-TCNQ, which is a remarkable finding. For completeness, the UV-vis-NIR spectra over the entire measured energy range of both series are shown in Figure B.1 in the Appendix.

6.4 Vibrational spectroscopy

FTIR spectroscopy was employed to confirm the CT scenarios described above and to determine the degree of CT in the CTCs. Figure 6.5 shows FTIR spectra of the energy region of the cyano $\text{C}\equiv\text{N}$ stretching mode for both, the PEN:F6-TCNNQ and the PEN:F4-TCNQ blends. Neat PEN, similar to neat TET, does not exhibit any signal in this energy region, allowing to assign all features found in the blends to the respective acceptor. The weak, narrow peaks at 2090 cm^{-1} , 2065 cm^{-1} and 2040 cm^{-1} that are visible in most spectra are artifacts from the background correction. The two neat acceptors show pronounced peaks of the $\text{C}\equiv\text{N}$ stretching mode, as already seen in Section 5.4. For neat F6-TCNNQ, in Figure 6.5a, they are found at 2223 cm^{-1} , 2216 cm^{-1} , and 2207 cm^{-1} , in accordance with the literature [38, 130, 197], with the strongest one being the peak at 2216 cm^{-1} . Starting from neat F6-TCNNQ, the intensity of the peaks at the mentioned positions decreases with increasing PEN fraction. Simultaneously, a new peak arises around 2191 cm^{-1} , which is the only clear signal remaining for the blend with 14 % F6-TCNNQ. This peak can be assigned to the $\text{C}\equiv\text{N}$ stretching mode of F6-TCNNQ^- anions based on the literature [38, 197]. The broad peak around 2065 cm^{-1} that is found in the FTIR spectra of the blends is tentatively assigned to interactions between the charged molecules in the organic film and oxygen vacancies in the silicon oxide layer of the substrate, based on the peak width [266]. In summary, the FTIR spectra indicate the presence of F6-TCNNQ^- anions (and neutral F6-TCNNQ molecules) in the blends, confirming the conclusion of ion pair formation drawn from the NIR spectra.

The FTIR spectra of the PEN:F4-TCNQ blends exhibit a slightly more complex behavior for increasing PEN fractions. The neat F4-TCNQ film shows a sharp peak at 2228 cm^{-1} [28]. For the equimolar blend and the blend with 60 % F4-TCNQ, three peaks are observed, at 2230 cm^{-1} , 2203 cm^{-1} , and 2193 cm^{-1} . Based on the literature [28, 254], the weak peak at 2230 cm^{-1} can be assigned to neutral F4-TCNQ molecules and the peak at 2193 cm^{-1} to F4-TCNQ^- anions. The peak at 2203 cm^{-1} is in between the two other peaks and is therefore

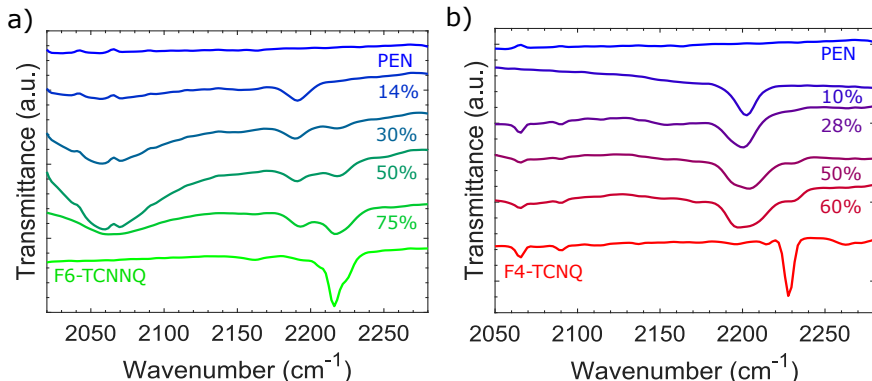


Figure 6.5: FTIR spectra of the a) PEN:F6-TCNNQ and b) PEN:F4-TCNQ blends in the energy region of the cyano stretching mode. The spectra are vertically offset for clarity and the acceptor fraction is given in the legend. Modified from Ref. [261].

assigned to a CTC formed by F4-TCNQ and PEN. The observed peak position results in $\delta_{CT} = (0.72 \pm 0.05) e$, again under the assumption of a linear dependence [28, 190, 267]. Hence, in these blends the coexistence of ion pairs and CTCs, as already derived from UV-vis-NIR spectroscopy, is confirmed by the FTIR spectra. Interestingly, for the blends with increasing PEN fraction, the peaks assigned to neutral and anionic F4-TCNQ molecules vanish while the one assigned to the CTC remains. This indicates the predominance of CTC formation in the blends with an excess of PEN, which is also consistent with the NIR spectrum of the 15% F4-TCNQ blend (Figure 6.4b). The implications of this finding, also in the context of previous experimental and theoretical studies, are discussed in Section 6.6.

6.5 Transient absorption spectroscopy

Based on the obtained details about the structure and the CT mechanisms in the mixed films of PEN and the two acceptors, the photophysics of these interesting systems at the boundary between CTC and ion pair formation was investigated by TA spectroscopy. The steady-state absorbance spectra of the investigated samples in the energy region probed by the TA measurements are displayed in Figure 6.6 for comparison. For the blends with an excess of PEN, the Davydov splitting and the vibronic progression of PEN are clearly resolved, as a result of the phase-separated PEN crystallites. In the spectra of the equimolar blends, these features are absent and the absorbance is overall relatively weak in the visible energy region. In the spectrum of the equimolar PEN:F6-TCNNQ (PEN:F4-TCNQ) blend, a weak peak around 2.5 eV (3.1 eV) is observed, thus in the energy region of the neat F6-TCNNQ (F4-TCNQ) film absorption (cf. Figure B.1).

The TA measurements of the neat acceptor films were already discussed in detail in Section 5.6. Therefore, only the TA data of the neat PEN thin film (Figure 6.7) and the blends are presented in the following. Additionally to the TA signal in the visible spectral region (Figure 6.7a,c), the TA signal in the NIR spectral region was measured (Figure 6.7b,d) because ESA features of PEN triplets have been reported in this region [170, 268]. The excitation

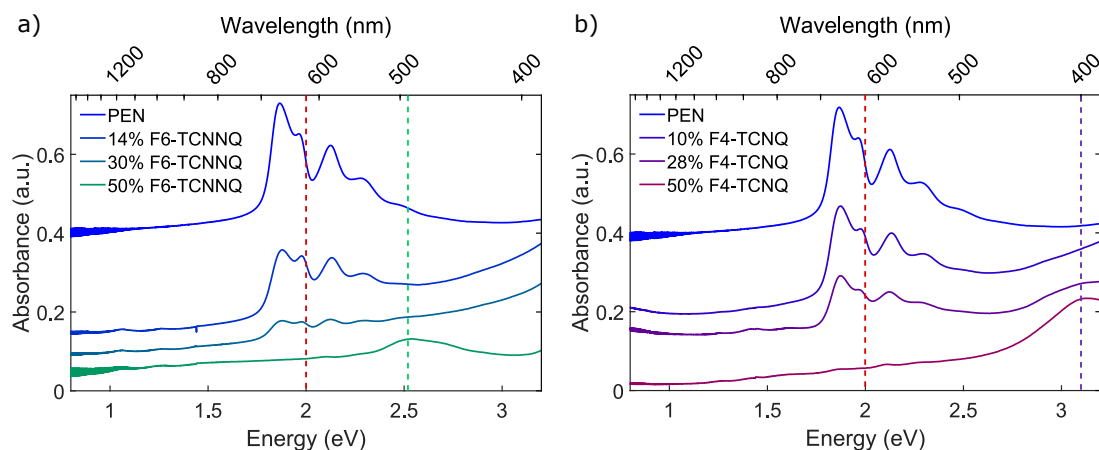


Figure 6.6: UV-vis-NIR absorbance spectra of the a) PEN:F6-TCNNQ and b) PEN:F4-TCNQ blends on cover slips, which were used for the TA measurements. The spectra are vertically offset for clarity. The dashed vertical lines indicate λ_{exc} for the blends with an excess of PEN (red) and the equimolar blends (green and purple). Modified from Ref. [261].

wavelength was $\lambda_{\text{exc}} = 620$ nm for both spectral regions, but for the NIR measurements higher pump fluences were required due to the weaker signal in this region. However, no fluence dependence was observed for any of the measurements presented in this chapter and the time constant uncertainties are extracted from measurements at different fluences.

Owing to its SF capability, the photophysics of PEN has already been thoroughly analyzed in the literature [15, 114, 170, 245]. At 675 nm, a strong GSB is visible at all delay times (Figure 6.7a), with vibronic replica at 630 nm, 585 nm, and 545 nm, thus at the steady-state absorption maxima of the PEN film (Figure 6.6). In the TA spectrum at a delay time of 50 fs in Figure 6.7c, SE is visible between 690 nm and 760 nm and singlet ESA below 620 nm, superimposed with the GSB [170]. Already at a delay time of 500 fs, these singlet features are absent, which demonstrates the ultrafast SF process. Simultaneously, in the NIR spectral region, a broad positive signal appears around 900 nm, which can be assigned to triplet ESA [170, 245, 268]. At even longer wavelengths, visible above 1100 nm, another signal is found in the spectra at a delay time of 50 fs and 500 fs, which is indicative for the coupled triplet pair state [114, 269].

The PEN TA data in the visible and NIR spectral region from measurements with several excitation fluences was fitted by GA to extract the involved time constants. A sequential model with three species was sufficient in both spectral regions to obtain a good fit to the data, as shown by the timetraces in Figure 6.8b,d. The time constants corresponding to the EAS in the visible and NIR spectral range shown in Figure 6.8a,c are, however, very different, which can be rationalized by the feature assignment above.

In the visible spectral region (Figure 6.8a), the time constant $\tau_1(\text{vis}) = 95 \left(\begin{smallmatrix} +20 \\ -7 \end{smallmatrix} \right)$ fs, extracted from a few measurements with differing fluences, corresponds to the transition from S_1 to $^1(\text{TT})$, apparent from the spectral changes described above and in very good agreement with the literature [118, 170]. The two EAS with larger decay time constants are spectrally similar and are assigned to $^1(\text{TT})$ and $^1(\text{T}\dots\text{T})/\text{T}_1$. These species ($^1(\text{TT})$ and $^1(\text{T}\dots\text{T})/\text{T}_1$)

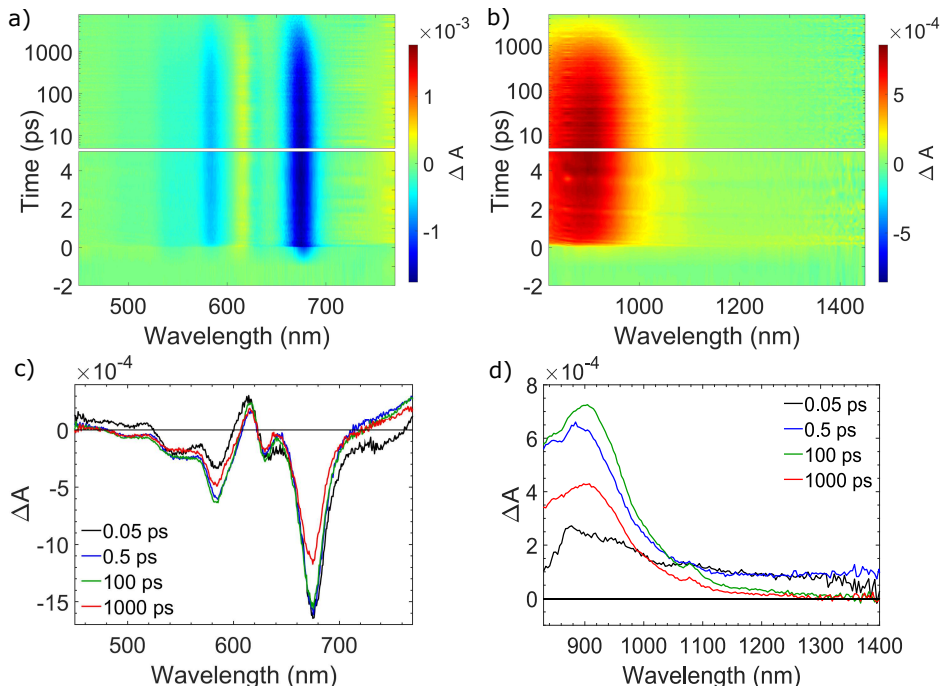


Figure 6.7: TA data of a neat PEN thin film, excited with $\lambda_{\text{exc}} = 620 \text{ nm}$. a,c) Probed in the visible spectral region and excited with a pump fluence of $100 \mu\text{J}/\text{cm}^2$. b,d) Probed in the NIR spectral region and excited with a pump fluence of $400 \mu\text{J}/\text{cm}^2$. The TA spectra in c) and d) are averaged around the delay times given in the legend. The time ranges were chosen from 0.03 ps to 0.07 ps, 0.3 ps to 0.7 ps, 70 ps to 130 ps and 700 ps to 1300 ps. For the TA spectra in the following figures, similar time ranges ($\sim \pm 30\%$, except for very short delay times) were chosen. Since the exact time ranges over which the spectra are averaged are not crucial for the obtained TA spectra, the time ranges are omitted in the following figure captions for better readability. Modified from Ref. [261].

cannot be discerned in the visible spectral region under normal incidence due to the absence of strong triplet features [270]. The necessity to involve two time constants for the decay of the PEN triplets can be rationalized by triplet-triplet annihilation [271]. This triplet-triplet annihilation leads to a non-exponential decay of the PEN triplets, which is approximated in the GA by two exponential decays.

In contrast, in the NIR spectral region, the PEN singlet features are too weak to resolve the ultrafast time constant. Thus, the first extracted time constant in Figure 6.8c corresponds to the transition from $^1(\text{TT})$ to $^1(\text{T}\dots\text{T})$, deducible from the slight shift of the ESA maximum around 900 nm toward longer wavelengths [114] and the loss of the ESA above 1100 nm [269]. The extracted time constant of $\tau_1(\text{NIR}) = 1.29 \left(\begin{smallmatrix} +0.13 \\ -0.12 \end{smallmatrix} \right) \text{ ps}$ is also consistent with earlier reports [269, 270]. The two EAS with longer time constants are nearly identical and the time constants are similar to the ones found from the measurements in the visible spectral region, underlining the assignment to non-exponential triplet decay.

Next, the TA measurements of the two equimolar blends are discussed. As mentioned above and seen in Figure 6.6, the absorption of these two blends in the visible spectral region is relatively weak, thus necessitating relatively high fluences between $125 \mu\text{J}/\text{cm}^2$ and

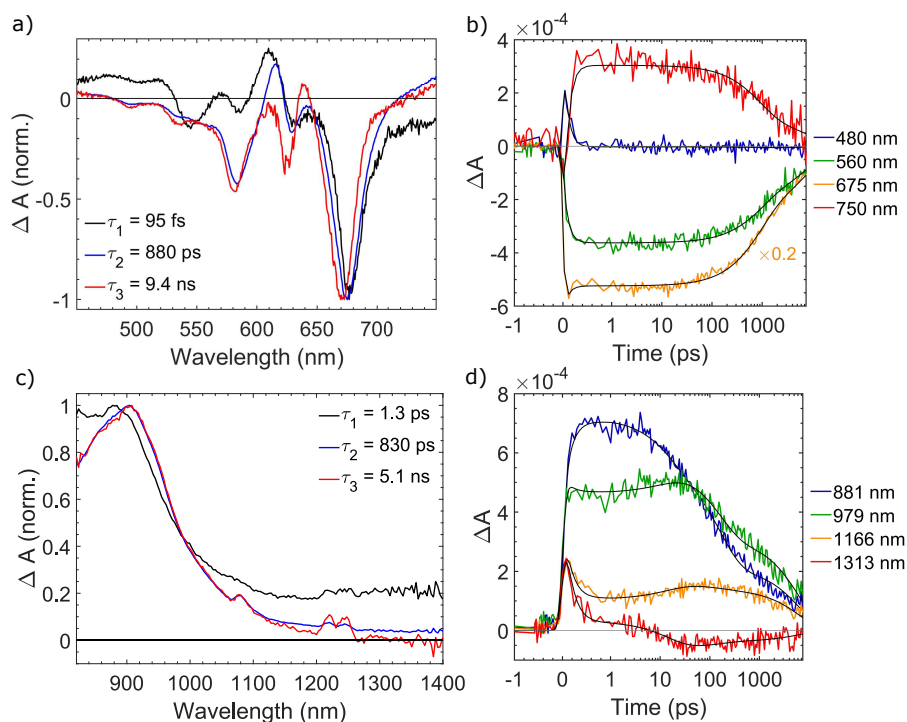


Figure 6.8: GA results of a TA measurement of PEN excited with $\lambda_{\text{exc}} = 620$ nm. a,b) Probed in the visible spectral region and excited with a pump fluence of $180 \mu\text{J}/\text{cm}^2$. c,d) Probed in the NIR spectral region and excited with a pump fluence of $400 \mu\text{J}/\text{cm}^2$. a,c) Normalized EAS, with the corresponding time constants given in the legend. b,d) Selected timetraces of PEN TA features and the corresponding fits by the GA, shown as black lines. The time-axis changes from linear to logarithmic scale at 1 ps. Modified from Ref. [261].

$1400 \mu\text{J}/\text{cm}^2$. Furthermore, the excitation wavelength was chosen at the steady-state absorption maximum (compare Figure 6.6), hence at $\lambda_{\text{exc}} = 495$ nm (2.51 eV) and $\lambda_{\text{exc}} = 400$ nm (3.10 eV) for the equimolar PEN:F6-TCNNQ and PEN:F4-TCNNQ blend, respectively. Despite the high pump fluences, no dependence of the dynamics on the pump fluence was observed for both blends.

TA maps and spectra in the visible and NIR of the equimolar PEN:F6-TCNNQ blend are shown in Figure 6.9. Both, the data in the NIR and the visible spectral region, show little spectral evolution but a slow decay of the initial features. In the visible spectral region, a GSB around the steady-state absorption maximum at 495 nm is obtained with a weaker positive signal at longer wavelengths, around 545 nm. In the NIR data, two pronounced peaks at 1170 nm and 1000 nm are observed together with a shoulder around 880 nm. These features are located at the energy positions of the F6-TCNNQ⁻ anion and PEN⁺ cation absorption peaks (cf. Figure 6.4) [191, 264], and are therefore assigned to PIA of these ions. This implies that due to the excitation, additional PEN⁺ cations and F6-TCNNQ⁻ anions are formed in the blend via excited state CT. Based on the similarity of the steady-state absorption spectra of this blends (Figure 6.6), of the neat F6-TCNNQ film (Figure B.1a) and of F6-TCNNQ in solution [191], it is concluded that in the equimolar blend mainly remaining uncharged F6-TCNNQ molecules are excited with $\lambda_{\text{exc}} = 495$ nm. These excited acceptor molecules can

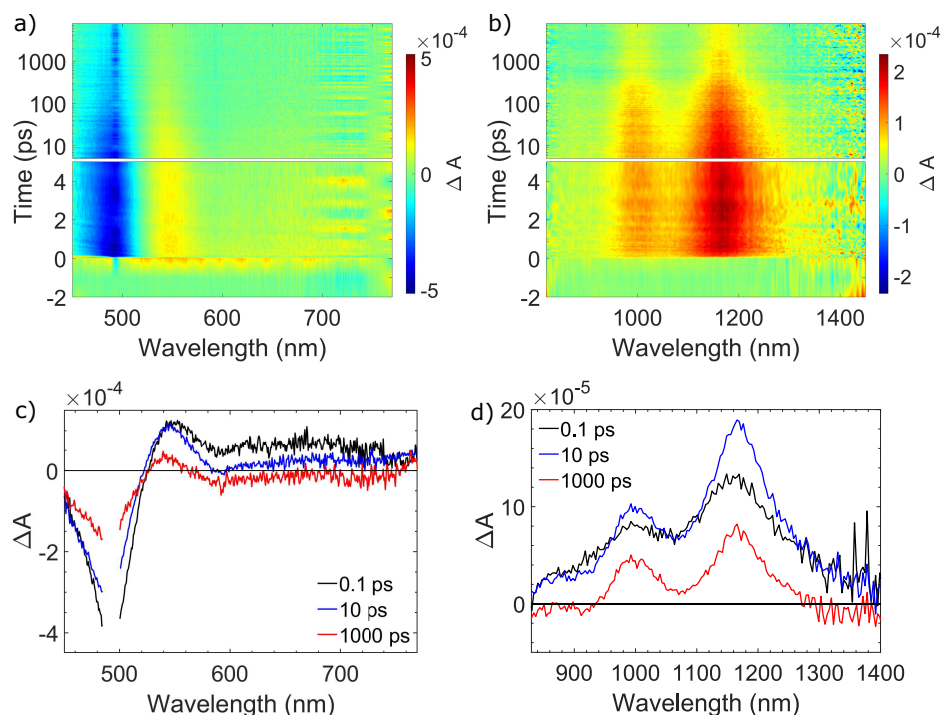


Figure 6.9: TA data of the equimolar PEN:F6-TCNNQ thin film, excited with $\lambda_{\text{exc}} = 495$ nm. a,c) Probed in the visible spectral region and excited with a pump fluence of $280 \mu\text{J}/\text{cm}^2$. b,d) Probed in the NIR spectral region and excited with a pump fluence of $125 \mu\text{J}/\text{cm}^2$. The TA spectra in c) and d) are averaged around the delay times given in the legend (cf. Figure 6.7). Around λ_{exc} , especially at long delay times, artifacts from scattering of the pump pulse are visible. Modified from Ref. [261].

then transfer a hole to a nearby PEN molecule, which results in a new ion pair. Within this scenario, the signal at 545 nm can be related to the Stark effect resulting from the charged species [244]. The overall decay of the TA signal in the visible and NIR spectral region is non-exponential, rendering a unique GA impossible. Hence, it is only possible to conclude on an ultrafast excited state CT, since the signals in the NIR develop within the first 0.5 ps, and a long lifetime (nanoseconds) of the formed ions.

The TA measurements on the equimolar PEN:F4-TCNQ blend lead to similar results, despite the different ground state CT mechanisms. For this blend, no GSB is found in the TA data in Figure 6.10, since the region of the steady-state absorption of the blend (around 400 nm, see Figure 6.6) was not covered by the TA measurements. Instead, PIA features with maxima below 450 nm and above 770 nm are seen in the data of the measurement in the visible spectral region (6.10a,c) and PIA features at 880 nm and 990 nm are found in the NIR data (6.10b,d). These wavelength positions correspond to the ones found for the absorption of PEN^+ cations and F4-TCNQ^- anions (see Figure 6.4 and Refs. [28, 264]), supporting the conclusion of excited state CT also in this blend. Similar to the equimolar blend with F6-TCNNQ, the steady-state absorption spectrum of the equimolar PEN:F4-TCNQ blend (Figure 6.6) resembles the neat F4-TCNQ film (Figure B.1) and solution absorption spectra [191]. Therefore, again a dominant excitation of uncharged acceptor molecules that are not

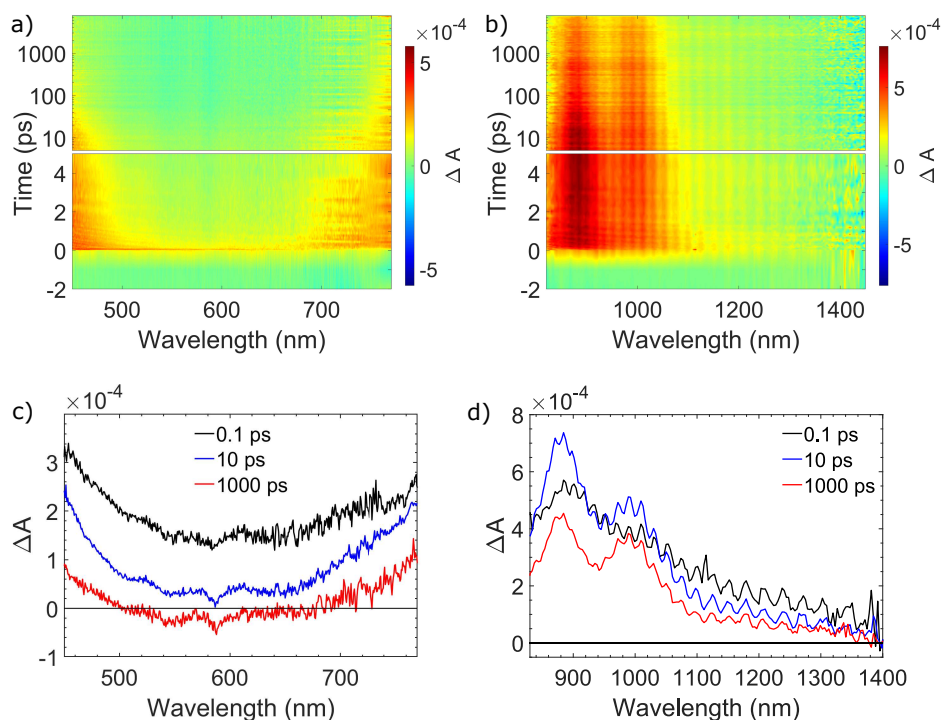


Figure 6.10: TA data of the equimolar PEN:F4-TCNQ thin film, excited with $\lambda_{\text{exc}} = 400$ nm. a,c) Probed in the visible spectral region and excited with a pump fluence of $1400 \mu\text{J}/\text{cm}^2$. b,d) Probed in the NIR spectral region and excited with a pump fluence of $560 \mu\text{J}/\text{cm}^2$. The TA spectra in c) and d) are averaged around the delay times given in the legend (cf. Figure 6.7). The strong oscillations in b) and d) arise from interference effects between the sealing glasses. Modified from Ref. [261].

part of a CTC is assumed in the equimolar blend with $\lambda_{\text{exc}} = 400$ nm. As for the blend with F6-TCNNQ, a GA does not provide a unique fit for both spectral regions due to the lack of spectral evolution and a non-exponential decay.

Finally, the TA signals of the blends with an excess of PEN are analyzed and compared to the TA signal of the neat PEN film in the following. The measurements were performed with $\lambda_{\text{exc}} = 620$ nm, thus exciting mainly the PEN molecules, and with pump fluences between $140 \mu\text{J}/\text{cm}^2$ and $1100 \mu\text{J}/\text{cm}^2$. In Figure 6.11, the TA data of the blend with 14 % F6-TCNNQ is shown, and the data of the blend with 30 % F6-TCNNQ can be found in Figure B.2 in the Appendix. In the visible spectral region, the TA spectra are similar to the TA spectra of the neat PEN film. This observation was expectable due to the similar steady-state absorbance spectra (Figure 6.6). However, at 540 nm and, weaker, at 500 nm, new positive features are present in the TA spectra at delay times of 10 ps and 100 ps. These features are more strongly pronounced in the TA spectra of the blend with 30 % F6-TCNNQ (Figure B.2). Moreover, in the NIR spectra, new positive features are detected around 1300 nm at short delay times, and around 1200 nm at long delay times. These features, which are absent in the signal of neat PEN, can be related to two different effects. First, as demonstrated by the reciprocal space maps in Figure 6.3, the PEN crystallites are randomly oriented in the blends, in contrast to the neat PEN film. This change in the orientation of the molecules and their TDMs influences

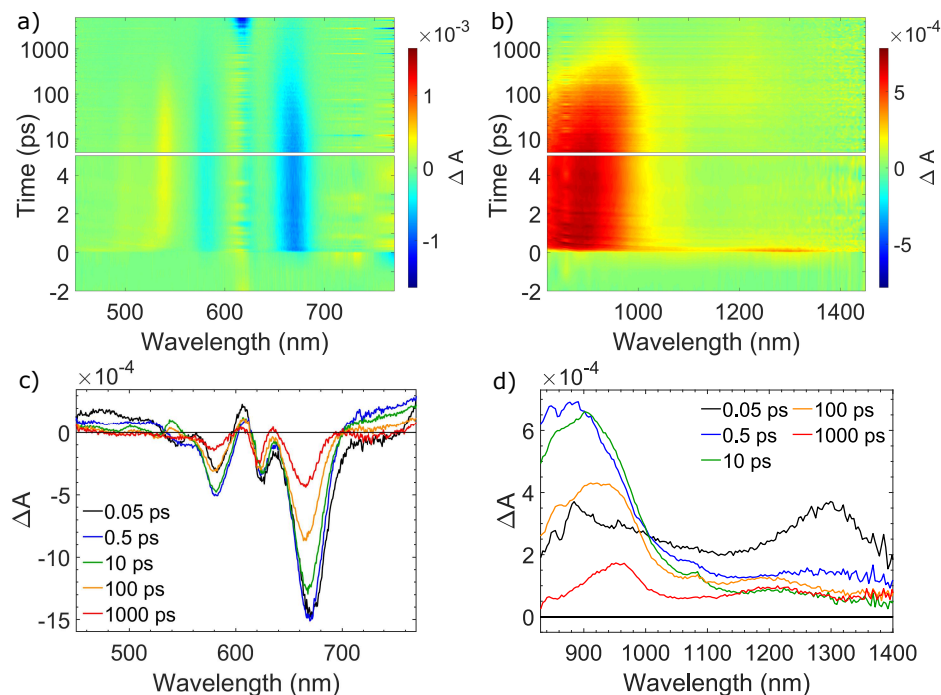


Figure 6.11: TA data of the blend with 14 % F6-TCNNQ, excited with $\lambda_{\text{exc}} = 620$ nm. a,c) Probed in the visible spectral region and excited with a pump fluence of $140 \mu\text{J}/\text{cm}^2$. b,d) Probed in the NIR spectral region and excited with a pump fluence of $700 \mu\text{J}/\text{cm}^2$. The TA spectra in c) and d) are averaged around the delay times given in the legend (cf. Figure 6.7). Around λ_{exc} , especially at long delay times, artifacts from scattering of the pump pulse are visible. Modified from Ref. [261].

the visibility of PEN transitions in the TA measurements [245, 268, 270]. Specifically, the sharp peaks at 540 nm and 500 nm can be assigned to PEN triplet ESA in the blends, which is not excitable in neat PEN thin films under normal-incidence excitation due to the TDM along the long molecular axis [245, 270]. These ESA features are slightly shifting within the first picoseconds, which is related to the evolution from $^1(\text{TT})$ to $^1(\text{T}\dots\text{T})$ according to Ref. [269]. This evolution can also be followed by the slight shift of the main ESA in the NIR [114]. The appearance of the strong and very short lived peak around 1300 nm can also be explained by the modified orientation, since at this position singlet ESA was reported in colloidal aggregates of PEN derivatives [269].

Additionally to these effects on the PEN crystallite orientation, the strong electron acceptors also influence the photophysics of the blends, which is apparent from the spectra at longer delay times. While for the neat PEN film the spectral evolution is completed after a few picoseconds, the spectra of the blends are still evolving on longer time scales. Specifically, the ESA of the triplets at 540 nm and 500 nm vanishes after 100 ps, while the GSB still remains. Additionally, the signal in the NIR changes on longer time scales, developing PIA features at the positions of the PEN^+ cation and F6-TCNNQ^- anion absorption peaks identified in the steady-state absorption measurements (Figure 6.4).

The TA data of the blends with F4-TCNNQ, presented in Figure 6.12 and Figure B.3 in the Appendix, show similar features as the blends with F6-TCNNQ. In the NIR data, a

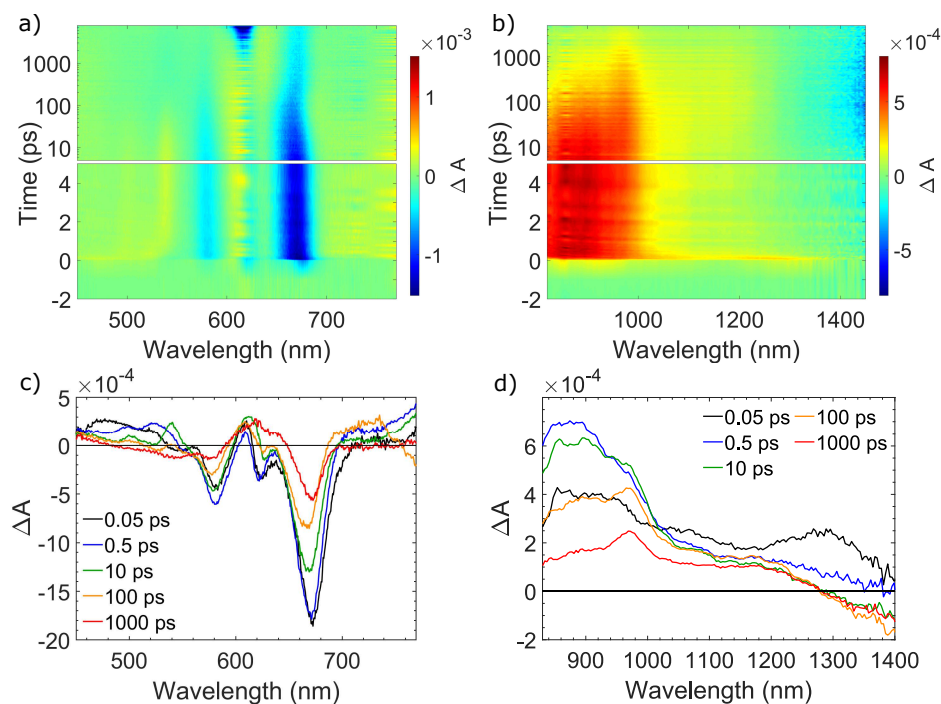


Figure 6.12: TA data of the blend with 10 % F4-TCNQ, excited with $\lambda_{\text{exc}} = 620$ nm. a,c) Probed in the visible spectral region and excited with a pump fluence of $140 \mu\text{J}/\text{cm}^2$. b,d) Probed in the NIR spectral region and excited with a pump fluence of $700 \mu\text{J}/\text{cm}^2$. The TA spectra in c) and d) are averaged around the delay times given in the legend (cf. Figure 6.7). Around λ_{exc} , especially at long delay times, artifacts from scattering of the pump pulse are visible. Modified from Ref. [261].

sharp peak appears around 970 nm at long delay times, hence at the position of PEN^+ cation absorption (see Figure 6.4). In addition, a negative feature is developing above 1300 nm at longer delay times, which can be assigned to the bleach of CTC transition in these blends (see also Figure 6.4). A possible scenario to explain the described feature evolution and GA results of the blends with an excess of PEN are discussed in the next section, since in these blends the most interesting and complex photophysics with several decay channels was found.

6.6 Discussion

Taken together, the results of the steady-state investigations provide evidence for the coexistence of CTCs and ion pairs in the blends of PEN with F4-TCNQ. Thus, the theoretical prediction that F4-TCNQ-doped PEN lies at the boundary between partial and integer CT [40] is experimentally confirmed. This also explains the earlier reports of either CTC or ion pair formation in PEN:F4-TCNQ systems [35, 41]. Most likely, the preferred CT mechanism in PEN:F4-TCNQ blends depends on the exact molecular arrangement and, consequently, on the preparation conditions. For a similar system consisting of a different donor and F6-TCNNQ as acceptor, a dependence of the CT mechanism on the molecular arrangement has recently been reported [38]. A preferential formation of CTCs has been found for an

ordered arrangement with molecular π -stacking, while less ordered arrangements favor ion pair formation [38]. This is in agreement with the observation of preferred CTC formation in the blends with an excess of PEN in this thesis, which exhibit Bragg peaks that indicate long-range order. In contrast, the equimolar PEN:F4-TCNQ blend and the blends with an excess of F4-TCNQ are amorphous and display increased ion pair formation. The increased disorder likely facilitates different molecular arrangements of donor and acceptor molecules with reduced orbital overlap and, therefore, reduced electronic coupling.

The comparison to the PEN:F6-TCNNQ blends demonstrates the special case of the PEN:F4-TCNQ system. In the blends of PEN with the slightly stronger acceptor F6-TCNNQ, only integer CT, resulting in ion pair formation, is detected. Thus, already the small change in acceptor size and strength is sufficient to realize a system in which only integer CT is obtained, independent of the mixing ratio. In contrast, as shown in Chapter 5, for TET with both acceptors only partial CT is realized, demonstrating the sensitivity of the preferred CT mechanism on minor changes in the system.

The photophysics of the equimolar blends was already discussed above, with the conclusion of an ultrafast excited state CT from F4-TCNQ and F6-TCNNQ to PEN, independent of the acceptor used. Consequently, the PIA signals of the ions slowly decay non-exponentially, probably due to back-transfer of the electrons with different time constants, depending on the local molecular arrangement. Therefore, here only the dynamics of the blends with an excess of PEN are discussed in detail. These blends are closest to a classical doping scenario with a small fraction of acceptor molecules. Furthermore, they can be directly compared to neat PEN due to the similar steady-state absorption spectra. Finally, a comparison of the blends with F4-TCNQ to the ones with F6-TCNNQ allows to shed light on the impact of CTC formation versus ion pair formation on the photophysics. The TA feature assignment and the changes of the spectra compared to neat PEN were already presented above. Here, the GA of the TA data of these blends is discussed and a kinetic scheme is proposed (Figure 6.14). The dynamics are rather complex and many species are involved, hence a varying number of species was required in the GA models for different blends and measurement conditions, as not all species were always discriminable. Here, only one GA of the TA data of one measurement of the blend with 10% F4-TCNQ is discussed in detail (Figure 6.13), while the GA results for the other blends are shown in Appendix B. A blend with F4-TCNQ was chosen for the following discussion because it contains ions and CTCs, in contrast to the blends with F6-TCNNQ, and, therefore, exhibits additional TA features.

In the visible spectral region, a model with five sequential species was necessary to fit the signal over the entire measurement range due to several involved processes. The obtained EASs are depicted in Figure 6.13a and the resulting fits to selected wavelengths are shown in Figure 6.13b. The spectral evolution from species 1 to species 2 (black to blue) with a time constant of 150 fs is indicative for the $S_1 \rightarrow {}^1(TT)$ transition [270]. This is apparent from the loss of the SE above 690 nm, the loss of the ESA around 480 nm, and the simultaneous rise of the ESA above 700 nm, in analogy to neat PEN (see EAS in Figure 6.8). This evolution is

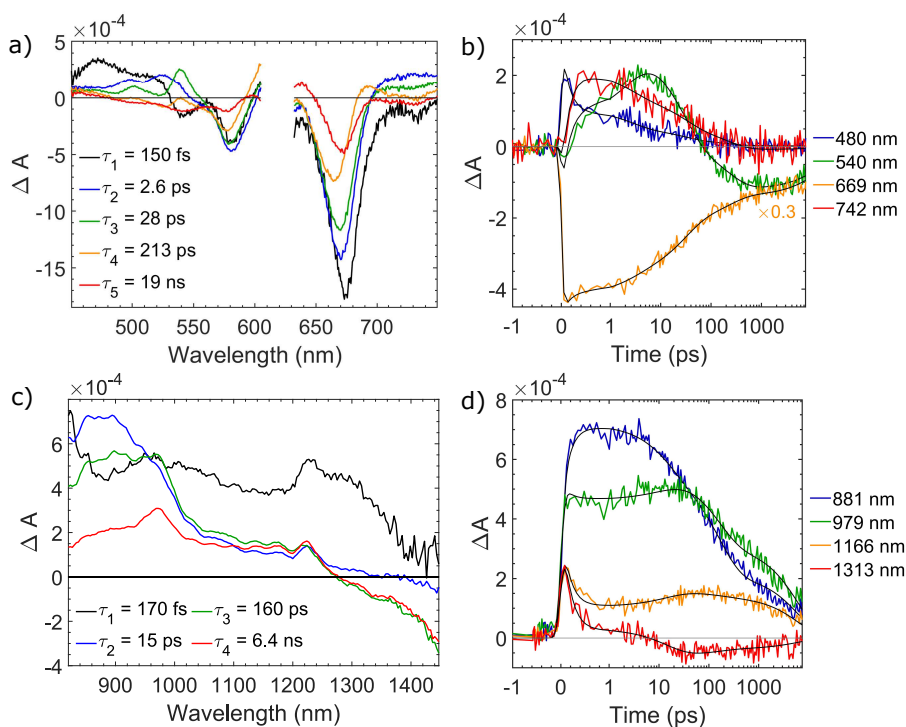


Figure 6.13: GA results of a TA measurement of the blend with 10 % F4-TCNQ excited with $\lambda_{\text{exc}} = 620$ nm. a,b) Probed in the visible spectral region and excited with a pump fluence of $210 \mu\text{J}/\text{cm}^2$. c,d) Probed in the NIR spectral region and excited with a pump fluence of $700 \mu\text{J}/\text{cm}^2$. a,c) EAS (not normalized for better visibility), with the corresponding time constants given in the legend. b,d) Selected timetraces of PEN TA features and the corresponding fits by the GA, shown as black lines. The time-axis changes from linear to logarithmic scale at 1 ps. Modified from Ref. [261].

seen in the EAS of all blends, see Figures B.4, B.5, and B.6 in the Appendix. The spectral evolution from species 2 to species 3 with a time constant of 2.6 ps (blue to green) is mainly seen by the shift and sharpening of the ESA at 500 nm and 540 nm, which has been attributed to the transition from $^1(\text{TT})$ to $^1(\text{T}\dots\text{T})$ [269]. This evolution is even more pronounced in the EAS of the blend with 30 % F6-TCNNQ, see Figure B.5 in the Appendix. Lastly, in the spectrum of the longest lived species, PEN triplet signals are missing, namely the ESA at 540 nm and above 700 nm. The remaining of the PEN GSB indicates that a CT from PEN molecules in the T_1 state to acceptor molecules or CTCs occurs with the time constant $\tau_4 = 213$ ps, resulting in remaining PEN^+ cations and acceptor/CTC anions as detailed below (Figure 6.14).

In the NIR spectral range, a model with four species was sufficient to fit the data, since not all transitions could be resolved in this measurement. The spectral evolution from species 1 to species 2 (black to blue) with a time constant of 170 fs can be again ascribed to the $\text{S}_1 \rightarrow ^1(\text{TT})$ transition. The transition from $^1(\text{TT})$ to $^1(\text{T}\dots\text{T})$ is not resolved here, but can be followed in the NIR EAS (blue to green) of the blend with 30 % F6-TCNNQ in Figure B.5 in the Appendix. In the last two NIR EAS in Figure 6.13 (green and red), the PEN^+ cation PIA at 970 nm and the bleach of the CTC transition below 1300 nm are clearly resolved.

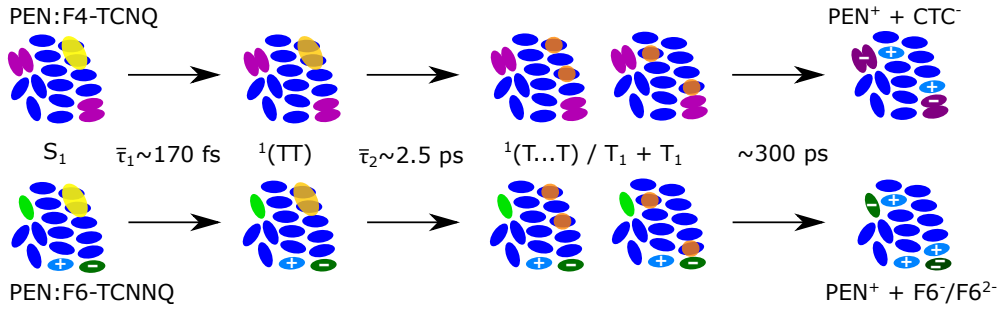


Figure 6.14: Schematic illustration of the SF process and the following CT in the blends of PEN with F4-TCNQ (upper row) and F6-TCNNQ (lower row). Blue and green ellipsoids represent PEN and F6-TCNNQ molecules, respectively, CTCs of PEN and F4-TCNQ are depicted in purple, and ions are marked by their charge and a slightly changed color. Singlet excitons are shown in yellow, and triplet excitons in orange. $^1(\text{T}\dots\text{T})$ and $\text{T}_1 + \text{T}_1$ are not distinguishable in TA measurements and the 300 ps for the CT step is only an approximated decay time. Reverse processes and decay to the ground state are omitted for clarity. Modified from Ref. [261].

To determine the average time constant $\bar{\tau}_1$ of the $S_1 \rightarrow ^1(\text{TT})$ transition (cf. Figure 6.14), the GA results of the TA data of all blends measured with different excitation fluences are taken together. In doing so, $\bar{\tau}_1 = 170$ fs was determined, with the single τ_1 values ranging from 110 fs to 230 fs. Thus, the triplet pair formation seems to be slightly slower in the blends than in the neat PEN film but still remains ultrafast. The determination of the average time constant $\bar{\tau}_2$ for the $^1(\text{TT}) \rightarrow ^1(\text{T}\dots\text{T})$ transition (cf. Figure 6.14) was slightly more complex, since this transition is not reflected in all GA results by independent spectra, due to overlapping PIA features from charged species. Thus, τ_2 was only extracted from GA results in which a clear assignment of the features in the second and third EAS to $^1(\text{TT})$ and $^1(\text{T}\dots\text{T})$, respectively, was possible. This results in $\bar{\tau}_2 = 2.5$ ps, with the single τ_2 values ranging from 1.8 ps to 3.3 ps, again slightly larger than for neat PEN. Nevertheless, the clear TA features and the similar time constants indicate that PEN still undergoes coherent SF in these blends. The slightly larger time constants might be related to minor changes in the molecular orientation due to the presence of the acceptor molecules in the film. However, the fact that they do not generally inhibit SF in the blends is an important finding as it demonstrates the robustness of the SF process, which is critical for potential device applications.

The photophysics on longer timescales differ for the blends with F4-TCNQ and F6-TCNNQ due to their different ground state CT mechanisms. In the blends with F4-TCNQ, the EAS at larger delay times present a long lived bleach of a CTC transition and a PIA of PEN^+ cations in the NIR (Figure 6.13 and Figure B.6), which leads to the conclusion of electron transfer from PEN molecules in the T_1 state to CTCs. It is not possible to extract a time constant for this step, since it is diffusion-driven and thus depends on the distance between the created triplet and a CTC, leading to a non-exponential decay. Still, a rough estimate of ~ 300 ps can be given for the decay time of the PEN triplets based on the disappearance of their ESA on this time scale (timetraces in Figure B.7 in the Appendix).

On the other hand, there are no CTCs in the blends of PEN with F6-TCNNQ, which excludes the PEN triplet decay path described above. Nevertheless, also in these blends the

PEN triplet ESA features in the visible and NIR spectral region disappear much faster than in neat PEN while the GSB remains, compare Figures B.4, B.5 and Figure 6.8. From the simultaneous appearance of PEN^+ cation- and, weaker, F6-TCNNQ^- anion PIA features, the following scenario with two possibilities for the triplet decay was developed (Figure 6.14 lower row). First, a PEN triplet may encounter a remaining neutral F6-TCNNQ molecule, leading to an electron transfer from the PEN molecule in the T_1 state to the F6-TCNNQ molecule, which can explain the PEN^+ cation and F6-TCNNQ^- anion PIA. Second, since most F6-TCNNQ molecules are already ionized in the ground state in these blends (see Figure 6.5), a PEN triplets can also encounter an F6-TCNNQ^- anion. Consequently, an electron transfer from the PEN molecule in the T_1 state to the F6-TCNNQ^- anion can occur, resulting in a PEN^+ cation and an F6-TCNNQ^{2-} dianion. This second possibility could explain the stronger PEN^+ cation PIA compared to the F6-TCNNQ^- anion PIA. F6-TCNNQ^{2-} dianions have been reported before in the context of double doping [131], but they do not exhibit any absorption in the spectral region measured here [132]. Thus, their existence cannot be proven here, but would be consistent with the obtained results. The formation of F6-TCNNQ^{2-} dianions could be probably verified by TA measurements with an even broader probe spectrum or by NIR measurements under simultaneous strong excitation with visible light (e.g. $\lambda_{\text{exc}} = 620 \text{ nm}$), which goes beyond the scope of this thesis. As for the blends with F4-TCNQ, the PEN triplet quenching in the blends with F6-TCNNQ is driven by diffusion and, therefore, described by non-exponential dynamics. Hence, it is not surprising that the disappearance of the PEN triplet ESA occurs on a similar time scale of $\sim 300 \text{ ps}$ for both systems (Figure B.7), resulting in the kinetic scheme shown in Figure 6.14. Lastly, the faster decay of the PEN GSB feature in the blends compared to the neat PEN film indicates that a fraction of the PEN triplets in the blends decays directly to the ground state, probably accelerated by an increased number of defects in the blends or energy transfer to CTCs.

6.7 Conclusion

To summarize, in this chapter the CT interactions in blends of PEN with the two strong acceptors F4-TCNQ and F6-TCNNQ were analyzed and compared. In the blends with F6-TCNNQ, only integer CT was found in the ground state, independent of the mixing ratio. In contrast, in the blends with F4-TCNQ, the coexistence of integer and partial CT was revealed, with partial CT being favored for small F4-TCNQ fractions and integer CT becoming more important for higher F4-TCNQ fractions. This is most likely related to a modified electronic coupling between PEN and F4-TCNQ in the different blends as a result of different molecular arrangements. The found coexistence of CTCs and ion pairs explains the existence of different models for the CT mechanism in the PEN:F4-TCNQ system [35, 40, 41], and experimentally clarifies the special behavior of this system at the boundary between partial and integer CT. The slightly higher acceptor strength of F6-TCNNQ was found to be already sufficient to suppress the CTC formation. The photophysics of the equimolar blends was dominated by

6. Ion pairs and charge transfer complexes of pentacene with strong acceptors

excited state CT and the formation of ions. For the blends with an excess of PEN, however, PEN triplet pair formation and separation was found to occur on only slightly larger time scales than in neat PEN, thus indicating the robustness of the coherent SF process in PEN, even in the presence of high acceptor fractions. On longer time scales, a CT from TET molecules in the T_1 state to CTCs or acceptor molecules was found, resulting in long lived ions in the blends.

7. Pentacene triplet pair state emission

In this chapter, the temperature dependent emission properties of neat PEN thin films are discussed and compared to literature reports. The focus is placed on the PL at low temperatures and the emission features found energetically below the free S_1 state emission, which are here assigned to emission of the electronically coupled $^1(TT)$ state. Possible explanations for the strong emission of this multiexciton state at low temperatures are given. The results presented in this chapter are unpublished and details about the contributions are given in Appendix F.

7.1 Introduction

In Chapter 6, the SF process in thin films of neat PEN and of PEN in blends with strong acceptors was analyzed. There, signatures of the electronically coupled triplet pair state were detected in the TA measurements, allowing to resolve both steps of the SF process, namely the triplet pair formation and separation. This electronically coupled triplet pair state and the entire SF process are examples of the importance of electronic coupling in neat OSC materials, as detailed in Chapter 1, and are therefore further investigated here. The triplet pair state has been discussed extensively in recent years as a crucial intermediate in the SF process and due to its multiexcitonic nature [16, 17, 115]. The existence of the electronically coupled $^1(TT)$ state as a real state has been concluded from its distinct signatures in TA spectroscopy measurements [114, 269] and a modified electron transfer behavior to acceptors from PEN molecules in the $^1(TT)$ state compared to PEN molecules in the T_1 state [272]. Furthermore, there are reports about emission from $^1(TT)$ states in OSCs [114, 171, 273].

The PL properties of PEN are, however, less studied, since PEN exhibits only a very weak emission from the S_1 state due to the competing, ultrafast SF process. Additionally, the electronically coupled $^1(TT)$ state in PEN is short lived at room temperature (~ 1.3 ps, compare Section 6.5), which prevents strong emission from this state, too. Hence, there are only a few reports of the temperature dependent PL properties of PEN thin films and crystals [274–277], but mostly from the time before the renewed interest in SF. Low-energy emission features have been reported in this literature, which have been assigned to self-

trapped excitons [274]. However, the PL of PEN single crystals has been reinvestigated recently, resulting in the conclusion that these low-energy features arise from $^1(\text{TT})$ emission via Herzberg-Teller intensity borrowing [171]. In this chapter, the temperature dependent PL of PEN thin films is revisited and distinct, sharp peaks are found which can be assigned to $^1(\text{TT})$ emission, without profound evidence for a Herzberg-Teller mechanism. This was achieved by cooling with liquid helium down to temperatures of 5 K, which strongly enhances the overall luminescence [277] and, in particular, the emission from $^1(\text{TT})$.

7.2 Sample description

For the temperature dependent PL measurements, several neat PEN thin films with different thicknesses were prepared. First, 20 nm thick films were prepared to allow for a direct comparison with the results in Ref. [277], and because in thinner films the PL is less affected by self-absorption [171]. Additionally, 50 nm thick films were prepared to investigate a possible thickness dependence of the PL spectra. These neat PEN thin films were prepared at substrate temperatures of ~ 305 K. Further reference films were prepared at different substrate temperatures and with an interrupted growth, but no significant influence on the PL spectra was observed, see Appendix C for details.

In Figure 7.1a, XRR data of a 20 nm and a 50 nm thick PEN thin film are shown. For both films, only Bragg peaks that can be assigned to the thin film phase of PEN are observed [94], which is consistent with the results of a 80 nm thick PEN thin film discussed in Section 6.2. Consequently, the PL properties of PEN in the thin film phase were investigated in this work. Yet, no major differences are expected for the PL properties of PEN in a bulk phase due to the similar absorption spectra [180], and the thin film PL spectra shown here are also compared to published PL data from PEN single crystals [171, 274, 275]. The different widths of the Bragg peaks in Figure 7.1a reflect the different film thicknesses [278].

To further characterize the as described samples, absorbance measurements were conducted and the normalized absorbance spectra of a 20 nm and a 50 nm thick PEN film are

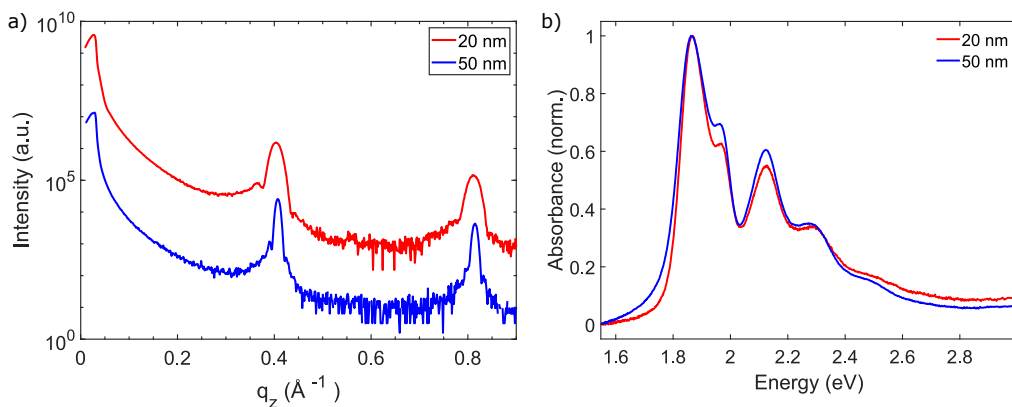


Figure 7.1: a) XRR data (vertically offset for clarity) and b) normalized absorbance spectra of neat PEN films with thicknesses of 20 nm and 50 nm.

shown in Figure 7.1b. As expected, very similar spectra were obtained for all PEN thin films. The absorption maximum of the energetically lower Davydov component (D_+) [180] is located at (1.864 ± 0.005) eV, which was determined from Gaussian fits to the spectra of the different films. The small differences between the normalized absorbance spectra of the 20 nm and 50 nm thick film are most likely partially related to fluctuations in the preparation conditions and partially related to thickness effects. For example, the faster increase of the absorbance at low energies in the spectra of the thicker films can be explained by increased scattering due to the larger roughness of these films [279]. Furthermore, also the difference in the relative intensity of the two DCs is related to the different thicknesses. This is a result of the perpendicular polarization of the two transitions, which leads to a decreased relative intensity of D_+ in the absorbance spectra of thicker films, as explained in detail in Ref. [97]. Taken together, only a minor influence of the different preparation conditions or thicknesses on the absorption properties of the thin films was found.

7.3 Temperature dependent photoluminescence spectroscopy

The PL spectra of the above described thin films were measured under continuous-wave laser excitation with a wavelength of 532 nm (2.33 eV). The samples were kept in high vacuum in a cryostat during the measurements and were cooled by liquid helium. The temperature dependent PL spectra of two samples, a 20 nm thick and a 50 nm thick one, are displayed in Figure 7.2. A very similar spectral shape and temperature behavior of the PL of these two blends is directly apparent. Further temperature dependent PL spectra of the reference samples are shown in Figure C.2 in the Appendix, which are similar, too. The slight differences in the relative peak intensities at a given temperature are most likely related to a slightly different local temperature at the measurement spot in the different measurements, which is influenced by the chosen laser power and the thermal contacting of the sample. Overall, no

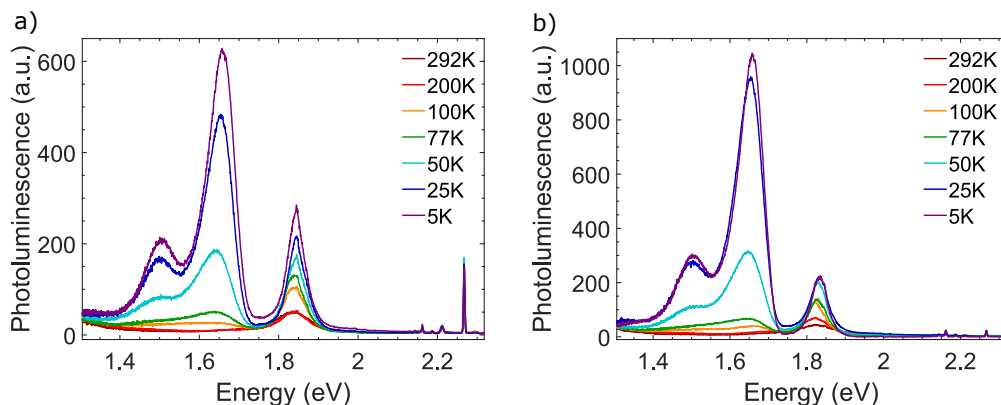


Figure 7.2: Temperature dependent PL spectra of a) a 20 nm thick PEN film, and b) a 50 nm thick PEN film, both measured during warm up. The excitation wavelength was 532 nm (2.33 eV). The sharp peaks at high energies result from Raman scattering by PEN and the substrate.

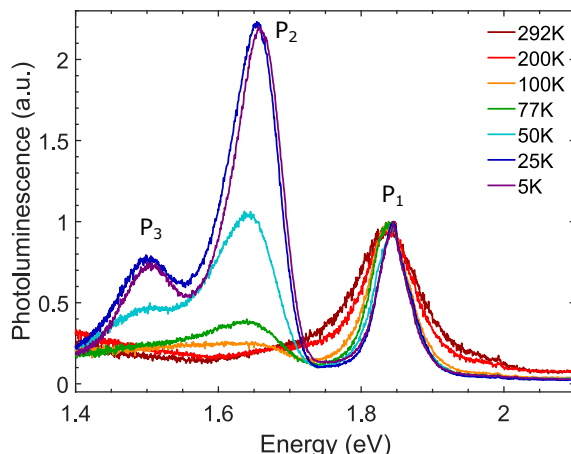


Figure 7.3: Normalized temperature dependent PL spectra of a 20 nm thick PEN film, deposited at ~ 305 K and measured during warm up. The excitation wavelength was 532 nm (2.33 eV).

major influence of the film thickness, preparation conditions or measurement procedure (during warm up or cool down) on the emission properties of the PEN thin films was detected. The high reproducibility of the results for different samples and measurements is emphasized here, since the obtained spectra are somewhat different from earlier reports [277].

Overall, a strong increase of the PL intensity for decreasing temperatures was observed (Figure 7.2), consistent with the literature [274, 277]. For an easier comparison of the spectra and a better visibility of the low-intensity spectra, the normalized PL spectra of a 20 nm thick film are shown in Figure 7.3. First, the room temperature spectrum is discussed, followed by a discussion of the more complex spectra at lower temperatures. At room temperature, the main PL peak (P_1) is found for all samples at $E(P_1) = (1.83 \pm 0.01)$ eV, thus slightly below the absorption maximum of D_+ (1.86 eV). This peak is assigned to the free singlet exciton emission in accordance with the literature [275, 276]. Toward smaller energies, a broad tail of this peak is visible, which is assigned to a smeared-out vibronic progression [277]. On the high-energy side of P_1 , a weak shoulder is found slightly below 2 eV, which has been attributed to emission from the upper DC before thermalization to the equilibrium [280]. The slight increase in intensity below 1.6 eV in the spectra at 292 K and 200 K is a measurement artifact that is only significant for small overall intensities.

With decreasing temperature, the spectral shape changes and new features appear. First, the free singlet exciton emission P_1 becomes narrower upon cooling, which is common for organic materials and explainable by decreased dynamic disorder [106] (compare Section 2.2.4). Second, P_1 is slightly blue-shifted by ~ 13 meV when the temperature is decreased to 5 K, which has been previously reported for PEN and other small molecules and has been explained by electron-phonon interactions [277, 281]. Third, the relative intensity of the vibronic progression and the high-energy shoulder decreases in accordance with the literature [277]. Finally, starting at a temperature of 100 K in the here presented spectra, new, low-

energy peaks (P_2 and P_3) arise, which dominate the spectra at 25 K and 5 K. They are as well blue-shifting with decreasing temperatures by ~ 15 meV and are located at $E(P_2) = (1.662 \pm 0.005)$ eV and $E(P_3) = (1.508 \pm 0.008)$ eV in the spectra at 5 K. The simultaneous appearance and rise in intensity of these two peaks suggest a common origin. This is further supported by their concomitant blue shift and their energy separation of ~ 150 meV, which is close to the energy spacing of the vibronic progression in the solution absorption spectrum of PEN [110]. In this low-energy region at low temperatures, different spectral shapes and features have been reported in the literature, measured from PEN thin films and single crystals [171, 274–277]. Hence, also different assignments exist, which will be detailed in the following discussion.

7.4 Discussion

Low temperature PL spectra of PEN single crystals have been already published in 2001 in Ref. [274], which will serve as a starting point for the following discussion. In this report, three different broad bands have been identified that are located at 1.82 eV (L1), 1.66 eV (L2), and 1.49 eV (L3), respectively, thus at similar energies as P_1 , P_2 , and P_3 in the spectra shown above. Additionally, they identified a low-energy peak L4 at 1.35 eV, which, however, is not reliably measurable in the setup used for this thesis and thus not further discussed. The first emission peak (L1), visible in all their spectra in the measured temperature range (7–200 K), has been assigned to the free exciton emission. The second peak (L2) has only been observed below 100 K with increasing intensity for decreasing temperature. So far, this is consistent with P_1 and P_2 in the here presented spectra. However, the two low-energy bands (L3 and L4) have been observed over the entire measured temperature range, showing a maximum intensity at 50 K [274]. This is in stark contrast to the spectra measured during this work, in which P_2 and P_3 always develop together as described above. The bands L2 to L4 have been assigned to shallow (L2) and deep self-trapped exciton luminescence, based on their energy positions [274]. Later, also temperature dependent PL spectra of 20 nm thick PEN films have been reported [277], which show a similar shape and temperature behavior as the crystal spectra in Ref. [274]. Two of these thin film PL spectra are reprinted in Figure 7.4a (green and purple), illustrating the differences to the PL data measured during this work, which are reprinted in Figure 7.4b for comparison.

A possible explanation for the observed differences in the PL spectra can be found in an article published in 2005, where the temperature dependent emission of PEN single crystals with different degrees of purity has been reported [275]. The peaks at the energy positions of L1 and L2 have been reproduced and similarly assigned as in Ref. [274]. However, by comparing the PL spectra of crystals grown from further purified material to the spectra of crystals grown from the as-received material, the emission bands in the energy range of L3 and L4 have been assigned to extrinsic emission from impurities, possibly from hydropentacene [275, 282]. Only a weak emission band at 1.49 eV, thus at a similar energy as P_3 /L3, still

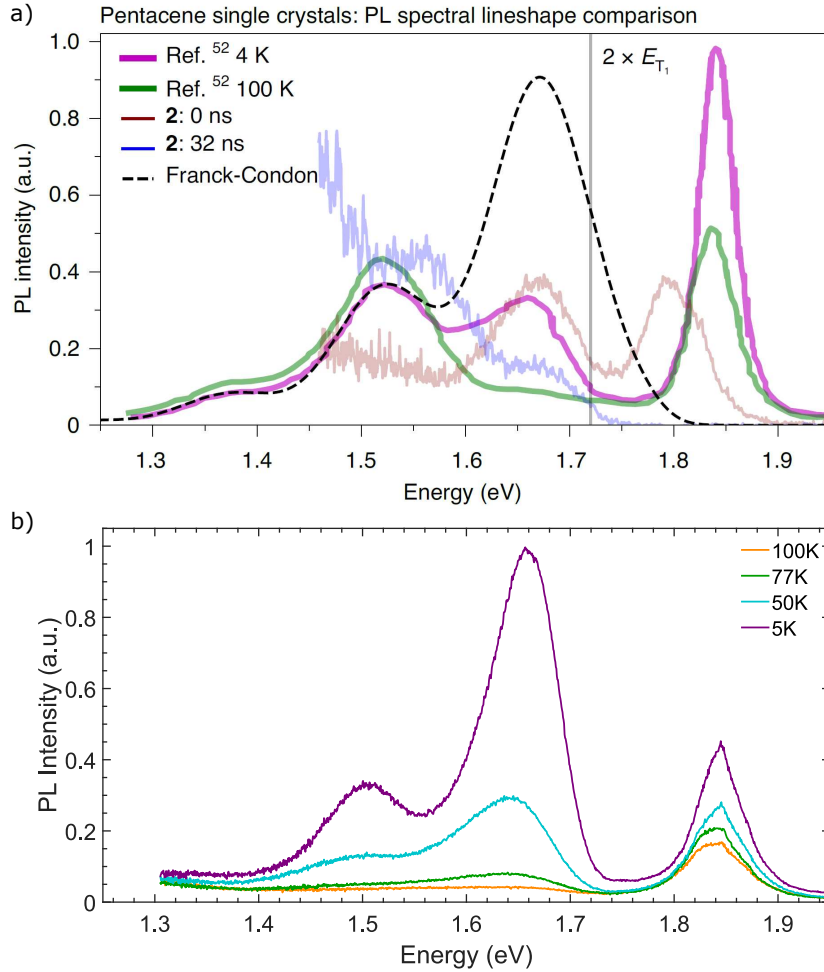


Figure 7.4: Comparison of PEN PL data with literature data. a) Literature PL spectra of a 20 nm thick PEN film (purple 4 K and green 100 K) [277], and of a PEN crystal, measured time-resolved at 77 K (blue and brown) [171]. In black, a simulated Franck-Condon progression is shown. Ref.⁵² in the legend of a) corresponds to Ref. [277] in this work. Adapted with permission from Ref. [171] and Ref. [277], AIP Publishing. b) Selected temperature dependent PL spectra of a 20 nm thick PEN film measured during this work.

remained in the spectra of the purified crystal. The PEN thin film PL spectra measured during this work resemble the ones of the purified crystal, indicating the high purity of these films, probably achieved by the usage of triple sublimed PEN (99.995 %) as starting material. In Ref. [277], the purity of the used PEN is given as 99.9 %, since a higher purity has probably not been available at that time, increasing the likelihood of extrinsic emission in these films.

Finally, in a report from 2021, the emission properties of PEN have been revisited in the context of the SF process [171]. Time-resolved PL spectra of PEN single crystals, measured at 77 K, have been presented and compared to the thin film spectra shown in Ref. [277]. This comparison is reprinted in Figure 7.4a. To allow for a direct comparison, the PL spectra measured at similar temperatures during this work are reprinted in Figure 7.4b. In Ref. [171], it has been argued that the peak at the energy of P₂ is unlikely to result from self-trapped excitons, since these should be unstable in PEN. This is consistent with the PL

spectra of PEN monolayers, which have been shown in Ref. [276] to also feature an emission peak at about 1.65 eV (compare with $E(P_2) = 1.66$ eV), while it is argued therein that self-trapped excitons may not occur in monolayers [276]. Eventually, also in a recent, detailed investigation of the excitons in PEN single crystals, the existence of self-trapped excitons at $E(P_2)$ has been questioned [283]. Instead, it has been suggested in Refs. [114, 171] that the low-energy emission features can be assigned to emission from the $^1(\text{TT})$ state, similar to other SF materials. Following this argumentation and due to their energy positions, P_2 and P_3 in the PL spectra measured for this thesis are assigned to vibronic bands of the $^1(\text{TT})$ emission.

The mechanism allowing this formally optically dark triplet pair state to exhibit PL requires some further discussion. In Ref. [171], emission via Herzberg-Teller intensity borrowing has been suggested. However, this conclusion has been based on the thin film PL spectra of Ref. [277], which are probably influenced by extrinsic emission as detailed above [275]. This extrinsic emission leads to an seemingly suppressed 0-0 transition (at $E(P_2)$) of the $^1(\text{TT})$ state by artificially increasing the intensity of the peaks assigned to the 0-1 (L3) and 0-2 (L4) transitions (Figure 7.4a). Though, such a suppression of the 0-0 transition was not found in the thin film spectra measured for this thesis (Figure 7.4b) or the spectra of the purified crystal in Ref. [275]. Further, also the PL spectrum of the crystal at 77 K directly after photoexcitation from Ref. [171] (brown curve, labeled as 0 ns in Figure 7.4a) exhibits a relatively strong peak at $E(P_2)$, while the spectral shape at lower energies has not been resolvable [171]. By comparing this spectrum to the spectrum at 50 K of the thin film prepared during this work (Figure 7.4b), a similar shape is noticed. This allows the conclusion that there is no suppression of the 0-0 transition in the measurements of Ref. [171], either. Indeed, the PL spectra measured at 5 K in this work nearly perfectly reproduce the Franck-Condon fit shown in Figure 7.4a.

With these new insights at hand, the emission process of the electronically coupled triplet pair state in PEN should be revisited. In the following, two possible explanations for the strong P_2 emission are described. P_2 is approximately located at the energy at which the 0-0 transition of the $^1(\text{TT})$ state is expected [114]. Thus, the first possibility is that P_2 actually corresponds to the 0-0 transition of the $^1(\text{TT})$ state. This possibility can be rationalized by theoretical calculations to the nature of the $^1(\text{TT})$ state [118]. These calculations lead to the conclusion that the adiabatic $^1(\text{TT})$ state possesses a small contribution from a bright (diabatic) state and thus a small oscillator strength [118]. This results in a not completely dark $^1(\text{TT})$ state that can show weak emission, also of the 0-0 transition, which would be consistent with the PL spectra presented in this thesis.

As the second possibility, the P_2 emission could actually be the 0-1 transition of the $^1(\text{TT})$ state which emits via a Herzberg-Teller mechanism. However, the involved vibrational mode should then have a very low energy, since otherwise the 0-0 transition of the $^1(\text{TT})$ state would lie higher in energy than $2 \times E(T_1)$, resulting in an unbound state. One important mode with ~ 33 meV has been identified for PEN in Refs. [118, 284, 285], which could fulfill

this requirement. Since the exact energy of the $^1(\text{TT})$ state is challenging to determine due to its multiexcitonic nature and the unknown binding energy between the two triplet excitons, such a small energy shift is difficult to exclude. In this case, the visible vibronic progression of the $^1(\text{TT})$ emission would result from different vibrations than the one which mediates the Herzberg-Teller intensity borrowing. Further investigations and calculations are required to clarify the exact emission mechanism from the electronically coupled $^1(\text{TT})$ state, which is beyond the scope of this thesis.

Independent of the exact mechanism, the fact that the $^1(\text{TT})$ emission is only observable at low temperatures can be explained by the fast loss of the electronic coupling of the $^1(\text{TT})$ state at room temperature ($\tau \approx 1.3$ ps, compare Section 6.5). This electronic dephasing of the $^1(\text{TT})$ state results from coupling to the phonon bath and spatial separation of the two triplets via triplet hopping [16, 17]. Thus, the $^1(\text{TT})$ state should have an increased lifetime at lower temperatures due to a decreased number of phonons and a decreased triplet hopping rate. For PEN, it is assumed that the dissociation rate is determined by the binding energy of the triplet pair state, which needs to be thermally overcome [17, 114]. From the PL spectra presented above, this binding energy is estimated as

$$E_b \leq 2 \times E(\text{T}_1) - E(\text{P}_2) = 1.72 \text{ eV} - 1.66 \text{ eV} = 60 \text{ meV}, \quad (7.1)$$

depending on the exact emission mechanism and consistent with reported values of $E_b \approx 30$ meV for several SF materials [114]. Since these values are in the range of $k_{\text{B}}T \approx 25$ meV at room temperature, a drastically increased lifetime of the coupled $^1(\text{TT})$ state can be expected at low temperatures. In a more detailed treatment, additionally the temperature dependent change in the entropy resulting from the splitting of the $^1(\text{TT})$ state should be considered [16]. Especially at very low temperatures, also disorder plays a significant role in the $^1(\text{TT})$ separation [17], and further non-radiative relaxation pathways of the triplet pair state might become important. Nevertheless, overall the probability for a radiative decay of the $^1(\text{TT})$ state increases with decreasing temperature due to the increasing lifetime of the $^1(\text{TT})$ state [114].

7.5 Conclusion

In this chapter, the temperature dependent PL of high purity, polycrystalline PEN thin films was investigated. At all temperatures, the emission of the free singlet exciton was detected, with increasing intensity at lower temperatures. Below 100 K, a new peak appeared around 1.66 eV, with a vibronic replica at 1.51 eV, which dominate the spectra below 50 K and are assigned to $^1(\text{TT})$ emission. Importantly, the peak at 1.66 eV, assigned previously to the 0-0 transition, is not suppressed. This is in stark contrast to temperature dependent PL spectra of PEN thin films that have been reported in the literature [277]. These reported spectra have probably been influenced by extrinsic emission features from impurities in the thin films [275]. Thus, the emission process of the $^1(\text{TT})$ state in PEN should be revisited, since the

conclusion of a Herzberg-Teller intensity borrowing mechanism has been mainly based on these reported spectra for PEN [114, 171]. The exact emission mechanism of the $^1(\text{TT})$ state cannot be identified here without further theoretical considerations and complementary experimental methods, which is beyond the scope of this thesis. Nevertheless, further insights into the emission process of PEN are obtained, which can help to improve the understanding of the electronically coupled triplet pair state and the SF process.

8. Strong light-matter coupling in pentacene on plasmonic arrays

This chapter analyzes the light-matter interactions in polycrystalline PEN thin films on open, thus easily accessible, plasmonic arrays of silver nanoparticles that support strong SLRs. In these samples, strong light-matter coupling is realized, leading to the formation of polaritons. This strong light-matter coupling represents another way to tune the properties of OSCs and can serve as a measure to influence the SF process. This chapter is based on Ref. [286], and the investigations were conducted in collaboration with the research group of Prof. Dr. Monika Fleischer. Details about the contributions can be found in Appendix F.

8.1 Introduction

In the previous three chapters, different types of electronic coupling and their influence on the electronic, optical and photophysical properties of OSCs were discussed. Blending different OSC materials was shown to be a viable way to significantly tune these properties. Alternatively, the effect of strong light-matter coupling can be exploited to influence the properties and photophysics of OSCs, as introduced in Chapter 1. Strong light-matter coupling in OSCs leads to the formation of polaritons, thus quasi-particles that contain photonic and excitonic contributions (cf. Section 2.4) [45]. As a consequence, the energy landscapes of the excited states of the OSC are modified, which can result in altered chemical reactivity and photophysics [25]. This type of coupling is investigated in this chapter at the model system of polycrystalline PEN thin films on arrays of silver nanoparticles that support strong SLRs (cf. Section 2.4.2). Open plasmonic arrays offer the advantages of a freely accessible surface and an easy in- and out-coupling of light, in contrast to closed microcavities that are composed of two mirrors (cf. Chapter 1). PEN was chosen as organic material for this investigation because its structural, optical and photophysical properties were already analyzed in detail in this work and because it exhibits ultrafast and exothermic SF. Recent theoretical reports [57, 60] have predicted that the SF process can be significantly influenced by strong light-matter coupling. This is schematically illustrated in Figure 8.1 for the case of PEN. Without a cavity, thus without strong light-matter coupling, the first step of the SF process occurs from the S_1 state to a vibrationally excited $^1(TT)$ state (cf. Section 2.2.5) [118, 119]. Yet, in

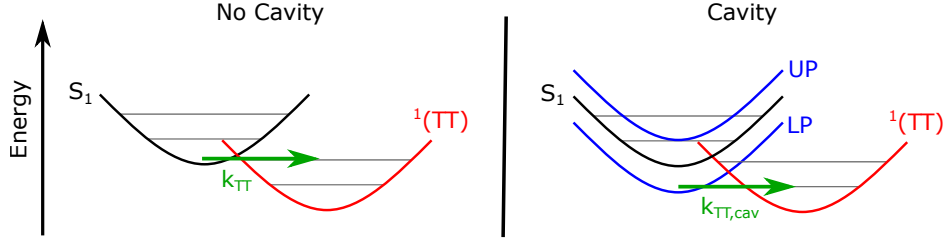


Figure 8.1: Schematic illustration of the energy levels of the SF process in PEN without and with coupling to a cavity photon. Without strong light-matter coupling, the (adiabatic) singlet state (S_1 , lower DC) and the electronically coupled triplet pair state, $^1(\text{TT})$, are shown as relevant states. Strong light-matter coupling leads to the formation of a lower polariton (LP) and an upper polariton (UP). k_{TT} and $k_{\text{TT,cav}}$ denote the triplet pair formation rate without and with strong light-matter coupling, respectively. Inspired by Ref. [57].

the presence of strong light-matter coupling, polaritons are formed with energies above and below the S_1 state. Consequently, the lower polariton can serve as the new initial state of the SF process, which results in a modified energy balance (ΔE_{SF} , cf. Section 2.2.5). Depending on the coupling strength, the lower polariton might energetically be either in resonance with the $^1(\text{TT})$ state dressed by another vibration, in resonance with the vibrationally relaxed $^1(\text{TT})$ state or even below the $^1(\text{TT})$ state. This should affect the triplet pair formation rate, which could experimentally be verified using the system presented in this chapter.

8.2 Sample description

In this work, different types of plasmonic arrays were produced to determine the influence of the particle size and shape and the particle arrangement on the appearance of SLRs and the shape of the extinction spectra. Subsequently, these parameters were experimentally optimized to achieve strong and sharp SLRs around the energy of the two DCs of the PEN thin film. Additionally, reference samples were produced for comparison reasons.

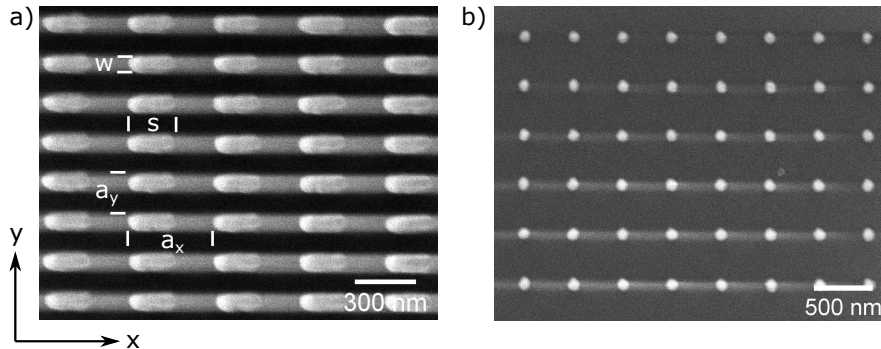


Figure 8.2: SEM images of exemplary ordered silver nanoparticle arrays on glass. a) Rectangular array of rods with length $s = 200$ nm and width $w = 85$ nm and lattice constants $a_x = 415$ nm and $a_y = 190$ nm. b) Square array of discs with diameter $d = 85$ nm and lattice constant $a = 415$ nm. See main text for standard deviations. The entire surface is covered by a 10 nm thick Al_2O_3 layer. The bright lines between the particles are measurement artifacts that result from charging of the sample. Modified from Ref. [286].

Two different types of ordered arrays were produced in this work, namely rectangular arrays of rods and square arrays of discs, see Figure 8.2 for exemplary SEM images of such arrays. These two different array geometries were chosen because they both exhibit specific advantages that are discussed below. Overall, the goal was to obtain strong and sharp SLRs at the energy of the DCs of PEN thin films, thus around 1.9 eV (650 nm) (cf. Section 3.2.1). This was realized by tuning a diffraction edge of the array, which mainly defines the position of the SLR (cf. Section 2.4.2), to an energy slightly below 2 eV (above 620 nm). Additionally, the LSPR of the single particles was tuned to be located at higher energies to allow for a high quality SLR [152]. A first order diffraction edge was utilized in both array geometries. Consequently, following from Equation 2.17 with the effective refractive index $n_{\text{eff}} = 1.53$ between the refractive indices of the Menzel coverslip and the covering organic layer, a lattice constant of ~ 415 nm was chosen. The effective refractive index was hereby experimentally determined from the position of the diffraction edges of several plasmonic arrays with varying lattice constants. The LSPR of the particles was tuned to be around 2.2-2.6 eV, resulting in a suitable detuning between the diffraction edge and the LSPR.

The advantage of square arrays of discs is that the excitation polarization does not significantly affect the position and width of the SLR due to the high symmetry of the lattice and the particles [161]. As a result, similar spectra are obtained under polarized and unpolarized excitation, which might be of interest for future investigations and applications. Yet, for a surrounding medium with the refractive index of PEN ($n \approx 1.6$), the diameter of the discs must be relatively small ($d \approx 90$ nm) to obtain a LSPRs at sufficiently high energies, which is required for high quality (large Q) SLRs. This small particle size and the overall small fraction of the surface that is covered by silver (cf. Figure 8.2b) lead, however, to a decreased LSPR and SLR strength. This issue can be solved by choosing rod-shaped silver particles in rectangular lattices (Figure 8.2a), which bear the advantage that stronger and still sharp SLRs can be realized as demonstrated below. The rods can be excited along their short axis ($w \approx 90$ nm) by light polarized in y -direction (Figure 8.2), giving rise to high-energy LSPRs. The dominant coupling between the particles is along the perpendicular x -axis (cf. Section 2.4.2), implying that the diffraction edge can be tuned by the lattice constant a_x , which is therefore chosen as $a_x \approx 415$ nm. The larger length $s \approx 210$ nm of the rods and the smaller lattice constant $a_y \approx 190$ nm result in a larger proportion of the substrate being covered by silver and, therefore, stronger signals. The standard deviation of the diameter d of the discs and of the width w and length s of the rods within an array was determined from SEM images of several samples of all sample types to be below 7%, 10%, and 3%, respectively. The standard deviation of the distance between individual nanoparticles within an array was determined to be below 3%. In the following and in the figure captions, only the average values for the different arrays are given for better readability.

Additionally to the ordered arrays, samples with randomly distributed discs and rods were produced for comparison, see Figure 8.3. Due to the absence of a regular lattice, no SLRs are expected to be found for these samples, which allows to contrast the impact of the ordered

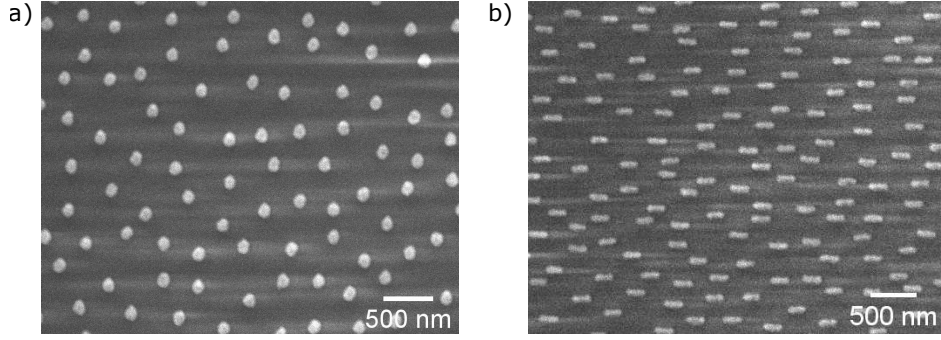


Figure 8.3: SEM images of exemplary samples with randomly distributed silver nanoparticles on glass, a) discs ($d = 110$ nm) and b) rods ($w = 85$ nm, $s = 225$ nm). The entire surface is covered by a 10 nm thick Al_2O_3 layer. Modified from Ref. [286].

arrangement. The rods are all oriented along one direction, to allow an excitation of a specific axis by polarized light.

Finally, also samples with much larger discs ($d \approx 180$ nm) were produced. This large diameter was chosen to obtain low-energy LSPRs that are far out of resonance of the PEN transitions. Hence, no coupling effects are expected to appear in these samples, allowing the comparison of the undisturbed spectra of the PEN thin film on and beside the array. From this comparison, information about the orientation of the PEN molecules on and beside the arrays can be obtained, *vide infra*.

8.3 Extinction measurements of the uncoupled systems

By comparing the extinction spectra of the uncoupled systems, namely the PEN thin film on glass and the plasmonic array covered by a PS reference film (cf. Section 3.4), with the extinction spectra of the coupled system, consisting of a PEN thin film on a plasmonic array, the change in the spectra and the formation of polaritons can be detected. Therefore, the extinction spectra of the uncoupled systems are analyzed first in this section. The general setup for the extinction measurements was described in Section 4.3. Here, only the measurement geometry and the illumination conditions are briefly discussed, as they are of major importance for the extinction spectra of the plasmonic arrays. In Figure 8.4, the general sample structure of a rod array and the important orientations and angles are shown. All spectra presented in this thesis were taken with light polarized along the y -direction, resulting in a dominant dipole coupling along the x -direction and an electric field of the SLR along the y -direction (cf. Section 2.4.2). Always the zero-order transmittance was recorded [164]. The illumination angle θ is defined as the angle between the surface normal (z -direction) and the wave vector of the incoming light in the x - z -plane, resulting in a non-vanishing k_x component for $\theta \neq 0$ ($k_z \neq 0$, $k_y = 0$ for all measurements). Thus, a TE illumination [63] was realized which implies that the wavelength (or energy) position of the diffraction edges can be calculated by Equation 2.17 (cf. Section 2.4.2).

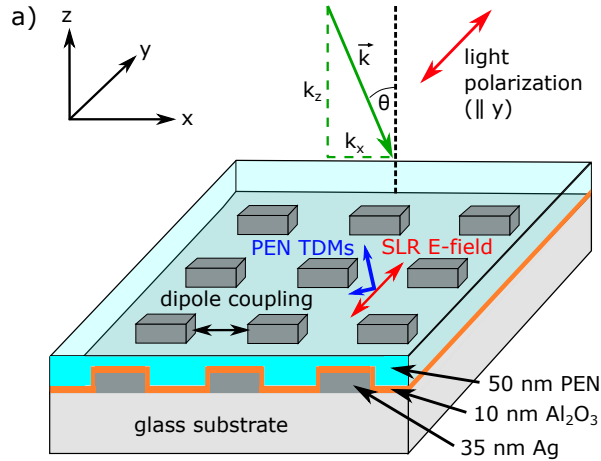


Figure 8.4: Schematic illustration of the sample structure of a rod array covered by PEN, together with the illumination conditions in the extinction measurements. The blue arrows indicate the TDMs of the two DCs of PEN for an exemplary crystallite. The reference measurements of the arrays covered by PS and the samples with randomly distributed nanoparticles were performed under the same conditions. See main text for details. Modified from Ref. [286].

In Figure 8.5, the extinction spectrum ($\theta = 0$) of a 50 nm thick PEN film on an Al_2O_3 layer on glass is shown, referenced to the bare substrate. The energetically lower (D_+) and the energetically upper Davydov component (D_-) are indicated, which exhibit different oscillator strengths and are polarized perpendicular to each other [180, 287]. The oscillator strength of a transition is connected to the magnitude of the TDM and the polarization of a transition is reflected by the direction of the TDM. These two properties are directly related to the coupling strength (cf. Equation 2.21) between an excitonic transition and a cavity field. As expected, the extinction spectrum in Figure 8.5 closely resembles the UV-vis-NIR absorbance spectra of PEN thin films on glass discussed in Chapter 7. Similar spectra were obtained under polarized and unpolarized excitation. This is a result of the polycrystallinity of the PEN thin films and the relatively large probing spot size ($5 \times 5 \mu\text{m}^2$), which leads

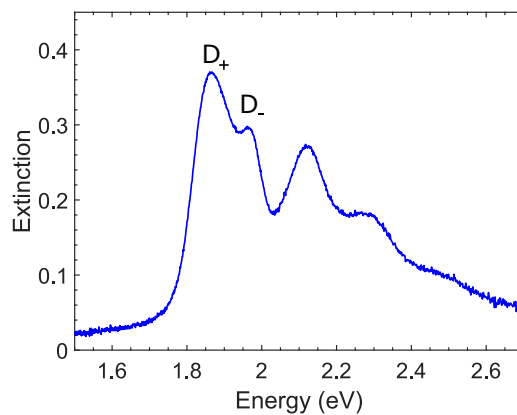


Figure 8.5: Extinction spectrum of a 50 nm thick PEN film on an Al_2O_3 layer on glass, with the two DCs D_+ and D_- indicated. Modified from Ref. [286].

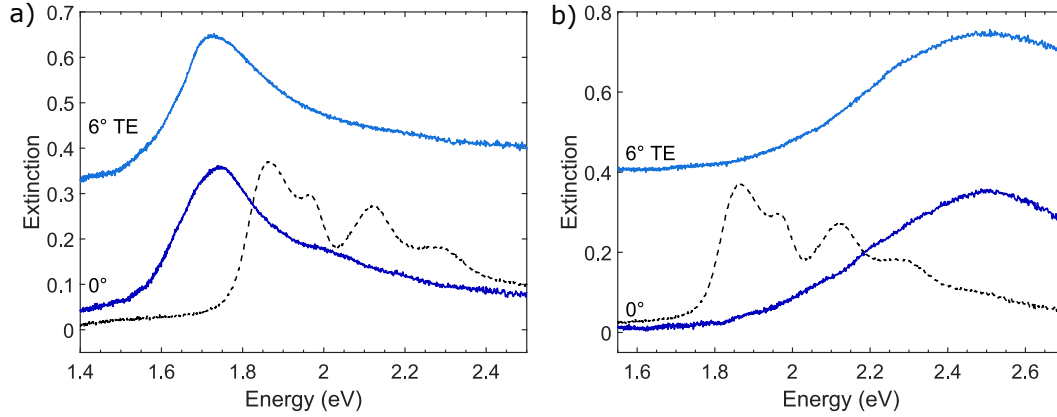


Figure 8.6: Extinction spectra of samples with randomly distributed a) discs with $d = 110$ nm and b) rods with $w = 85$ nm and $s = 220$ nm, covered by a PS layer. The spectra taken under $\theta = 6^\circ$ are vertically offset for clarity. The dashed black line shows the extinction spectrum of a PEN thin film. Modified from Ref. [286].

to an averaged measured signal from many crystallites with random in-plane orientations. No significant changes in the extinction spectra were observed for illumination under small angles ($\theta \leq 6^\circ$).

Next, the extinction spectra of the plasmonic arrays covered by a PS reference layer are discussed. These spectra are referenced to the extinction of the PS layer beside the arrays. First, in Figure 8.6, extinction spectra of exemplary samples with randomly oriented discs and rods are shown. They show only broad extinction features, which can be attributed to the LSPR of the single nanoparticles. As expected, due to the lack of long-range order, there are no sharp features that would indicate SLRs. Consequently, the spectra taken under normal illumination and under small θ closely resemble each other. The extinction spectra of the sample with randomly distributed discs with diameter $d = 110$ nm (Figure 8.6a) exhibit an extinction maximum at ~ 1.75 eV, thus at smaller energies than the two DCs of PEN. This illustrates that smaller discs are required to achieve a LSPR at suitable energies above the energy of the DCs. Alternatively, nanorods can be used to meet this requirement. For example, the spectra of the sample with randomly distributed rods with $w = 85$ nm and $s = 220$ nm (Figure 8.6b) show an extinction maximum at ~ 2.5 eV, thus in the desired energy range.

In Figure 8.7, extinction spectra of exemplary square nanodisc and rectangular nanorod arrays, covered by a PS layer, are presented. Similar extinction spectra of further arrays with slightly different dimensions are shown in Figures D.1 and D.2 in the Appendix, illustrating the reproducibility of the results. These ordered arrays of nanoparticles exhibit drastically different spectra compared to the randomly distributed nanoparticles discussed above. The spectra taken under normal incident illumination ($\theta = 0$) exhibit one sharp extinction feature at the energy of the DCs of PEN and a broader feature at higher energies. The sharp feature represents a SLR of the array that appears, as expected, at slightly smaller energies than the $(\pm 1, 0)$ diffraction edge, which is also indicated in Figure 8.7 [156, 164]. The broader

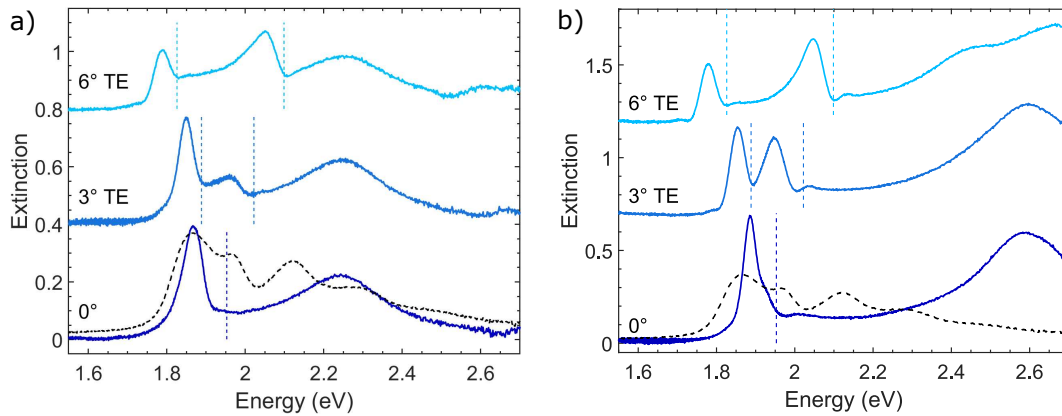


Figure 8.7: Extinction spectra of plasmonic arrays covered by a PS reference layer. a) Square array of discs with $d = 85$ nm and $a_x = a_y = 415$ nm. b) Rectangular array of rods with $w = 85$ nm, $s = 200$ nm, $a_x = 415$ nm, and $a_y = 190$ nm. The spectra taken under $\theta = 3^\circ$ and $\theta = 6^\circ$ are vertically offset for clarity. The dashed blue lines indicate the $(-1,0)$ and $(+1,0)$ diffraction edges and the black dashed line is the extinction spectrum of a 50 nm thick PEN film. Modified from Ref. [286].

feature has mainly plasmonic character from the LSPR of the single particles and is therefore referred to as LSPR in the following (cf. Section 2.4.2). By comparing the extinction spectra of the arrays of discs (Figure 8.7a) and rods (Figure 8.7b), the greater strength of the SLR and LSPR of the arrays of rods becomes apparent. Therefore, the focus is placed on these nanorod arrays in the following. Due to the slightly different chosen rod dimensions in the different arrays (cf. Appendix D), the SLRs exhibit different strengths (maximum extinction between 0.6 and 0.8), quality factors ($25 < Q < 40$), and resonance energies (1.85 eV-1.89 eV), which were determined by Lorentzian fits.

The spectra taken under $\theta = 3^\circ$ and $\theta = 6^\circ$ that are also included in Figure 8.7 nicely demonstrate the different behavior of the LSPR and SLR for oblique illumination. While the energy position of the LSPR is insensitive to such small rotations, consistent with the results of the samples with randomly arranged nanoparticles, the SLR splits into two SLRs, which follow the $(-1,0)$ and $(+1,0)$ diffraction edges. The SLR at lower energies, correlated to the $(-1,0)$ diffraction edge, exhibits a smaller width compared to the SLR at higher energies, illustrating the importance of the energy detuning between the LSPR and the diffraction edge for the quality factor of the SLR. The dip around 2.5 eV in the LSPR of the spectra of the rod arrays taken under $\theta = 6^\circ$ is most likely related to coupling to a higher order diffraction edge under this angle. Since the DCs of PEN are at much lower energies, this effect is not discussed further. In contrast, the ability to shift the SLRs out of resonance with respect to the DCs of PEN by rotating the sample is a useful feature for the investigation of the coupled systems.

The last system that is discussed in this section consists of a PEN thin film on a plasmonic array composed of large discs ($d = 180$ nm). The extinction spectrum of this sample, referenced to the bare substrate, is presented in Figure 8.8, together with the extinction spectrum

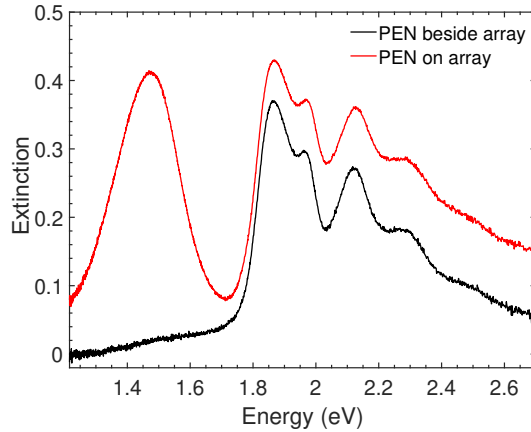


Figure 8.8: Extinction spectra of a 50 nm thick PEN film on an Al_2O_3 layer on glass, beside (black) and on (red) a plasmonic array consisting of large discs ($d = 180$ nm). The strong, broad peak around 1.48 eV is assigned to the LSPR of the discs. Modified from Ref. [286].

of the PEN thin film beside the array. Due to the large diameter, the LSPR of these discs is located at low energies (~ 1.48 eV). Therefore, no significant influence of the LSPR on the extinction spectrum of the PEN thin film is observed. Indeed, above 1.8 eV, the two spectra exhibit a very similar shape. The overall vertical offset of the red spectrum is due to light being blocked by the large silver structures. From the similar shape and intensity of the PEN absorption features on the array and beside the array, a similar molecular orientation can be concluded for both cases, with nearly upright-standing molecules on weakly interacting substrates, as introduced in Section 3.2.1. If the molecular orientation on the array would be significantly different, a reduced extinction would be obtained, as the TDMs of the DCs would not be almost perpendicular to the illumination direction anymore. This observation allows to assume a nearly upright-standing molecular orientation for the coupled systems, too, which are discussed in the next section.

8.4 Extinction measurements of the coupled systems

After this characterization of the uncoupled systems, the coupled systems of PEN thin films on plasmonic arrays are analyzed next. To realize these systems, first the PS reference layer was removed from the plasmonic arrays using toluene. Then, a 50 nm thick PEN layer was deposited on top of the plasmonic structures via OMBD and the extinction under several angles was measured. The extinction spectra of these coupled samples are referenced to the extinction of the PEN layer beside the arrays. In Figure 8.9 and in Figure D.3 in the Appendix, extinction spectra of different, rectangular arrays of rods, covered by PEN, are shown. As mentioned above, the focus is placed on these nanorod arrays due to their greater SLR strength and quality factor, especially under non-normal illumination. Extinction spectra of square arrays of discs and of plasmonic samples with randomly distributed nanoparticles, all covered with PEN, are shown and discussed in Appendix D.

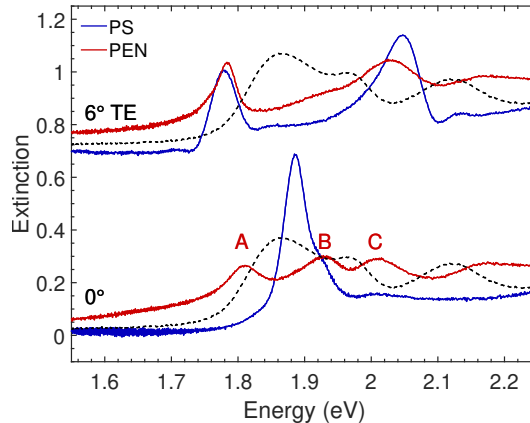


Figure 8.9: Extinction spectra of a rectangular, plasmonic array of rods, covered by a 50 nm thick PEN film (red) or a PS layer (blue) for reference. The lattice constants are $a_x = 415$ nm and $a_y = 190$ nm and the rod dimensions are $w = 85$ nm and $s = 200$ nm. The spectra taken under $\theta = 6^\circ$ are vertically offset for clarity. The black dashed line is the extinction spectrum of the 50 nm thick PEN film on Al_2O_3 on glass beside the array for peak position comparison. Modified from Ref. [286].

First, the extinction spectra under normal illumination ($\theta = 0^\circ$) of the nanorod arrays covered by PEN are analyzed and compared to the reference spectra of the uncoupled systems. Clearly, the extinction spectra of the coupled systems cannot be described as a superposition of the individual reference spectra. Instead, three new peaks, labeled by A, B, and C in Figure 8.9, appear around the energy region of the DCs of PEN. These peaks are assigned to three polariton bands that result from the coupling of the SLR of the array and the two DCs of PEN, in accordance to the assignment in similar systems [63, 163, 288]. From the splitting between A and B (B and C), the coupling strength between the SLR and D_+ (D_-) can be approximated [288]. This is an approximation because there is always a small energy detuning between at least one of the DCs and the SLR. Additionally, the other DC and the first vibronic transition will also slightly influence the peak positions [47]. Nevertheless, the larger splitting between A and B compared to B and C indicates a larger coupling strength between the SLR and D_+ than between the SLR and D_- , which is nicely consistent (cf. Equation 2.21) with the larger TDM of D_+ ($\mu = 5.76$ D) compared to D_- ($\mu = 3.53$ D) [289]. The similar extinction spectra of further rod arrays covered by PEN, presented in Figure D.3 in the Appendix, underline the reproducibility of these results.

Next, the extinction spectra under an illumination angle of $\theta = 6^\circ$ of the nanorod arrays covered by PEN are considered. In these spectra, only two clear peaks are observable, which are located at very similar energies as the SLR peaks of the arrays covered by PS. This implies that, due to this illumination angle, the SLRs of the arrays are already far enough out of resonance with the PEN transitions to suppress a significant influence of the coupling on the SLR energies. The slight shift of the energetically upper SLR, confer also Figure D.3, is most likely related to influences of the first vibronic transition. This ability to shift the SLR out of resonance with the DCs, especially D_+ , is useful for the investigation of the influence of the polariton formation on the photophysics of these systems, as it allows to minimize the

effect by rotating the sample. Therefore, reference measurements can be conducted at the exact same sample position. Thus, the same PEN film thickness and array properties are guaranteed in the reference measurements. This could be used to determine the influence of the polariton formation on the SF rate via TA measurements under various illumination angles. Finally, the extinction spectra under $\theta = 6^\circ$ confirm the similarity of the refractive indices of PS and PEN and the reliability of the background correction, as no PEN features appear.

8.5 Discussion

In Section 2.4.3, the connection between the collective coupling strength $\hbar g$ and the Rabi splitting $\hbar\Omega$ at zero detuning between the energy of the SLR and the energy of the exciton was introduced (Equation 2.20). Since there is a minimal energy detuning between the two DCs and the SLR for the spectra under normal illumination, the energy splitting between A and B (B and C) corresponds approximately to the Rabi splitting, allowing to approximate the coupling strength between the SLR and D_+ (D_-). For the energy splitting between A and B a value of 120 meV was extracted from the four different nanorod arrays covered by PEN (Figures 8.9 and D.3), while for the energy splitting between B and C values of 80 meV to 90 meV were found. Hence, the collective coupling strengths follow as $\hbar g(D_+) \approx 60$ meV and $\hbar g(D_-) \approx 40$ meV, respectively. The ratio of ~ 1.5 between these coupling strengths meets the expectations based on the ratio of ~ 1.6 [289] between the TDMs of D_+ and D_- (cf. Section 8.4).

For the relative categorization of these coupling strengths, the linewidths of the uncoupled oscillators are required. Hence, the linewidths (full width at half maximum) of D_+ and D_- of the PEN thin film on glass (cf. Figure 8.5) were determined by Gaussian fits as $\gamma(D_+) = 120$ meV and $\gamma(D_-) = 90$ meV, respectively. The linewidths of the SLRs of the different nanorod arrays covered by PS were obtained by Lorentzian fits as $55 \text{ meV} \leq \gamma(\text{SLR}) \leq 75 \text{ meV}$. These linewidths enter the criterion for strong coupling (cf. Section 2.4.3), which is given as [165]

$$\hbar\Omega > \frac{\gamma(D_{\pm}) + \gamma(\text{SLR})}{2}. \quad (8.1)$$

From Equation 8.1 follows that the light-matter coupling between the SLR and D_+ can be categorized as strong coupling, while the coupling between the SLR and D_- is in the regime between strong and weak coupling.

It should be noted that the above-obtained values for the collective coupling strengths ($\hbar g(D_+) \approx 60$ meV and $\hbar g(D_-) \approx 40$ meV) are average values of the coupling strength in the here investigated systems. The coupling strength depends on the relative orientation of the TDM with respect to the cavity field, as introduced in Section 2.4.3. Here, polycrystalline PEN thin films were investigated, which implies that there is no perfect alignment between

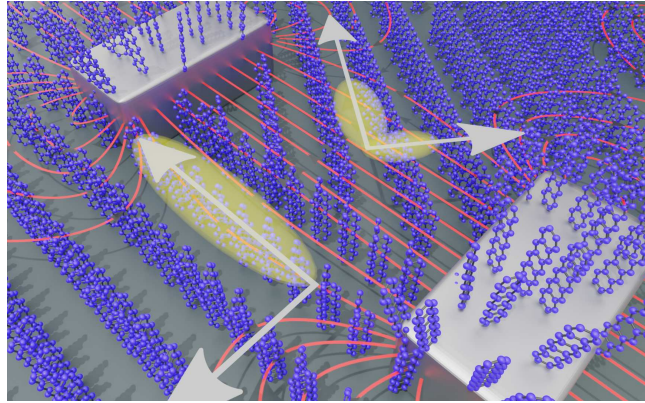


Figure 8.10: Graphical illustration of two PEN crystallites with different orientation on a plasmonic rod array. The gray arrows depict the TDMs of D_+ and D_- , the red lines the SLR E-field and the size of the yellow hallos the coupling strength. Modified from Ref. [286].

the TDM and the SLR field. This is schematically illustrated in Figure 8.4 by the blue arrows for an exemplary crystallite and graphically depicted in Figure 8.10. As mentioned in Section 8.3, the two DCs of PEN are polarized perpendicular to each other, such that at most the TDM of one DC can be aligned with the SLR field. In the extinction measurements, the signal is always averaged over many different crystallites with different orientations due to the relatively large probing spot size ($5 \times 5 \mu\text{m}^2$).

Under the assumption of a nearly upright-standing molecular orientation, as suggested by the results presented in Section 8.3, the measured, average coupling strengths between D_+ or D_- and the SLR correspond to $\sim 64\%$ of the maximal coupling strength at perfect alignment. This value is obtained by integrating Equation 2.21 over all possible in-plane orientations of the TDMs. Thus, the maximal coupling strength at perfect, parallel alignment of the TDM of one DC and the SLR E-field would be ~ 1.56 times larger than the averaged, measured value. This indicates that strong coupling could be realized for both DCs of PEN. If one would assume a completely random orientation of the molecules around the silver structures due to the uneven substrates, the integration should be performed over all in-plane and out-of-plane orientations, leading to the result that the maximal coupling strength at perfect alignment could be even ~ 2.44 times larger than the measured one.

Finally, also the theoretically achievable coupling strength for the here investigated systems can be approximated by Equation 2.21, but with N denoting now the number of coupled unit cells instead of molecules. This modification is required as the Davydov transitions are related to both molecules in the unit cell. By assuming the entire mode volume to be filled with PEN molecules, the $\frac{N}{V}$ term under the square root can be replaced by the unit cell density of the PEN (thin film) crystal structure, which is taken from the literature as $\rho_{\text{uc}} = 1.43 \times 10^{27} \text{ m}^{-3}$ [94]. Furthermore, $E_{\text{SLR}} = 1.86 \text{ eV}$ is chosen, implying zero detuning between the energy of the SLR and the energy of D_+ . Together with the TDM of D_+ ($\mu = 5.76 \text{ D}$) [289], the maximal theoretical coupling strength between the SLR and D_+ is obtained as $\hbar g(D_+) \approx 590 \text{ meV}$. As expected, this value is much larger than the experimentally determined coupling strength

due to the assumptions made. Namely, a perfect alignment of the SLR E-field and the TDM was assumed, as well as the entire mode volume to be filled by PEN. In the measurement, different orientations are averaged due to the polycrystallinity of the thin film, as discussed above. Additionally, not the entire mode volume can be filled by PEN as it extends into the glass substrate and the protective Al_2O_3 layer, which reduces the number of coupled molecules and, therefore, the experimentally obtained collective coupling strength. Thus, the coupling strength can most likely be further increased by optimizing the sample geometry, which underlines the promising coupling capability of the PEN Davydov transitions.

8.6 Conclusion

In summary, in this chapter strong light-matter coupling was realized in polycrystalline PEN thin films on arrays of silver nanoparticles that support SLRs. The coupling between the SLR and D_+ was shown to be strong while the coupling between the SLR and D_- is in the regime between strong and weak coupling. The strong coupling results in the formation of a polariton band around 1.80 eV, thus ~ 60 meV below the energy of the lower Davydov transition of PEN without strong light-matter coupling. This lower polariton can serve as the new initial state of the SF process [57]. The energy of the $^1(\text{TT})$ state, as intermediate in the SF process, is most likely in the range of 1.66 eV to 1.72 eV, confer Chapter 7. As the coupling of the $^1(\text{TT})$ state to the SLR should be negligible due to its small TDM [57, 60], the magnitude of ΔE_{SF} is expected to be significantly reduced, but the SF process remains exothermic. Thus, SF should still be possible in the coupled system, but a modification of the $^1(\text{TT})$ formation rate is expectable, since now probably another vibrational mode needs to be involved in the process (cf. Figure 8.1). The $^1(\text{TT})$ formation rate could be measured by TA spectroscopy on similar samples but with larger array sizes, which is beyond the scope of this thesis. Overall, strong light-matter coupling was demonstrated in polycrystalline PEN thin films on open nanoparticle arrays, which can serve as alternative measure to tune the optical and photophysical properties of OSCs without chemical modifications.

9. CdSe quantum dots coupled with aryleneethynylenes

This last results chapter discusses the investigations of the mixed organic-inorganic semiconductor samples consisting of AE derivatives and CdSe QDs. The focus is placed on the short-range organization and the chemical binding in these systems, since these important characteristics have been barely studied in coupled organic-inorganic nanostructures. Furthermore, the optical and photophysical properties of the hybrid materials are analyzed, as these can give insights into possible electronic coupling between the different components. The presented investigations have been published in Ref. [290] and were conducted in collaboration with the groups of Prof. Dr. Marcus Scheele and Prof. Dr. Petra Tegeder, see Appendix F for details about the contributions.

9.1 Introduction

In the previous result chapters, purely organic donor:acceptor systems and OSC thin films on plasmonic arrays, exhibiting strong light-matter coupling, were discussed. As introduced in Chapter 1, the combination of organic and inorganic semiconductors into one hybrid material promises new, functional materials with properties that exceed the sum of the properties of the pure components [24, 64, 65]. Therefore, such hybrid materials are the subject of this chapter. There has been significant research progress in the last few years and promising hybrid materials for various applications have been identified [24, 77–79]. However, there is still a lack of detailed understanding of the concrete organic-inorganic interface and its electronic and chemical structure. Yet, this interface is of fundamental importance for such hybrid systems [24], as explained in Chapter 1. Hence, it was studied during this work on the exemplary systems of AE derivatives coupled with CdSe QDs by using PMIRRAS and FTIR spectroscopy, as well as GIXD. Subsequently, the influence of the found chemical binding on the optical properties and the photophysics of the systems was investigated by means of UV-vis-NIR absorbance, PL, and TA spectroscopy. Additionally, atomic force microscopy (AFM) images and surface profiles, which were taken to characterize the morphology and thickness of the samples, respectively, are presented in Appendix E.1.

9.2 Vibrational spectroscopy

After the preparation of the hybrid organic-inorganic thin films from the solution phase with consecutive washing steps (cf. Section 3.3.3), the presence of both components in the final film was first verified by FTIR spectroscopy. The presence of both components in the hybrid films is also evident from the UV-vis absorbance spectra shown in Section 9.4. Infrared spectra offer the advantage that also functional groups of the native organic ligands can be detected, which additionally allows to monitor their presence in the produced samples. FTIR spectra covering the fingerprint region of the AEs (1100-1800 cm^{-1}) and the region of the characteristic C-H stretching vibrations above 2800 cm^{-1} , mainly found in the native ligands, are shown in Figure 9.1. In all spectra, narrow peaks between 1300 cm^{-1} and 2000 cm^{-1} are visible that originate from water vapor in the measurement atmosphere. These peaks cannot be perfectly subtracted with the reference measurement on a clean silicon substrate, probably due to slightly differing water vapor concentrations between different measurements. Similarly, around 2350 cm^{-1} , some artifacts are left from the strong C=O band from atmospheric carbon dioxide.

Taking this into account, the only remaining signals in the CdSe/nat film spectrum are the peaks above 2800 cm^{-1} , which can be assigned to C-H stretching vibrations in the native ligands that all have long aliphatic tails. The absence of these peaks in the spectrum of the CdSe/I⁻ film indicates that the ligand exchange to inorganic iodide was successful and that (most of) the organic ligands were removed.

In contrast, the spectra of the pure AE films exhibit several strong peaks between 1150 cm^{-1} and 1750 cm^{-1} which can be assigned to vibrations of the backbone and the functional groups, as detailed below [101]. Additionally, at 2195 cm^{-1} , a weak peak, assigned

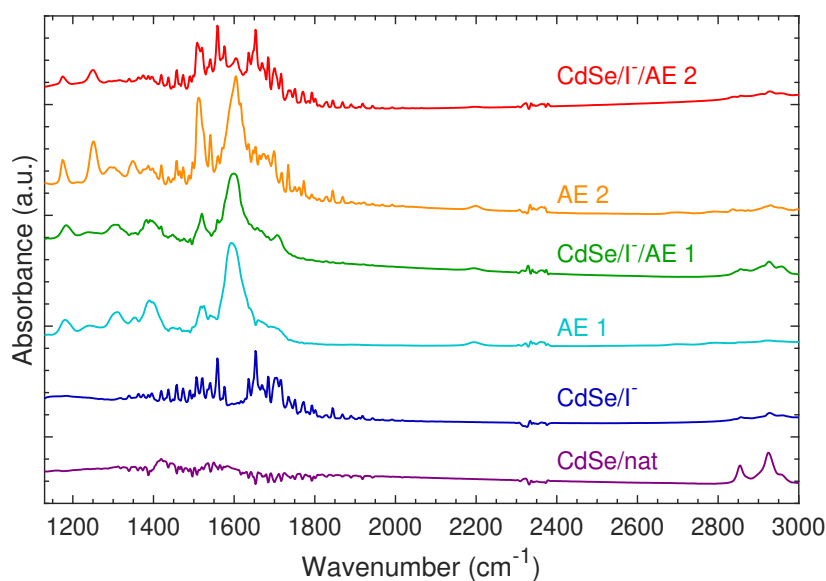


Figure 9.1: FTIR spectra of the hybrid organic-inorganic films and of the pure component films for reference. Modified from Ref. [290].

to the characteristic $C\equiv C$ stretching vibration of the alkyne moieties, can be observed. These peaks of the AEs also dominate the spectra of the CdSe/I⁻/AE samples, proving the successful incorporation of the organic molecules into the hybrid system. Additionally, some modifications of the spectra of the hybrid samples compared to the neat AE film spectra can be recognized, namely in the peak positions and relative strengths, but these are hard to quantify as they are obscured by the superimposed water vapor bands.

This problem of artificial peaks arising from gases in the beam path can be minimized by the use of PMIRRAS, as described in Section 4.2. This technique additionally benefits from the electric field enhancement at the metal interface, which allows to detect small amounts of material in the thin film with high sensitivity, yielding high quality infrared spectra [235]. PMIRRAS spectra covering the spectral region of the characteristic vibrations of the functional groups of the AEs are shown in Figure 9.2 together with the molecular structures of the two AEs. The better signal-to-noise ratio compared to the FTIR spectra and the disappearance of the artificial peaks are clearly visible. Especially for the two CdSe QD films peaks in this wavenumber region are now clearly visible, which were not distinguishable in the FTIR spectra. For the CdSe/nat film, these peaks at 1421 cm^{-1} , 1464 cm^{-1} and 1545 cm^{-1} are assigned to the native ligands trioctylphosphineoxide and oleate based on Ref. [291]. The spectrum of the CdSe/I⁻ film lacks these peaks which confirms once more the successful removal of the native ligands during the ligand exchange to iodide stabilized QDs. Instead, this spectrum exhibits new peaks at 1014 cm^{-1} , 1600 cm^{-1} , 1642 cm^{-1} , and 1706 cm^{-1} that resemble the ones reported in Ref. [207] for iodide-capped CdSe QDs. They are, however, relatively weak (the spectra in Figure 9.2 are normalized), which explains their absence in the FTIR spectra. This implies that the peaks seen in the spectra of the mixed films can be mainly attributed to the incorporated AEs, which is also evident from a direct comparison. The high quality of the PMIRRAS spectra allows a detailed comparison of the peak positions and intensities of the neat AE film spectra and the CdSe/I⁻/AE film spectra, which is outlined in the following as the basis for the development of a binding scenario.

First, the neat AE 1 film spectrum is discussed because AE 1 is a highly symmetric molecule and, thus, exhibits relatively few and pronounced peaks. They are located at 974 cm^{-1} , 1182 cm^{-1} , 1311 cm^{-1} , 1398 cm^{-1} , 1522 cm^{-1} , and 1614 cm^{-1} . The last mentioned peak is clearly the strongest one and is located in a region where aromatic ring stretching and carboxylate vibrations are expected (see color code in Figure 9.2) [101, 292]. AE 1 contains several aromatic rings and carboxylate groups, thus, the peak at 1614 cm^{-1} should be the result of a superposition of peaks assignable to these groups. This also explains the asymmetric appearance of this peak. Both mentioned groups generally show further peaks at different wavenumbers, which are also found in the AE 1 film spectrum. Namely, the sharp peak at 1522 cm^{-1} can be assigned to aromatic ring vibrations and the smaller peaks at 1311 cm^{-1} and 1398 cm^{-1} to carboxylate vibrations [101]. Thus, only the peaks at 974 cm^{-1} and 1182 cm^{-1} remain to be assigned. The former is weak but probably belongs to aromatic C-H bending vibrations, which are commonly found in this wavenumber region. The latter

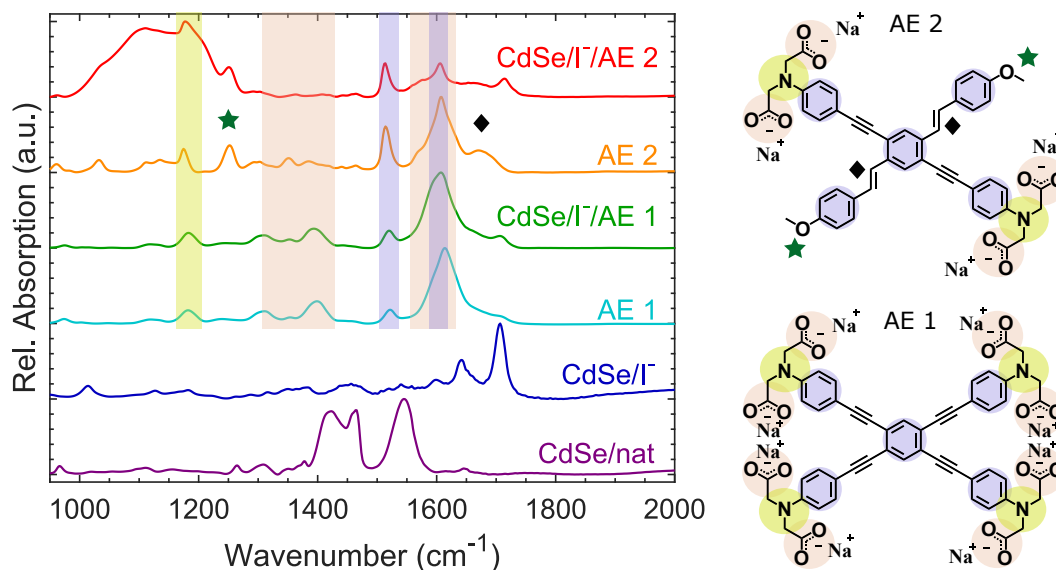


Figure 9.2: PMIRRAS spectra of the hybrid organic-inorganic thin films and the corresponding reference films. On the right, the molecular structure of the two AEs is shown with color-coded functional groups. Their expected peak regions are highlighted in the spectra [101]. For AE 2, additionally the C=C bond and its assigned stretching mode are marked by a black diamond and the alkyl aryl ether C-O stretching mode by a green star. Modified from Ref. [290].

at 1182 cm^{-1} is more pronounced and perfectly matches the known position of the tertiary amino C-N stretching mode [101], completing the assignment of all distinct peaks in the spectrum to groups found in the molecule.

Next, the spectrum of the CdSe/I⁻/AE 1 film is analyzed. It strongly resembles the spectrum of the neat AE 1 film. The peaks at smaller wavenumbers, namely here at 1184 cm^{-1} , 1310 cm^{-1} , 1394 cm^{-1} , and 1520 cm^{-1} , are barely shifted in position and are assigned to the same vibrations, as summarized in Table 9.1. However, some changes are detected for the main peak and the larger wavenumber region. The main peak is slightly shifted to 1607 cm^{-1} and exhibits a shoulder on the low-energy side. This can be an indication for some changes in the intensities of the superimposed peaks of the aromatic ring stretching and carboxylate vibrations and will be discussed in detail below. Additionally, at 1707 cm^{-1} , a new peak is present in the CdSe/I⁻/AE 1 film spectrum, while only a weak shoulder is observable in the AE 1 film spectrum in this wavenumber region. This new peak is located at a position where carbonyl vibrations are found and will also be discussed below.

Continuing with the AE 2 thin film spectrum, similarities but also differences to the AE 1 film spectrum appear. Overall, the shape of the spectrum is similar, again with the main peak slightly above 1600 cm^{-1} , this time at 1607 cm^{-1} , assigned to a superposition of carboxylate and aromatic ring stretching modes. The sharp peaks at 1513 cm^{-1} and 1175 cm^{-1} are again assigned to aromatic ring and tertiary amino vibrations, respectively. Compared to the AE 1 film spectrum, the relative intensities of the peaks assigned the aromatic ring stretching modes are increased with respect to the carboxylate and tertiary amino mode peaks. This

Table 9.1: Summary of the main vibrational peaks of the samples containing AEs and their assigned functional groups, compare Figure 9.2. The vibrational frequencies are given in cm^{-1} .

| | AE 1 | CdSe/I ⁻ /AE 1 | AE 2 | CdSe/I ⁻ /AE 2 |
|------------------|------------------|---------------------------|-----------------|---------------------------|
| carboxylate | 1614, 1398, 1311 | 1607, 1394, 1310 | 1607, 1300-1400 | 1606 |
| aromatic ring | 1614, 1522 | 1607, 1520 | 1607, 1513 | 1606, 1513 |
| tertiary amino | 1182 | 1184 | 1175 | 1177 |
| aromatic C-H | < 1150 | < 1150 | < 1150 | < 1150 |
| alkene C=C | - | - | 1670 | 1665 |
| alkyl aryl ether | - | - | 1252 | 1251 |
| carbonyl | - | 1707 | - | 1714 |
| ether C-O-Cd | - | - | - | 1130 |

can be rationalized by the fact that the number of carboxylate and tertiary amino groups is halved in AE2 compared to AE1, while the number of aromatic rings is the same (cf. Figure 9.2). The intensities of the peaks between 1300 cm^{-1} and 1400 cm^{-1} , assigned to the carboxylate groups, are also reduced. In contrast, the number and strength of the peaks below 1150 cm^{-1} , assigned to C-H bending modes, is increased. Completely new peaks are also visible in the spectrum of the AE2 film compared to the spectrum of the AE1 film due to the distyrylbenzene segment and the alkyl aryl ether group. The peak at 1252 cm^{-1} can be assigned to the stretching mode of the latter, marked by a green star in Figure 9.2, and the new, broad peak around 1670 cm^{-1} can be assigned to the C=C stretching mode, marked by a black diamond [101].

Finally, the spectrum of the CdSe/I⁻/AE2 film is analyzed, which shows pronounced differences compared to the AE2 film spectrum. First, the peak slightly above 1600 cm^{-1} , which was the dominant peak in the three last discussed spectra, is drastically less pronounced in the CdSe/I⁻/AE2 film spectrum. Additionally, the peaks between 1300 cm^{-1} and 1400 cm^{-1} , assigned to carboxylate vibrations, are nearly absent in this spectrum, while the peak at 1513 cm^{-1} , assigned to aromatic ring vibrations, retains its high intensity. This allows the conclusion that the carboxylate vibrations contributing to the superposition peak at 1606 cm^{-1} declined. This indicates modifications of the carboxylate groups in the hybrid film, which will be discussed in detail below. The sharp peaks assigned to the tertiary amino stretching mode and the alkyl aryl ether stretching mode at 1177 cm^{-1} and 1251 cm^{-1} , respectively, are still present in the CdSe/I⁻/AE2 film spectrum. Furthermore, two new peaks compared to the neat AE2 film spectrum arise, a very broad and strong one around 1130 cm^{-1} , in a region where C-O stretching vibrations are located, and a sharp one at 1714 cm^{-1} , again in the region of carbonyl vibrations.

Taken together, the vibrational spectra confirm the successful ligand exchange from the native ligands to iodide in the CdSe QD dispersions and allow to unambiguously prove the incorporation of the organic materials into the hybrid thin films. The high quality PMIRRAS spectra also reveal some changes in the vibrational peak positions (Table 9.1) and peak intensities between the spectra of the purely organic and the hybrid thin films. These changes

provide valuable information about the possible binding scenario, which will be discussed in Section 9.6.

9.3 X-ray diffraction

Further information about the incorporation of the AEs in between the QDs and the resulting changes in the structural organization was derived from grazing-incidence small-angle X-ray scattering (GISAXS) measurements. They were carried out on CdSe/nat, CdSe/I⁻, and CdSe/I⁻/AE films on glass, silicon, and gold-coated substrates. These different substrates were required for the other characterization methods and a possible influence of the substrate on the structure formation was investigated. Figure 9.3a shows an exemplary reciprocal space map of a CdSe/I⁻/AE 1 hybrid film on silicon. It exhibits a strong signal around the specular reflection which decays toward larger absolute q values. At $q \approx 0.1 \text{ \AA}^{-1}$, a broad scattering ring is observed and at $q \approx 0.2 \text{ \AA}^{-1}$, a second, weaker ring is detected. These rings are the result of constructive interference between X-rays scattered from neighboring QDs. Yet, sharp Bragg peaks, as found for less complex systems before, are missing [293, 294]. Thus, some short-range ordering with an average center-to-center distance is found for the sample, but a lack of long-range ordering can be concluded from the missing Bragg peaks.

The reciprocal space maps of the other films, namely the CdSe/nat, CdSe/I⁻, and CdSe/I⁻/AE 2 films, have the same general shape, independent of the substrate. Figure 9.3b demonstrates the absence of an influence of the substrate on the structure formation for the CdSe/I⁻ films. Normalized, horizontal cuts along q_{xy} through the reciprocal space maps, averaged for $0.02 \text{ \AA}^{-1} < q_z < 0.03 \text{ \AA}^{-1}$, are shown for different CdSe/I⁻ films on gold, silicon and glass substrates, respectively. They all show a maximum at $q_{xy} = 0.12 \text{ \AA}^{-1}$ which indicates similar characteristic distances in these samples. The peaks are differently pronounced

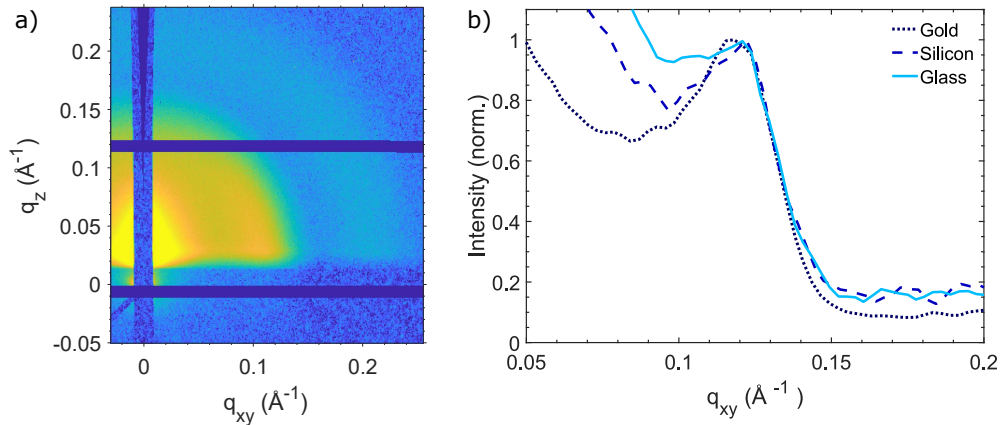


Figure 9.3: GISAXS data for structure analysis. a) Reciprocal space map of a CdSe/I⁻/AE 1 hybrid film on silicon. b) Normalized averaged intensity for $0.02 \text{ \AA}^{-1} < q_z < 0.03 \text{ \AA}^{-1}$ as function of the in-plane scattering vector q_{xy} for CdSe/I⁻ films on different substrates. Modified from Ref. [290].

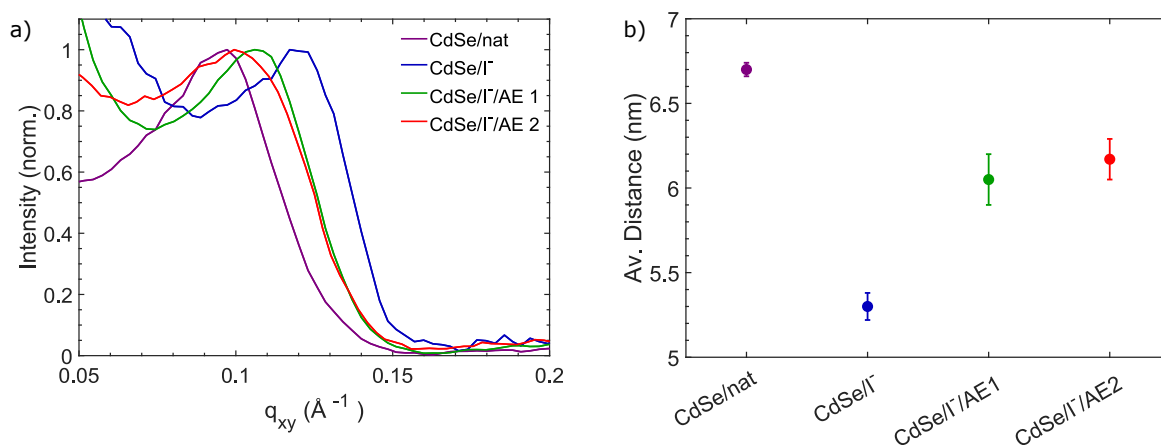


Figure 9.4: GISAXS data for structure analysis. a) Line cuts with averaged intensity for $0.02 \text{ \AA}^{-1} < q_z < 0.03 \text{ \AA}^{-1}$ as function of the in-plane scattering vector q_{xy} for the different samples. b) Extracted average distances between the centers of neighboring QDs. The error bars are derived from measurements of several samples on different substrates. Modified from Ref. [290].

in the different samples. However, this is not characteristic for the substrates but depends on the specific sample, probably due to small differences in the preparation conditions and different thicknesses. Thus, as expected due to the drop-casting method, an influence of the substrate on the structure formation was not found.

In contrast, significant differences in the scattering ring positions were found for the different thin films, as illustrated in Figure 9.4a by horizontal cuts through the reciprocal space maps. The peak position for the CdSe/I⁻ film is clearly at the largest q_{xy} value and the one of the CdSe/nat film is at the smallest q_{xy} value, while the two hybrid films show peaks in between. The high q_{xy} side of these peaks was fitted by a Gaussian to extract the peak positions, which were then converted to an average center-to-center distance (Figure 9.4b) as described in Section 4.1. The smallest average center-to-center distance of 5.3 nm was found for the CdSe/I⁻ film. This distance matches the diameter of the CdSe QD cores, determined by UV-vis spectroscopy (cf. Section 3.3.2), markedly well, which implies that the QDs are in direct contact in these films. For the CdSe/nat films, in contrast, an average center-to-center distance of 6.7 nm was extracted, indicating that, on average, a gap of 1.4 nm in between two neighboring QDs exists. Exactly the same gap size has been reported for oleic acid capped PbS QDs films [295]. This gap between the cores results from the native ligand shell of the QDs. The other ligands of the QDs investigated here, namely hexadecylamine, trioctylphosphineoxide, and trioctylphosphine have (slightly) shorter chain lengths than oleate and hence do not increase the gap size.

The two hybrid films show similar average QD center-to-center distances of 6.1 nm and 6.2 nm for films with AE1 and AE2, respectively, which can be explained by the similar structure of the two molecules. This results in an average gap of 0.8 nm to 0.9 nm between neighboring QDs in these films, which fits the size of one AE molecule. Thus, the GISAXS

data indicate that the AE molecules are incorporated in between the QDs and a connection of neighboring QDs by the AEs seems likely due to the carboxylate groups on both sides of the molecule.

9.4 Optical spectroscopy

The optical properties and photophysics of the hybrid organic-inorganic systems are of great interest. They are the basis for many promising effects of hybrid materials and can give insights into the electronic coupling between the components [24, 72, 296]. In Figure 9.5, UV-vis absorbance spectra of the thin films on glass are presented. Again, first the spectra of the single component films are analyzed, followed by the hybrid films. The CdSe/nat film (Figure 9.5a) exhibits a typical absorbance spectrum for QDs, with a sharp first transition at 2.01 eV, followed by several, partially resolved transitions at higher energies. The thin film spectrum closely resembles the absorbance spectrum of the QDs dissolved in hexane (see Section 3.3.2). The resolved transitions are labeled according to the literature as $1S(e)-1S_{3/2}(h)$ at 2.01 eV, $1S(e)-2S_{3/2}(h)$ at 2.11 eV, $1P(e)-1P_{3/2}(h)$ at 2.30 eV, and $1S(e)-2S_{1/2}(h)$ at 2.45 eV [142, 145, 216]. The CdSe/I⁻ film displays a similar spectrum (Figure 9.5b) with only slight modifications resulting from the changed polarizability of the environment due to the iodide capping instead of the organic ligands. The spectrum is slightly broadened and red-shifted, with the $1S(e)-1S_{3/2}(h)$ transition now appearing at 1.99 eV.

The absorbance spectra of the two neat AE films (Figure 9.5c,d) show only very broad features above 2.5 eV without any clearly pronounced peaks, similar to the AE absorption in solution (see Section 3.3.1). The broad appearance most likely results from the absorption of different rotamers in the thin films, which all have slightly different energy landscapes and hence different transition energies [297]. The spectra of the hybrid films (Figure 9.5e,f) can be

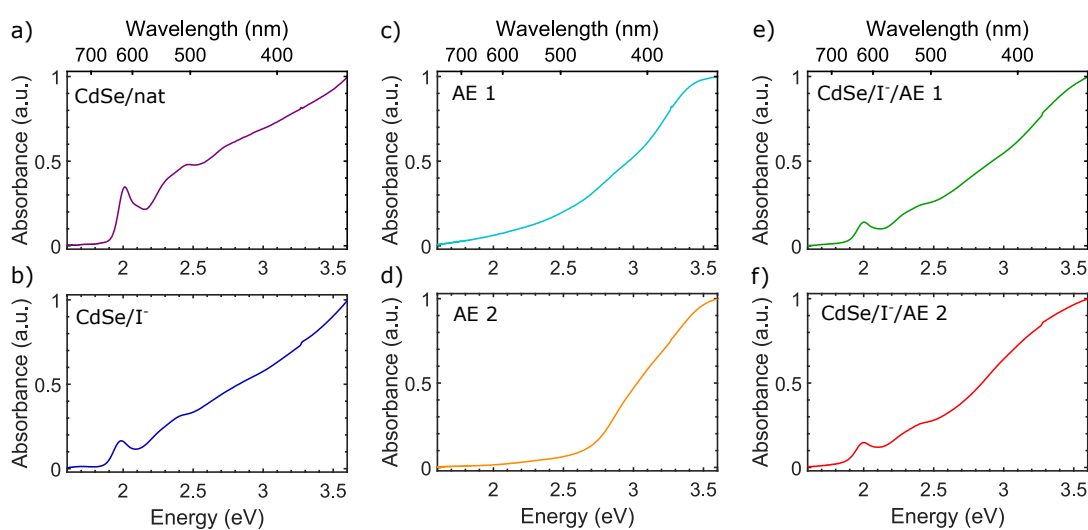


Figure 9.5: Normalized absorbance spectra of the hybrid organic-inorganic semiconductor films and the neat reference films.

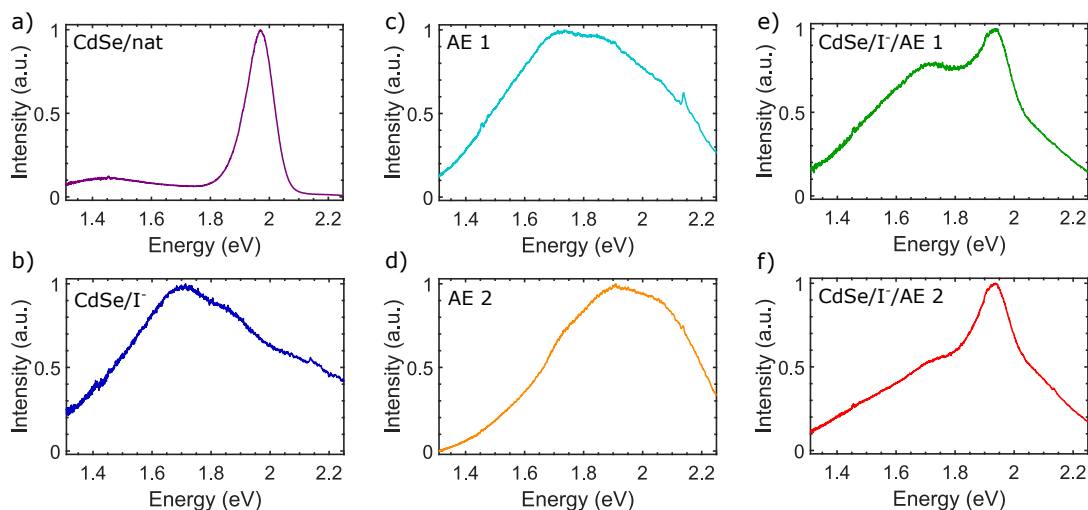


Figure 9.6: Normalized PL spectra of the hybrid organic-inorganic semiconductor films and the neat reference films, excited with a wavelength of 532 nm (2.33 eV).

described as a superposition of the slightly shifted absorption spectra of the neat component films. The first QD absorption peak is now found at 2.00 eV. This indicates that the organic as well as the inorganic materials are present in the hybrid films and the slight shifts can be again attributed to the changed environment. However, the absence of larger changes in the absorbance spectra gives a first indication that strong electronic coupling between the CdSe QDs and the AE molecules is unlikely.

Next, the PL spectra of the different films are analyzed, which are presented in Figure 9.6. They were recorded under continuous-wave laser excitation with a wavelength of 532 nm (2.33 eV). In contrast to the UV-vis absorbance spectra, a strong difference between the CdSe/nat film PL spectrum (Figure 9.6a) and the CdSe/I⁻ film PL spectrum (Figure 9.6b) is apparent. The former shows a characteristic, sharp, and strong QD emission around 1.97 eV, thus, with a Stokes shift of 40 meV. The latter shows only weak and substantially broader emission without a sharp maximum. This most likely results from a drastically increased number of surface trap states in the CdSe/I⁻ QDs compared to the CdSe/nat QDs, since no organic ligands are present to saturate these surface states. This results in an increased PL quenching in these samples [146, 298, 299]. The fact that the remaining PL is broad and red-shifted is also consistent with surface trap states with energies within the band gap. The electrons and holes trapped therein can also recombine radiatively, but generally with a small quantum yield [146, 206]. The emission spectra of the two neat AE films (Figure 9.6c,d) are also broad and unstructured as expected due to the different rotamers in the films [213, 297].

The PL spectra of the two hybrid films (Figure 9.6e,f) show several interesting features. First, they are clearly not a superposition of the spectra of the CdSe/I⁻ film and the respective AE film, but instead show a sharper peak at 1.93 eV. Concluding from its position and sharpness, this peak is assigned to QD emission from untrapped electrons and holes, resulting in a Stokes shift of 70 meV for the QDs in these samples. The appearance of this sharp QD photoluminescence in the hybrid films indicates that at least some of the QDs have well

passivated surfaces. The surface trap state passivation in these samples is most likely realized by the binding of AE molecules. Hence, the native, electronically isolating ligands can be replaced by the shorter, semiconducting AE molecules without losing the QD emission. Yet, the weaker overall emission indicates that the passivation of the CdSe QDs by the AEs is less effective than by the native ligands. There is, additionally to the sharp peak, a broader signal visible in the PL spectra of the hybrid films, which is centered at smaller energies. This resembles the emission spectra of the neat AE films and the neat CdSe/I⁻ film and could stem from one or the other.

The PL spectrum of a CdSe/I⁻/AE1 film has been reported before in Ref. [213]. The spectrum shown there exhibits overall a similar shape and similar peak positions, but has a stronger pronounced and sharper peak at smaller energies. One reason could be a larger organic fraction in their films and a slightly different preparation method. For very specific points in their CdSe/I⁻/AE1 films, they additionally reported periodic fluorescence variations which have been explained by energy transfer between the QDs and the AE1 molecules [213]. Such variations could not be found in the PL measurements presented here, probably due to a larger spot size and since no specific points were selected. Thus, the steady-state optical spectra do not provide any indications for strong electronic coupling or charge or energy transfer in the hybrid samples.

9.5 Transient absorption spectroscopy

The above-shown steady-state spectra provide the basis for the realization and interpretation of the TA measurements presented in the following, which were performed to obtain time-resolved information about possible transfer processes. From the absorbance maxima of the thin films, the pump wavelengths for the TA measurements were chosen. First, the samples were excited at 2.00 eV ($\lambda_{\text{exc}} = 620$ nm), hence at the 1S(e)-1S_{3/2}(h) transition of the QDs, to selectively excite the QDs. Consequently, further measurements were performed with excitation at 3.54 eV ($\lambda_{\text{exc}} = 350$ nm), thus around the absorbance maximum of the AEs, where both components can be excited. For the measurements with $\lambda_{\text{exc}} = 620$ nm, the excitation densities were kept below 0.37 electron-hole pairs per QD to avoid many-particle interactions. Details about the excitation density calculation and the values for the measurements with $\lambda_{\text{exc}} = 350$ nm are given in Appendix E.2. As for the steady-state measurements, first the TA data of the neat reference films is analyzed below, followed by the hybrid samples.

For the neat AE films, no TA signal was obtained under $\lambda_{\text{exc}} = 620$ nm excitation, since these films do not exhibit significant absorption at this wavelength. In contrast, as expected, strong TA signals were detected from the CdSe/nat and CdSe/I⁻ samples. In Figure 9.7a, an exemplary TA map of a CdSe/nat sample is shown, with long-lived negative and positive features. A TA map of a CdSe/I⁻ film with similar features can be found in Appendix E.3. The features do not change their position with time but remain at the same wavelengths. This

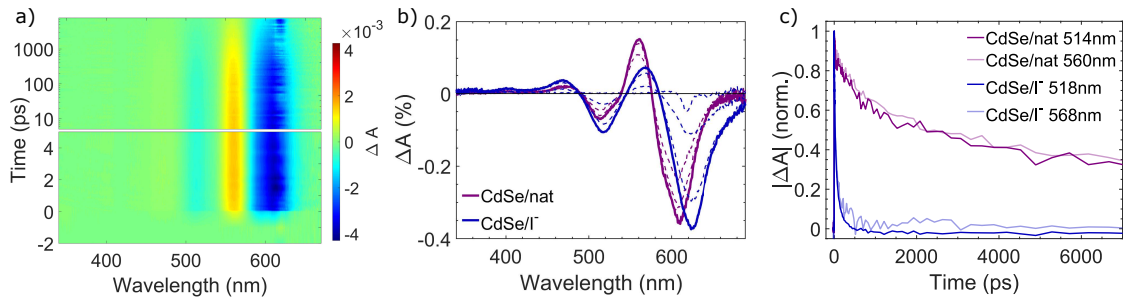


Figure 9.7: TA data of the neat CdSe QD samples excited with $\lambda_{\text{exc}} = 620$ nm. a) TA map of a CdSe/nat sample. b) TA spectra of a CdSe/nat and a CdSe/I⁻ sample, averaged from 0.5 ps to 1 ps (solid line), 5 ps to 10 ps, 50 ps to 100 ps, and 500 ps to 1000 ps (dashed lines), demonstrating the consistency of the spectral shape. At long times, scattered pump light disturbs the spectra around 620 nm. c) Timetraces along the negative feature around 515 nm and the positive feature around 565 nm, all averaged over 20 nm around the wavelength position given in the legend. The overlapping timetraces of the two features indicate their common origin.

can also be seen from the TA spectra presented in Figure 9.7b, which are obtained from the maps by averaging horizontal cuts in a certain time interval. These TA spectra only decrease in intensity with time but do not change their shape. This is an indication for only one excited species that just decays back to the ground state. The shape of the TA spectra of the CdSe/nat and CdSe/I⁻ films is similar. They are only slightly shifted, corresponding to the shifted steady-state absorption of the films. The TA spectra are dominated by a bleach around 620 nm, thus at the first absorption and emission maximum of the films. Toward smaller wavelengths, a positive feature around 565 nm follows, again followed by a second negative feature around 515 nm and a weak positive feature around 470 nm. Based on the spectral positions and the literature, the bleaches around 620 nm and 515 nm can be attributed to the filling of the 1S(e) state by excited electrons (see Figure 3.5) and, for the former, also to stimulated emission [142, 145, 300]. The positive features around 565 nm and 470 nm and the negative shoulder at 530 nm are explained by biexciton and Stark effects, which produce first and second derivative-like features of the steady-state absorption spectrum (cf. Section 4.5) [142, 243].

By averaging vertical cuts through the TA maps in a small wavelength region, timetraces of the decay of certain features can be generated. They are presented in Figure 9.7c and clearly demonstrate the different lifetimes in the two samples. Here, the absolute, normalized value of the TA signal is shown to allow for an easy comparison of the different curves. By this, the overlapping timetraces for different features in the TA data of one sample, e.g., the bleach around 515 nm and the PIA around 565 nm, are evident, which indicates that they have a common origin, consistent with the assignment above. In contrast, the features of the CdSe/I⁻ sample decay much faster than the features of the CdSe/nat sample, as already visible from the spectra at different times in Figure 9.7b. This can be rationalized by the different surface passivation in the two samples and consequently differing number of trap states. These trap states can lead to a faster relaxation back to the ground state, which is

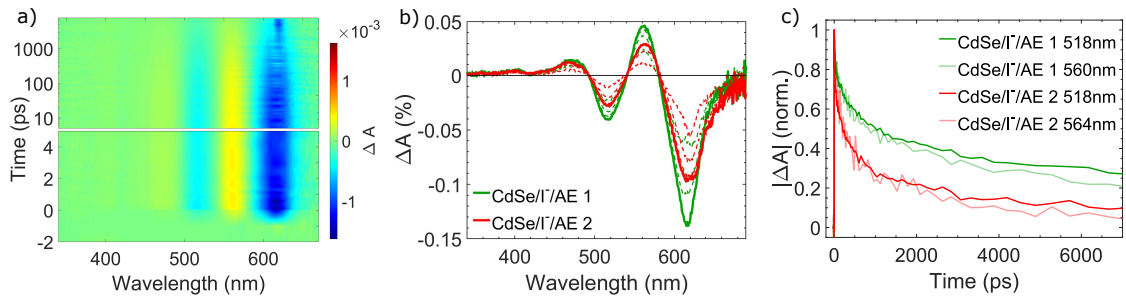


Figure 9.8: TA data of the hybrid samples excited with $\lambda_{\text{exc}} = 620$ nm. a) TA map of a CdSe/I⁻/AE1 film. b) TA spectra of a CdSe/I⁻/AE1 and a CdSe/I⁻/AE2 sample, averaged from 0.5 ps to 1 ps (solid line), 5 ps to 10 ps, 50 ps to 100 ps, and 500 ps to 1000 ps (dashed lines), demonstrating the consistency of the spectral shape. At long times, scattered pump light disturbs the spectra around 620 nm. c) Timetraces along the negative feature around 515 nm and the positive feature around 565 nm, all averaged over 20 nm around the wavelength position given in the legend. The mostly overlapping timetraces of the two features indicate their common origin.

clearly the case for the CdSe/I⁻ sample. Furthermore, the multi-exponential decay of the features in both samples has previously been attributed to a differing number and type of trap states on different QDs in each sample [145].

In Figure 9.8, TA data of the hybrid samples with $\lambda_{\text{exc}} = 620$ nm are presented. In Figure 9.8a, the TA map of a CdSe/I⁻/AE1 film is shown which closely resembles the one in Figure 9.7a and the ones shown in Appendix E.3 for the other samples. The TA maps of the hybrid samples are clearly dominated by signals assignable to the CdSe QDs and the spectra of the two hybrid samples, shown in Figure 9.8b, are extremely similar to each other and the spectra in Figure 9.7b. Again, no change in the spectral shape is observed, and the assignment of the features is the same as for the neat QD samples. The timetraces in Figure 9.8c show again similar, multi-exponential dynamics for the different features in the spectrum of one sample, with only minor deviations on long timescales. The TA signal of the CdSe/I⁻/AE2 film decays faster than the TA signal of the CdSe/I⁻/AE1 film, and both signals decay faster than the signal of the CdSe/nat sample, but slower than the signal of the CdSe/I⁻ sample. Following the argumentation above, this can be explained by fewer surface trap states in the hybrid films than in the CdSe/I⁻ film but more than in the CdSe/nat film, which is consistent with the PL results. Hence, for 620 nm wavelength excitation, the TA data of the hybrid films are dominated by the QD contributions without clear impact of the AEs besides their surface passivation effect.

Consequently, further measurements with $\lambda_{\text{exc}} = 350$ nm were performed to directly excite the AEs and to examine the influence on the photophysics of the hybrid systems. Higher pump fluences were required for these measurements as detailed in Appendix E.2. The TA data of the neat AE films is displayed in Figure 9.9. Again, an exemplary TA map of an AE1 film is shown in Figure 9.9a, exhibiting a bleach around the steady-state absorption maximum at 350 nm and a broad ESA starting at ~ 420 nm and reaching until the high wavelength end of the measured spectral region. The TA map of an AE2 film is presented in Appendix E.3

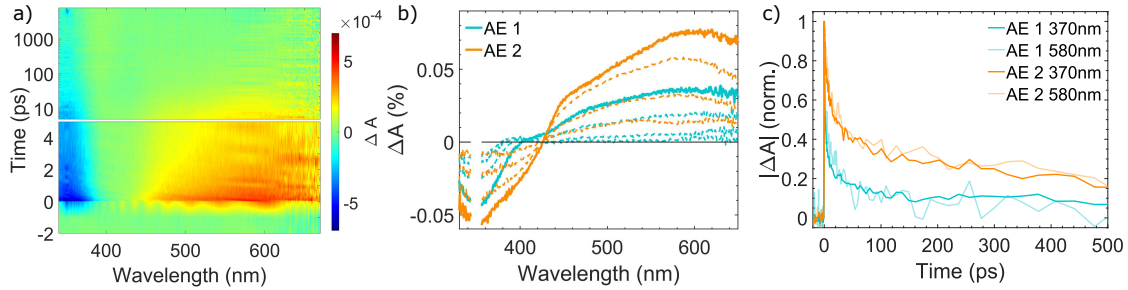


Figure 9.9: TA data of the neat AE films excited with $\lambda_{\text{exc}} = 350$ nm. a) TA map of an AE 1 sample. b) TA spectra of an AE 1 and an AE 2 sample, averaged from 0.5 ps to 1 ps (solid line), 5 ps to 10 ps, 50 ps to 100 ps, and 500 ps to 1000 ps (dashed lines), demonstrating the consistency of the spectral shape. c) Timetraces along the negative feature around 360 nm and the positive feature around 580 nm, all averaged over 30 nm around the wavelength position given in the legend. The overlapping timetraces of the two features indicate their common origin.

and exhibits similar features. The negative feature is assigned as GSB due to the spectral position and the broad, unstructured ESA can be explained by different, fixed rotamers in the films that exhibit different energy landscapes and consequently different transition energies. The TA spectra in Figure 9.9b show little evolution for both samples, indicating again a common decay of all features back to the ground state. This is verified by the timetraces of the GSB and the ESA in Figure 9.9c that overlap in each sample. Overall, the signal of the AE 1 film decays faster than the signal of the AE 2 film.

Resulting from the changed excitation wavelength, a modified photophysics of the neat QD samples is expected, since now also higher transitions can be excited. This expectation is verified by the TA data shown in Figure 9.10. The TA map of the CdSe/I⁻ film in Figure 9.10a clearly shows some evolution on very short timescales. This evolution can be also followed in the TA spectra in Figure 9.10b. Here, the solid lines depict the spectra at short delay times, averaged from 0.1 ps to 0.5 ps, while the dashed lines are the spectra averaged from 5 ps to 10 ps, which are almost identical to the spectra after 620 nm excitation (cf. Figure 9.7b). The spectra at short delay times exhibit new features, namely a PIA around 650 nm, a shift of the PIA found before at ~ 565 nm toward longer wavelengths, and negative features

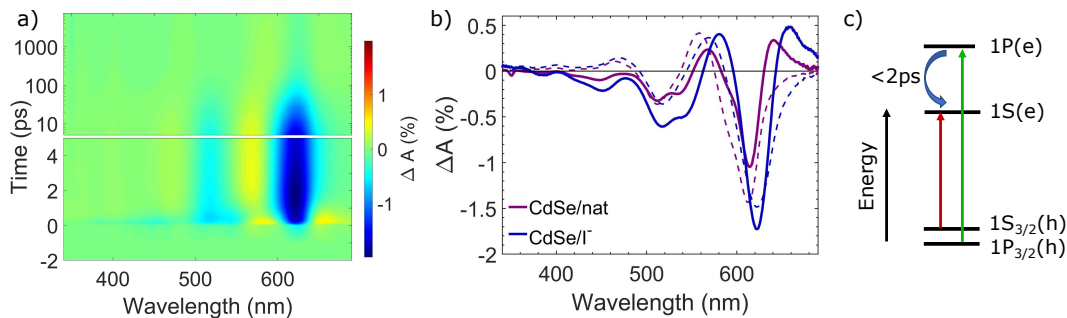


Figure 9.10: TA data of the CdSe QD samples excited with $\lambda_{\text{exc}} = 350$ nm. a) TA map of a CdSe/I⁻ sample. b) TA spectra of a CdSe/nat and a CdSe/I⁻ sample, averaged from 0.1 ps to 0.5 ps (solid line) and from 5 ps to 10 ps (dashed lines), demonstrating the ultrafast change of the spectral shape. At long times, the spectra are similar to the ones obtained with $\lambda_{\text{exc}} = 620$ nm (cf. Figure 9.7). c) Electron relaxation scheme.

around 540 nm and 450 nm. These new features are explainable by the fact that electrons were excited to higher states, e.g., the $1P(e)$ state. As a result, transitions to this state are bleached at short delay times, as indicated in Figure 9.10c for the $1P(e)-1P_{3/2}(h)$ transition. This transition is located at a wavelength of 540 nm (2.3 eV), thus explaining the bleach found at this wavelength. The PIA at 650 nm is also related to electrons occupying the $1P(e)$ state and results from the biexciton effect (cf. Section 4.5.2) [145]. The bleach around 450 nm is probably a result of electrons that are excited to even higher states. The apparent shift of the PIA around 565 nm at short delay times is most likely related to the new bleach on the short wavelength side, accompanied by a decreased $1S(e)$ bleach on the long wavelength side, as many electrons are still in higher states. The short lifetime of these features illustrates the rapid relaxation of the electrons toward the $1S(e)$ state.

Finally, as for the measurements with $\lambda_{\text{exc}} = 620$ nm, the TA data of the hybrid thin films with $\lambda_{\text{exc}} = 350$ nm is clearly dominated by the QD signals, see Appendix E.3 for the TA maps. However, at short wavelengths and short delay times, small differences are visible between the TA spectra of the hybrid films and the neat QD films around the bleach of the AEs. These TA spectra are shown in Figure 9.11a and the bleach region of the AEs is indicated by a black arrow. This change in the spectrum is clearly visible for the CdSe/I⁻/AE 2 film, while it is only weakly observable for the film containing AE 1. Overall, the influence of the AEs on the spectral shape is too small to extract meaningful changes in the time constants by GA. Nevertheless, to get an impression of the dynamics of the AE bleach feature, normalized timetraces of the hybrid and reference films, averaged from 355 nm to 385 nm, are shown in Figure 9.11b. The CdSe QD reference films show a weak positive signal in this wavelength region that again decays slower for the CdSe/nat film than for the CdSe/I⁻ film. The two AE films exhibit a bleach in this wavelength region, as seen before. Finally, the signal and the dynamics of the two hybrid films can be approximately described as a superposition of

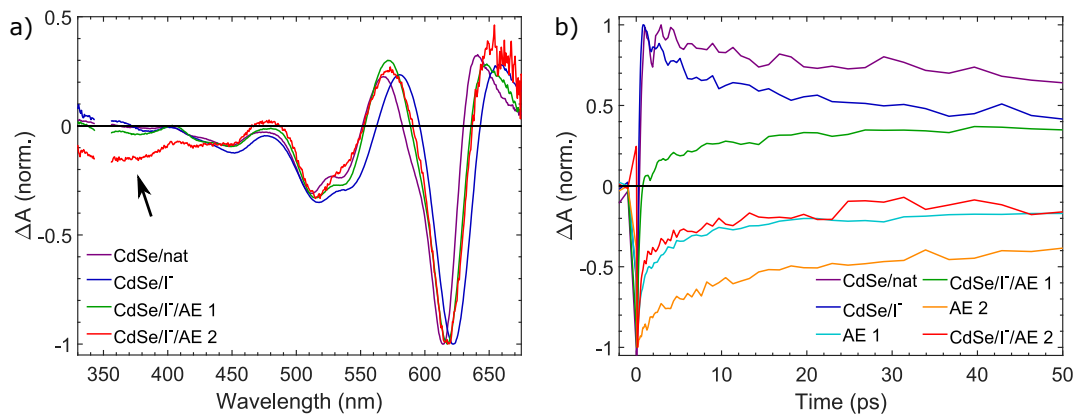


Figure 9.11: TA data of the hybrid and reference samples excited with $\lambda_{\text{exc}} = 350$ nm. a) TA spectra averaged from 0.1 ps to 0.5 ps. The black arrow indicates the spectral region of the AE bleach, where differences in the spectra appear. b) Timetraces averaged from 355 nm to 385 nm, thus around the bleach of the AEs. Modified from Ref. [290].

the signals of the neat reference films without clear deviations. Thus, no clear signs of charge or energy transfer were found.

9.6 Discussion

Taking all the above described results from the different characterization methods together, a scenario for the organization and interaction of the organic and inorganic components in the hybrid films can be developed. Starting from the structural results obtained by the GISAXS measurements, an idea of the organization can be obtained. The differences found in the distance between adjacent QDs for the different films indicate modified QD surfaces. In the CdSe/nat films, the QD cores have a relatively large gap in between each other due to the native ligands. For the CdSe/I⁻ films, this gap completely vanishes, explainable by the absence of organic ligands. In contrast, a gap of approximately 1 nm was found for the CdSe/I⁻/AE1 and CdSe/I⁻/AE2 films, which indicates the structural similarity and an incorporation of the AE molecules as ligands in between the QDs. The reappearance of the sharp QD PL in the hybrid films, in contrast to the CdSe/I⁻ films, further indicates an actual binding of the AEs to the QDs. This sharp PL can be explained by a passivation of surface trap states of the QDs, which quench the PL, by the binding of AE molecules.

A more detailed picture of the exact binding motive can be extracted from the above presented PMIRRAS spectra (compare Section 9.2). The sharp peaks around 1520 cm⁻¹ and 1180 cm⁻¹, assigned to the aromatic ring stretching mode and the tertiary amino C-N stretching mode, respectively, are clearly present in all AE containing films and do not change significantly when going from the neat AE films to the hybrid CdSe/I⁻/AE films. This demonstrates that these groups are not directly involved in the binding event and that these peaks can be used as internal references in the spectra. This is shown in Figure 9.12, where all spectra are normalized at the aromatic ring stretching mode around 1520 cm⁻¹. The resulting nearly perfect overlap and intensity match of the tertiary amino peak at 1183 cm⁻¹ in the AE1 containing samples confirms the usability of these peaks as internal reference.

First, the remaining peaks of the AE1 containing samples are analyzed. Most prominently, the intensity of the peaks assigned to the carboxylate group vibrations (marked by blue pentagons in Figure 9.12) is clearly decreased if the AE1 molecules are incorporated in the hybrid film compared to the neat AE1 film. Additionally, as already mentioned above, an increased intensity of the peak at 1707 cm⁻¹ is found for the spectrum of the CdSe/I⁻/AE1 film, which might be assigned to C=O group vibrations. For this peak, however, also an influence of the iodide capped QDs cannot be excluded. Nevertheless, by considering these two changes and under the assumption that the peaks of the free carboxylate groups disappear if they are bound to CdSe QDs [292], the overall binding probability of the carboxylate groups of the AE1 molecules to the QDs can be estimated. The peak around 1395 cm⁻¹ was chosen to fit because it is clearly pronounced and does not have the background from aromatic ring vibrations like the peak around 1600 cm⁻¹. From a single Gaussian fit of this peak in the

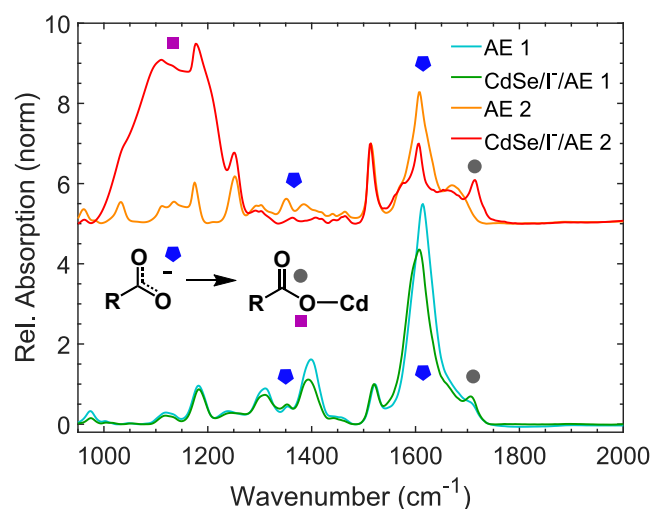


Figure 9.12: PMIRRAS spectra from Figure 9.2 of the AE containing films, normalized to the peak of the aromatic ring stretching mode around 1520 cm^{-1} . The spectra of the AE 2 containing films are vertically offset for clarity. The inset depicts the proposed binding model and the colored symbols mark the peaks assigned to the vibrations of the involved groups. Modified from Ref. [290].

CdSe/I⁻/AE 1 film spectrum and the neat AE 1 film spectrum, an area and hence intensity reduction of $\sim 30\%$ was obtained for the CdSe/I⁻/AE 1 film. With the fact that each AE 1 molecule contains eight carboxylate groups, this implies that, on average, more than two carboxylate groups per molecule bind to a CdSe QD.

With the spectra of the AE 2 containing samples, the binding scenario can be refined, as shown in the inset of Figure 9.12. Clearly pronounced differences between the spectra of the neat AE 2 film and the hybrid CdSe/I⁻/AE 2 film are visible as detailed above. The sharp peak at 1714 cm^{-1} that appears in the hybrid film can be assigned to a C=O group vibration, which suggests a monodentate binding. This is again supported by the decrease in intensity of the peaks assigned to the free carboxylate group vibrations in the hybrid film. Besides, the prominent, broad peak around 1130 cm^{-1} fits to this scenario as it is located in a wavenumber region of ether C-O stretching vibrations [101]. Thus, it might stem from the monodentate binding of the AE molecules over one oxygen atom to a cadmium atom [205]. The remarkably broad appearance might be explained by different spatial configurations of different AE molecules with respect to the QDs, as well as different binding sites.

The quantification of the number of bound carboxylate groups per AE 2 molecule is more challenging than for the AE 1 molecules, since the carboxylate peaks between 1300 cm^{-1} and 1400 cm^{-1} are less pronounced and not suitable to fit. Hence, the wavenumber region from 1550 cm^{-1} to 1750 cm^{-1} , containing carboxylate and aromatic ring vibrations, was fitted by multiple Gaussians, see Figure 9.13. The black Gaussian with identical parameters was fixed in the fits shown in the two subfigures, as this peak is assigned to an aromatic ring stretching vibration, which does not change upon binding. The broad peak around 1670 cm^{-1} is assigned to a C=C stretching mode and fitted by a similar Gaussian for both spectra. As stated

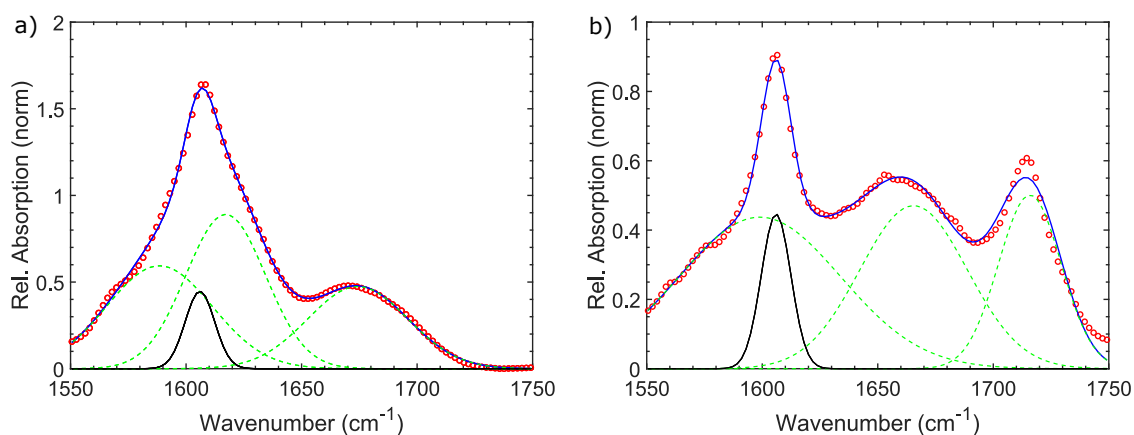


Figure 9.13: Gaussian fits to the PMIRRAS spectra of a) a neat AE2 film and b) a CdSe/I⁻/AE2 film in the wavenumber region from 1550 cm⁻¹ to 1750 cm⁻¹. Both spectra are normalized to the aromatic ring stretching vibration peak at 1513 cm⁻¹ (compare Figure 9.12). The red circles symbolize the measured data points, the blue curve is the overall fit that consists of the Gaussians shown by the green dashed and black lines. The black Gaussian was fixed in both fits. For details see text. Modified from Ref. [290].

above, the Gaussian around 1714 cm⁻¹ fits the peak of the C=O vibration. The remaining peaks are attributed to the carboxylate group vibrations and the area beneath these fitted Gaussians was used to estimate the intensity of these vibrations. With this method, an intensity reduction of $\sim 50\%$ of the peaks assigned to the carboxylate vibrations in the hybrid film compared to the neat AE2 film is concluded. This implies that, on average, two of the four carboxylate groups per AE2 molecule bind to the QDs. This number might be underestimated if there are other weak peaks within the fit range that should be assigned to other vibrations. Considering the structure of the AE2 molecule, a connection of neighboring QDs by AE2 molecules is most realized, which is consistent with the found gap of ~ 1 nm between neighboring QDs. The similar number of bound carboxylate groups, the similar molecular structure and the similar found gap between the QDs in the CdSe/I⁻/AE1 films suggest a connection of neighboring QDs by AE1 molecules, too.

The direct binding of the AE molecules to the CdSe QDs renders charge or energy transfer processes between the two components likely. TA spectroscopy was used to analyze the dynamics in the samples and find indications for these processes. After band-edge excitation of the QDs in the different samples ($\lambda_{\text{exc}} = 620$ nm), differences in their relaxation dynamics were found. The TA data from several samples of each kind and from measurements with slightly varying excitation densities were globally fitted with a parallel model with two species (compare Section 4.5.3). The extracted average decay time constants are summarized in Table 9.2. The CdSe/I⁻ films clearly exhibit the fastest time constants. The CdSe/nat films feature the slowest decay time constants and the CdSe/I⁻/AE films slightly faster ones. The fraction of the signal decaying with τ_2 follows the same trend, being largest for the CdSe/nat films, followed by the CdSe/I⁻/AE1 and CdSe/I⁻/AE2 films.

9. CdSe quantum dots coupled with aryleneethylenes

Table 9.2: Time constants extracted from GA of the TA data of the QD containing samples after 620 nm wavelength excitation.

| | CdSe/nat | CdSe/I ⁻ | CdSe/I ⁻ /AE 1 | CdSe/I ⁻ /AE 2 |
|----------|----------|---------------------|---------------------------|---------------------------|
| τ_1 | 250 ps | 15 ps | 250 ps | 170 ps |
| τ_2 | 10 ns | 0.1 ns | 7 ns | 3 ns |

These differences can, however, be explained simply by differences in the surface passivation of the QDs due to the different ligands without the need to involve transfer processes. The QDs with the native ligands have the best passivated surfaces and, hence, the smallest trap state density. This increases the lifetime of the electron-hole pair, which is also consistent with the strong PL signal. The AE 1 molecules seem to passivate the surface better than the AE 2 molecules. This can be rationalized by the higher number of carboxylate groups per molecule and is consistent with the slightly higher number of bound groups per molecule for AE 1 found above. The absence of organic ligands in the CdSe/I⁻ films is clearly reflected by the very fast decay times of the TA signal and by the lack of strong PL due to the domination of the decay via trap states.

Under 350 nm wavelength excitation, the TA spectra of the QD containing films exhibit an initial, fast intraband relaxation of the excited electrons toward the 1S(e) state within 1.5 ps [242]. There is no significant difference in this decay time found for the different samples. No unique time constants for the decay on longer time scales could be extracted from the TA data of the hybrid CdSe/I⁻/AE films, since too many different species are involved. Additionally, both the signals of the QDs and the AEs decay non-exponentially and the AEs show only relatively weak and broad signals compared to the QDs. However, the possibility to approximately describe the TA signal of the hybrid films by a superposition of the TA signals of the neat compound films, as shown above, questions the presence of charge or energy transfer processes between the two compounds.

Taken together, the presented results provide no indications for an electronic coupling of the AEs and the QDs. One possible explanation is that the TA signal of the AEs is simply too weak to draw sound conclusions, but also the other employed methods do not hint toward charge or energy transfer. Their absence could be explained by an unfavorable energy level alignment between the QDs and the AEs. A type I alignment might be realized (compare Section 2.3.3), which would result in confinement of excited electrons and holes in the QDs. Additionally, energy transfer between different AE rotamers could out-compete charge or energy transfer to the QDs, maybe due to an unfavorable orientation or a lack of frontier orbital overlap. These suggestions are, however, difficult to verify, as a detailed and exact calculation of the energy level alignment, the orientation, and the binding of the compounds in a solid film is almost impossible. It would need to include different AE rotamers in a fixed geometry, which would result in always different energy landscapes as deducible from the absorption and emission properties of the neat AE films.

9.7 Conclusion

In summary, in this chapter, the short-range organization and photophysical properties of complex hybrid thin films composed of organic and inorganic semiconductors, namely AE derivatives and CdSe QDs, were investigated. With the structural information obtained from GISAXS measurements, the emission properties measured by PL spectroscopy and the vibrational properties examined by PMIRRAS spectroscopy, the short-range organization and the binding of the AEs to the QDs was demonstrated. By a detailed analysis of the PMIRRAS spectra, a monodentate binding scenario and a connection of neighboring QDs by AE molecules was derived. This information about the organic-inorganic interface is crucial and frequently missing for such hybrid materials. Despite this chemical binding, no indication for charge or energy transfer could be found by the performed TA measurements. This might be due to an unfavorable energy level alignment. The changed QD decay dynamics visible in the TA data are explainable by differences in the surface trap state passivation, in agreement with the PL data. The good passivation and binding properties render the AEs promising candidates for hybrid materials with other QDs. Finally, PMIRRAS was shown to be a powerful technique to study binding events in complex hybrid thin films with possible application in the investigation of other new and promising hybrid materials.

10. Conclusion and Outlook

This chapter summarizes the main findings of this thesis and provides an outlook for further research. Overall, several heterogeneous, coupled systems that contain OSCs were studied in this work. The main objective of this thesis was to obtain a better understanding of the fundamental properties of such systems, as they promise new and superior functionality. A large part of this work focused on systems containing TET and PEN, two acene molecules that serve as prototypical OSCs and SF materials. Different kinds of coupling were identified to be of fundamental importance for the investigated systems and effects. For OSC materials, electronic coupling due to orbital overlap and Coulomb interaction influences the photophysical properties, including the SF process with the intermediate, coupled triplet pair state. The SF process was investigated in blends of TET and PEN with the two strong acceptors F4-TCNQ and F6-TCNNQ, and additionally, the emission from the coupled triplet pair state was studied in neat PEN thin films. Furthermore, the acenes TET and PEN functioned as donors in these blends. Depending on the donor:acceptor combination and their electronic coupling, different CT mechanisms were revealed in the mentioned blends. In PEN thin films on plasmonic arrays, the possibility of strong light-matter coupling was studied as another kind of coupling. In addition to these investigations of acene-containing systems, further investigations of hybrid organic-inorganic semiconductor samples that contain OSC molecules with anchoring groups were conducted. In such hybrid organic-inorganic semiconductor systems, the mechanical coupling via chemical bonding is critical for a defined interface and can lead to electronic coupling between the different components, which was analyzed in the last results chapter of this thesis.

10.1 Conclusion

The conclusions of the individual projects were already presented at the end of each result chapter. Here, only the main findings are summarized and connected to each other. From the purely organic donor:acceptor blends valuable insights into the different CT mechanisms were obtained. As shown in Figure 10.1, remarkably different ground state CT mechanisms were realized for the four different donor:acceptor combinations, ranging from exclusively ion pairs (PEN:F6-TCNNQ) over a coexistence of ion pairs and CTCs (PEN:F4-TCNQ) to exclusively CTCs (TET:F6-TCNNQ and TET:F4-TCNQ). Additionally, for the blends

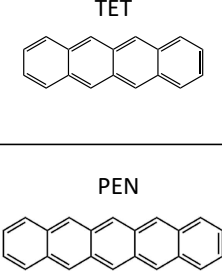
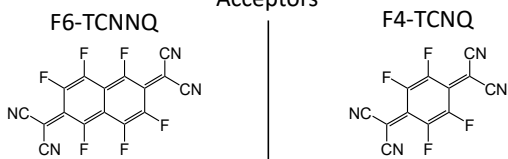
| Binding energy (eV) | PEN | TET | F4 | F6 | Acceptors | |
|---|--|-----------|-----------|---|---|---------|
| | 4.9 IP | 5.2 IP | 5.2 EA | 5.4 EA | F6-TCNNQ | F4-TCNQ |
| Donors |  | | | |  | |
| | <ul style="list-style-type: none"> • 1:1 CTC formation • Independent of the mixing ratio | | | | <ul style="list-style-type: none"> • CTC formation • Multi-donor CTCs for blends with an excess of donors | |
| <ul style="list-style-type: none"> • Ion pair formation • Independent of the mixing ratio | | | | <ul style="list-style-type: none"> • Coexistence of CTCs and ion pairs • Fraction depending on the mixing ratio | | |

Figure 10.1: Summary of the different CT mechanisms observed in the investigated donor:acceptor systems, see main text for details. In the upper left corner, the IP and EA values of the donors and acceptors, respectively, are shown (cf. Figures 5.1 and 6.1 for details). F4 and F6 abbreviate F4-TCNQ and F6-TCNNQ, respectively.

with F4-TCNQ, a mixing ratio dependence of the ground state CT was observed. Overall, several conclusions can be extracted from these results. First, in the blends of PEN with F6-TCNNQ, exclusively ion pairs were found. This can be rationalized by the fact that the EA of F6-TCNNQ is significantly larger than the IP of PEN (cf. Figure 10.1, upper left corner). Thus, a relatively large amount of energy is gained by the transfer of an integer electron from PEN to F6-TCNNQ. As a result, ion pair formation is the favored CT mechanism in PEN:F6-TCNNQ blends, independent of the electronic coupling and the mixing ratio. For all three other material combinations, which have a smaller energy offset between the IP of the donor and the EA of the acceptor, CTCs with a band gap below 1 eV were found. In the blends with TET, exclusively CTCs were detected, which implies strong electronic coupling between the donor and acceptor molecules in these blends. Interestingly, for the TET:F4-TCNQ blends, CTCs with different stoichiometry were found depending on the mixing ratio. For equimolar blends and blends with an excess of acceptor molecules, 1:1 CTCs were formed, while in blends with an excess of donor molecules multi-donor CTC were realized. This is in contrast to the TET:F6-TCNNQ blends in which only 1:1 CTCs and a pronounced phase separation into neat TET domains and 1:1 mixed domains were found. This illustrates the impact of the mixing ratio and mixing behavior on the composition of the CTCs. Finally, in the PEN:F4-TCNQ blends, the coexistence of CTCs and ion pairs was detected, with their relative amount depending on the mixing ratio. This is an excellent example of the importance of the electronic coupling and the molecular arrangement for the realization of different CT mechanisms. Moreover, this finding clarifies why different CT mechanisms, namely CTC versus ion pair formation, have been proposed for this prototypical PEN:F4-TCNQ system [35, 40, 41].

The photophysics of the different organic donor:acceptor systems was studied with a particular focus on the SF process of TET and PEN. In the equimolar blends and blends with an excess of acceptor molecules, no indication for SF was observed. However, for the blends with an excess of donor molecules, SF occurred in neat PEN and TET domains. In the TET blends, the SF process was found to compete with charge or energy transfer from TET molecules to CTCs due to the relatively small SF rate. In contrast, in the blends with PEN, only slight modifications of the time constants of the SF process were found, as PEN exhibits very fast, coherent SF. Overall, this demonstrates the robustness of the SF process to impurities, which is important for the utilization of SF in devices. For PEN, additionally the temperature dependent photoluminescence of neat thin films was investigated to gain further insight into the electronically coupled triplet pair state as an important part of the SF process. At low temperatures, a strong emission from this multiexcitonic triplet pair state was found around the predicted energy of the 0-0 transition. This finding can provide the basis for an in-depth investigation of the exact emission mechanism of this multiexcitonic state in PEN by modern quantum chemical approaches and represents another interesting effect that is enabled by electronic coupling.

Strong light-matter coupling represents another kind of coupling that offers the opportunity of influencing and further deciphering the SF process. In this thesis, strong light-matter coupling was realized in polycrystalline PEN thin films on open plasmonic arrays. This was achieved by producing silver nanoparticle arrays that support a strong and sharp SLR around the energy of the DCs of the PEN thin film. Simultaneous coupling of both DCs was accomplished and the formation of three polariton bands was observed. From the energy splitting between these polaritons, the coupling between the lower DCs and the SLR was categorized as strong while the coupling between the upper DC and the SLR was found to be in the regime between strong and weak coupling. These determined coupling strengths represented averaged values due to the polycrystallinity of the thin film. The lower polariton was found at an energy that is significantly below the energy of the lower DC of the PEN thin film in absence of a plasmonic array. Consequently, an influence of the strong light-matter coupling on the SF process can be expected, which has been predicted by calculations [57, 59, 60].

Finally, the coupling between organic and inorganic semiconductors was investigated at model systems of CdSe QDs and two different AE derivatives. For these systems, a chemical coupling via a monodentate binding of the carboxylate groups of the AE molecules to the CdSe QDs was revealed. Thus, the AE molecules can serve as connectors between neighboring QDs. Consequently, the short-range organization of the organic-inorganic interface was revealed, which is of critical importance for such hybrid systems. The binding of the AE molecules led to a good passivation of the surface trap states of the QDs. Despite the chemical coupling, no evidence of electronic coupling between the different components was observed in these model systems, illustrating the complexity of such hybrid organic-inorganic systems. In general, various materials could be combined in such hybrid organic-inorganic semiconductor systems with potential use in a variety of investigations and applications. For example, a

hybrid, coupled system composed of organic SF molecules and inorganic QDs with band gaps that are tuned to the triplet energy of the molecules could be employed to effectively harvest the formed triplets [301, 302].

In summary, fundamental structural, electronic, optical, and photophysical properties of heterogeneous, coupled systems containing OSCs were analyzed in this work. It was shown that different kinds of coupling in these systems lead to new properties that are beyond the sum of the properties of the individual components. This thesis broadens the general understanding of coupling effects in such promising hybrid materials and may contribute to their successful application in advanced devices.

10.2 Outlook

As summarized above, this thesis covers a few exemplary coupled systems which exhibit interesting and promising effects. Naturally, further questions arise from the presented results. In addition, there is an almost infinite number of possible material combinations and, thus, an even larger number of open questions and further possible investigations, which are beyond the scope of this thesis. Below, only a few possible follow-up experiments and ideas related to the different projects and chapters of this thesis are suggested.

Mixed OSCs and especially donor:acceptor systems received considerable scientific attention during the last decades. In this thesis, the CT mechanisms and photophysics of blends of TET and PEN with F6-TCNNQ and F4-TCNQ were revealed. Nevertheless, still open questions remain, and further research might focus on

- the verification of the F6-TCNNQ²⁻ dianion formation in blends with PEN after photoexcitation, which could probably be revealed by NIR spectroscopy under simultaneous electronic excitation with visible light.
- the exact emission mechanism of the coupled triplet pair state in PEN, which might be examined by calculations and time-resolved PL measurements.
- the CT mechanism and the SF process in blends of F4-TCNQ and F6-TCNNQ with hexacene as an even larger acene, for which simultaneous coherent and incoherent SF has been demonstrated [117].
- the possibility to influence the molecular arrangement and consequently the electronic coupling by the preparation conditions, which would allow to control the ground state CT mechanism and consequently the doping efficiency [36].

The successful demonstration of strong light-matter coupling in polycrystalline PEN thin films on plasmonic arrays opens the possibility for future work which might include

-
- angle-resolved extinction measurements with high angle resolution, which could be used to determine the polariton dispersion [47].
 - investigations of the molecular orientation close to the silver nanostructures, which might be realized by AFM imaging of PEN (sub-) monolayers on the plasmonic arrays.
 - TA measurements of PEN thin films on larger plasmonic arrays to experimentally examine the theoretically predicted modification of the $^1(\text{TT})$ formation rate due to the strong light-matter coupling [57].
 - investigations of strong light-matter coupling in other polycrystalline OSC thin films which show interesting excited state dynamics.

For the organic-inorganic samples of CdSe QDs coupled with AE derivatives, the short-range organization and the binding motive was revealed, which is critical information for such hybrid systems. Especially PMIRRAS was shown to be a very useful technique to investigate these properties. Yet, no electronic coupling was observed in the particular investigated samples. Further insights could be gained by

- exchanging the here investigated AE derivatives by other AE derivatives, which might result in electronically coupled systems. Especially interesting could be the investigation of AEs with spatially separated frontier orbitals [203].
- employing different sizes of CdSe QDs to modify the energy level alignment, which could render charge or energy transfer processes possible.
- conducting time-resolved PL measurements, which could help to unravel the PL signal of the hybrid samples and to detect possible energy transfer processes between the components [213].
- performing PMIRRAS and GIWAXS measurements on other coupled organic-inorganic nanostructures that show electronic coupling [72, 73].

These and further investigations can contribute to a more detailed understanding of the coupling effects between light and matter and between different components in hybrid materials, which will pave the way for their successful implementation in new, advanced devices.

Part III

Appendix

A. Tetracene:acceptor blends

In this part of the Appendix, further details about the samples and measurements discussed in Chapter 5 are presented, namely reciprocal space maps, the excitation density determination for the TA measurements and additional details to the TA data.

A.1 Reciprocal space maps

Figure A.1 presents reciprocal space maps of a neat TET film, a TET:F6-TCNNQ blend, and a TET:F4-TCNQ blend, both with an excess of TET. With the marked reference peak positions of the thin film phase and the bulk phase of TET [178], it can be concluded that the TET film consists mainly of the thin film polymorph with only a small fraction of the bulk polymorph, consistent with the XRR data shown in Figure 5.2. The reciprocal space map of the TET:F6-TCNNQ blend also exhibits clear TET features, while they are only weakly expressed in the reciprocal space map of the TET:F4-TCNQ blend, again in consistency with the XRR results. No peaks assignable to the TET:F4-TCNQ 1:1 crystal structure reported in Ref. [42] are found in the reciprocal space map of the TET:F4 blend, indicating rather an amorphous, mixed phase.

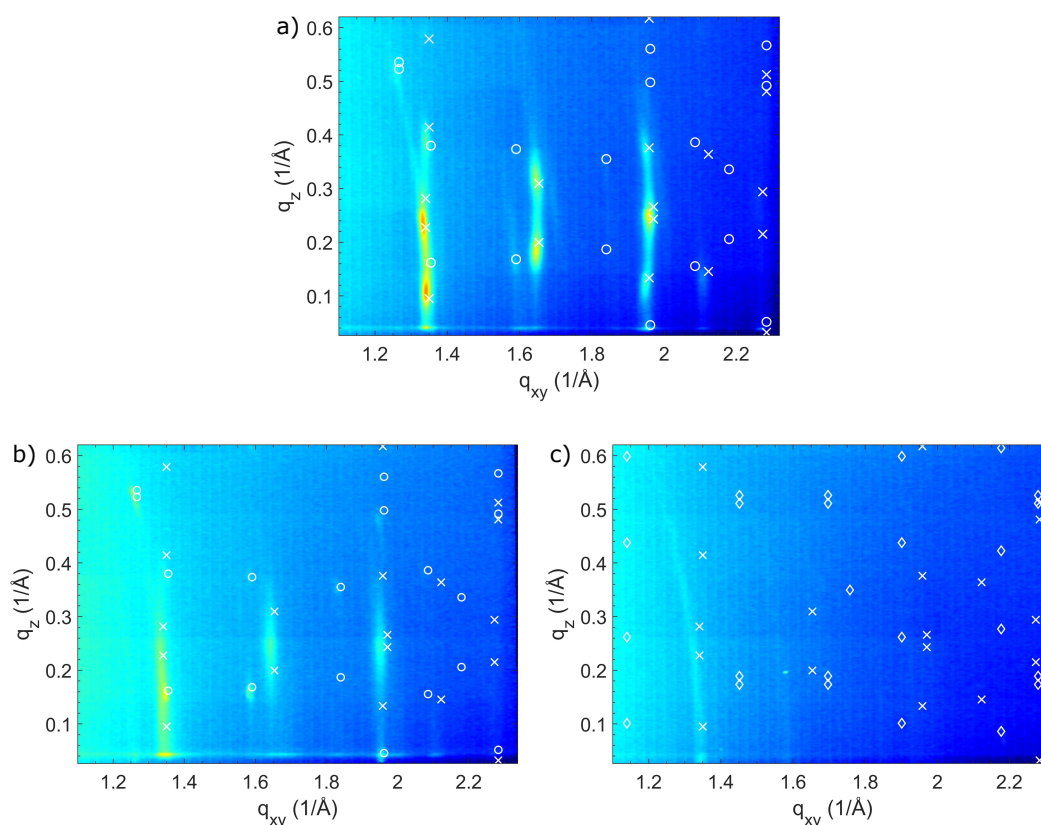


Figure A.1: Reciprocal space maps of a) a TET thin film, b) a TET:F6-TCNNQ blend with 25 % F6-TCNNQ, and c) a TET:F4-TCNNQ blend with 33 % F4-TCNNQ, all with a thickness of 20 nm. The white crosses indicate the expected TET thin film phase peak positions in all maps and the circles in a) and b) indicate the TET bulk polymorph peak positions [178]. The diamonds in c) display the peak positions of a TET:F4-TCNNQ 1:1 crystal reported in Ref. [42]. Modified from Ref. [129].

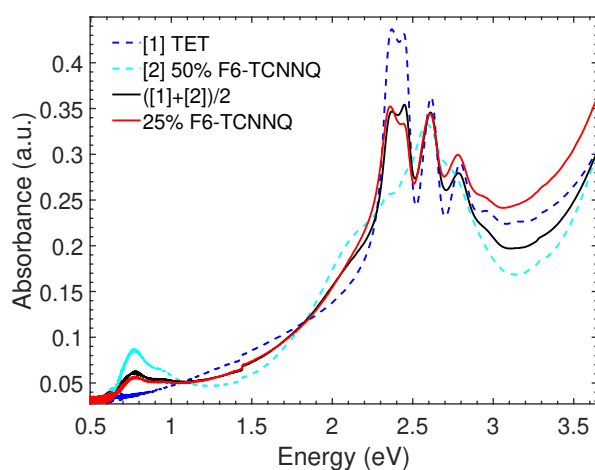


Figure A.2: UV-vis-NIR absorbance spectra of a TET thin film, an equimolar TET:F6-TCNNQ blend, and a blend with 25 % F6-TCNNQ (red). The black line shows the 1:1 superposition of the first two spectra which closely resembles the red spectrum.

A.2 Details to the TA data of neat TET

As mentioned in the main text, the time constants extracted for TET by GA of the TA measurements depend on the used excitation density. These excitation densities were calculated from the energy of a single pump laser pulse, the area of the pump laser spot on the sample ($\sim 7 \times 10^{-4} \text{ cm}^2$), the film thickness, and the TET absorbance at the pump laser wavelength. The energy of a single pulse was adjusted by different gray filters in the optical path of the pump beam. The sample thickness was 80 nm, resulting in a pumped volume of $\sim 6 \times 10^{-9} \text{ cm}^3$. From the steady-state spectrum of the TET film, an absorbance (decadic absorbance) of $A = 0.29$ at 520 nm was extracted, indicating that 49% of the photons of each pulse are absorbed. Thus, per 1 nJ of pump pulse energy with $\lambda_{\text{exc}} = 520 \text{ nm}$, 1.28×10^9 photons are absorbed, resulting in an excitation density of $2.1 \times 10^{17} \text{ cm}^{-3}$. The used pump pulse energies were in the range of 18 nJ to 115 nJ, resulting in the excitation densities given in Table A.1. The corresponding pump fluences, given by the pulse energy per area, were $25 \mu\text{J}/\text{cm}^2$ to $165 \mu\text{J}/\text{cm}^2$. For the TA measurements of the neat acceptor films and the blends, pump fluences between $25 \mu\text{J}/\text{cm}^2$ and $100 \mu\text{J}/\text{cm}^2$ were used.

For the GA, a sequential model with three species with exponential decays was fitted to the data (EAS in Figure A.3). The obtained time constants can only give a rough idea of the real time constants, since singlet-singlet annihilation leads to a non-exponential decay due to the second order rate equation. Nevertheless, the dependence of the extracted time constants (Table A.1) on the excitation density is confirmed. The decrease of τ_1 for increasing excitation densities demonstrates the increasing influence of the rapid singlet-singlet annihilation process. The second decay constant, τ_2 is rather robust and in the range of the reported SF time constants (see main text). Finally, τ_3 also decreases for increasing excitation densities, which can be rationalized by an increase of triplet fusion ($T_1+T_1 \rightarrow S_1$) and annihilation ($T_1+T_1 \rightarrow T_n$) processes [303].

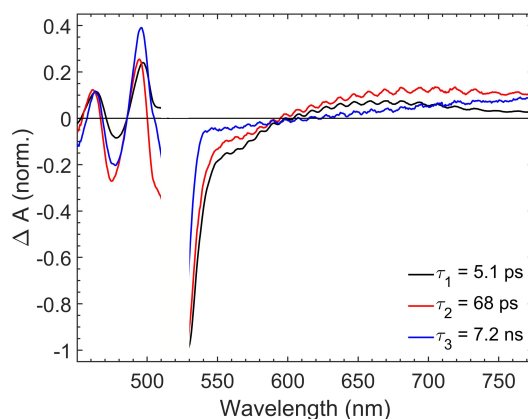


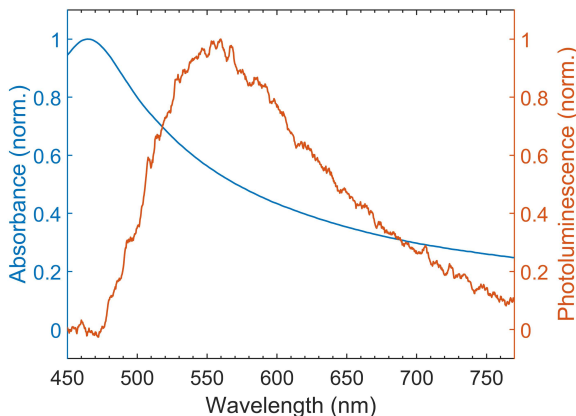
Figure A.3: EAS and their decay constants obtained from a GA of the TA data of a neat TET film. The measurement was performed with $\lambda_{\text{exc}} = 520 \text{ nm}$ and a pump fluence of $100 \mu\text{J}/\text{cm}^2$. In the GA, a sequential model with three species was fitted to the data. Modified from Ref. [129].

Table A.1: Time constants obtained from a GA of TA measurements on neat TET at different excitation densities.

| Excitation density (cm^{-3}) | τ_1 (ps) | τ_2 (ps) | τ_3 (ns) |
|---|---------------|---------------|---------------|
| $3.8 \cdot 10^{18}$ | 13.2 | 91 | 13.5 |
| $7.4 \cdot 10^{18}$ | 8.7 | 76 | 8.2 |
| $1.5 \cdot 10^{19}$ | 5.1 | 68 | 7.2 |
| $2.4 \cdot 10^{19}$ | 4.4 | 71 | 6.1 |

A.3 Details to the TA data of the neat acceptors

In the TA data of the neat F4-TCNQ film, a weak negative feature over the entire measured wavelength region is observed (Figure 5.10 in the main text). Possible explanations for this feature can be deduced from the absorption and emission spectra, which are shown in Figure A.4 as a function of the wavelength for easier comparison with the TA data. The absorbance spectrum shows a long tail below the energetically lowest absorption peak. This might be due to the existence of trap states with lower energy in the amorphous film. If these are populated directly by excitation from the pump pulse or indirectly via energy transfer from surrounding molecules, a bleach feature would appear in the TA data. Another possible explanation for the long absorbance tail is scattering from the rough surface of the thin film (inferred from the lack of Kiessig fringes in the XRR data in Figure 5.2b). A changed scattering of the thin film after excitation, due to a changed permittivity of the film, could also contribute to the negative TA signal. Finally, the weak but broad photoluminescence of the F4-TCNQ film makes also SE in a broad wavelength region possible, which would lead to a negative feature in the TA spectra, too. Superimposed with the overall negative feature in the TA spectrum, signs of F4-TCNQ²⁻ dianion absorption peaks above 500 nm on longer time scales are observable, which have been reported in Ref. [196].

**Figure A.4:** Normalized absorbance and emission spectrum of a neat F4-TCNQ thin film. The excitation wavelength was 470 nm. Modified from Ref. [129].

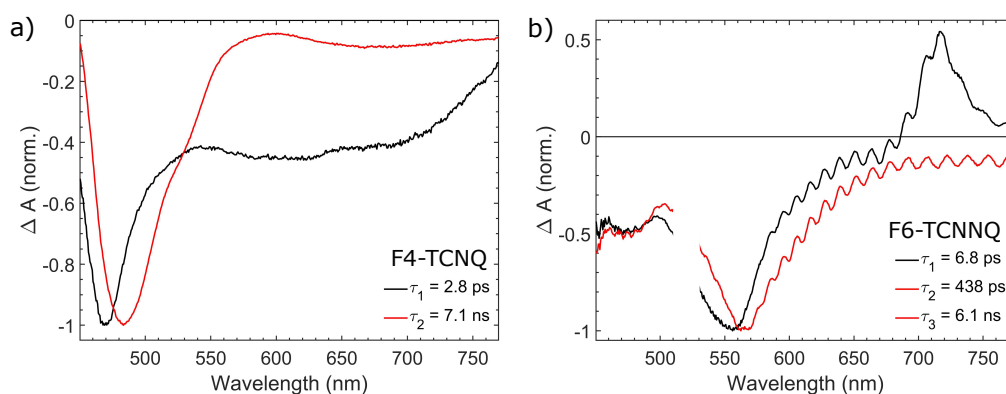


Figure A.5: Evolution/species associated spectra and their decay constants. a) EAS from a GA of the TA data of an F4-TCNQ film, excited with $\lambda_{\text{exc}} = 400$ nm. A sequential model with two species was chosen. b) Species associated spectra from a target analysis of the TA data of an F6-TCNNQ film with $\lambda_{\text{exc}} = 520$ nm. A model with two species was chosen, where species 2 decays with two different time constants. Modified from Ref. [129].

A.4 Details to the TA data of the blends

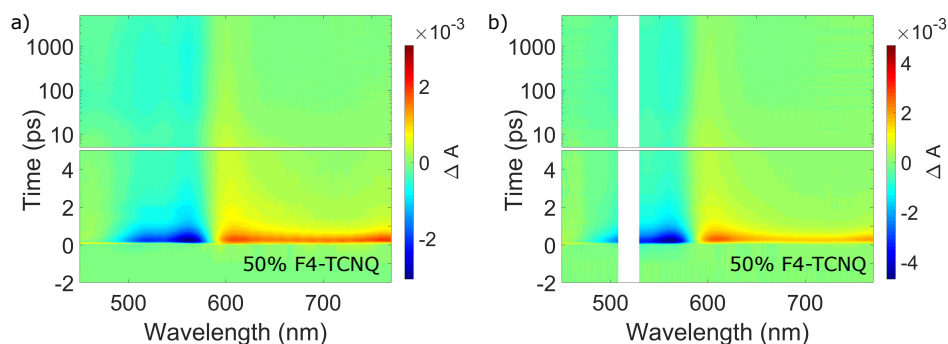


Figure A.6: TA data of the equimolar TET:F4-TCNQ blend, measured with a) $\lambda_{\text{exc}} = 400$ nm and b) $\lambda_{\text{exc}} = 520$ nm. They exhibit very similar signals and dynamics. Modified from Ref. [129].

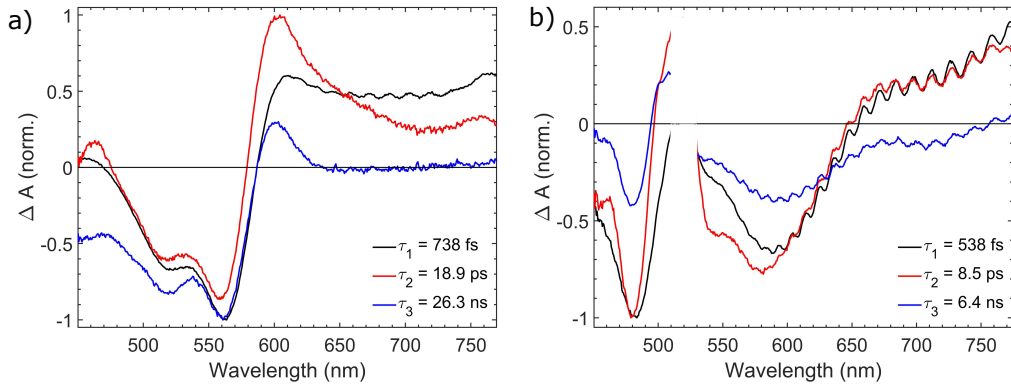


Figure A.7: EAS and their decay constants from a GA with a sequential model with three species. a) Equimolar TET:F4-TCNQ blend with $\lambda_{\text{exc}} = 400$ nm. b) Equimolar TET:F4-TCNQ blend with $\lambda_{\text{exc}} = 520$ nm. Modified from Ref. [129].

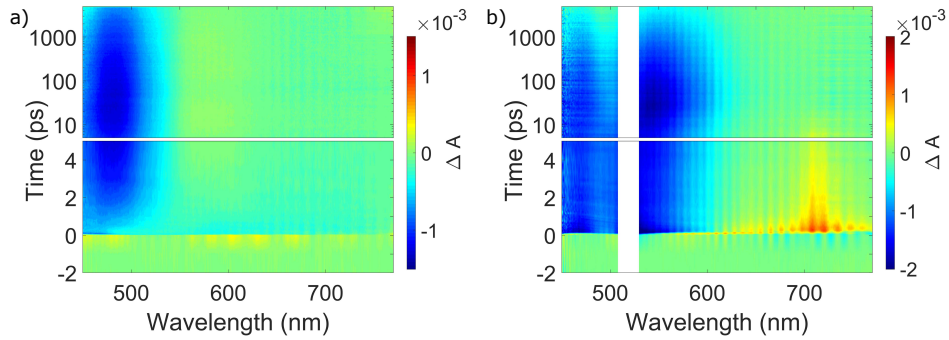


Figure A.8: Linear combination of TA maps, demonstrating the possibility to construct the TA signal of the 75% acceptor blend by a superposition of the TA signals of the neat acceptor blend and the equimolar blend. a) (75% F4-TCNQ blend signal) - (equimolar TET:F4-TCNQ blend signal), $\lambda_{\text{exc}} = 400$ nm, reproducing the neat F4-TCNQ film signal (cf. Figure 5.10). b) Similar as in a) but for F6-TCNNQ, $\lambda_{\text{exc}} = 520$ nm (cf. Figure 5.11). Modified from Ref. [129].

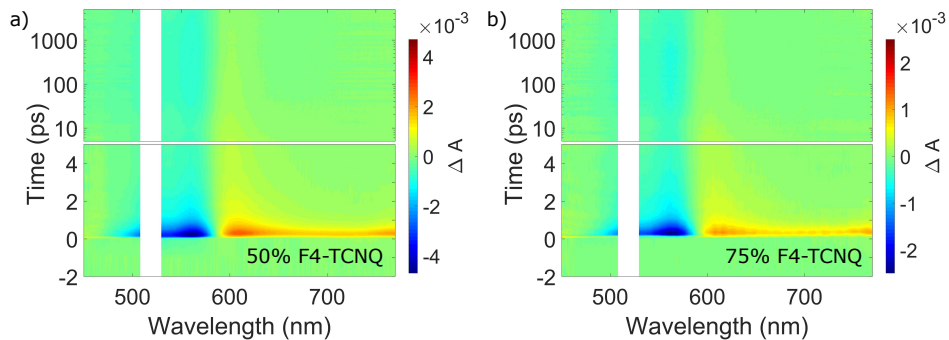


Figure A.9: TA data of a) the equimolar TET:F4-TCNQ blend and b) the TET:F4-TCNQ blend with 75% F4-TCNQ, both with $\lambda_{\text{exc}} = 520$ nm. They exhibit very similar signals and dynamics because only the CTCs are excited. Modified from Ref. [129].

B. Pentacene:acceptor blends

In this part of the Appendix, additional information and figures supporting the results discussed in Chapter 6 are presented, including further UV-vis-NIR spectra, TA data, and results from GA of the blends with an excess of PEN.

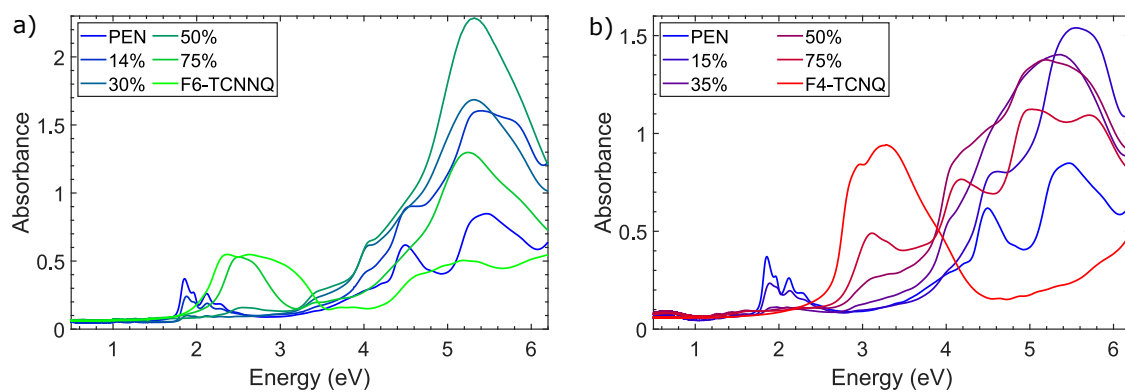


Figure B.1: Full UV-vis-NIR spectra of the a) PEN:F6-TCNNQ and b) PEN:F4-TCNNQ blends. In the legend the acceptor fraction is given. Modified from Ref. [261].

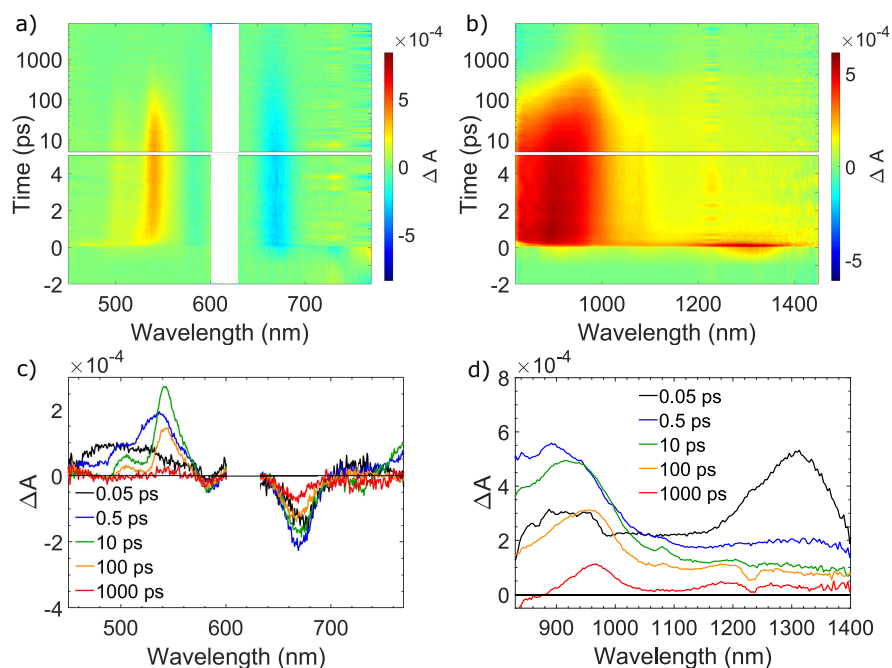


Figure B.2: TA data of the blend with 30% F6-TCNQ, excited with $\lambda_{\text{exc}} = 620$ nm. a,c) Probed in the visible spectral region and excited with a pump fluence of $140 \mu\text{J}/\text{cm}^2$. b,d) Probed in the NIR spectral region and excited with a pump fluence of $700 \mu\text{J}/\text{cm}^2$. The TA spectra in c) and d) are averaged around the delay times given in the legend (cf. Figure 6.7). Modified from Ref. [261].

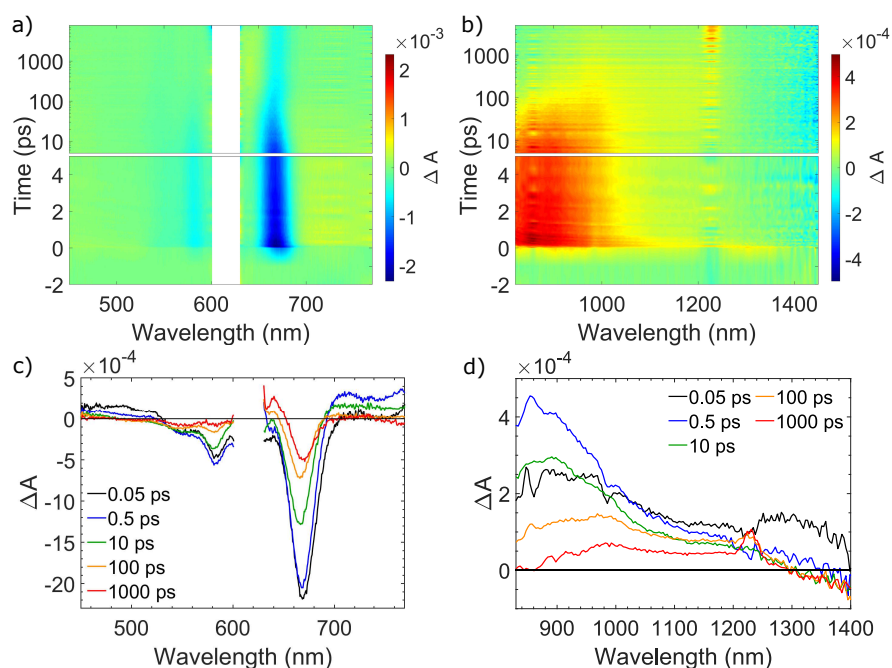


Figure B.3: TA data of the blend with 28% F4-TCNQ, excited with $\lambda_{\text{exc}} = 620$ nm. a,c) Probed in the visible spectral region and excited with a pump fluence of $280 \mu\text{J}/\text{cm}^2$. b,d) Probed in the NIR spectral region and excited with a pump fluence of $700 \mu\text{J}/\text{cm}^2$. The TA spectra in c) and d) are averaged around the delay times given in the legend (cf. Figure 6.7). Modified from Ref. [261].

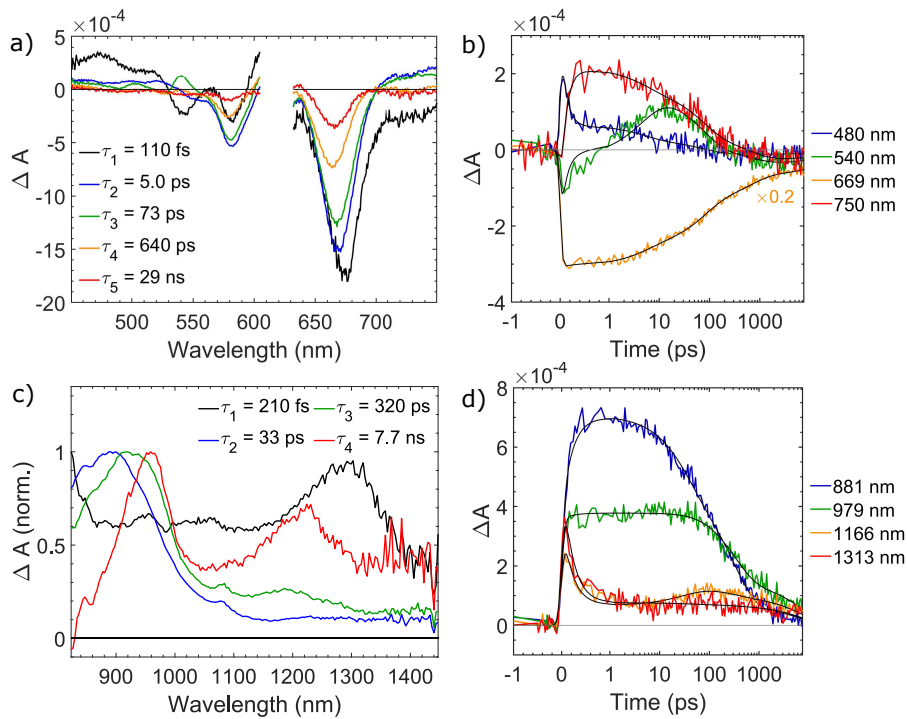


Figure B.4: GA results of a TA measurement of the blend with 14% F6-TCNNQ excited with $\lambda_{\text{exc}} = 620 \text{ nm}$. a,b) Probed in the visible spectral region and excited with a pump fluence of $140 \mu\text{J}/\text{cm}^2$. c,d) Probed in the NIR spectral region and excited with a pump fluence of $700 \mu\text{J}/\text{cm}^2$. a,c) EAS, with the corresponding time constants given in the legend. b,d) Selected timetraces at PEN features and the corresponding fits by the GA, shown as black lines. The time-axis changes from linear to logarithmic scale at 1 ps. Modified from Ref. [261].

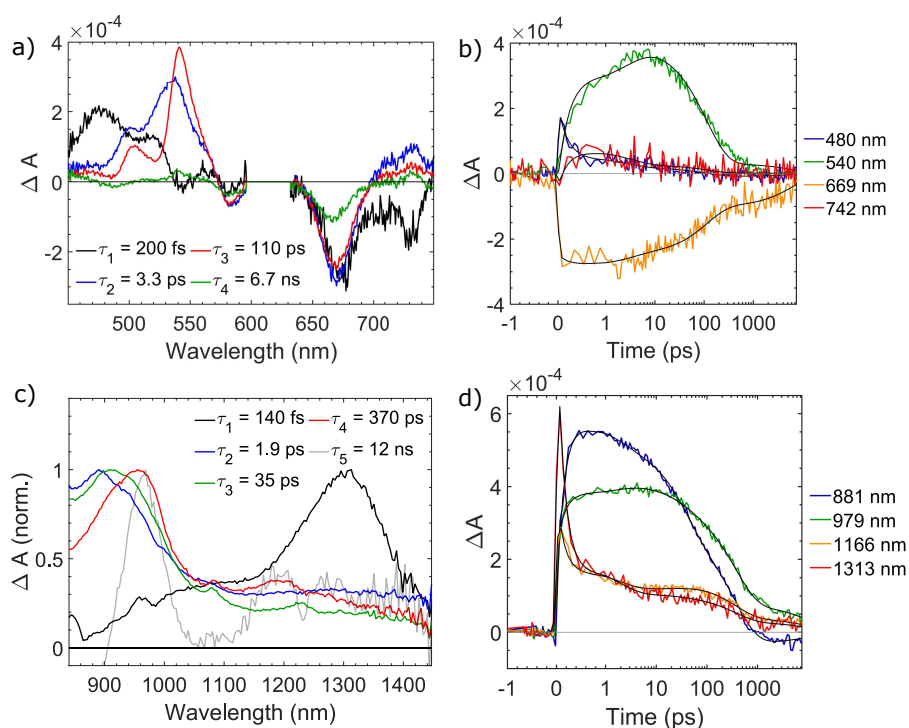


Figure B.5: GA results of a TA measurement of the blend with 30% F6-TCNNQ excited with $\lambda_{\text{exc}} = 620 \text{ nm}$. a,b) Probed in the visible spectral region and excited with a pump fluence of $280 \mu\text{J}/\text{cm}^2$. c,d) Probed in the NIR spectral region and excited with a pump fluence of $700 \mu\text{J}/\text{cm}^2$. a,c) EAS, with the corresponding time constants given in the legend. b,d) Selected timetraces at PEN features and the corresponding fits by the GA, shown as black lines. The time-axis changes from linear to logarithmic scale at 1 ps. Modified from Ref. [261].

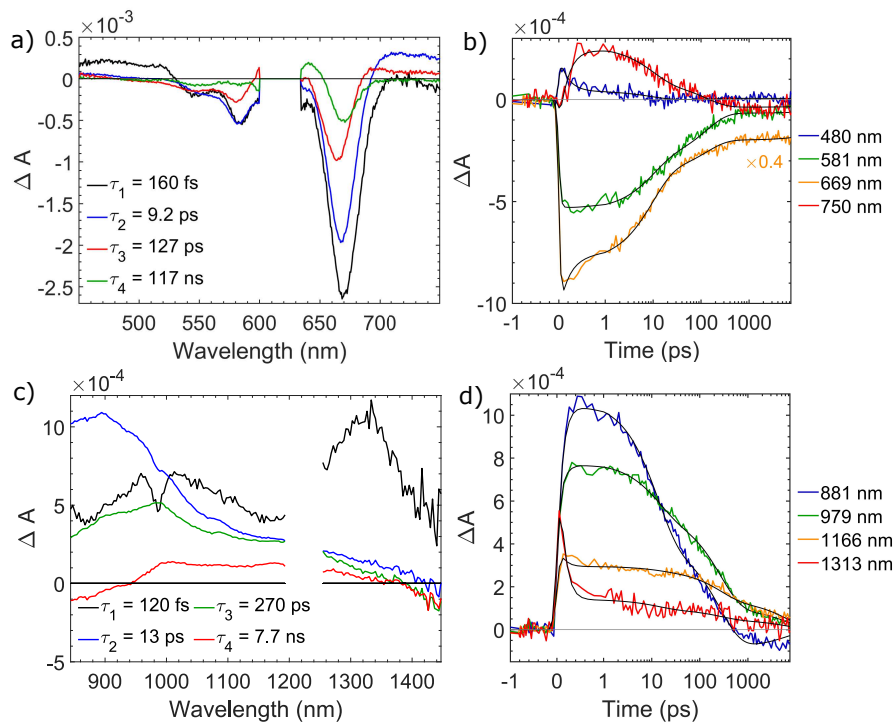


Figure B.6: GA results of a TA measurement of the blend with 28% F4-TCNQ excited with $\lambda_{\text{exc}} = 620 \text{ nm}$. a,b) Probed in the visible spectral region and excited with a pump fluence of $280 \mu\text{J}/\text{cm}^2$. c,d) Probed in the NIR spectral region and excited with a pump fluence of $700 \mu\text{J}/\text{cm}^2$. a,c) EAS (not normalized for better visibility), with the corresponding time constants given in the legend. b,d) Selected timetraces at PEN features and the corresponding fits by the GA, shown as black lines. The time-axis changes from linear to logarithmic scale at 1 ps. Modified from Ref. [261].

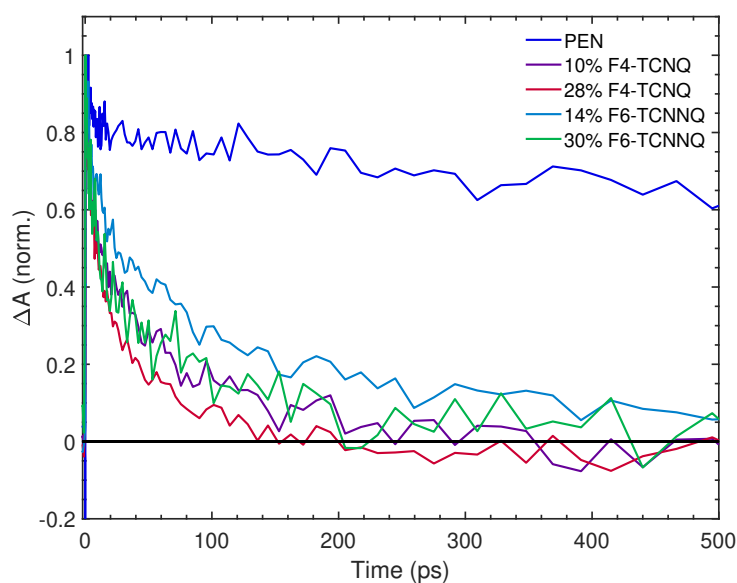


Figure B.7: Timetraces of the PEN triplet ESA extracted from the TA measurements with $\lambda_{\text{exc}} = 620$ nm and probed in the visible spectral region. For PEN (pump fluence $\sim 100 \mu\text{J}/\text{cm}^2$), the 28 % F4-TCNQ ($\sim 280 \mu\text{J}/\text{cm}^2$), and the 14 % F6-TCNNQ blend ($\sim 140 \mu\text{J}/\text{cm}^2$), the time-traces are averaged from 725 nm to 775 nm and for the 10 % F4-TCNQ blend ($\sim 140 \mu\text{J}/\text{cm}^2$) from 715 nm to 765 nm due to noise at higher wavelengths. For the 30 % F6-TCNNQ blend ($\sim 280 \mu\text{J}/\text{cm}^2$), the PEN triplet signal at these wavelengths was too weak to extract a time-trace, thus the triplet ESA from 490 nm to 520 nm is averaged for this blend. Modified from Ref. [261].

C. Pentacene triplet pair state emission

In this part of the Appendix, additional data to the results presented in Chapter 7 is given, namely absorbance spectra and temperature dependent PL spectra of further PEN thin films that were prepared under slightly different conditions. Specifically, spectra of a 20 nm thick film grown at ~ 275 K and of a 50 nm thick film grown in two steps by first depositing a 15 nm thick layer of PEN, and after a few days another 35 nm thick layer of PEN, are shown. These reference films were grown to examine a possible influence of the substrate temperature during the growth and of overall changed growth conditions, respectively. Yet, the absorbance (Figure C.1) as well as the PL spectra (Figure C.2) are very similar to the ones shown in the main text, illustrating the high reproducibility of the measurements, independent of slightly different sample preparation conditions.

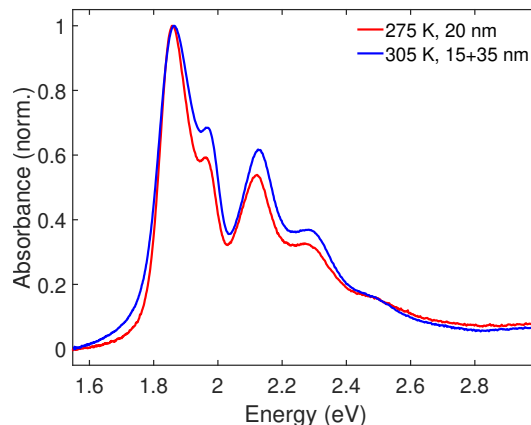


Figure C.1: Normalized absorbance spectra of the two PEN thin films described above. In the legend the substrate temperatures during the growth and the thicknesses of the films are given.

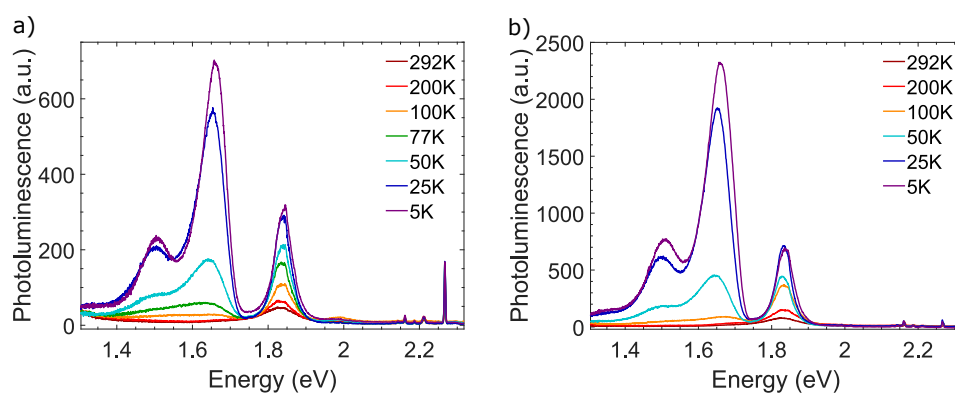


Figure C.2: Temperature dependent PL spectra of a) a 20 nm thick PEN film, deposited at ~ 275 K and measured during warm up, and b) a 50 nm thick PEN film deposited in two steps at ~ 305 K, measured during cool down. The excitation wavelength was 532 nm (2.33 eV). The sharp peaks at high energies result from Raman scattering by PEN and the substrate.

D. Pentacene on plasmonic arrays

In this part of the Appendix, additional data and details to Chapter 8 are presented. Specifically, further extinction spectra of plasmonic arrays with slightly different dimensions and covered with PS or PEN are provided and discussed.

Figures D.1 and D.2 show additional extinction spectra of square arrays of discs and rectangular arrays of rods, all covered by a PS reference layer. These spectra are similar to the ones presented in Figure 8.7 in the main text, illustrating the reproducibility of the results.

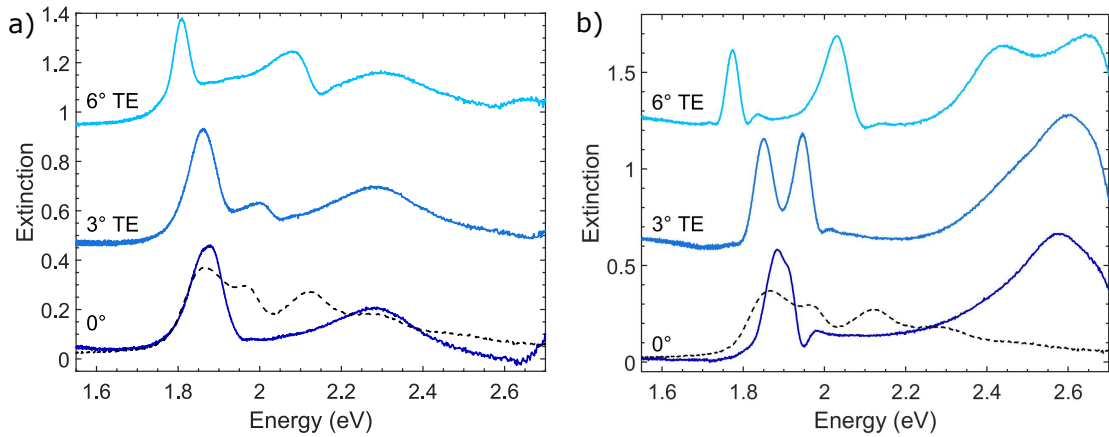


Figure D.1: Extinction spectra of plasmonic arrays covered by a PS layer. a) Square array of discs with $d = 100$ nm and $a_x = a_y = 410$ nm. b) Rectangular array of rods with $w = 95$ nm, $s = 215$ nm, $a_x = 415$ nm, and $a_y = 190$ nm. The spectra taken under $\theta = 3^\circ$ and $\theta = 6^\circ$ are vertically offset for clarity. The black dashed line is the extinction spectrum of a 50 nm thick PEN film for peak position comparison. Modified from Ref. [286].

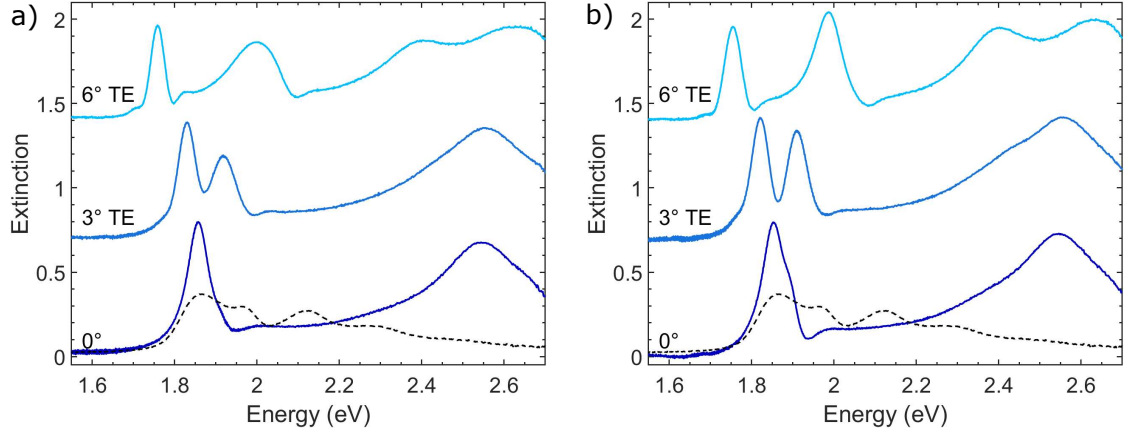


Figure D.2: Extinction spectra of plasmonic rod arrays covered by a PS layer. The lattice constants are $a_x = 415$ nm and $a_y = 190$ nm for both arrays and the rod dimensions are a) $w = 90$ nm and $s = 220$ nm and b) $w = 95$ nm and $s = 220$ nm. The spectra taken under $\theta = 3^\circ$ and $\theta = 6^\circ$ are vertically offset for clarity. The black dashed line is the extinction spectrum of a 50 nm thick PEN film for peak position comparison. Modified from Ref. [286].

Further extinction spectra of coupled systems composed of a 50 nm thick PEN film on top of the nanorod or nanodisc arrays are presented in Figures D.3 and D.4, respectively. The spectra in Figure D.3 of the nanorod arrays covered by PEN closely resemble the ones presented in Figure 8.9 in the main text, demonstrating the reproducible appearance of strong light-matter coupling in these systems. Only the relative intensities of the polariton peaks vary between the different samples as a result of the slightly different SLR energies.

The extinction spectra under normal illumination ($\theta = 0^\circ$) of the nanodisc arrays covered by PEN (Figure D.4) demonstrate that light-matter coupling occurs in these systems, too. Yet, the polariton features are less nicely pronounced, most likely due to the smaller strength and quality factor of the SLR of the nanodisc arrays compared to the nanorod arrays. Furthermore, the spectra under $\theta = 6^\circ$ are more difficult to interpret, which is beyond the scope of this thesis.

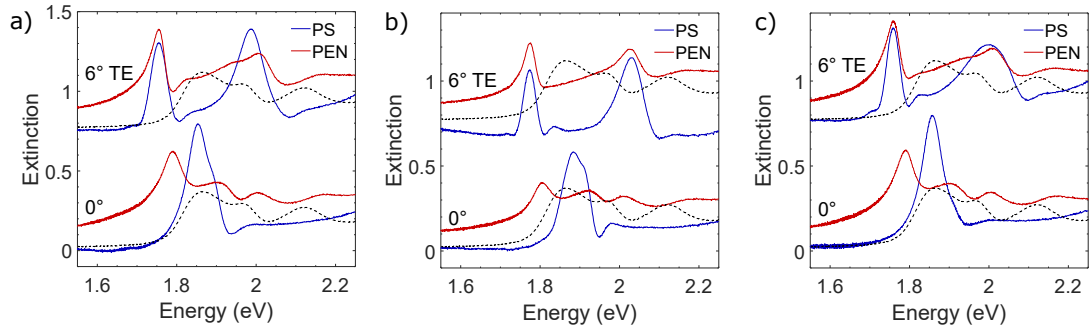


Figure D.3: Extinction spectra of rectangular, plasmonic arrays of rods, covered by a 50 nm thick PEN film (red) or a PS layer (blue) for reference. The lattice constants are $a_x = 415$ nm and $a_y = 190$ nm for all arrays and the rod dimensions are a) $w = 95$ nm and $s = 220$ nm, b) $w = 90$ nm and $s = 220$ nm, and c) $w = 95$ nm and $s = 215$ nm. The spectra taken under $\theta = 6^\circ$ are vertically offset for clarity. The black dashed line is the extinction spectrum of a 50 nm thick PEN film on Al_2O_3 on glass for peak position comparison. Modified from Ref. [286].

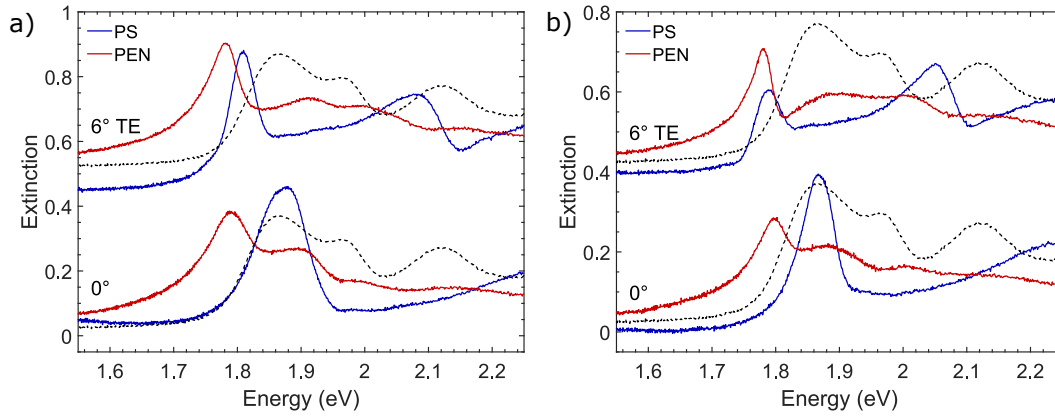


Figure D.4: Extinction spectra of square arrays of discs, covered by a 50 nm thick PEN film (red) or a PS layer (blue) for reference. The lattice and discs dimensions are a) $a_x = a_y = 410$ nm and $d = 100$ nm, and b) $a_x = a_y = 415$ nm and $d = 85$ nm. The spectra taken under $\theta = 6^\circ$ are vertically offset for clarity. The black dashed line is the extinction spectrum of a 50 nm thick PEN film on Al_2O_3 on glass for peak position comparison. Modified from Ref. [286].

Finally, Figure D.5 shows extinction spectra of the plasmonic samples with randomly distributed discs or rods covered by PEN. Also for these systems, some spectral changes appear compared to the spectra of the same plasmonic samples but covered by a PS layer. For the sample with randomly distributed discs, the extinction maximum is shifted to ~ 1.67 eV and additionally a second peak appears around the energy of D_+ . This second peak can be explained by neat PEN absorption that was not completely subtracted by the background correction. This can occur as always several background spectra of the PEN thin film beside the arrays were recorded. These spectra slightly differ in absolute intensity due to minor fluctuation in the local film thickness. Always the background spectrum with the lowest intensity was chosen to calculate the final extinction spectrum using Equation 4.8. This conservative choice was taken for all spectra presented in this thesis to avoid the possibility of subtracting too much intensity, which could result in an overestimation of the coupling strength. Thus, this peak can be considered as a background feature. In contrast, the shift of the main peak in these spectra indicates some near-field coupling between the LSPR of the plasmonic particles and the PEN molecules in the direct vicinity. Yet, since this coupling is short-ranged and thus limited to a very small fraction of the PEN molecules, no significant influence on the signal in the energy region of the PEN absorption is observed. Lastly, the extinction spectra of the rods are overall less modified by the replacement of the PS layer by a PEN film, as the LSPR is located at higher energies and, therefore, further out of resonance of the DCs of PEN.

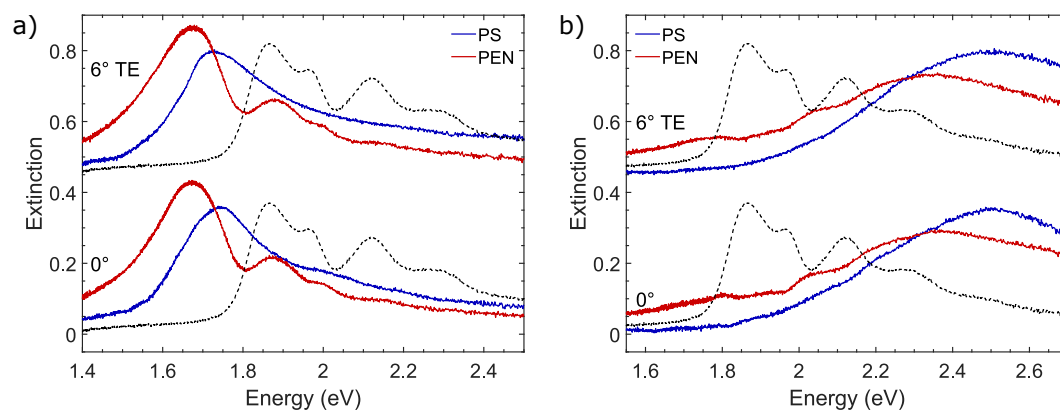


Figure D.5: Extinction spectra of a sample with randomly distributed a) discs with $d = 110$ nm and b) rods with $w = 85$ nm and $s = 220$ nm, covered by a 50 nm thick PEN film (red) or a PS layer (blue) for reference. The spectra taken under $\theta = 6^\circ$ are vertically offset for clarity. The black dashed line is the extinction spectrum of a 50 nm thick PEN film on Al_2O_3 on glass for peak position comparison. Modified from Ref. [286].

E. Organic-inorganic thin films

In this part of the Appendix, additional details to the samples and results presented in Chapter 9 are given. The thickness and morphology measurements on the samples are described here, as well as the excitation density determination for the TA measurements. Additionally, further TA data is provided.

E.1 Thickness and morphology

The morphology and thickness of the organic-inorganic thin films and the corresponding reference films were characterized by AFM and profilometer measurements. Both techniques have in common that the surface of a sample is scanned by a sharp tip, giving real space information of the topography. A DektakXT stylus profilometer (Bruker) was used in this work to approximately determine the thickness of the thin films prepared by drop casting. During the profilometer measurement, a diamond-tipped stylus is moved over the sample surface with a defined force, and the lateral deflection is electromechanically read out and converted into a height profile [304]. Since only the surface profile can be measured, several scratches through the thin films were made and several profiles were taken orthogonal to these scratches. Exemplary profiles are shown in Figure E.1 and the obtained thicknesses for the different samples are given in Section 3.3.3. It should be mentioned that the measured scratch depths might sometimes not directly reflect the film thickness, since it can be difficult to confirm that the entire thin film material is removed while the substrate is kept intact. However, for most of the profiles, the bottom of the scratch is flat (see Figure E.1), indicating that the glass substrate is hard enough to not get damaged while the entire thin film material on top was removed. The purely organic films were relatively thin and difficult to scratch off. The QD-containing films were thicker and easier to remove.

In Figure E.2, exemplary AFM images of the organic-inorganic semiconductor samples are shown. They were taken with a JPK Nanowizard instrument in tapping mode. All samples exhibit relatively smooth and uniform surfaces without larger features. Only in Figure E.2c, larger cracks are visible which most likely result from the annealing process, but next to these cracks the surface is also rather smooth.

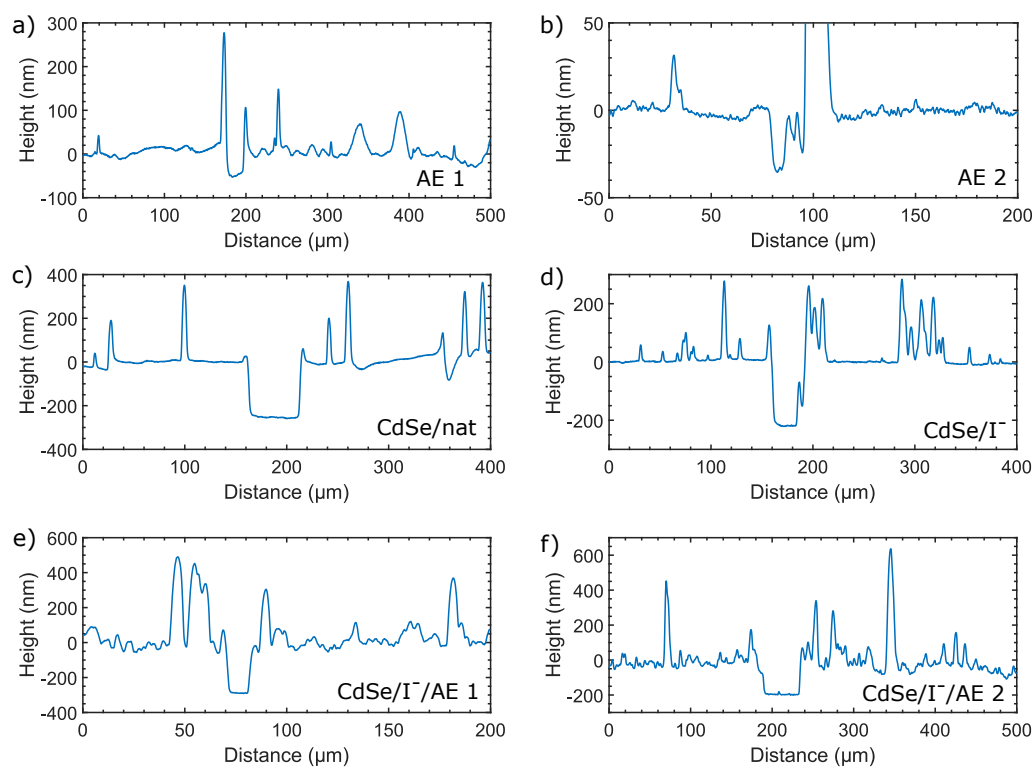


Figure E.1: Exemplary profilometer measurements of scratches through the thin films prepared by drop casting (described in Section 3.3.3). The respective sample compositions are given in the images. The high peaks around the scratches are from material that was removed during scratching and deposited beside the scratch. Modified from Ref. [290].

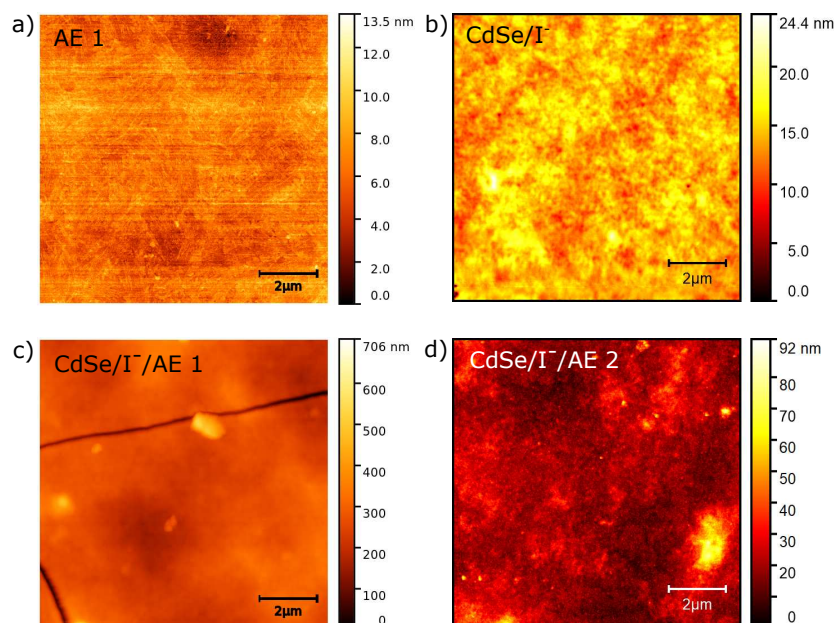


Figure E.2: AFM images of a) a purely organic, b) a purely inorganic and c,d) two hybrid films. The respective sample compositions are indicated in each image separately. Modified from Ref. [290].

E.2 TA excitation density

The excitation density during TA measurements plays an important role for the observed photophysics, since high excitation densities can lead to many-particle interactions, e.g., annihilation. These can appear when excitons encounter in the sample, which is more likely for high excitation densities. Since many-particle interactions complicate the interpretation of the results, the excitation density is kept as low as possible but high enough to still obtain a sufficient signal. The excitation density can be adjusted by the pump fluence, which is controlled by gray filters in the pump beam path. By comparing the photophysics of a sample under different pump fluences, conclusions about the presence or absence of many-particle interactions can be drawn.

The excitation density N_{eh} , given here as the average number of electron-hole pairs per QD, was calculated from the pump pulse power, which was measured before the TA measurement at the position of the sample. The measured, time-averaged power was converted into the energy per pulse with the known repetition frequency, taking into account that every second pulse is blocked. With the known photon energy (2.00 eV or 3.54 eV), the number of photons per pulse was then calculated and, together with the illuminated area ($\sim 7 \times 10^{-4} \text{ cm}^2$), the pump fluence j_p in photons per area was received. With j_p and the absorption cross section σ of the QDs at 2.00 eV (620 nm) or 3.54 eV (350 nm), taken from the literature as $\sigma_{2.00} \approx 1.7 \times 10^{-15} \text{ cm}^2$ and $\sigma_{3.54} \approx 1 \times 10^{-14} \text{ cm}^2$ [136, 305], respectively, the excitation density was calculated by $N_{eh} = \sigma j_p$.

For all measurements with 2.00 eV (620 nm) excitation, $N_{eh} < 0.37$ was satisfied. To check for any remaining fluence dependence, additional measurements with $N_{eh} < 0.1$ were performed, which, however, showed similar dynamics, indicating a negligible fluence dependence in this range. The measurements at 3.54 eV (350 nm) excitation energy yielded a TA signal for all samples, including the neat AE films due to the excitation at the AE absorption maximum. Since the absorption cross section for molecules is generally smaller than for QDs, higher pump fluences were required for the neat AE films to receive sufficient signal. To ensure direct comparability between all measurements at 3.54 eV (350 nm) excitation, they were all carried out with one common pump fluence. This fluence resulted in $N_{eh} \approx 1.2$ for the QD-containing samples. Again, reference measurements for the neat QD films were performed with 1/10 of this fluence, which resulted in slower decay dynamics, indicating probably exciton annihilation for the high fluence measurements. Nevertheless, the changes in the relative dynamics between the different samples can still be compared based on the high fluence measurements.

E.3 Further TA data

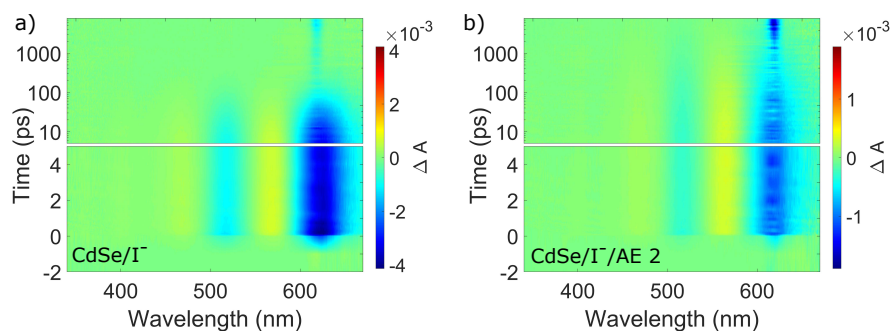


Figure E.3: TA maps of a) CdSe/I⁻ and b) CdSe/I⁻/AE2 sample. The excitation wavelength was $\lambda_{\text{exc}} = 620$ nm. At long delay times, artifacts due to scattered pump laser light are visible at λ_{exc} . Modified from Ref. [290].

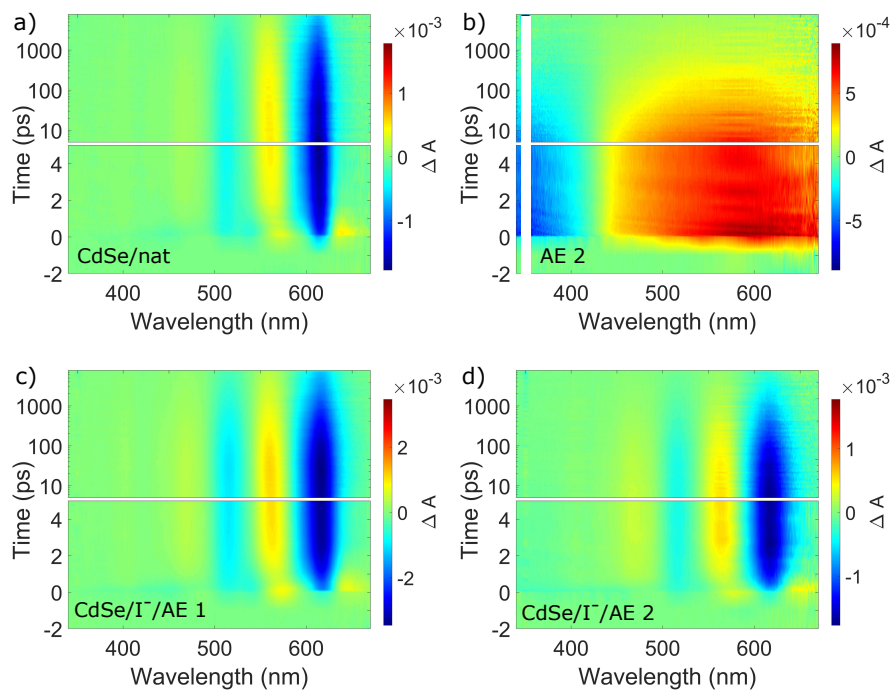


Figure E.4: TA maps of a) CdSe/nat, b) AE2, c) CdSe/I⁻/AE1, and d) CdSe/I⁻/AE2 sample with $\lambda_{\text{exc}} = 350$ nm. Modified from Ref. [290].

F. Contributions

Several collaborators contributed to the different projects presented in this thesis. They are listed below, organized according to project/chapter. For contributions from cooperation partners the head of the group is given in parentheses. The contributions by the author of this thesis are abbreviated by C.T.

Chapter 5, CTCs of TET with strong acceptors

TET:F4-TCNQ

| | |
|----------------------------|--|
| Sample preparation: | C.T., J. Hausch |
| Theoretical calculations: | Dr. A. M. Valencia (Prof. Dr. C. Cocchi) |
| Steady-state measurement.: | C.T., J. Hausch, Dr. C. Zeiser |
| Steady-state analysis: | C.T., J. Hausch |
| TA measurements: | C.T., J. Hausch, Dr. C. Zeiser, Dr. V. Sivanesan (Prof. Dr. P. Tegeder) |
| TA analysis: | C.T., J. Hausch |

TET:F6-TCNNQ

| | |
|----------------------------|--|
| Sample preparation: | C.T. |
| Theoretical calculations: | Dr. A. M. Valencia (Prof. Dr. C. Cocchi) |
| Steady-state measurement.: | C.T., Dr. C. Zeiser |
| Steady-state analysis: | C.T. |
| TA measurements: | C.T., J. Hausch, Dr. C. Zeiser, Dr. V. Sivanesan (Prof. Dr. P. Tegeder) |
| TA analysis: | C.T. |

Chapter 6, PEN with strong acceptors

| | |
|-------------------------|--|
| Sample preparation: | C.T. |
| Steady-state measurem.: | C.T. |
| Steady-state analysis: | C.T. |
| TA measurements: | C.T., M. Richter (Prof. Dr. P. Tegeder), Dr. D. Rana |
| TA analysis: | C.T. |

Chapter 7, PEN triplet pair state emission

| | |
|---------------------|----------------|
| Sample preparation: | C.T., F. Unger |
| PL measurements: | C.T. |
| PL analysis: | C.T. |

Chapter 8, PEN on plasmonic arrays

| | |
|-----------------------|--|
| Sample preparation: | C.T. |
| Extinction measurem.: | C.T., Dr. F. Laible (Prof. Dr. M. Fleischer) |
| Extinction analysis: | C.T. |

Chapter 9, CdSe QDs coupled with AEs

| | |
|-------------------------|--|
| AE synthesis: | Dr. M. Bender (Prof. Dr. U. Bunz) |
| CdSe QD synthesis: | P. Michel, Dr. K. Kumar (both Prof. Dr. M. Scheele) |
| Sample preparation: | C.T., A. Weber |
| Steady-state measurem.: | C.T., A. Weber |
| Steady-state analysis: | C.T. |
| TA measurements: | C.T., M. Richter (Prof. Dr. P. Tegeder), Dr. D. Rana |
| TA analysis: | C.T. |

G. List of abbreviations

| | |
|------------------------------|---|
| AE | aryleneethynylene |
| AE 1 | sodium 2, 2', 2'', 2''', 2'''' , 2''''' , 2'''''' , 2''''''' -(((benzene-1,2,4,5-tetrayltetrakis-(ethyne-2,1-diyl)) tetrakis(benzene-4,1-diyl))tetrakis(azanetriyl))octaacetate |
| AE 2 | sodium 2, 2', 2'', 2''' -(((2,5-bis((E)-4-methoxystyryl)-1,4-phenylene)bis-(ethyne-2,1-diyl))-bis(4,1-phenylene))bis(azanetriyl))tetraacetate |
| AFM | atomic force microscopy |
| CdSe/I⁻ | iodide stabilized cadmium selenide quantum dots |
| CdSe/I⁻/AE | mixed films of iodide stabilized cadmium selenide quantum dots and aryleneethynylene derivatives |
| CdSe/nat | cadmium selenide quantum dots with the native ligands |
| CT | charge transfer |
| CTC | charge transfer complex |
| DC | Davydov component |
| D₊ | energetically lower Davydov component |
| D₋ | energetically upper Davydov component |
| δ_{CT} | degree of charge transfer |
| EA | electron affinity |
| EAS | evolution associated spectra |
| ESA | excited state absorption |
| F4-TCNQ | 2,3,5,6-tetrafluoro-7,7,8,8-tetracyanoquinodimethane |
| F6-TCNNQ | 2,2'-(perfluoronaphthalene-2,6-diylidene)dimalononitrile |
| FRET | Förster resonance energy transfer |

| | |
|----------------|---|
| FTIR | Fourier-transform infrared |
| GA | global analysis |
| GISAXS | grazing-incidence small-angle X-ray scattering |
| GIWAXS | grazing-incidence wide-angle X-ray scattering |
| GIXD | grazing-incidence X-ray diffraction |
| GSB | ground state bleach |
| HOMO | highest occupied molecular orbital |
| IP | ionization potential |
| LSPR | localized surface plasmon resonance |
| LUMO | lowest unoccupied molecular orbital |
| NIR | near-infrared |
| NMF | N-methylformamide |
| OLED | organic light-emitting diode |
| OMBD | organic molecular beam deposition |
| OSC | organic semiconductor |
| PEM | photoelastic modulator |
| PEN | pentacene |
| PIA | photoinduced absorption |
| PL | photoluminescence |
| PMIRRAS | polarization-modulation infrared reflection-absorption spectroscopy |
| PMMA | poly(methyl methacrylate) |
| PS | polystyrene |
| QCM | quartz crystal microbalance |
| QD | quantum dot |
| SE | stimulated emission |
| SEM | scanning electron microscope |

| | |
|------------|---------------------------|
| SF | singlet fission |
| SLR | surface lattice resonance |
| TA | transient absorption |
| TDM | transition dipole moment |
| TE | transverse electric |
| TET | tetracene |
| UV | ultraviolet |
| vis | visible |
| XRR | X-ray reflectivity |

Bibliography

- [1] M. Grundmann, *The physics of semiconductors*, Springer, Cham, 4th edition (2021).
- [2] K. Y. Kamal, The silicon age: trends in semiconductor devices industry, *J. Eng. Sci. Technol.*, **15**, 110, doi:[10.25103/jestr.151.14](https://doi.org/10.25103/jestr.151.14) (2022).
- [3] T. U. Kampen, *Low molecular weight organic semiconductors*, Wiley-VCH, Weinheim (2010).
- [4] M. Schwoerer and H. C. Wolf, *Organische molekulare Festkörper: Einführung in die Physik von π -Systemen*, Wiley-VCH, Weinheim (2005).
- [5] C. Wöll, editor, *Organic electronics: Structural and electronic properties of OFETs*, Wiley-VCH, Weinheim (2009).
- [6] A. Köhler and H. Bässler, *Electronic processes in organic semiconductors: An introduction*, Wiley-VCH, Weinheim (2015).
- [7] A. Salehi, X. Fu, D.-H. Shin, and F. So, Recent advances in OLED optical design, *Adv. Funct. Mater.*, **29**, 1808803, doi:[10.1002/adfm.201808803](https://doi.org/10.1002/adfm.201808803) (2019).
- [8] N. Thejo Kalyani and S. J. Dhoble, Organic light emitting diodes: Energy saving lighting technology—a review, *Renew. Sust. Energ. Rev.*, **16**, 2696, doi:[10.1016/j.rser.2012.02.021](https://doi.org/10.1016/j.rser.2012.02.021) (2012).
- [9] M. Kaltenbrunner, M. S. White, E. D. Głowacki, T. Sekitani, T. Someya, N. S. Sariciftci, and S. Bauer, Ultrathin and lightweight organic solar cells with high flexibility, *Nat. Commun.*, **3**, 770, doi:[10.1038/ncomms1772](https://doi.org/10.1038/ncomms1772) (2012).
- [10] S. R. Forrest, The path to ubiquitous and low-cost organic electronic appliances on plastic, *Nature*, **428**, 911, doi:[10.1038/nature02498](https://doi.org/10.1038/nature02498) (2004).
- [11] K. Fukuda, K. Yu, and T. Someya, The future of flexible organic solar cells, *Adv. Energy Mater.*, **10**, 2000765, doi:[10.1002/aenm.202000765](https://doi.org/10.1002/aenm.202000765) (2020).
- [12] M. A. Green, Third generation photovoltaics: solar cells for 2020 and beyond, *Phys. E: Low-Dimens. Syst. Nanostructures*, **14**, 65, doi:[10.1016/S1386-9477\(02\)00361-2](https://doi.org/10.1016/S1386-9477(02)00361-2) (2002).
- [13] M. B. Smith and J. Michl, Singlet fission, *Chem. Rev.*, **110**, 6891, doi:[10.1021/cr1002613](https://doi.org/10.1021/cr1002613) (2010).
- [14] A. Rao and R. H. Friend, Harnessing singlet exciton fission to break the shockley–queisser limit, *Nat. Rev. Mater.*, **2**, 1, doi:[10.1038/natrevmats.2017.63](https://doi.org/10.1038/natrevmats.2017.63) (2017).
- [15] D. N. Congreve, J. Lee, N. J. Thompson, E. Hontz, S. R. Yost, P. D. Reusswig, M. E. Bahlke, S. Reineke, T. Van Voorhis, and M. A. Baldo, External quantum efficiency

- above 100% in a singlet-exciton-fission-based organic photovoltaic cell, *Science*, **340**, 334, doi:[10.1126/science.1232994](https://doi.org/10.1126/science.1232994) (2013).
- [16] K. Miyata, F. S. Conrad-Burton, F. L. Geyer, and X.-Y. Zhu, Triplet pair states in singlet fission, *Chem. Rev.*, **119**, 4261, doi:[10.1021/acs.chemrev.8b00572](https://doi.org/10.1021/acs.chemrev.8b00572) (2019).
- [17] A. J. Musser and J. Clark, Triplet-pair states in organic semiconductors, *Annu. Rev. Phys. Chem.*, **70**, 323, doi:[10.1146/annurev-physchem-042018-052435](https://doi.org/10.1146/annurev-physchem-042018-052435) (2019).
- [18] R. W. MacQueen, M. Liebhaber, J. Niederhausen, M. Mews, C. Gersmann, S. Jäckle, K. Jäger, M. J. Y. Tayebjee, T. W. Schmidt, B. Rech, and K. Lips, Crystalline silicon solar cells with tetracene interlayers: the path to silicon-singlet fission heterojunction devices, *Mater. Horiz.*, **5**, 1065, doi:[10.1039/c8mh00853a](https://doi.org/10.1039/c8mh00853a) (2018).
- [19] M. Einzinger, T. Wu, J. F. Kompalla, H. L. Smith, C. F. Perkinson, L. Nienhaus, S. Wieghold, D. N. Congreve, A. Kahn, M. G. Bawendi, and M. A. Baldo, Sensitization of silicon by singlet exciton fission in tetracene, *Nature*, **571**, 90, doi:[10.1038/s41586-019-1339-4](https://doi.org/10.1038/s41586-019-1339-4) (2019).
- [20] W. Shockley and H. J. Queisser, Detailed balance limit of efficiency of p - n junction solar cells, *J. Appl. Phys.*, **32**, 510, doi:[10.1063/1.1736034](https://doi.org/10.1063/1.1736034) (1961).
- [21] M. C. Hanna and A. J. Nozik, Solar conversion efficiency of photovoltaic and photoelectrolysis cells with carrier multiplication absorbers, *J. Appl. Phys.*, **100**, 074510, doi:[10.1063/1.2356795](https://doi.org/10.1063/1.2356795) (2006).
- [22] M. J. Y. Tayebjee, S. N. Sanders, E. Kumarasamy, L. M. Campos, M. Y. Sfeir, and D. R. McCamey, Quintet multiexciton dynamics in singlet fission, *Nat. Phys.*, **13**, 182 (2017).
- [23] R. D. Pensack, A. J. Tilley, C. Grieco, G. E. Purdum, E. E. Ostroumov, D. B. Granger, D. G. Oblinsky, J. C. Dean, G. S. Doucette, J. B. Asbury, Y.-L. Loo, D. S. Seferos, J. E. Anthony, and G. D. Scholes, Striking the right balance of intermolecular coupling for high-efficiency singlet fission, *Chem. Sci.*, **9**, 6240, doi:[10.1039/C8SC00293B](https://doi.org/10.1039/C8SC00293B) (2018).
- [24] A. M. Steiner, F. Lissel, A. Fery, J. Lauth, and M. Scheele, Prospects of coupled organic-inorganic nanostructures for charge and energy transfer applications, *Angew. Chem. Int. Ed.*, **60**, 1152, doi:[10.1002/anie.201916402](https://doi.org/10.1002/anie.201916402) (2021).
- [25] M. Hertzog, M. Wang, J. Mony, and K. Börjesson, Strong light-matter interactions: a new direction within chemistry, *Chem. Soc. Rev.*, **48**, 937, doi:[10.1039/C8CS00193F](https://doi.org/10.1039/C8CS00193F) (2019).
- [26] I. Salzmann, G. Heimel, M. Oehzelt, S. Winkler, and N. Koch, Molecular electrical doping of organic semiconductors: Fundamental mechanisms and emerging dopant design rules, *Acc. Chem. Res.*, **49**, 370, doi:[10.1021/acs.accounts.5b00438](https://doi.org/10.1021/acs.accounts.5b00438) (2016).
- [27] K. Vandewal, Interfacial charge transfer states in condensed phase systems, *Annu. Rev. Phys. Chem.*, **67**, 113, doi:[10.1146/annurev-physchem-040215-112144](https://doi.org/10.1146/annurev-physchem-040215-112144) (2016).

-
- [28] H. Méndez, G. Heimel, S. Winkler, J. Frisch, A. Opitz, K. Sauer, B. Wegner, M. Oehzelt, C. Röthel, S. Duhm, D. Többens, N. Koch, and I. Salzmann, Charge-transfer crystallites as molecular electrical dopants, *Nat. Commun.*, **6**, 8560, doi:[10.1038/ncomms9560](https://doi.org/10.1038/ncomms9560) (2015).
- [29] H. Méndez, G. Heimel, A. Opitz, K. Sauer, P. Barkowski, M. Oehzelt, J. Soeda, T. Okamoto, J. Takeya, J.-B. Arlin, J.-Y. Balandier, Y. Geerts, N. Koch, and I. Salzmann, Doping of organic semiconductors: Impact of dopant strength and electronic coupling, *Angew. Chem. Int. Ed.*, **52**, 7751, doi:[10.1002/anie.201302396](https://doi.org/10.1002/anie.201302396) (2013).
- [30] V. Belova, P. Beyer, E. Meister, T. Linderl, M.-U. Halbich, M. Gerhard, S. Schmidt, T. Zechel, T. Meisel, A. V. Generalov, A. S. Anselmo, R. Scholz, O. Konovalov, A. Gerlach, M. Koch, A. Hinderhofer, A. Opitz, W. Brütting, and F. Schreiber, Evidence for anisotropic electronic coupling of charge transfer states in weakly interacting organic semiconductor mixtures, *J. Am. Chem. Soc.*, **139**, 8474, doi:[10.1021/jacs.7b01622](https://doi.org/10.1021/jacs.7b01622) (2017).
- [31] G. Duva, L. Pithan, C. Zeiser, B. Reisz, J. Dieterle, B. Hofferberth, P. Beyer, L. Bogula, A. Opitz, S. Kowarik, A. Hinderhofer, A. Gerlach, and F. Schreiber, Thin-film texture and optical properties of donor/acceptor complexes. Diindenoperylene/F6TCNNQ vs alpha-sexithiophene/F6TCNNQ, *J. Phys. Chem. C*, **122**, 18705, doi:[10.1021/acs.jpcc.8b03744](https://doi.org/10.1021/acs.jpcc.8b03744) (2018).
- [32] K. Vandewal, S. Albrecht, E. T. Hoke, K. R. Graham, J. Widmer, J. D. Douglas, M. Schubert, W. R. Mateker, J. T. Bloking, G. F. Burkhard, A. Sellinger, J. M. J. Fréchet, A. Amassian, M. K. Riede, M. D. McGehee, D. Neher, and A. Salleo, Efficient charge generation by relaxed charge-transfer states at organic interfaces, *Nat. Mater.*, **13**, 63, doi:[10.1038/nmat3807](https://doi.org/10.1038/nmat3807) (2014).
- [33] H. Lee, C. Park, D. H. Sin, J. H. Park, and K. Cho, Recent advances in morphology optimization for organic photovoltaics, *Adv. Mater.*, **30**, 1800453, doi:[10.1002/adma.201800453](https://doi.org/10.1002/adma.201800453) (2018).
- [34] M. L. Tietze, J. Benduhn, P. Pahner, B. Nell, M. Schwarze, H. Kleemann, M. Krammer, K. Zojer, K. Vandewal, and K. Leo, Elementary steps in electrical doping of organic semiconductors, *Nat. Commun.*, **9**, 1182, doi:[10.1038/s41467-018-03302-z](https://doi.org/10.1038/s41467-018-03302-z) (2018).
- [35] I. Salzmann, G. Heimel, S. Duhm, M. Oehzelt, P. Pingel, B. M. George, A. Schnegg, K. Lips, R.-P. Blum, A. Vollmer, and N. Koch, Intermolecular hybridization governs molecular electrical doping, *Phys. Rev. Lett.*, **108**, 035502, doi:[10.1103/PhysRevLett.108.035502](https://doi.org/10.1103/PhysRevLett.108.035502) (2012).
- [36] I. Salzmann and G. Heimel, Toward a comprehensive understanding of molecular doping organic semiconductors (review), *J. Electron Spectrosc. Relat. Phenom.*, **204**, 208, doi:[10.1016/j.elspec.2015.05.001](https://doi.org/10.1016/j.elspec.2015.05.001) (2015).
- [37] B. Siegmund, A. Mischok, J. Benduhn, O. Zeika, S. Ullbrich, F. Nehm, M. Böhm, D. Spoltore, H. Fröb, C. Körner, K. Leo, and K. Vandewal, Organic narrowband near-infrared photodetectors based on intermolecular charge-transfer absorption, *Nat. Com-*

- mun.*, **8**, 15421, doi:[10.1038/ncomms15421](https://doi.org/10.1038/ncomms15421) (2017).
- [38] P. Beyer, D. Pham, C. Peter, N. Koch, E. Meister, W. Brütting, L. Grubert, S. Hecht, D. Nabok, C. Cocchi, C. Draxl, and A. Opitz, State-of-matter-dependent charge-transfer interactions between planar molecules for doping applications, *Chem. Mater.*, **31**, 1237, doi:[10.1021/acs.chemmater.8b01447](https://doi.org/10.1021/acs.chemmater.8b01447) (2019).
- [39] J. Li, I. Duchemin, O. M. Roscioni, P. Friederich, M. Anderson, E. Da Como, G. Kociok-Köhn, W. Wenzel, C. Zannoni, D. Beljonne, X. Blase, and G. D’Avino, Host dependence of the electron affinity of molecular dopants, *Mater. Horiz.*, **6**, 107, doi:[10.1039/c8mh00921j](https://doi.org/10.1039/c8mh00921j) (2019).
- [40] J. Li, G. D’Avino, A. Pershin, D. Jacquemin, I. Duchemin, D. Beljonne, and X. Blase, Correlated electron-hole mechanism for molecular doping in organic semiconductors, *Phys. Rev. Mater.*, **1**, 025602, doi:[10.1103/PhysRevMaterials.1.025602](https://doi.org/10.1103/PhysRevMaterials.1.025602) (2017).
- [41] S. D. Ha and A. Kahn, Isolated molecular dopants in pentacene observed by scanning tunneling microscopy, *Phys. Rev. B*, **80**, 195410, doi:[10.1103/PhysRevB.80.195410](https://doi.org/10.1103/PhysRevB.80.195410) (2009).
- [42] P. Hu, H. Li, Y. Li, H. Jiang, and C. Kloc, Single-crystal growth, structures, charge transfer and transport properties of anthracene-F₄TCNQ and tetracene-F₄TCNQ charge-transfer compounds, *CrystEngComm*, **19**, 618, doi:[10.1039/c6ce02116f](https://doi.org/10.1039/c6ce02116f) (2017).
- [43] H. L. Luk, J. Feist, J. J. Toppari, and G. Groenhof, Multiscale molecular dynamics simulations of polaritonic chemistry, *J. Chem. Theory. Comput.*, **13**, 4324, doi:[10.1021/acs.jctc.7b00388](https://doi.org/10.1021/acs.jctc.7b00388) (2017).
- [44] P. Törmä and W. L. Barnes, Strong coupling between surface plasmon polaritons and emitters: a review, *Rep. Prog. Phys.*, **78**, 013901, doi:[10.1088/0034-4885/78/1/013901](https://doi.org/10.1088/0034-4885/78/1/013901) (2014).
- [45] D. G. Lidzey, D. D. C. Bradley, M. S. Skolnick, T. Virgili, S. Walker, and D. M. Whittaker, Strong exciton–photon coupling in an organic semiconductor microcavity, *Nature*, **395**, 53, doi:[10.1038/25692](https://doi.org/10.1038/25692) (1998).
- [46] C. Schneider, K. Winkler, M. D. Fraser, M. Kamp, Y. Yamamoto, E. A. Ostrovskaya, and S. Höfling, Exciton-polariton trapping and potential landscape engineering, *Rep. Prog. Phys.*, **80**, 016503, doi:[10.1088/0034-4885/80/1/016503](https://doi.org/10.1088/0034-4885/80/1/016503) (2016).
- [47] M. Ramezani, A. Halpin, J. Feist, N. Van Hoof, A. I. Fernández-Domínguez, F. J. Garcia-Vidal, and J. Gómez Rivas, Dispersion anisotropy of plasmon–exciton–polaritons in lattices of metallic nanoparticles, *ACS Photonics*, **5**, 233, doi:[10.1021/acsphotonics.7b00661](https://doi.org/10.1021/acsphotonics.7b00661) (2018).
- [48] D. Polak, R. Jayaprakash, T. P. Lyons, L. Á. Martínez-Martínez, A. Leventis, K. J. Fallon, H. Coulthard, D. G. Bossanyi, K. Georgiou, A. J. Petty, II, J. Anthony, H. Bronstein, J. Yuen-Zhou, A. I. Tartakovskii, J. Clark, and A. J. Musser, Manipulating molecules with strong coupling: harvesting triplet excitons in organic exciton microcavities, *Chem. Sci.*, **11**, 343, doi:[10.1039/C9SC04950A](https://doi.org/10.1039/C9SC04950A) (2020).

-
- [49] A. I. Väkeväinen, R. J. Moerland, H. T. Rekola, A.-P. Eskelinen, J.-P. Martikainen, D.-H. Kim, and P. Törmä, Plasmonic surface lattice resonances at the strong coupling regime, *Nano Lett.*, **14**, 1721, doi:[10.1021/nl4035219](https://doi.org/10.1021/nl4035219) (2014).
- [50] S. R. K. Rodriguez and J. Gómez Rivas, Surface lattice resonances strongly coupled to rhodamine 6G excitons: tuning the plasmon-exciton-polariton mass and composition, *Opt. Express*, **21**, 27411, doi:[10.1364/OE.21.027411](https://doi.org/10.1364/OE.21.027411) (2013).
- [51] D. Sanvitto and S. Kéna-Cohen, The road towards polaritonic devices, *Nat. Mater.*, **15**, 1061, doi:[10.1038/nmat4668](https://doi.org/10.1038/nmat4668) (2016).
- [52] J. Schachenmayer, C. Genes, E. Tignone, and G. Pupillo, Cavity-enhanced transport of excitons, *Phys. Rev. Lett.*, **114**, 196403, doi:[10.1103/PhysRevLett.114.196403](https://doi.org/10.1103/PhysRevLett.114.196403) (2015).
- [53] S. Kéna-Cohen and S. R. Forrest, Room-temperature polariton lasing in an organic single-crystal microcavity, *Nat. Photonics*, **4**, 371, doi:[10.1038/nphoton.2010.86](https://doi.org/10.1038/nphoton.2010.86) (2010).
- [54] A. V. Zasedatelev, A. V. Baranikov, D. Urbonas, F. Scafrimuto, U. Scherf, T. Stöferle, R. F. Mahrt, and P. G. Lagoudakis, A room-temperature organic polariton transistor, *Nat. Photonics*, **13**, 378, doi:[10.1038/s41566-019-0392-8](https://doi.org/10.1038/s41566-019-0392-8) (2019).
- [55] X. Zhong, T. Chervy, S. Wang, J. George, A. Thomas, J. A. Hutchison, E. Devaux, C. Genet, and T. W. Ebbesen, Non-radiative energy transfer mediated by hybrid light-matter states, *Angew. Chem. Int. Ed.*, **55**, 6202, doi:[10.1002/anie.201600428](https://doi.org/10.1002/anie.201600428) (2016).
- [56] T. W. Ebbesen, Hybrid light-matter states in a molecular and material science perspective, *Acc. Chem. Res.*, **49**, 2403, doi:[10.1021/acs.accounts.6b00295](https://doi.org/10.1021/acs.accounts.6b00295) (2016).
- [57] L. A. Martínez-Martínez, M. Du, R. F. Ribeiro, S. Kéna-Cohen, and J. Yuen-Zhou, Polariton-assisted singlet fission in acene aggregates, *J. Phys. Chem. Lett.*, **9**, 1951, doi:[10.1021/acs.jpcclett.8b00008](https://doi.org/10.1021/acs.jpcclett.8b00008) (2018).
- [58] A. M. Berghuis, A. Halpin, Q. Le-Van, M. Ramezani, S. Wang, S. Murai, and J. Gómez Rivas, Enhanced delayed fluorescence in tetracene crystals by strong light-matter coupling, *Adv. Funct. Mater.*, **29**, 1901317, doi:[10.1002/adfm.201901317](https://doi.org/10.1002/adfm.201901317) (2019).
- [59] B. Gu and S. Mukamel, Optical-cavity manipulation of conical intersections and singlet fission in pentacene dimers, *J. Phys. Chem. Lett.*, **12**, 2052, doi:[10.1021/acs.jpcclett.0c03829](https://doi.org/10.1021/acs.jpcclett.0c03829) (2021).
- [60] C. Climent, D. Casanova, J. Feist, and F. J. Garcia-Vidal, Not dark yet for strong light-matter coupling to accelerate singlet fission dynamics, *Cell Rep. Phys. Sci.*, **3**, 100841, doi:[10.1016/j.xcrp.2022.100841](https://doi.org/10.1016/j.xcrp.2022.100841) (2022).
- [61] S. Takahashi, K. Watanabe, and Y. Matsumoto, Singlet fission of amorphous rubrene modulated by polariton formation, *J. Chem. Phys.*, **151**, 074703, doi:[10.1063/1.5108698](https://doi.org/10.1063/1.5108698) (2019).
- [62] B. Liu, V. M. Menon, and M. Y. Sfeir, The role of long-lived excitons in the dynamics of strongly coupled molecular polaritons, *ACS Photonics*, **7**, 2292, doi:[10.1021/acsp Photonics.0c00895](https://doi.org/10.1021/acsp Photonics.0c00895) (2020).
- [63] A. M. Berghuis, V. Serpenti, M. Ramezani, S. Wang, and J. Gómez Rivas, Light-matter coupling strength controlled by the orientation of organic crystals in plasmonic cavities,

- J. Phys. Chem. C*, **124**, 12030, doi:[10.1021/acs.jpcc.0c00692](https://doi.org/10.1021/acs.jpcc.0c00692) (2020).
- [64] J. Kao, K. Thorkelsson, P. Bai, B. J. Rancatore, and T. Xu, Toward functional nanocomposites: taking the best of nanoparticles, polymers, and small molecules, *Chem. Soc. Rev.*, **42**, 2654, doi:[10.1039/c2cs35375j](https://doi.org/10.1039/c2cs35375j) (2013).
- [65] M. Scheele, W. Brütting, and F. Schreiber, Coupled organic–inorganic nanostructures (COIN), *Phys. Chem. Chem. Phys.*, **17**, 97, doi:[10.1039/c4cp03094j](https://doi.org/10.1039/c4cp03094j) (2015).
- [66] Q. Zhang, T. Atay, J. R. Tischler, M. S. Bradley, V. Bulović, and A. V. Nurmikko, Highly efficient resonant coupling of optical excitations in hybrid organic/inorganic semiconductor nanostructures, *Nat. Nanotech.*, **2**, 555, doi:[10.1038/nnano.2007.253](https://doi.org/10.1038/nnano.2007.253) (2007).
- [67] S. Coe-Sullivan, W.-K. Woo, J. S. Steckel, M. Bawendi, and V. Bulović, Tuning the performance of hybrid organic/inorganic quantum dot light-emitting devices, *Org. Electron.*, **4**, 123, doi:[10.1016/j.orgel.2003.08.016](https://doi.org/10.1016/j.orgel.2003.08.016) (2003).
- [68] T. Rauch, M. Böberl, S. F. Tedde, J. Fürst, M. V. Kovalenko, G. Hesser, U. Lemmer, W. Heiss, and O. Hayden, Near-infrared imaging with quantum-dot-sensitized organic photodiodes, *Nat. Photonics*, **3**, 332, doi:[10.1038/nphoton.2009.72](https://doi.org/10.1038/nphoton.2009.72) (2009).
- [69] B. Ehrler, B. J. Walker, M. L. Böhm, M. W. B. Wilson, Y. Vaynzof, R. H. Friend, and N. C. Greenham, In situ measurement of exciton energy in hybrid singlet-fission solar cells, *Nat. Commun.*, **3**, 1019, doi:[10.1038/ncomms2012](https://doi.org/10.1038/ncomms2012) (2012).
- [70] M. Wright and A. Uddin, Organic-inorganic hybrid solar cells: A comparative review, *Sol. Energy Mater. Sol. Cells*, **107**, 87, doi:[10.1016/j.solmat.2012.07.006](https://doi.org/10.1016/j.solmat.2012.07.006) (2012).
- [71] P. Reiss, E. Couderc, J. De Girolamo, and A. Pron, Conjugated polymers/semiconductor nanocrystals hybrid materials—preparation, electrical transport properties and applications, *Nanoscale*, **3**, 446 (2011).
- [72] A. André, C. Theurer, J. Lauth, S. Maiti, M. Hodas, M. Samadi Khoshkhoo, S. Kinge, A. J. Meixner, F. Schreiber, L. D. A. Siebbeles, K. Braun, and M. Scheele, Structure, transport and photoconductance of PbS quantum dot monolayers functionalized with a copper phthalocyanine derivative, *Chem. Commun.*, **53**, 1700, doi:[10.1039/c6cc07878h](https://doi.org/10.1039/c6cc07878h) (2017).
- [73] J. Lauth, G. Grimaldi, S. Kinge, A. J. Houtepen, L. D. A. Siebbeles, and M. Scheele, Ultrafast charge transfer and upconversion in zinc β -tetraaminophthalocyanine-functionalized PbS nanostructures probed by transient absorption spectroscopy, *Angew. Chem. Int. Ed.*, **56**, 14061, doi:[10.1002/anie.201707443](https://doi.org/10.1002/anie.201707443) (2017).
- [74] X. Li, A. Fast, Z. Huang, D. A. Fishman, and M. L. Tang, Complementary lock-and-key ligand binding of a triplet transmitter to a nanocrystal photosensitizer, *Angew. Chem. Int. Ed.*, **56**, 5598, doi:[10.1002/anie.201701929](https://doi.org/10.1002/anie.201701929) (2017).
- [75] Z. Huang, X. Li, M. Mahboub, K. M. Hanson, V. M. Nichols, H. Le, M. L. Tang, and C. J. Bardeen, Hybrid molecule–nanocrystal photon upconversion across the visible and near-infrared, *Nano Lett.*, **15**, 5552, doi:[10.1021/acs.nanolett.5b02130](https://doi.org/10.1021/acs.nanolett.5b02130) (2015).

-
- [76] Z. Huang and M. L. Tang, Designing transmitter ligands that mediate energy transfer between semiconductor nanocrystals and molecules, *J. Am. Chem. Soc.*, **139**, 9412, doi:[10.1021/jacs.6b08783](https://doi.org/10.1021/jacs.6b08783) (2017).
- [77] K. M. Wurst, M. Bender, J. Lauth, S. Maiti, T. Chassé, A. Meixner, L. D. A. Siebbeles, U. H. F. Bunz, K. Braun, and M. Scheele, Correlated, dual-beam optical gating in coupled organic–inorganic nanostructures, *Angew. Chem. Int. Ed.*, **57**, 11559, doi:[10.1002/anie.201803452](https://doi.org/10.1002/anie.201803452) (2018).
- [78] M. Wu, D. N. Congreve, M. W. B. Wilson, J. Jean, N. Geva, M. Welborn, T. Van Voorhis, V. Bulović, M. G. Bawendi, and M. A. Baldo, Solid-state infrared-to-visible upconversion sensitized by colloidal nanocrystals, *Nat. Photonics*, **10**, 31, doi:[10.1038/NPHOTON.2015.226](https://doi.org/10.1038/NPHOTON.2015.226) (2016).
- [79] V. Gray, J. R. Allardice, Z. Zhang, and A. Rao, Organic-quantum dot hybrid interfaces and their role in photon fission/fusion applications, *Chem. Phys. Rev.*, **2**, 031305, doi:[10.1063/5.0050464](https://doi.org/10.1063/5.0050464) (2021).
- [80] V. M. Agranovich, Y. N. Gartstein, and M. Litinskaya, Hybrid resonant organic–inorganic nanostructures for optoelectronic applications, *Chem. Rev.*, **111**, 5179, doi:[10.1021/cr100156x](https://doi.org/10.1021/cr100156x) (2011).
- [81] L. Novotny, Strong coupling, energy splitting, and level crossings: A classical perspective, *Am. J. Phys.*, **78**, 1199, doi:[10.1119/1.3471177](https://doi.org/10.1119/1.3471177) (2010).
- [82] L. Novotny and B. Hecht, Principles of nano-optics, Cambridge university press, Cambridge, 2nd edition (2012).
- [83] N. J. Hestand and F. C. Spano, Expanded theory of H-and J-molecular aggregates: the effects of vibronic coupling and intermolecular charge transfer, *Chem. Rev.*, **118**, 7069, doi:[10.1021/acs.chemrev.7b00581](https://doi.org/10.1021/acs.chemrev.7b00581) (2018).
- [84] V. May and O. Kühn, Charge and energy transfer dynamics in molecular systems, WILEY-VCH, Weinheim, 3rd edition (2011).
- [85] C.-P. Hsu, The electronic couplings in electron transfer and excitation energy transfer, *Acc. Chem. Res.*, **42**, 509, doi:[10.1021/ar800153f](https://doi.org/10.1021/ar800153f) (2009).
- [86] W. Brütting and C. Adachi, editors, Physics of organic semiconductors, Wiley-VCH, Weinheim, 2nd edition, doi:[10.1002/9783527654949](https://doi.org/10.1002/9783527654949) (2012).
- [87] H. Haken and H. C. Wolf, Molekülphysik und Quantenchemie: Einführung in die experimentellen und theoretischen Grundlagen, Springer-Verlag, Heidelberg, 5th edition (2005).
- [88] C. F. Zeiser, Controlled variation of intermolecular coupling in polycrystalline thin films of singlet fission chromophores, Ph.D. thesis, Eberhard Karls Universität Tübingen (2021).
- [89] C. Schmuck, Basisbuch Organische Chemie, Pearson Deutschland GmbH, München (2013).
- [90] E. A. Meyer, R. K. Castellano, and F. Diederich, Interactions with aromatic rings in chemical and biological recognition, *Angew. Chem. Int. Ed.*, **42**, 1210,

- doi:[10.1002/anie.200390319](https://doi.org/10.1002/anie.200390319) (2003).
- [91] J. H. Williams, The molecular electric quadrupole moment and solid-state architecture, *Acc. Chem. Res.*, **26**, 593, doi:[10.1021/ar00035a005](https://doi.org/10.1021/ar00035a005) (1993).
- [92] A.-L. Barabási and H. E. Stanley, Fractal concepts in surface growth, Cambridge University Press, Cambridge (1995).
- [93] S. Kowarik, A. Gerlach, and F. Schreiber, Organic molecular beam deposition: fundamentals, growth dynamics, and *in situ* studies, *J. Phys.: Condens. Matter*, **20**, 184005, doi:[10.1088/0953-8984/20/18/184005](https://doi.org/10.1088/0953-8984/20/18/184005) (2008).
- [94] S. Schiefer, M. Huth, A. Dobrinevski, and B. Nickel, Determination of the crystal structure of substrate-induced pentacene polymorphs in fiber structured thin films, *J. Am. Chem. Soc.*, **129**, 10316, doi:[10.1021/ja0730516](https://doi.org/10.1021/ja0730516) (2007).
- [95] A. Aufderheide, K. Broch, J. Novák, A. Hinderhofer, R. Nervo, A. Gerlach, R. Banerjee, and F. Schreiber, Mixing-induced anisotropic correlations in molecular crystalline systems, *Phys. Rev. Lett.*, **109**, 156102, doi:[10.1103/PhysRevLett.109.156102](https://doi.org/10.1103/PhysRevLett.109.156102) (2012).
- [96] K. Kang, S. Watanabe, K. Broch, A. Sepe, A. Brown, I. Nasrallah, M. Nikolka, Z. Fei, M. Heeney, D. Matsumoto, K. Marumoto, H. Tanaka, S. Kuroda, and H. Sirringhaus, 2D coherent charge transport in highly ordered conducting polymers doped by solid state diffusion, *Nat. Mater.*, **15**, 896, doi:[10.1038/nmat4634](https://doi.org/10.1038/nmat4634) (2016).
- [97] W. Hofberger, Structure and optical properties of polycrystalline evaporated tetracene films, *Phys. Status Solidi A*, **30**, 271, doi:[10.1002/pssa.2210300128](https://doi.org/10.1002/pssa.2210300128) (1975).
- [98] R. Ruiz, A. C. Mayer, G. G. Malliaras, B. Nickel, G. Scoles, A. Kazimirov, H. Kim, R. L. Headrick, and Z. Islam, Structure of pentacene thin films, *Appl. Phys. Lett.*, **85**, 4926, doi:[10.1063/1.1826229](https://doi.org/10.1063/1.1826229) (2004).
- [99] H. J. Kupka, Transitions in molecular systems, Wiley-VCH, Weinheim (2011).
- [100] T. Van Voorhis, T. Kowalczyk, B. Kaduk, L.-P. Wang, C.-L. Cheng, and Q. Wu, The diabatic picture of electron transfer, reaction barriers, and molecular dynamics, *Annu. Rev. Phys. Chem.*, **61**, 149, doi:[10.1146/annurev.physchem.012809.103324](https://doi.org/10.1146/annurev.physchem.012809.103324) (2010).
- [101] J. Coates, Interpretation of infrared spectra, a practical approach. In Encyclopedia of Analytical Chemistry (eds R.A. Meyers and M.L. McKelvy), John Wiley & Sons, Ltd, Chichester, doi:[10.1002/9780470027318.a5606](https://doi.org/10.1002/9780470027318.a5606) (2000).
- [102] P. Larkin, Infrared and raman spectroscopy: Principles and spectral interpretation., Elsevier, Waltham (2011).
- [103] M. Kasha, Characterization of electronic transitions in complex molecules, *Discuss. Faraday Soc.*, **9**, 14, doi:[10.1039/DF9500900014](https://doi.org/10.1039/DF9500900014) (1950).
- [104] N. Kanamaru, Radiationless transition between randomly fluctuating levels. S₁-T₂-T₁ intersystem crossing in condensed phase, *Bull. Chem. Soc. Jpn.*, **55**, 3093, doi:[10.1246/bcsj.55.3093](https://doi.org/10.1246/bcsj.55.3093) (1982).
- [105] J. W. Arbogast, A. P. Darmanyan, C. S. Foote, F. N. Diederich, R. L. Whetten, Y. Rubin, M. M. Alvarez, and S. J. Anz, Photophysical properties of sixty atom carbon

-
- molecule (C_{60}), *J. Phys. Chem.*, **95**, 11, doi:[10.1021/j100154a006](https://doi.org/10.1021/j100154a006) (1991).
- [106] K. Tvingstedt, J. Benduhn, and K. Vandewal, Temperature dependence of the spectral line-width of charge-transfer state emission in organic solar cells; static vs. dynamic disorder, *Mater. Horiz.*, **7**, 1888, doi:[10.1039/D0MH00385A](https://doi.org/10.1039/D0MH00385A) (2020).
- [107] M. Kasha, H. R. Rawls, and M. A. El-Bayoumi, The exciton model in molecular spectroscopy, *Pure Appl. Chem.*, **11**, 371, doi:[10.1351/pac196511030371](https://doi.org/10.1351/pac196511030371) (1965).
- [108] J. Frenkel, On the transformation of light into heat in solids. II, *Phys. Rev.*, **37**, 1276, doi:[10.1103/PhysRev.37.1276](https://doi.org/10.1103/PhysRev.37.1276) (1931).
- [109] A. S. Davydov, The theory of molecular excitons, *Sov. Phys. Uspekhi*, **7**, 145, doi:[10.1070/PU1964v007n02ABEH003659](https://doi.org/10.1070/PU1964v007n02ABEH003659) (1964).
- [110] N. J. Hestand, H. Yamagata, B. Xu, D. Sun, Y. Zhong, A. R. Harutyunyan, G. Chen, H.-L. Dai, Y. Rao, and F. C. Spano, Polarized absorption in crystalline pentacene: theory vs experiment, *J. Phys. Chem. C*, **119**, 22137, doi:[10.1021/acs.jpcc.5b07163](https://doi.org/10.1021/acs.jpcc.5b07163) (2015).
- [111] D. Beljonne, H. Yamagata, J. L. Brédas, F. C. Spano, and Y. Olivier, Charge-transfer excitations steer the Davydov splitting and mediate singlet exciton fission in pentacene, *Phys. Rev. Lett.*, **110**, 226402, doi:[10.1103/PhysRevLett.110.226402](https://doi.org/10.1103/PhysRevLett.110.226402) (2013).
- [112] L. Graf, A. Kusber, B. Büchner, and M. Knupfer, Strong exciton bandwidth reduction in pentacene as a function of temperature, *Phys. Rev. B*, **106**, 165429, doi:[10.1103/PhysRevB.106.165429](https://doi.org/10.1103/PhysRevB.106.165429) (2022).
- [113] N. Monahan and X.-Y. Zhu, Charge transfer-mediated singlet fission, *Annu. Rev. Phys. Chem.*, **66**, 601, doi:[10.1146/annurev-physchem-040214-121235](https://doi.org/10.1146/annurev-physchem-040214-121235) (2015).
- [114] C. K. Yong, A. J. Musser, S. L. Bayliss, S. Lukman, H. Tamura, O. Bubnova, R. K. Hallani, A. Meneau, R. Resel, M. Maruyama, S. Hotta, L. M. Herz, D. Beljonne, J. E. Anthony, J. Clark, and H. Sirringhaus, The entangled triplet pair state in acene and heteroacene materials, *Nat. Commun.*, **8**, 15953, doi:[10.1038/ncomms15953](https://doi.org/10.1038/ncomms15953) (2017).
- [115] S. N. Sanders, A. B. Pun, K. R. Parenti, E. Kumarasamy, L. M. Yablon, M. Y. Sfeir, and L. M. Campos, Understanding the bound triplet-pair state in singlet fission, *Chem*, **5**, 1988, doi:[10.1016/j.chempr.2019.05.012](https://doi.org/10.1016/j.chempr.2019.05.012) (2019).
- [116] S. R. Yost, J. Lee, M. W. B. Wilson, T. Wu, D. P. McMahon, R. R. Parkhurst, N. J. Thompson, D. N. Congreve, A. Rao, K. Johnson, M. Y. Sfeir, M. G. Bawendi, T. M. Swager, R. H. Friend, M. A. Baldo, and T. Van Voorhis, A transferable model for singlet-fission kinetics, *Nat. Chem.*, **6**, 492, doi:[10.1038/NCHEM.1945](https://doi.org/10.1038/NCHEM.1945) (2014).
- [117] N. R. Monahan, D. Sun, H. Tamura, K. W. Williams, B. Xu, Y. Zhong, B. Kumar, C. Nuckolls, A. R. Harutyunyan, G. Chen, H.-L. Dai, D. Beljonne, Y. Rao, and X. Y. Zhu, Dynamics of the triplet-pair state reveals the likely coexistence of coherent and incoherent singlet fission in crystalline hexacene, *Nat. Chem.*, **9**, 341, doi:[10.1038/nchem.2665](https://doi.org/10.1038/nchem.2665) (2017).

- [118] A. A. Bakulin, S. E. Morgan, T. B. Kehoe, M. W. B. Wilson, A. W. Chin, D. Zigmantas, D. Egorova, and A. Rao, Real-time observation of multiexcitonic states in ultrafast singlet fission using coherent 2D electronic spectroscopy, *Nat. Chem.*, **8**, 16, doi:[10.1038/NCHEM.2371](https://doi.org/10.1038/NCHEM.2371) (2016).
- [119] R. Tempelaar and D. R. Reichman, Vibronic exciton theory of singlet fission. III. How vibronic coupling and thermodynamics promote rapid triplet generation in pentacene crystals, *J. Chem. Phys.*, **148**, 244701, doi:[10.1063/1.5031778](https://doi.org/10.1063/1.5031778) (2018).
- [120] T. C. Berkelbach, M. S. Hybertsen, and D. R. Reichman, Microscopic theory of singlet exciton fission. I. General formulation, *J. Chem. Phys.*, **138**, 114102, doi:[10.1063/1.4794425](https://doi.org/10.1063/1.4794425) (2013).
- [121] R. Tempelaar and D. R. Reichman, Vibronic exciton theory of singlet fission. I. Linear absorption and the anatomy of the correlated triplet pair state, *J. Chem. Phys.*, **146**, 174703, doi:[10.1063/1.4982362](https://doi.org/10.1063/1.4982362) (2017).
- [122] A. Wadsworth, Z. Hamid, J. Kosco, N. Gasparini, and I. McCulloch, The bulk heterojunction in organic photovoltaic, photodetector, and photocatalytic applications, *Adv. Mater.*, **32**, 2001763, doi:[10.1002/adma.202001763](https://doi.org/10.1002/adma.202001763) (2020).
- [123] A. I. Kitaigorodsky, Mixed crystals, Springer, Heidelberg, doi:[10.1007/978-3-642-81672-7](https://doi.org/10.1007/978-3-642-81672-7) (1984).
- [124] J. Dieterle, K. Broch, A. Hinderhofer, H. Frank, J. Novák, A. Gerlach, T. Breuer, R. Banerjee, G. Witte, and F. Schreiber, Structural properties of picene–perfluoropentacene and picene–pentacene blends: superlattice formation versus limited intermixing, *J. Phys. Chem. C*, **119**, 26339, doi:[10.1021/acs.jpcc.5b08866](https://doi.org/10.1021/acs.jpcc.5b08866) (2015).
- [125] A. Hinderhofer and F. Schreiber, Organic-organic heterostructures: Concepts and applications, *ChemPhysChem*, **13**, 628, doi:[10.1002/cphc.201100737](https://doi.org/10.1002/cphc.201100737) (2012).
- [126] L. Zhu, E.-G. Kim, Y. Yi, and J.-L. Brédas, Charge transfer in molecular complexes with 2,3,5,6-tetrafluoro-7,7,8,8-tetracyanoquinodimethane (F4-TCNQ): A density functional theory study, *Chem. Mater.*, **23**, 5149, doi:[10.1021/cm201798x](https://doi.org/10.1021/cm201798x) (2011).
- [127] A. A. Bakulin, A. Rao, V. G. Pavelyev, P. H. M. van Loosdrecht, M. S. Pshenichnikov, D. Niedzialek, J. Cornil, D. Beljonne, and R. H. Friend, The role of driving energy and delocalized states for charge separation in organic semiconductors, *Science*, **335**, 1340, doi:[10.1126/science.1217745](https://doi.org/10.1126/science.1217745) (2012).
- [128] K. P. Goetz, D. Vermeulen, M. E. Payne, C. Kloc, L. E. McNeil, and O. D. Jurchescu, Charge-transfer complexes: new perspectives on an old class of compounds, *J. Mater. Chem. C*, **2**, 3065, doi:[10.1039/C3TC32062F](https://doi.org/10.1039/C3TC32062F) (2014).
- [129] C. P. Theurer, A. M. Valencia, J. Hausch, C. Zeiser, V. Sivanesan, C. Cocchi, P. Tegeder, and K. Broch, Photophysics of charge transfer complexes formed by tetracene and strong acceptors, *J. Phys. Chem. C*, **125**, 6313, doi:[10.1021/acs.jpcc.0c10815](https://doi.org/10.1021/acs.jpcc.0c10815) (2021).

-
- [130] G. Duva, P. Beyer, R. Scholz, V. Belova, A. Opitz, A. Hinderhofer, A. Gerlach, and F. Schreiber, Ground-state charge-transfer interactions in donor:acceptor pairs of organic semiconductors – a spectroscopic study of two representative systems, *Phys. Chem. Chem. Phys.*, **21**, 17190, doi:[10.1039/c9cp02939g](https://doi.org/10.1039/c9cp02939g) (2019).
- [131] D. Kiefer, R. Kroon, A. I. Hofmann, H. Sun, X. Liu, A. Giovannitti, D. Stegerer, A. Cano, J. Hynynen, L. Yu, Y. Zhang, D. Nai, T. F. Harrelson, M. Sommer, A. J. Moulé, M. Kemerink, S. R. Marder, I. McCulloch, M. Fahlman, S. Fabiano, and C. Müller, Double doping of conjugated polymers with monomer molecular dopants, *Nat. Mater.*, **18**, 149, doi:[10.1038/s41563-018-0263-6](https://doi.org/10.1038/s41563-018-0263-6) (2019).
- [132] T. Meisel, M. Sparenberg, M. Gawek, S. Sadofev, B. Kobin, L. Grubert, S. Hecht, E. List-Kratochvil, and S. Blumstengel, Fingerprint of charge redistribution in the optical spectra of hybrid inorganic/organic semiconductor interfaces, *J. Phys. Chem. C*, **122**, 12913, doi:[10.1021/acs.jpcc.8b03580](https://doi.org/10.1021/acs.jpcc.8b03580) (2018).
- [133] K. Feron, W. J. Belcher, C. J. Fell, and P. C. Dastoor, Organic solar cells: understanding the role of Förster resonance energy transfer, *Int. J. Mol. Sci.*, **13**, 17019, doi:[10.3390/ijms131217019](https://doi.org/10.3390/ijms131217019) (2012).
- [134] N. W. Ashcroft and D. N. Mermin, *Festkörperphysik*, Oldenbourg Wissenschaftsverlag GmbH, München, 3rd edition (2007).
- [135] G. H. Wannier, The structure of electronic excitation levels in insulating crystals, *Phys. Rev.*, **52**, 191, doi:[10.1103/PhysRev.52.191](https://doi.org/10.1103/PhysRev.52.191) (1937).
- [136] J. Jasieniak, L. Smith, J. Van Embden, P. Mulvaney, and M. Califano, Re-examination of the size-dependent absorption properties of CdSe quantum dots, *J. Phys. Chem. C*, **113**, 19468, doi:[10.1021/jp906827m](https://doi.org/10.1021/jp906827m) (2009).
- [137] S. Lindsay, *Introduction to nanoscience*, Oxford University Press, New York (2010).
- [138] L. Brus, Electronic wave functions in semiconductor clusters: experiment and theory, *J. Phys. C*, **90**, 2555 (1986).
- [139] A. L. Efros and A. L. Efros, Interband absorption of light in a semiconductor sphere, *Sov. Phys. Semicond.*, **16**, 772 (1982).
- [140] D. J. Norris and M. G. Bawendi, Measurement and assignment of the size-dependent optical spectrum in CdSe quantum dots, *Phys. Rev. B*, **53**, 16338, doi:[10.1103/PhysRevB.53.16338](https://doi.org/10.1103/PhysRevB.53.16338) (1996).
- [141] Y. Kayanuma, Wannier exciton in microcrystals, *Solid State Commun.*, **59**, 405, doi:[10.1016/0038-1098\(86\)90573-9](https://doi.org/10.1016/0038-1098(86)90573-9) (1986).
- [142] D. J. Norris, A. Sacra, C. B. Murray, and M. G. Bawendi, Measurement of the size dependent hole spectrum in CdSe quantum dots, *Phys. Rev. Lett.*, **72**, 2612, doi:[10.1103/PhysRevLett.72.2612](https://doi.org/10.1103/PhysRevLett.72.2612) (1994).
- [143] Y. Kayanuma and H. Momiji, Incomplete confinement of electrons and holes in microcrystals, *Phys. Rev. B*, **41**, 10261, doi:[10.1103/PhysRevB.41.10261](https://doi.org/10.1103/PhysRevB.41.10261) (1990).
- [144] A. I. Ekimov, F. Hache, M. C. Schanne-Klein, D. Ricard, C. Flytzanis, I. A. Kudryavtsev, T. V. Yazeva, A. V. Rodina, and A. L. Efros, Absorption and intensity-dependent

- photoluminescence measurements on CdSe quantum dots: assignment of the first electronic transitions, *J. Opt. Soc. Am. B*, **10**, 100, doi:[10.1364/JOSAB.10.000100](https://doi.org/10.1364/JOSAB.10.000100) (1993).
- [145] V. I. Klimov, D. W. McBranch, C. A. Leatherdale, and M. G. Bawendi, Electron and hole relaxation pathways in semiconductor quantum dots, *Phys. Rev. B*, **60**, 13740, doi:[10.1103/PhysRevB.60.13740](https://doi.org/10.1103/PhysRevB.60.13740) (1999).
- [146] D. Bera, L. Qian, T.-K. Tseng, and P. H. Holloway, Quantum dots and their multimodal applications: a review, *Materials*, **3**, 2260, doi:[10.3390/ma3042260](https://doi.org/10.3390/ma3042260) (2010).
- [147] X. Peng, M. C. Schlamp, A. V. Kadavanich, and A. P. Alivisatos, Epitaxial growth of highly luminescent CdSe/CdS core/shell nanocrystals with photostability and electronic accessibility, *J. Am. Chem. Soc.*, **119**, 7019, doi:[10.1021/ja970754m](https://doi.org/10.1021/ja970754m) (1997).
- [148] N. C. Anderson, M. P. Hendricks, J. J. Choi, and J. S. Owen, Ligand exchange and the stoichiometry of metal chalcogenide nanocrystals: spectroscopic observation of facile metal-carboxylate displacement and binding, *J. Am. Chem. Soc.*, **135**, 18536, doi:[10.1021/ja4086758](https://doi.org/10.1021/ja4086758) (2013).
- [149] D. V. Talapin, J.-S. Lee, M. V. Kovalenko, and E. V. Shevchenko, Prospects of colloidal nanocrystals for electronic and optoelectronic applications, *Chem. Rev.*, **110**, 389, doi:[10.1021/cr900137k](https://doi.org/10.1021/cr900137k) (2010).
- [150] S. A. Maier, *Plasmonics: Fundamentals and applications*, Springer, New York, doi:[10.1007/0-387-37825-1](https://doi.org/10.1007/0-387-37825-1) (2007).
- [151] I. Zorić, M. Zäch, B. Kasemo, and C. Langhammer, Gold, platinum, and aluminum nanodisk plasmons: material independence, subradiance, and damping mechanisms, *ACS Nano*, **5**, 2535, doi:[10.1021/mn102166t](https://doi.org/10.1021/mn102166t) (2011).
- [152] V. G. Kravets, A. V. Kabashin, W. L. Barnes, and A. N. Grigorenko, Plasmonic surface lattice resonances: A review of properties and applications, *Chem. Rev.*, **118**, 5912, doi:[10.1021/acs.chemrev.8b00243](https://doi.org/10.1021/acs.chemrev.8b00243) (2018).
- [153] K. L. Kelly, E. Coronado, L. L. Zhao, and G. C. Schatz, The optical properties of metal nanoparticles: The influence of size, shape, and dielectric environment, *J. Phys. Chem. B*, **107**, 668, doi:[10.1021/jp026731y](https://doi.org/10.1021/jp026731y) (2003).
- [154] M. B. Ross, C. A. Mirkin, and G. C. Schatz, Optical properties of one-, two-, and three-dimensional arrays of plasmonic nanostructures, *J. Phys. Chem. C*, **120**, 816, doi:[10.1021/acs.jpcc.5b10800](https://doi.org/10.1021/acs.jpcc.5b10800) (2016).
- [155] V. A. Markel, Coupled-dipole approach to scattering of light from a one-dimensional periodic dipole structure, *J. Mod. Opt.*, **40**, 2281, doi:[10.1080/09500349314552291](https://doi.org/10.1080/09500349314552291) (1993).
- [156] B. Auguie and W. L. Barnes, Collective resonances in gold nanoparticle arrays, *Phys. Rev. Lett.*, **101**, 143902, doi:[10.1103/PhysRevLett.101.143902](https://doi.org/10.1103/PhysRevLett.101.143902) (2008).
- [157] V. V. Gozhenko, D. A. Smith, J. L. Vedral, V. V. Kravets, and A. O. Pinchuk, Tunable resonance absorption of light in a chain of gold nanoparticles, *J. Phys. Chem. C*, **115**, 8911, doi:[10.1021/jp2005106](https://doi.org/10.1021/jp2005106) (2011).
- [158] A. G. Nikitin, A. V. Kabashin, and H. Dallaporta, Plasmonic resonances in diffractive arrays of gold nanoantennas: near and far field effects, *Opt. Express*, **20**, 27941,

-
- doi:[10.1364/OE.20.027941](https://doi.org/10.1364/OE.20.027941) (2012).
- [159] G. Vecchi, V. Giannini, and J. Gómez Rivas, Shaping the fluorescent emission by lattice resonances in plasmonic crystals of nanoantennas, *Phys. Rev. Lett.*, **102**, 146807, doi:[10.1103/PhysRevLett.102.146807](https://doi.org/10.1103/PhysRevLett.102.146807) (2009).
- [160] V. G. Kravets, F. Schedin, and A. N. Grigorenko, Extremely narrow plasmon resonances based on diffraction coupling of localized plasmons in arrays of metallic nanoparticles, *Phys. Rev. Lett.*, **101**, 087403, doi:[10.1103/PhysRevLett.101.087403](https://doi.org/10.1103/PhysRevLett.101.087403) (2008).
- [161] A. D. Humphrey and W. L. Barnes, Plasmonic surface lattice resonances on arrays of different lattice symmetry, *Phys. Rev. B*, **90**, 075404, doi:[10.1103/PhysRevB.90.075404](https://doi.org/10.1103/PhysRevB.90.075404) (2014).
- [162] J. W. S. Lord Rayleigh, On the dynamical theory of gratings, *Proc. Math. Phys. Eng. Sci.*, **79**, 399 (1907).
- [163] M. Ramezani, Q. Le-Van, A. Halpin, and J. Gómez Rivas, Nonlinear emission of molecular ensembles strongly coupled to plasmonic lattices with structural imperfections, *Phys. Rev. Lett.*, **121**, 243904, doi:[10.1103/PhysRevLett.121.243904](https://doi.org/10.1103/PhysRevLett.121.243904) (2018).
- [164] G. Vecchi, V. Giannini, and J. Gómez Rivas, Surface modes in plasmonic crystals induced by diffractive coupling of nanoantennas, *Phys. Rev. B*, **80**, 201401, doi:[10.1103/PhysRevB.80.201401](https://doi.org/10.1103/PhysRevB.80.201401) (2009).
- [165] G. Khitrova, H. M. Gibbs, M. Kira, S. W. Koch, and A. Scherer, Vacuum rabi splitting in semiconductors, *Nat. Phys.*, **2**, 81, doi:[10.1038/nphys227](https://doi.org/10.1038/nphys227) (2006).
- [166] J. E. Anthony, The larger acenes: versatile organic semiconductors, *Angew. Chem. Int. Ed.*, **47**, 452, doi:[10.1002/anie.200604045](https://doi.org/10.1002/anie.200604045) (2008).
- [167] N. Nijegorodov, V. Ramachandran, and D. P. Winkoun, The dependence of the absorption and fluorescence parameters, the intersystem crossing and internal conversion rate constants on the number of rings in polyacene molecules, *Spectrochim. Acta, Part A*, **53**, 1813, doi:[10.1016/S1386-1425\(97\)00071-1](https://doi.org/10.1016/S1386-1425(97)00071-1) (1997).
- [168] V. Y. Butko, X. Chi, D. V. Lang, and A. P. Ramirez, Field-effect transistor on pentacene single crystal, *Appl. Phys. Lett.*, **83**, 4773, doi:[10.1063/1.1631736](https://doi.org/10.1063/1.1631736) (2003).
- [169] C.-W. Chu, Y. Shao, V. Shrotriya, and Y. Yang, Efficient photovoltaic energy conversion in tetracene-C₆₀ based heterojunctions, *Appl. Phys. Lett.*, **86**, 243506, doi:[10.1063/1.1946184](https://doi.org/10.1063/1.1946184) (2005).
- [170] M. W. B. Wilson, A. Rao, J. Clark, R. S. S. Kumar, D. Brida, G. Cerullo, and R. H. Friend, Ultrafast dynamics of exciton fission in polycrystalline pentacene, *J. Am. Chem. Soc.*, **133**, 11830, doi:[10.1021/ja201688h](https://doi.org/10.1021/ja201688h) (2011).
- [171] D. G. Bossanyi, M. Matthiesen, S. Wang, J. A. Smith, R. C. Kilbride, J. D. Shipp, D. Chekulaev, E. Holland, J. E. Anthony, J. Zaumseil, A. J. Musser, and J. Clark, Emissive spin-0 triplet-pairs are a direct product of triplet-triplet annihilation in pentacene single crystals and anthradithiophene films, *Nat. Chem.*, **13**, 163, doi:[10.1038/s41557-020-00593-y](https://doi.org/10.1038/s41557-020-00593-y) (2021).

- [172] N. Sato, K. Seki, and H. Inokuchi, Polarization energies of organic solids determined by ultraviolet photoelectron spectroscopy, *J. Chem. Soc., Faraday Trans 2*, **77**, 1621, doi:[10.1039/F29817701621](https://doi.org/10.1039/F29817701621) (1981).
- [173] H. Yoshida, K. Yamada, J. Tsutsumi, and N. Sato, Complete description of ionization energy and electron affinity in organic solids: Determining contributions from electronic polarization, energy band dispersion, and molecular orientation, *Phys. Rev. B*, **92**, 075145, doi:[10.1103/PhysRevB.92.075145](https://doi.org/10.1103/PhysRevB.92.075145) (2015).
- [174] M. Kochi, Y. Harada, T. Hirooka, and H. Inokuchi, Photoemission from organic crystal in vacuum ultraviolet region. IV, *Bull. Chem. Soc. Jpn.*, **43**, 2690, doi:[10.1246/bcsj.43.2690](https://doi.org/10.1246/bcsj.43.2690) (1970).
- [175] R. B. Campbell, J. M. Robertson, and J. Trotter, The crystal structure of hexacene, and a revision of the crystallographic data for tetracene, *Acta Crystallogr.*, **15**, 289, doi:[10.1107/S0365110X62000699](https://doi.org/10.1107/S0365110X62000699) (1962).
- [176] T. Siegrist, C. Kloc, J. H. Schön, B. Batlogg, R. C. Haddon, S. Berg, and G. A. Thomas, Enhanced physical properties in a pentacene polymorph, *Angew. Chem. Int. Ed.*, **40**, 1732, doi:[10.1002/1521-3773\(20010504\)40:9<1732::AID-ANIE17320>3.0.CO;2-7](https://doi.org/10.1002/1521-3773(20010504)40:9<1732::AID-ANIE17320>3.0.CO;2-7) (2001).
- [177] B. Gompf, D. Faltermeier, C. Redling, M. Dressel, and J. Pflaum, Tetracene film morphology: Comparative atomic force microscopy, X-ray diffraction and ellipsometry investigations, *Eur. Phys. J. E*, **27**, 421, doi:[10.1140/epje/i2008-10405-5](https://doi.org/10.1140/epje/i2008-10405-5) (2008).
- [178] R. K. Nahm and J. R. Engstrom, Who's on first? Tracking in real time the growth of multiple crystalline phases of an organic semiconductor: Tetracene on SiO₂, *J. Chem. Phys.*, **146**, 052815, doi:[10.1063/1.4971288](https://doi.org/10.1063/1.4971288) (2017).
- [179] I. P. M. Bouchoms, W. A. Schoonveld, J. Vrijmoeth, and T. M. Klapwijk, Morphology identification of the thin film phases of vacuum evaporated pentacene on SiO₂ substrates, *Synth. Met.*, **104**, 175, doi:[10.1016/S0379-6779\(99\)00050-8](https://doi.org/10.1016/S0379-6779(99)00050-8) (1999).
- [180] C. Cocchi, T. Breuer, G. Witte, and C. Draxl, Polarized absorbance and Davydov splitting in bulk and thin-film pentacene polymorphs, *Phys. Chem. Chem. Phys.*, **20**, 29724, doi:[10.1039/C8CP06384B](https://doi.org/10.1039/C8CP06384B) (2018).
- [181] H. B. Klevens and J. R. Platt, Spectral resemblances of cata-condensed hydrocarbons, *J. Chem. Phys.*, **17**, 470, doi:[10.1063/1.1747291](https://doi.org/10.1063/1.1747291) (1949).
- [182] Y. Tomkiewicz, R. P. Groff, and P. Avakian, Spectroscopic approach to energetics of exciton fission and fusion in tetracene crystals, *J. Chem. Phys.*, **54**, 4504, doi:[10.1063/1.1674702](https://doi.org/10.1063/1.1674702) (1971).
- [183] J. Burgos, M. Pope, C. E. Swenberg, and R. R. Alfano, Heterofission in pentacene-doped tetracene single crystals, *Phys. Status Solidi B*, **83**, 249, doi:[10.1002/pssb.2220830127](https://doi.org/10.1002/pssb.2220830127) (1977).
- [184] M. J. Y. Tayebjee, R. G. C. R. Clady, and T. W. Schmidt, The exciton dynamics in tetracene thin films, *Phys. Chem. Chem. Phys.*, **15**, 14797, doi:[10.1039/c3cp52609g](https://doi.org/10.1039/c3cp52609g) (2013).

-
- [185] W.-L. Chan, M. Ligges, A. Jailaubekov, L. Kaake, L. Miaja-Avila, and X.-Y. Zhu, Observing the multiexciton state in singlet fission and ensuing ultrafast multielectron transfer, *Science*, **334**, 1541, doi:[10.1126/science.1213986](https://doi.org/10.1126/science.1213986) (2011).
- [186] C. Zeiser, C. Cruz, D. R. Reichman, M. Seitz, J. Hagenlocher, E. L. Chronister, C. J. Bardeen, R. Tempelaar, and K. Broch, Vacancy control in acene blends links exothermic singlet fission to coherence, *Nat. Commun.*, **12**, 5149, doi:[10.1038/s41467-021-25395-9](https://doi.org/10.1038/s41467-021-25395-9) (2021).
- [187] J. J. Burdett, D. Gosztola, and C. J. Bardeen, The dependence of singlet exciton relaxation on excitation density and temperature in polycrystalline tetracene thin films: kinetic evidence for a dark intermediate state and implications for singlet fission, *J. Chem. Phys.*, **135**, 214508, doi:[10.1063/1.3664630](https://doi.org/10.1063/1.3664630) (2011).
- [188] M. W. B. Wilson, A. Rao, K. Johnson, S. G elinas, R. Di Pietro, J. Clark, and R. H. Friend, Temperature-independent singlet exciton fission in tetracene, *J. Am. Chem. Soc.*, **135**, 16680, doi:[10.1021/ja408854u](https://doi.org/10.1021/ja408854u) (2013).
- [189] Y. Karpov, T. Erdmann, I. Raguzin, M. Al-Husseini, M. Binner, U. Lappan, M. Stamm, K. L. Gerasimov, T. Beryozkina, V. Bakulev, D. V. Anokhin, D. A. Ivanov, F. G unther, S. Gemming, G. Seifert, B. Voit, R. Di Pietro, and A. Kiriy, High conductivity in molecularly p-doped diketopyrrolopyrrole-based polymer: The impact of a high dopant strength and good structural order, *Adv. Mater.*, **28**, 6003, doi:[10.1002/adma.201506295](https://doi.org/10.1002/adma.201506295) (2016).
- [190] J. C. Stires IV, E. J. McLaurin, and C. P. Kubiak, Infrared spectroscopic determination of the degree of charge transfer in complexes of TCNE with methyl-substituted benzenes, *Chem. Commun.*, 3532, doi:[10.1039/B504416B](https://doi.org/10.1039/B504416B) (2005).
- [191] P. K. Koech, A. B. Padmaperuma, L. Wang, J. S. Swensen, E. Polikarpov, J. T. Darsell, J. E. Rainbolt, and D. J. Gaspar, Synthesis and application of 1,3,4,5,7,8-hexafluorotetracyanonaphthoquinodimethane (F6-TNAP): A conductivity dopant for organic light-emitting devices, *Chem. Mater.*, **22**, 3926, doi:[10.1021/cm1002737](https://doi.org/10.1021/cm1002737) (2010).
- [192] F. Zhang and A. Kahn, Investigation of the high electron affinity molecular dopant F6-TCNNQ for hole-transport materials, *Adv. Funct. Mater.*, **28**, 1703780, doi:[10.1002/adfm.201703780](https://doi.org/10.1002/adfm.201703780) (2018).
- [193] K. Kanai, K. Akaike, K. Koyasu, K. Sakai, T. Nishi, Y. Kamizuru, T. Nishi, Y. Ouchi, and K. Seki, Determination of electron affinity of electron accepting molecules, *Appl. Phys. A*, **95**, 309, doi:[10.1007/s00339-008-5021-1](https://doi.org/10.1007/s00339-008-5021-1) (2009).
- [194] W. Gao and A. Kahn, Controlled p-doping of zinc phthalocyanine by coevaporation with tetrafluorotetracyanoquinodimethane: A direct and inverse photoemission study, *Appl. Phys. Lett.*, **79**, 4040, doi:[10.1063/1.1424067](https://doi.org/10.1063/1.1424067) (2001).
- [195] Z. Q. Gao, B. X. Mi, G. Z. Xu, Y. Q. Wan, M. L. Gong, K. W. Cheah, and C. H. Chen, An organic p-type dopant with high thermal stability for an organic semiconductor, *Chem. Commun.*, 117, doi:[10.1039/b713566a](https://doi.org/10.1039/b713566a) (2008).

- [196] L. Ma, P. Hu, H. Jiang, C. Kloc, H. Sun, C. Soci, A. A. Voityuk, M. E. Michel-Beyerle, and G. G. Gurzadyan, Single photon triggered dianion formation in TCNQ and F₄TCNQ crystals, *Sci. Rep.*, **6**, 28510, doi:[10.1038/srep28510](https://doi.org/10.1038/srep28510) (2016).
- [197] Y. Karpov, T. Erdmann, M. Stamm, U. Lappan, O. Guskova, M. Malanin, I. Raguzin, T. Beryozkina, V. Bakulev, F. Günther, S. Gemming, G. Seifert, M. Hambusch, S. Mannsfeld, B. Voit, and A. Kiriy, Molecular doping of a high mobility diketopyrrolopyrrole–dithienylthieno [3, 2-*b*] thiophene donor–acceptor copolymer with F₆TCNNQ, *Macromolecules*, **50**, 914, doi:[10.1021/acs.macromol.6b02452](https://doi.org/10.1021/acs.macromol.6b02452) (2017).
- [198] T. J. Emge, M. Maxfield, D. O. Cowan, and T. J. Kistenmacher, Solution and solid state studies of tetrafluoro-7,7,8,8-tetracyano-*p*-quinodimethane, TCNQF₄. Evidence for long-range amphoteric intermolecular interactions and low-dimensionality in the solid state structure, *Mol. Cryst. Liq. Cryst.*, **65**, 161, doi:[10.1080/00268948108082132](https://doi.org/10.1080/00268948108082132) (1981).
- [199] N. T. Johnson, M. R. Probert, and P. G. Waddell, Structural investigations into a new polymorph of F₄TCNQ: towards enhanced semiconductor properties, *Acta Crystallogr. C*, **77**, 426, doi:[10.1107/S2053229621006252](https://doi.org/10.1107/S2053229621006252) (2021).
- [200] R. R. Dasari, X. Wang, R. A. Wiscons, H. F. Haneef, A. Ashokan, Y. Zhang, M. S. Fonari, S. Barlow, V. Coropceanu, T. V. Timofeeva, O. D. Jurchescu, J.-L. Brédas, A. J. Matzger, and S. R. Marder, Charge-transport properties of F₆TNAP-based charge-transfer cocrystals, *Adv. Funct. Mater.*, **29**, 1904858, doi:[10.1002/adfm.201904858](https://doi.org/10.1002/adfm.201904858) (2019).
- [201] S. R. Forrest, Ultrathin organic films grown by organic molecular beam deposition and related techniques, *Chem. Rev.*, **97**, 1793, doi:[10.1021/cr941014o](https://doi.org/10.1021/cr941014o) (1997).
- [202] J. N. Wilson, M. Josowicz, Y. Wang, and U. H. F. Bunz, Cruciform π -systems: hybrid phenylene-ethynylene/phenylene-vinylene oligomers, *Chem. Commun.*, 2962, doi:[10.1039/B312156A](https://doi.org/10.1039/B312156A) (2003).
- [203] J. N. Wilson and U. H. F. Bunz, Switching of intramolecular charge transfer in cruciforms: metal ion sensing, *J. Am. Chem. Soc.*, **127**, 4124, doi:[10.1021/ja050017n](https://doi.org/10.1021/ja050017n) (2005).
- [204] A. J. Zuccherro, J. N. Wilson, and U. H. F. Bunz, Cruciforms as functional fluorophores: response to protons and selected metal ions, *J. Am. Chem. Soc.*, **128**, 11872, doi:[10.1021/ja061112e](https://doi.org/10.1021/ja061112e) (2006).
- [205] B. Fritzing, R. K. Capek, K. Lambert, J. C. Martins, and Z. Hens, Utilizing self-exchange to address the binding of carboxylic acid ligands to CdSe quantum dots, *J. Am. Chem. Soc.*, **132**, 10195, doi:[10.1021/ja104351q](https://doi.org/10.1021/ja104351q) (2010).
- [206] M. Nirmal, D. J. Norris, M. Kuno, M. G. Bawendi, A. L. Efros, and M. Rosen, Observation of the "dark exciton" in CdSe quantum dots, *Phys. Rev. Lett.*, **75**, 3728, doi:[10.1103/PhysRevLett.75.3728](https://doi.org/10.1103/PhysRevLett.75.3728) (1995).
- [207] V. Sayevich, C. Guhrenz, V. M. Dzhagan, M. Sin, M. Werheid, B. Cai, L. Borchardt, J. Widmer, D. R. T. Zahn, E. Brunner, V. Lesnyak, N. Gaponik, and A. Eychmüller, Hybrid *N*-butylamine-based ligands for switching the colloidal sol-

-
- ubility and regimentation of inorganic-capped nanocrystals, *ACS Nano*, **11**, 1559, doi:[10.1021/acsnano.6b06996](https://doi.org/10.1021/acsnano.6b06996) (2017).
- [208] S. K. Panda, S. G. Hickey, C. Waurisch, and A. Eychmüller, Graded alloyed CdZnSe nanocrystals with high luminescence quantum yields and stability for optoelectronic and biological applications, *J. Mater. Chem.*, **21**, 11550, doi:[10.1039/C1JM11375E](https://doi.org/10.1039/C1JM11375E) (2011).
- [209] B. K. H. Yen, A. Günther, M. A. Schmidt, K. F. Jensen, and M. G. Bawendi, A micro-fabricated gas–liquid segmented flow reactor for high-temperature synthesis: The case of CdSe quantum dots, *Angew. Chem. Int. Ed.*, **44**, 5447, doi:[10.1002/anie.200500792](https://doi.org/10.1002/anie.200500792) (2005).
- [210] Z. Deng, L. Cao, F. Tang, and B. Zou, A new route to zinc-blende CdSe nanocrystals: mechanism and synthesis, *J. Phys. Chem. B*, **109**, 16671, doi:[10.1021/jp052484x](https://doi.org/10.1021/jp052484x) (2005).
- [211] L. Qu and X. Peng, Control of photoluminescence properties of CdSe nanocrystals in growth, *J. Am. Chem. Soc.*, **124**, 2049, doi:[10.1021/ja017002j](https://doi.org/10.1021/ja017002j) (2002).
- [212] C. B. Murray, D. J. Norris, and M. G. Bawendi, Synthesis and characterization of nearly monodisperse CdE (E= sulfur, selenium, tellurium) semiconductor nanocrystallites, *J. Am. Chem. Soc.*, **115**, 8706, doi:[10.1021/ja00072a025](https://doi.org/10.1021/ja00072a025) (1993).
- [213] K. Kumar, J. Hiller, M. Bender, S. Nosrati, Q. Liu, M. Edelmann, S. Maier, T. Rammeler, F. Wackenhut, A. J. Meixner, K. Braun, U. H. F. Bunz, and M. Scheele, Periodic fluorescence variations of CdSe quantum dots coupled to arylenethynyls with aggregation-induced emission, *ACS Nano*, **15**, 480, doi:[10.1021/acsnano.0c05121](https://doi.org/10.1021/acsnano.0c05121) (2021).
- [214] W. W. Yu, L. Qu, W. Guo, and X. Peng, Experimental determination of the extinction coefficient of CdTe, CdSe, and CdS nanocrystals, *Chem. Mater.*, **15**, 2854, doi:[10.1021/cm034081k](https://doi.org/10.1021/cm034081k) (2003).
- [215] N. S. Pesika, K. J. Stebe, and P. C. Searson, Relationship between absorbance spectra and particle size distributions for quantum-sized nanocrystals, *J. Phys. Chem. B*, **107**, 10412, doi:[10.1021/jp0303218](https://doi.org/10.1021/jp0303218) (2003).
- [216] J. R. Caram, H. Zheng, P. D. Dahlberg, B. S. Rolczynski, G. B. Griffin, A. F. Fidler, D. S. Dolzhenkov, D. V. Talapin, and G. S. Engel, Persistent interexcitonic quantum coherence in CdSe quantum dots, *J. Phys. Chem. Lett.*, **5**, 196, doi:[10.1021/jz402336t](https://doi.org/10.1021/jz402336t) (2014).
- [217] A. K. S. Kumar, Y. Zhang, D. Li, and R. G. Compton, A mini-review: How reliable is the drop casting technique?, *Electrochem. Commun.*, **121**, 106867, doi:[10.1016/j.elecom.2020.106867](https://doi.org/10.1016/j.elecom.2020.106867) (2020).
- [218] X. Jiang, A. Ishizumi, N. Suzuki, M. Naito, and Y. Yamauchi, Vertically-oriented conjugated polymer arrays in mesoporous alumina *via* simple drop-casting and appearance of anisotropic photoluminescence, *Chem. Commun.*, **48**, 549, doi:[10.1039/C1CC14502A](https://doi.org/10.1039/C1CC14502A) (2012).
- [219] S. Budavari, M. J. O’Neil, A. Smith, and P. E. Heckelman, editors, *The Merck Index - An Encyclopedia of Chemicals, Drugs, and Biologicals*, Merck, Rahway, 11 edition

- (1989).
- [220] Z. Lu, C. Wang, W. Deng, M. T. Achille, J. Jie, and X. Zhang, Meniscus-guided coating of organic crystalline thin films for high-performance organic field-effect transistors, *J. Mater. Chem. C*, **8**, 9133, doi:[10.1039/D0TC01887B](https://doi.org/10.1039/D0TC01887B) (2020).
- [221] J. E. B. Katari, V. L. Colvin, and A. P. Alivisatos, X-ray photoelectron spectroscopy of CdSe nanocrystals with applications to studies of the nanocrystal surface, *J. Phys. Chem.*, **98**, 4109, doi:[10.1021/j100066a034](https://doi.org/10.1021/j100066a034) (1994).
- [222] P. B. Johnson and R. W. Christy, Optical constants of the noble metals, *Phys. Rev. B*, **6**, 4370, doi:[10.1103/PhysRevB.6.4370](https://doi.org/10.1103/PhysRevB.6.4370) (1972).
- [223] N. C. Lindquist, P. Nagpal, K. M. McPeak, D. J. Norris, and S.-H. Oh, Engineering metallic nanostructures for plasmonics and nanophotonics, *Rep. Prog. Phys.*, **75**, 036501, doi:[10.1088/0034-4885/75/3/036501](https://doi.org/10.1088/0034-4885/75/3/036501) (2012).
- [224] T. E. Graedel, Corrosion mechanisms for silver exposed to the atmosphere, *J. Electrochem. Soc.*, **139**, 1963, doi:[10.1149/1.2221162](https://doi.org/10.1149/1.2221162) (1992).
- [225] S. M. George, Atomic layer deposition: an overview, *Chem. Rev.*, **110**, 111, doi:[10.1021/cr900056b](https://doi.org/10.1021/cr900056b) (2010).
- [226] A. Hinderhofer, U. Heinemeyer, A. Gerlach, S. Kowarik, R. M. J. Jacobs, Y. Sakamoto, T. Suzuki, and F. Schreiber, Optical properties of pentacene and perfluoropentacene thin films, *J. Chem. Phys.*, **127**, 194705, doi:[10.1063/1.2786992](https://doi.org/10.1063/1.2786992) (2007).
- [227] J. Als-Nielsen and D. McMorrow, Elements of modern X-ray physics, John Wiley & Sons, Chichester, 2nd edition, doi:[10.1002/9781119998365](https://doi.org/10.1002/9781119998365) (2011).
- [228] M. Tolan, X-ray scattering from soft-matter thin films: Materials science and basic research, Springer, Berlin (1999).
- [229] A. Hinderhofer, C. Frank, T. Hosokai, A. Resta, A. Gerlach, and F. Schreiber, Structure and morphology of coevaporated pentacene-perfluoropentacene thin films, *J. Chem. Phys.*, **134**, 104702, doi:[10.1063/1.3557476](https://doi.org/10.1063/1.3557476) (2011).
- [230] H. Günzler and H.-U. Gremlich, IR-Spektroskopie: Eine Einführung, Wiley-VCH Weinheim, 4th edition (2003).
- [231] B. C. Smith, Fundamentals of Fourier transform infrared spectroscopy, CRC press, Boca Raton, 2nd edition, doi:[10.1201/b10777](https://doi.org/10.1201/b10777) (2011).
- [232] B. L. Frey, R. M. Corn, and S. C. Weibel, Polarization-modulation approaches to reflection-absorption spectroscopy. In Handbook of Vibrational Spectroscopy (eds J. M. Chalmers and P. R. Griffiths), John Wiley & Sons, Ltd, Chichester, doi:[10.1002/0470027320.s2206](https://doi.org/10.1002/0470027320.s2206) (2006).
- [233] S. Zorn, *In-situ* studies of protein-resistant self-assembling monolayers, Ph.D. thesis, Eberhard Karls Universität Tübingen (2010).
- [234] V. Zamlynny, Electrochemical and spectroscopic studies of pyridine surfactants at the gold-electrolyte interface, Ph.D. thesis, University of Guelph (2002).
- [235] K. W. Hipps and G. A. Crosby, Applications of the photoelastic modulator to polarization spectroscopy, *J. Phys. Chem.*, **83**, 555, doi:[10.1021/j100468a001](https://doi.org/10.1021/j100468a001) (1979).

-
- [236] G. Gauglitz and D. S. Moore, editors, Handbook of spectroscopy, Second, Enlarged Edition, Wiley-VCH Weinheim (2014).
- [237] A. D. Utyushev, V. I. Zakomirnyi, and I. L. Rasskazov, Collective lattice resonances: Plasmonics and beyond, *Rev. Phys.*, **6**, 100051, doi:[10.1016/j.revip.2021.100051](https://doi.org/10.1016/j.revip.2021.100051) (2021).
- [238] C. Ruckebusch, M. Sliwa, P. Pernot, A. de Juan, and R. Tauler, Comprehensive data analysis of femtosecond transient absorption spectra: A review, *J. Photochem. Photobiol. C*, **13**, 1, doi:[10.1016/j.jphotochemrev.2011.10.002](https://doi.org/10.1016/j.jphotochemrev.2011.10.002) (2012).
- [239] R. Berera, R. van Grondelle, and J. T. M. Kennis, Ultrafast transient absorption spectroscopy: principles and application to photosynthetic systems, *Photosynth. Res.*, **101**, 105, doi:[10.1007/s11120-009-9454-y](https://doi.org/10.1007/s11120-009-9454-y) (2009).
- [240] T. B. Norris, Femtosecond pulse amplification at 250 kHz with a Ti:sapphire regenerative amplifier and application to continuum generation, *Opt. Lett.*, **17**, 1009, doi:[10.1364/OL.17.001009](https://doi.org/10.1364/OL.17.001009) (1992).
- [241] G. Cerullo and S. De Silvestri, Ultrafast optical parametric amplifiers, *Rev. Sci. Instrum.*, **74**, 1, doi:[10.1063/1.1523642](https://doi.org/10.1063/1.1523642) (2003).
- [242] V. I. Klimov, Optical nonlinearities and ultrafast carrier dynamics in semiconductor nanocrystals, *J. Phys. Chem. B*, **104**, 6112, doi:[10.1021/jp9944132](https://doi.org/10.1021/jp9944132) (2000).
- [243] V. Klimov, S. Hunsche, and H. Kurz, Biexciton effects in femtosecond nonlinear transmission of semiconductor quantum dots, *Phys. Rev. B*, **50**, 8110, doi:[10.1103/PhysRevB.50.8110](https://doi.org/10.1103/PhysRevB.50.8110) (1994).
- [244] Y. Ishino, K. Miyata, T. Sugimoto, K. Watanabe, Y. Matsumoto, T. Uemura, and J. Takeya, Ultrafast exciton dynamics in dinaphtho[2,3-*b*:2'3'-*f*]thieno[3,2-*b*]-thiophene thin films, *Phys. Chem. Chem. Phys.*, **16**, 7501, doi:[10.1039/C3CP54157F](https://doi.org/10.1039/C3CP54157F) (2014).
- [245] A. Rao, M. W. B. Wilson, S. Albert-Seifried, R. Di Pietro, and R. H. Friend, Photophysics of pentacene thin films: The role of exciton fission and heating effects, *Phys. Rev. B*, **84**, 195411, doi:[10.1103/PhysRevB.84.195411](https://doi.org/10.1103/PhysRevB.84.195411) (2011).
- [246] C. Zeiser, L. Moretti, D. Lepple, G. Cerullo, M. Maiuri, and K. Broch, Singlet heterofission in tetracene-pentacene thin-film blends, *Angew. Chem. Int. Ed.*, **59**, 19966, doi:[10.1002/anie.202007412](https://doi.org/10.1002/anie.202007412) (2020).
- [247] I. H. M. van Stokkum, D. S. Larsen, and R. van Grondelle, Global and target analysis of time-resolved spectra, *Biochim. Biophys. Acta*, **1657**, 82, doi:[10.1016/j.bbabi.2004.04.011](https://doi.org/10.1016/j.bbabi.2004.04.011) (2004).
- [248] J. J. Snellenburg, S. P. Laptinok, R. Seger, K. M. Mullen, and I. H. M. van Stokkum, Glotaran: A java-based graphical user interface for the R-package TIMP, *J. Stat. Softw.*, **49**, 1, doi:[10.18637/jss.v049.i03](https://doi.org/10.18637/jss.v049.i03) (2012).
- [249] B. Wegner, L. Grubert, C. Dennis, A. Opitz, A. Röttger, Y. Zhang, S. Barlow, S. R. Marder, S. Hecht, K. Müllen, and N. Koch, Predicting the yield of ion pair formation in molecular electrical doping: redox-potentials *versus* ionization energy/electron affinity, *J. Mater. Chem. C*, **7**, 13839, doi:[10.1039/c9tc04500g](https://doi.org/10.1039/c9tc04500g) (2019).

- [250] K. H. Frank, P. Yannoulis, R. Dudde, and E. E. Koch, Unoccupied molecular orbitals of aromatic hydrocarbons adsorbed on Ag (111), *J. Chem. Phys.*, **89**, 7569, doi:[10.1063/1.455720](https://doi.org/10.1063/1.455720) (1988).
- [251] S. Milita, M. Servidori, F. Cicoira, C. Santato, and A. Pifferi, Synchrotron X-ray investigation of tetracene thin films grown at different deposition fluxes, *Nucl. Instrum. Methods Phys. Res., B*, **246**, 101, doi:[10.1016/j.nimb.2005.12.042](https://doi.org/10.1016/j.nimb.2005.12.042) (2006).
- [252] P. Brodard, A. Sarbach, J.-C. Gumy, T. Bally, and E. Vauthey, Excited-state dynamics of organic radical ions in liquids and in low-temperature matrices, *J. Phys. Chem. A*, **105**, 6594, doi:[10.1021/jp010808l](https://doi.org/10.1021/jp010808l) (2001).
- [253] O. Kataeva, M. Nohr, K. Ivshin, S. Hampel, B. Büchner, and M. Knupfer, Understanding intermolecular interactions in a tetracene–F₄TCNQ cocrystal via its electron density distribution and topology, *Cryst. Growth Des.*, **21**, 471, doi:[10.1021/acs.cgd.0c01287](https://doi.org/10.1021/acs.cgd.0c01287) (2021).
- [254] M. Meneghetti and C. Pecile, Charge–transfer organic crystals: Molecular vibrations and spectroscopic effects of electron–molecular vibration coupling of the strong electron acceptor TCNQF₄, *J. Chem. Phys.*, **84**, 4149, doi:[10.1063/1.450086](https://doi.org/10.1063/1.450086) (1986).
- [255] A. M. Valencia, M. Guerrini, and C. Cocchi, *Ab initio* modelling of local interfaces in doped organic semiconductors, *Phys. Chem. Chem. Phys.*, **22**, 3527, doi:[10.1039/C9CP06655A](https://doi.org/10.1039/C9CP06655A) (2020).
- [256] F. L. Hirshfeld, Bonded-atom fragments for describing molecular charge densities, *Theor. Chim. Acta*, **44**, 129, doi:[10.1007/BF00549096](https://doi.org/10.1007/BF00549096) (1977).
- [257] C. Müller, T. Pascher, A. Eriksson, P. Chabera, and J. Uhlig, KiMoPack: A python package for kinetic modeling of the chemical mechanism, *J. Phys. Chem. A*, **126**, 4087, doi:[10.1021/acs.jpca.2c00907](https://doi.org/10.1021/acs.jpca.2c00907) (2022).
- [258] R. Englman and J. Jortner, The energy gap law for radiationless transitions in large molecules, *Mol. Phys.*, **18**, 145, doi:[10.1080/00268977000100171](https://doi.org/10.1080/00268977000100171) (1970).
- [259] A. A. Bakulin, D. S. Martyanov, D. Y. Paraschuk, M. S. Pshenichnikov, and P. H. M. van Loosdrecht, Ultrafast charge photogeneration dynamics in ground-state charge-transfer complexes based on conjugated polymers, *J. Phys. Chem. B*, **112**, 13730, doi:[10.1021/jp8048839](https://doi.org/10.1021/jp8048839) (2008).
- [260] N. Hofeditz, M. Gerhard, C. P. Theurer, J. Hausch, K. Broch, W. Heimbrodtt, and M. Koch, Photoexcitation dynamics in strongly interacting donor/acceptor blends probed by time-resolved photoluminescence spectroscopy, *J. Phys. Chem. C*, **125**, 17194, doi:[10.1021/acs.jpcc.1c04183](https://doi.org/10.1021/acs.jpcc.1c04183) (2021).
- [261] C. P. Theurer, M. Richter, D. Rana, G. Duva, D. Lepple, A. Hinderhofer, F. Schreiber, P. Tegeder, and K. Broch, Coexistence of ion pairs and charge-transfer complexes and their impact on pentacene singlet fission, *J. Phys. Chem. C*, **125**, 23952, doi:[10.1021/acs.jpcc.1c07457](https://doi.org/10.1021/acs.jpcc.1c07457) (2021).
- [262] H. Kleemann, C. Schuenemann, A. A. Zakhidov, M. Riede, B. Lüssem, and K. Leo, Structural phase transition in pentacene caused by molecular doping and its effect on

-
- charge carrier mobility, *Org. Electron.*, **13**, 58, doi:[10.1016/j.orgel.2011.09.027](https://doi.org/10.1016/j.orgel.2011.09.027) (2012).
- [263] A. Hinderhofer, J. Hagenlocher, A. Gerlach, J. Krug, M. Oettel, and F. Schreiber, Nonequilibrium roughness evolution of small molecule mixed films reflecting equilibrium phase behavior, *J. Phys. Chem. C*, **126**, 11348, doi:[10.1021/acs.jpcc.2c02177](https://doi.org/10.1021/acs.jpcc.2c02177) (2022).
- [264] M. Brinkmann, V. S. Videva, A. Bieber, J. J. André, P. Turek, L. Zuppiroli, P. Bugnon, M. Schaer, F. Nuesch, and R. Humphry-Baker, Electronic and structural evidences for charge transfer and localization in iodine-doped pentacene, *J. Phys. Chem. A*, **108**, 8170, doi:[10.1021/jp048343x](https://doi.org/10.1021/jp048343x) (2004).
- [265] C. Isenberg and T. P. I. Saragi, Revealing the origin of magnetoresistance in unipolar amorphous organic field-effect transistors, *J. Mater. Chem. C*, **2**, 8569, doi:[10.1039/c4tc00702f](https://doi.org/10.1039/c4tc00702f) (2014).
- [266] Z.-Y. Lu, C. J. Nicklaw, D. M. Fleetwood, R. D. Schrimpf, and S. T. Pantelides, Structure, properties, and dynamics of oxygen vacancies in amorphous SiO₂, *Phys. Rev. Lett.*, **89**, 285505, doi:[10.1103/PhysRevLett.89.285505](https://doi.org/10.1103/PhysRevLett.89.285505) (2002).
- [267] K. Harada, M. Sumino, C. Adachi, S. Tanaka, and K. Miyazaki, Improved thermoelectric performance of organic thin-film elements utilizing a bilayer structure of pentacene and 2,3,5,6-tetrafluoro-7,7,8,8-tetracyanoquinodimethane (F₄-TCNQ), *Appl. Phys. Lett.*, **96**, 253304, doi:[10.1063/1.3456394](https://doi.org/10.1063/1.3456394) (2010).
- [268] S. Khan and S. Mazumdar, Theory of transient excited state absorptions in pentacene and derivatives: Triplet–triplet biexciton versus free triplets, *J. Phys. Chem. Lett.*, **8**, 5943, doi:[10.1021/acs.jpcclett.7b02748](https://doi.org/10.1021/acs.jpcclett.7b02748) (2017).
- [269] R. D. Pensack, E. E. Ostroumov, A. J. Tilley, S. Mazza, C. Grieco, K. J. Thorley, J. B. Asbury, D. S. Seferos, J. E. Anthony, and G. D. Scholes, Observation of two triplet-pair intermediates in singlet exciton fission, *J. Phys. Chem. Lett.*, **7**, 2370, doi:[10.1021/acs.jpcclett.6b00947](https://doi.org/10.1021/acs.jpcclett.6b00947) (2016).
- [270] H. Marciniak, I. Pugliesi, B. Nickel, and S. Lochbrunner, Ultrafast singlet and triplet dynamics in microcrystalline pentacene films, *Phys. Rev. B*, **79**, 235318, doi:[10.1103/PhysRevB.79.235318](https://doi.org/10.1103/PhysRevB.79.235318) (2009).
- [271] H. Marciniak, M. Fiebig, M. Huth, S. Schiefer, B. Nickel, F. Selmaier, and S. Lochbrunner, Ultrafast exciton relaxation in microcrystalline pentacene films, *Phys. Rev. Lett.*, **99**, 176402, doi:[10.1103/PhysRevLett.99.176402](https://doi.org/10.1103/PhysRevLett.99.176402) (2007).
- [272] M. T. Trinh, A. Pinkard, A. B. Pun, S. N. Sanders, E. Kumarasamy, M. Y. Sfeir, L. M. Campos, X. Roy, and X.-Y. Zhu, Distinct properties of the triplet pair state from singlet fission, *Sci. Adv.*, **3**, e1700241, doi:[10.1126/sciadv.1700241](https://doi.org/10.1126/sciadv.1700241) (2017).
- [273] S. Lukman, J. M. Richter, L. Yang, P. Hu, J. Wu, N. C. Greenham, and A. J. Musser, Efficient singlet fission and triplet-pair emission in a family of zethrene diradicaloids, *J. Am. Chem. Soc.*, **139**, 18376, doi:[10.1021/jacs.7b10762](https://doi.org/10.1021/jacs.7b10762) (2017).
- [274] T. Aoki-Matsumoto, K. Furuta, T. Yamada, H. Moriya, K. Mizuno, and A. H. Matsui, Excitonic photoluminescence in pentacene single crystal, *Int. J. Mod. Phys. B*, **15**, 3753, doi:[10.1142/S0217979201008585](https://doi.org/10.1142/S0217979201008585) (2001).

- [275] R. He, X. Chi, A. Pinczuk, D. V. Lang, and A. P. Ramirez, Extrinsic optical recombination in pentacene single crystals: Evidence of gap states, *Appl. Phys. Lett.*, **87**, 211117, doi:[10.1063/1.2135494](https://doi.org/10.1063/1.2135494) (2005).
- [276] R. He, N. G. Tassi, G. B. Blanchet, and A. Pinczuk, Intense photoluminescence from pentacene monolayers, *Appl. Phys. Lett.*, **96**, 263303, doi:[10.1063/1.3458816](https://doi.org/10.1063/1.3458816) (2010).
- [277] F. Anger, J. O. Ossó, U. Heinemeyer, K. Broch, R. Scholz, A. Gerlach, and F. Schreiber, Photoluminescence spectroscopy of pure pentacene, perfluoropentacene, and mixed thin films, *J. Chem. Phys.*, **136**, 054701, doi:[10.1063/1.3677839](https://doi.org/10.1063/1.3677839) (2012).
- [278] M. Birkholz, Thin film analysis by X-ray scattering, WILEY-VCH, Weinheim (2006).
- [279] C. K. Carniglia, Scalar scattering theory for multilayer optical coatings, *Opt. Eng.*, **18**, 182104, doi:[10.1117/12.7972335](https://doi.org/10.1117/12.7972335) (1979).
- [280] R. He, N. G. Tassi, G. B. Blanchet, and A. Pinczuk, Fundamental optical recombination in pentacene clusters and ultrathin films, *Appl. Phys. Lett.*, **87**, 103107, doi:[10.1063/1.2040011](https://doi.org/10.1063/1.2040011) (2005).
- [281] S. Guha, J. D. Rice, Y. T. Yau, C. M. Martin, M. Chandrasekhar, H. R. Chandrasekhar, R. Guentner, P. Scanduicci de Freitas, and U. Scherf, Temperature-dependent photoluminescence of organic semiconductors with varying backbone conformation, *Phys. Rev. B*, **67**, 125204, doi:[10.1103/PhysRevB.67.125204](https://doi.org/10.1103/PhysRevB.67.125204) (2003).
- [282] J. E. Northrup and M. L. Chabinyc, Gap states in organic semiconductors: Hydrogen- and oxygen-induced states in pentacene, *Phys. Rev. B*, **68**, 041202, doi:[10.1103/PhysRevB.68.041202](https://doi.org/10.1103/PhysRevB.68.041202) (2003).
- [283] M. Pinterić, S. Roh, S. Hammer, J. Pflaum, M. Dressel, and E. Uykur, Distinction of charge transfer and frenkel excitons in pentacene traced *via* infrared spectroscopy, *J. Mater. Chem. C*, **10**, 5582, doi:[10.1039/D1TC04297A](https://doi.org/10.1039/D1TC04297A) (2022).
- [284] Y. Qian, X. Li, A. R. Harutyunyan, G. Chen, Y. Rao, and H. Chen, Herzberg–Teller effect on the vibrationally resolved absorption spectra of single-crystalline pentacene at finite temperatures, *J. Phys. Chem. A*, **124**, 9156, doi:[10.1021/acs.jpca.0c07896](https://doi.org/10.1021/acs.jpca.0c07896) (2020).
- [285] Y. Qian, T. Zhang, J. Han, A. R. Harutyunyan, G. Chen, Y. Rao, and H. Chen, Symmetry-breaking enhanced Herzberg–Teller effect with brominated polyacenes, *J. Phys. Chem. A*, **125**, 3589, doi:[10.1021/acs.jpca.1c01293](https://doi.org/10.1021/acs.jpca.1c01293) (2021).
- [286] C. P. Theurer, F. Laible, J. Tang, K. Broch, M. Fleischer, and F. Schreiber, Strong light-matter coupling in pentacene thin films on plasmonic arrays, *under review* (2023).
- [287] I. Meyenburg, T. Breuer, A. Karthäuser, S. Chatterjee, G. Witte, and W. Heimbrodt, Temperature-resolved optical spectroscopy of pentacene polymorphs: variation of herringbone angles in single-crystals and interface-controlled thin films, *Phys. Chem. Chem. Phys.*, **18**, 3825, doi:[10.1039/C5CP07836A](https://doi.org/10.1039/C5CP07836A) (2016).
- [288] R. Deshmukh, P. Marques, A. Panda, M. Y. Sfeir, S. R. Forrest, and V. M. Menon, Modifying the spectral weights of vibronic transitions via strong coupling to surface plasmons, *ACS Photonics*, **7**, 43, doi:[10.1021/acsphotonics.9b01357](https://doi.org/10.1021/acsphotonics.9b01357) (2020).

-
- [289] T. Zeng, R. Hoffmann, and N. Ananth, The low-lying electronic states of pentacene and their roles in singlet fission, *J. Am. Chem. Soc.*, **136**, 5755, doi:[10.1021/ja500887a](https://doi.org/10.1021/ja500887a) (2014).
- [290] C. P. Theurer, A. Weber, M. Richter, M. Bender, P. Michel, D. Rana, K. Kumar, U. Bunz, M. Scheele, P. Tegeder, F. Schreiber, and K. Broch, Short-range organization and photophysical properties of CdSe quantum dots coupled with aryleneethynylenes, *Nanotechnol.*, **33**, 230001, doi:[10.1088/1361-6528/ac52bd](https://doi.org/10.1088/1361-6528/ac52bd) (2022).
- [291] A. G. Young, N. Al-Salim, D. P. Green, and A. J. McQuillan, Attenuated total reflection infrared studies of oleate and trioctylphosphine oxide ligand adsorption and exchange reactions on CdS quantum dot films, *Langmuir*, **24**, 3841, doi:[10.1021/la703655v](https://doi.org/10.1021/la703655v) (2008).
- [292] A. Y. Koposov, T. Cardolaccia, V. Albert, E. Badaeva, S. Kilina, T. J. Meyer, S. Tretiak, and M. Sykora, Formation of assemblies comprising Ru–polypyridine complexes and CdSe nanocrystals studied by ATR-FTIR spectroscopy and DFT modeling, *Langmuir*, **27**, 8377, doi:[10.1021/la200531s](https://doi.org/10.1021/la200531s) (2011).
- [293] I. A. Zaluzhnyy, R. P. Kurta, A. André, O. Y. Gorobtsov, M. Rose, P. Skopintsev, I. Besedin, A. V. Zozulya, M. Sprung, F. Schreiber, I. A. Vartanyants, and M. Scheele, Quantifying angular correlations between the atomic lattice and the superlattice of nanocrystals assembled with directional linking, *Nano Lett.*, **17**, 3511, doi:[10.1021/acs.nanolett.7b00584](https://doi.org/10.1021/acs.nanolett.7b00584) (2017).
- [294] I. A. Zaluzhnyy, R. P. Kurta, M. Scheele, F. Schreiber, B. I. Ostrovskii, and I. A. Vartanyants, Angular X-ray cross-correlation analysis (AXCCA): Basic concepts and recent applications to soft matter and nanomaterials, *Materials*, **12**, 3464, doi:[10.3390/ma12213464](https://doi.org/10.3390/ma12213464) (2019).
- [295] B. Lee, P. Podsiadlo, S. Rupich, D. V. Talapin, T. Rajh, and E. V. Shevchenko, Comparison of structural behavior of nanocrystals in randomly packed films and long-range ordered superlattices by time-resolved small angle X-ray scattering, *J. Am. Chem. Soc.*, **131**, 16386, doi:[10.1021/ja906632b](https://doi.org/10.1021/ja906632b) (2009).
- [296] O. Voznyy, B. R. Sutherland, A. H. Ip, D. Zhitomirsky, and E. H. Sargent, Engineering charge transport by heterostructuring solution-processed semiconductors, *Nat. Rev. Mater.*, **2**, 17026, doi:[10.1038/natrevmats.2017.26](https://doi.org/10.1038/natrevmats.2017.26) (2017).
- [297] J. N. Wilson, M. D. Smith, V. Enkelmann, and U. H. F. Bunz, Cruciform π -systems: effect of aggregation on emission, *Chem. Commun.*, 1700, doi:[10.1039/B406495J](https://doi.org/10.1039/B406495J) (2004).
- [298] S. F. Wuister, C. de Mello Donegá, and A. Meijerink, Influence of thiol capping on the exciton luminescence and decay kinetics of CdTe and CdSe quantum dots, *J. Phys. Chem. B*, **108**, 17393, doi:[10.1021/jp047078c](https://doi.org/10.1021/jp047078c) (2004).
- [299] Y. Gao and X. Peng, Photogenerated excitons in plain core CdSe nanocrystals with unity radiative decay in single channel: The effects of surface and ligands, *J. Am. Chem. Soc.*, **137**, 4230, doi:[10.1021/jacs.5b01314](https://doi.org/10.1021/jacs.5b01314) (2015).
- [300] C. Zhang, T. N. Do, X. Ong, Y. Chan, and H.-S. Tan, Understanding the features in the ultrafast transient absorption spectra of CdSe quantum dots, *Chem. Phys.*, **481**,

- 157, doi:[10.1016/j.chemphys.2016.08.027](https://doi.org/10.1016/j.chemphys.2016.08.027) (2016).
- [301] M. Tabachnyk, B. Ehrler, S. Gélinas, M. L. Böhm, B. J. Walker, K. P. Musselman, N. C. Greenham, R. H. Friend, and A. Rao, Resonant energy transfer of triplet excitons from pentacene to PbSe nanocrystals, *Nat. Mater.*, **13**, 1033, doi:[10.1038/NMAT4093](https://doi.org/10.1038/NMAT4093) (2014).
- [302] N. J. Thompson, M. W. B. Wilson, D. N. Congreve, P. R. Brown, J. M. Scherer, T. S. Bischof, M. Wu, N. Geva, M. Welborn, T. V. Voorhis, V. Bulović, M. G. Bawendi, and M. A. Baldo, Energy harvesting of non-emissive triplet excitons in tetracene by emissive PbS nanocrystals, *Nat. Mater.*, **13**, 1039, doi:[10.1038/nmat4097](https://doi.org/10.1038/nmat4097) (2014).
- [303] J. J. Burdett and C. J. Bardeen, Quantum beats in crystalline tetracene delayed fluorescence due to triplet pair coherences produced by direct singlet fission, *J. Am. Chem. Soc.*, **134**, 8597, doi:[10.1021/ja301683w](https://doi.org/10.1021/ja301683w) (2012).
- [304] DektakXT stylus profilometer user manual, Bruker Corporation (2011).
- [305] C. A. Leatherdale, W.-K. Woo, F. V. Mikulec, and M. G. Bawendi, On the absorption cross section of CdSe nanocrystal quantum dots, *J. Phys. Chem. B*, **106**, 7619, doi:[10.1021/jp025698c](https://doi.org/10.1021/jp025698c) (2002).

List of publications

1. C. P. Theurer, A. M. Valencia, J. Hausch, C. Zeiser, V. Sivanesan, C. Cocchi, P. Tegeder, and K. Broch, Photophysics of charge transfer complexes formed by tetracene and strong acceptors, *J. Phys. Chem. C*, **125**, 6313-6323, doi:[10.1021/acs.jpcc.0c10815](https://doi.org/10.1021/acs.jpcc.0c10815) (2021)
2. C. P. Theurer, M. Richter, D. Rana, G. Duva, D. Lepple, A. Hinderhofer, F. Schreiber, P. Tegeder, and K. Broch, Coexistence of ion pairs and charge-transfer complexes and their impact on pentacene singlet fission, *J. Phys. Chem. C*, **125**, 23952-23959, doi:[10.1021/acs.jpcc.1c07457](https://doi.org/10.1021/acs.jpcc.1c07457) (2021)
3. C. P. Theurer, A. Weber, M. Richter, M. Bender, P. Michel, D. Rana, K. Kumar, U. Bunz, M. Scheele, P. Tegeder, F. Schreiber, and K. Broch, Short-range organization and photophysical properties of CdSe quantum dots coupled with aryleneethynylenes, *Nanotechnol.*, **33**, 230001, doi:[10.1088/1361-6528/ac52bd](https://doi.org/10.1088/1361-6528/ac52bd) (2022)
4. C. P. Theurer, F. Laible, J. Tang, K. Broch, M. Fleischer, and F. Schreiber, Strong light-matter coupling in pentacene thin films on plasmonic arrays, *Nanoscale*, **15**, 11707-11713, doi:[10.1039/d3nr01108a](https://doi.org/10.1039/d3nr01108a) (2023)
5. N. Hofeditz, M. Gerhard, C. P. Theurer, J. Hausch, K. Broch, W. Heimbrodtt, and M. Koch, Photoexcitation dynamics in strongly interacting donor/acceptor blends probed by time-resolved photoluminescence spectroscopy, *J. Phys. Chem. C*, **125**, 17194–17201, doi:[10.1021/acs.jpcc.1c04183](https://doi.org/10.1021/acs.jpcc.1c04183) (2021)

Danksagung

An dieser Stelle möchte ich mich von Herzen bei allen bedanken, die mich beim Erstellen dieser Arbeit unterstützt haben. Ganz besonders danke ich Prof. Dr. Dr. h.c. Frank Schreiber für die Möglichkeit, meine Doktorarbeit in seiner Arbeitsgruppe anzufertigen und dabei viele spannende, interdisziplinäre Forschungsbereiche erkunden zu können, seine gute Betreuung sowie das mir entgegengebrachte Vertrauen. Ebenso dankbar bin ich Dr. Katharina Broch für die enge Betreuung dieser Arbeit, viele inspirierende wissenschaftliche Diskussionen und die stete Unterstützung. Bei JProf. Dr. Jannika Lauth möchte ich mich für die Übernahme des Zweitgutachtens dieser Arbeit bedanken.

Des Weiteren danke ich Prof. Dr. Marcus Scheele für die gute Zusammenarbeit und die Möglichkeit, spannende Materialsysteme im Rahmen einer Kooperation zu untersuchen. In diesem Zusammenhang möchte ich mich auch bei Dr. Krishan Kumar, Patrick Michel, Dr. Björn Märker, Markus Bender und Prof. Dr. Uwe H. F. Bunz für die Synthese und Bereitstellung von Materialien bedanken. Ebenfalls möchte ich mich bei Prof. Dr. Monika Fleischer für die gute und unkomplizierte Zusammenarbeit im Rahmen einer Kooperation bedanken, die es mir ermöglichte, ein weiteres interessantes Themengebiet zu erforschen. Hierbei geht auch ein großes Dankeschön an Dr. Florian Laible, Jia Tang und Dr. Ronny Löffler für die Einführung in verschiedene Methoden sowie für die Diskussion der erhaltenen Ergebnisse.

Bei Prof. Dr. Petra Tegeder möchte ich mich für die angenehme und fruchtbare Kooperation bedanken, durch welche die Untersuchung der photophysikalischen Eigenschaften der Systeme in dieser Arbeit möglich wurde. Ein besonderer Dank gilt an dieser Stelle Martin Richter, Dr. Debkumar Rana und Dr. Vipilan Sivanesan für die Unterstützung während der Messungen. Ebenso danke ich Prof. Dr. Caterina Cocchi und Dr. Ana M. Valencia für die theoretischen Berechnungen im Rahmen einer weiteren Kooperation, die ein tieferes Verständnis der untersuchten Systeme ermöglichte.

Ein großes Dankeschön geht an Antonia Weber, Julian Hausch, Dr. Clemens Zeiser und Frederik Unger für die sehr konstruktive, stets unkomplizierte und oft heitere Zusammenarbeit in verschiedenen Projekten, die mir viel Spaß gemacht und wesentlich zum Gelingen dieser Arbeit beigetragen hat. Auch bei allen anderen Mitgliedern der Arbeitsgruppen Schreiber und Broch möchte ich mich für die viele Unterstützung bei verschiedensten Herausforderungen sowie die sehr freundliche Atmosphäre bedanken, wobei an dieser Stelle Katja Schick, Daniel Lepple, Dr. Madeleine Fries, Nina Conzelmann und Dr. Giuliano Duva namentlich

erwähnt werden sollen. Für das Korrekturlesen von Teilen dieser Arbeit danke ich Frederik Unger, Julian Hausch, Dr. Katharina Broch, Dr. Clemens Zeiser, Dr. Ralph Maier, Michael Zimmermann, Fabian Strauß und Lukas Lang.

Bei meinen treuen Nano-Studienkollegen und guten Freunden Frederik Unger, Dr. Ralph Maier, Michael Zimmermann und Robert Illinseer möchte ich mich für die großartige Zeit in Tübingen und darüber hinaus bedanken, an die ich mich immer gerne erinnern werde. Zu guter Letzt gilt ein großer Dank meiner Familie und meiner Freundin für die sichere und bedingungslose Unterstützung während all dieser Jahre.